New developments in the theory of figures. : Rotating multi-layer, multibody polytropic systems

Baptiste Boutin-Basillais

université de BORDEAUX

université de BORDEAUX

THÈSE PRÉSENTÉE

POUR OBTENIR LE GRADE DE

DOCTEUR
DE L'UNIVERSITÉ DE BORDEAUX

ECOLE DOCTORALE 209

SCIENCES PHYSIQUES ET DE L'INGENIEUR

ASTROPHYSIQUE, PLASMA, NUCLEAIRE

Par **Baptiste BASILLAIS**

Nouvelle contribution à la théorie des figures. Les systèmes polytropiques multi-objets multi-couches en rotation différentielle

Sous la direction de : **Jean-Marc HURÉ**

Soutenue le 15 décembre 2020

Membres du jury :

M. Joel E. TOHLINE	Professeur Émérite	Louisiana State Univ.	Rapporteur
M. Georges MEYNET	Professeur	Observatoire de Genève	Rapporteur
M. Jean-Pierre DELVILLE	Directeur de Recherche	Univ. Bordeaux	Président
M. Tristan GUILLOT	Directeur de Recherche	Obs. de la Côte d'Azur	Examinateur
M. Emmanuel DI FOLCO	Astronome-Adjoint	Univ. Bordeaux	Examinateur
M. Jean-Marc HURÉ	Professeur	Univ. Bordeaux	Directeur

Résumé

Nouvelle contribution à la théorie des figures. Les systèmes polytropiques multi-objets multi-couches en rotation différentielle

Cette thèse est consacrée aux systèmes auto-gravitants en rotation différentielle. Elle apporte une contribution originale à l'étude des équilibres à symétrie axiale de type "multi-domaines" se déclinant en des configurations multi-objets et/ou multi-couches. Grâce à une approche multi-échelle, elle offre de nouveaux outils de diagnostics permettant de sonder la structure interne d'une grande diversité de systèmes astrophysiques en rotation rapide allant des étoiles au anneaux en passant par les planètes et les exoplanètes.

Notre travail s'est appuyé sur la résolution numérique de l'équation de Bernoulli couplée à l'équation de Poisson pour des fluides d'équation d'état polytropique. Il a notamment nécessité le développement d'un algorithme de champ auto-cohérent (méthode SCF) spécifique implémenté dans le code DROP et dont la validité a été largement testée.

S'agissant de l'aspect multi-objets, une vaste exploration de l'espace des paramètres a permis de positionner les configurations binaires de type sphéroïde-anneau dans le diagramme de référence "rotation-moment cinétique". Nous avons ainsi mis en évidence les bifurcations connectant la séquence de Maclaurin et celle des anneaux, des solutions dégénérées ainsi qu'un ensemble de rotations limites. Concernant l'aspect multi-couches, nous avons caractérisé l'impact du profil de rotation et celui d'un champ gravitationnel externe sur la structure interne d'un système à deux couches de type "coeur-enveloppe". Nous confirmons la diminution de la masse limite de type Schönberg-Chandrasekhar sous l'effet d'une rotation différentielle globale. Nous montrons que ce seuil se trouve en revanche réhaussé en présence d'un compagnon massif. Le couplage d'un saut de densité et d'une discontinuité de rotation aux interfaces apparaît comme critique sur la structure globale. Enfin, en dépit du faible nombre de paramètres libres, nous montrons qu'il existe des solutions auto-gravitantes qui partagent la même forme, la même masse et la même vitesse de surface mais qui possédent des structures internes différentes.

Le code de calcul permet dès à présent de générer des équilibres composés de plusieurs objets et de plusieurs couches et devrait ainsi permettre d'accroître le réalisme des modèles en prédisant des observables plus pertinantes. Une application à l'anneau massif entourant le système triple de GG Tau est proposée. Une étude de la structure interne de Jupiter et de Saturne est en cours.

Mots clés : Gravitation, Théorie, Simulation, Equilibre, Fluide, Etoile, Planète

Abstract

New developments in the theory of figures. Rotating multi-layer, multibody polytropic systems

This thesis is devoted to the study of self-gravitating systems in differential rotation. It brings a novel contribution to the theory of figures in the axisymmetrical regime, by considering multibody and multi-layer configurations. In this purpose, we have developed a scale-free approach that provides us with new theoretical and numerical diagnostic tools enabling to better understand the internal structure of astrophysical objects such as planets, exoplanets, stars and rings.

We have improved the DROP code based on a Self-Consistent Field method in order to solve the Bernoulli equation coupled with the Poisson's equation for polytropic fluids. From a wide exploration of the parameter space, we show how the spheroid-ring configurations populate the rotation-angular momentum reference diagram. We find that there are many connections between the Maclaurin sequence and the One-Ring sequence along with a maximum rotation rate for all permitted equilibria. We have characterized the influence of differential rotation and of an external gravitational potential on the internal structure of a two-layer system made of a core and an envelope. We corroborate that the mass limit of the core given by a Schönberg-Chandrakhar-like limit is indeed reduced by differential rotation. However, this mass limit is increased by the presence of a massive toroidal companion. Strikingly, we show that different internal structures can lead to the same mass-radius-surface velocity relationship. We highlight the critical effect of a density jump paired with a rotation discontinuity at each layer interface.

The new version of the DROP code is already able to generate equilibria composed of multiple multi-layer objects, and, thereby, it gives us the opportunity to fine-tune observables. A short application to the internal structure of the massive ring in the GG tau is presented. The internal structure of Jupiter and Saturn as two-layer systems in currently being investigated.
Keywords : Gravitation, Theory, Simulation, Equilibrium, Fluid, Star, Planet

Contents

List of Figures

List of Tables

Chapter 1

Introduction

Contents

1.1 Figures of equilibrium

What is the shape of the Earth ? The majority of people would claim that it is a solid sphere, some people affirm that it is a flat disk, and other might even think that it is a ring. Even though all of the previous answers are theoretically valid for a self-gravitating body without any observations, none of the above are correct in the "common" sense for the Earth. Although, the solid sphere answer is the closest to the truth, the Earth's shape departs slightly from a perfect sphere due to its rotation. The first modern scientists arguing about this were Isaac Newton (1643-1727) and Jean-Dominique Cassini (1625-1712) in the early 18th century. Cassini defended a prolate (polar radius greater than the equatorial radius) Earth while Newton an oblate (equatorial radius greater than the polar radius) Earth. This disagreement was settled after an unequivocal observation of the Earth's oblatness by Maupertuis in Lapland in 1737.

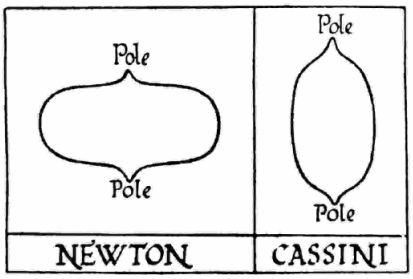

Figure 1.1: Caricature of the controversy between Isaac Newton and Jean-Dominique Cassini about the shape of the Earth. From Chandrasekhar (1969)

This discord was the dawn of the theory of figures : a field aiming to have a grasp on the properties, stability and dynamics of self-gravitating bodies under the effect of their own rotation (or spin). Massive bodies such as galaxies, stars, star clusters, planets and moons are held together by their own gravity, also called self-gravity : under the influence of their mass, all their components stick together as a whole if isolated "enough". Gravitation is responsible for the evolution of most astrophysical systems from birth to death at any astrophysical scales : from planetary to cosmological. It often leads to the formation of multiple components systems : star with disc/planets, binary stars, clusters, planets with rings/moons, black holes with accretion disc.

Initially devoted to the internal structure of stars and planets in the classical framework of Newton's laws, the theory of figures has applications in several fields of science : nuclear physics, biology, fluid mechanics and study all kind of shape : spherical Lane (1870); Ebert (1955); Bonnor (1956), ellipsoidal (Jacobi, 1834; Vandervoort, 1980), spheroidal (Ostriker and Mark, 1968; Hachisu, 1986), cylindrical (Toci and Galli, 2015a,b; Coughlin and Nixon, 2020) and toroidal (Wong, 1973, 1974; Shukhman, 1983; Huré and Hersant, 2017).

1.2 Rotation in the universe

Rotation is ubiquitous in the universe and yet frequently neglected in planetary and stellar evolution. Nonetheless, in the life of a star, rotation is of great importance and interest. It

is one of the key properties that determines all subsequent steps of the evolution and can even prevent formation of systems (see for instance the problem of angular momentum in disks). There is a short rewiew listing the self-gravitating system this thesis is concerned with.

1.2.1 Molecular clouds and filaments

Molecular clouds are star-forming regions. They are mainly constituted of molecular hydrogen H_2. Indeed, due to their rather low temperatures, when reaching a critical mass (Bonnor-Ebert mass or Jeans mass), their internal pressure cannot counterbalance the gravitational force thus triggering a gravitational collapse (Ebert, 1955; Bonnor, 1956). As a consequence, the cloud shrinks in size while its density rises up tremendously forming a protostar core at the center. During the fall down, the gravitational energy is converted into heat, thereby increasing the temperature. The rotation of matter increases due to the conservation of angular momentum and it often leads to the formation of a protostellar disk around the central seed. This phase is referred as the pre-stellar phase.

Molecular clouds exhibit substructures arranged in a filamentary network linking the densest regions (Arzoumanian et al., 2011; André et al., 2014a,b; Mattern et al., 2018). They are also observed at cosmological scales. The existence of such elongated structures in molecular clouds were already known (Schneider and Elmegreen, 1979; Johnstone and Bally, 1999; Myers, 2009b,a) but it was recently shown that every molecular clouds exhibits such structure (Men'shchikov et al., 2010; Hill et al., 2011; Wang et al., 2015) and play a key role in the star formation process : most of the prestellar cores are found within dense filaments (André, 2017). The filaments can be as long as 100 pc with a width of 0.1 pc, typically.

Molecular clouds can be studied with the theory of figures when considering spheres of isothermal fluids. This theoretical object is reffered as the Bonnor-Ebert spheres.

Bonnor-Ebert spheres are appropriate to model and understand star-forming regions and the gravitational collapse of giant molecular clouds (Ebert, 1955; Bonnor, 1956) (Aikawa et al., 2005; Kaminski et al., 2014). It approximates various prestellar cores (Bacmann et al., 2000; Alves et al., 2001; Kandori et al., 2005; Horedt, 2013; Marsh et al., 2014; Gong and Ostriker, 2015) and even the formation of circumstellar disks (Machida et al., 2014). However, some molecular clouds are not well described (Pattle and Ward-Thompson, 2015). One limit to the isothermal sphere is the uncertainty on the true isothermality of observed cores : due to the attenuation of light by the molecular cloud itself, it is possible that the temperature drops close to the center (Zucconi et al., 2001; Ward-Thompson et al., 2002; Crapsi et al., 2007). A new kind of Bonnor-Ebert sphere were therefore investigated : non-isothermal spheres to take into account this temperature variation (Evans et al., 2001; Galli et al., 2002; Sipilä et al., 2011, 2015, 2017).

1.2.2 Accretion disks and rings

Accretion disks are present around supermassive black holes (e.g. Active Galaxy Nuclei), around stellar black holes or neutron stars (e.g. X-ray binary) and around protostars (e.g. circumstellar disk). Planetary rings can be regarded as small accretion disk in which small

bodies and moons can form.

Protostellar envelopes and circumstellar disks are made of the leftover gas from the collapsing molecular cloud that formed the central body. At first, these accretion disks are most likely quasi-spherical accretion clouds. Matter from the disk falls toward the star but get replenished by the parent cloud. After exhausting all the gas reservoir from the parent cloud, this envelope adopt a disk shape under the influence of its own gravity (self-gravity). At the earliest stages, the disk is massive and account for a few percents of the total mass of the system and its self-gravity generates some deviation from the assumed keplerian rotation law and instabilities redistributing angular momentum. Circumstellar disks are thought to be the place where protoplanets, planet embryos, and planets form. Matter from the disc falls onto the star and produce jets (Maeder, 2009).

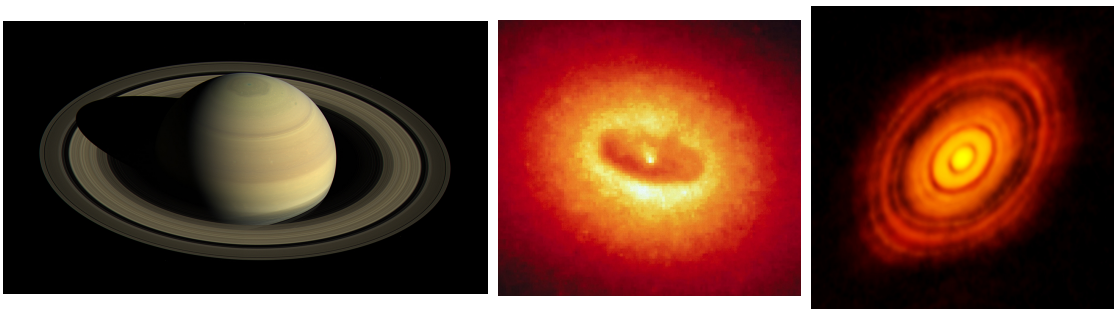

Figure 1.2: (left) Saturn and its rings taken from Cassini probe. (center) NGC 4261, an AGN. Image credit : HST. (right) HL Tauri, a protoplanetery system displaying multiple concentric rings. Image credit : ALMA / ESO.

1.2.3 Stars

Main-sequence stars

When a star is born following the collapse of a molecular cloud, it spends most of its life on what is called the main-sequence in the Hertzsprung–Russell diagram (see Fig.1.3) and is referred as a main-sequence star. While on this sequence, thermonuclear fusion of hydrogen into helium occurs. If the star's mass is high enough, helium get fused into heavier elements. Depending on the mass, stars do not have the same fate. A star with a mass lower than the Chandrasekhar limit, i.e. $M \lesssim 1.4\mathrm{M}_\odot$, evolves into a red giant (see Sect.1.2.3) and end its life as a white dwarf (see Sect.1.2.3). A star with an intermediate mass $1.4\mathrm{M}_\odot \leq M \leq 8\mathrm{M}_\odot$ fuses heavier elements. For a massive star with $M \gtrsim 8\mathrm{M}_\odot$, it evolves into a red supergiant and a neutron star. With a mass even higher than $40\mathrm{M}_\odot$, it ends in a black hole. A ain-sequence star has a surface temperature of about a few thousands Kelvin and a radius up to $200\mathrm{R}_\odot$.

Be stars : Be stars are particularly fast spinning B-type stars characterized by an emission in the Balmer series lines (Porter and Rivinius, 2003). Be stars have masses ranging from 3 to $20\mathrm{M}_\odot$, radius from 2 to 8 $\mathrm{R}_\odot$ and have a high rotation velocity, a few hundreds kilometers per second at the equator. A relevant criterion is the critical velocity

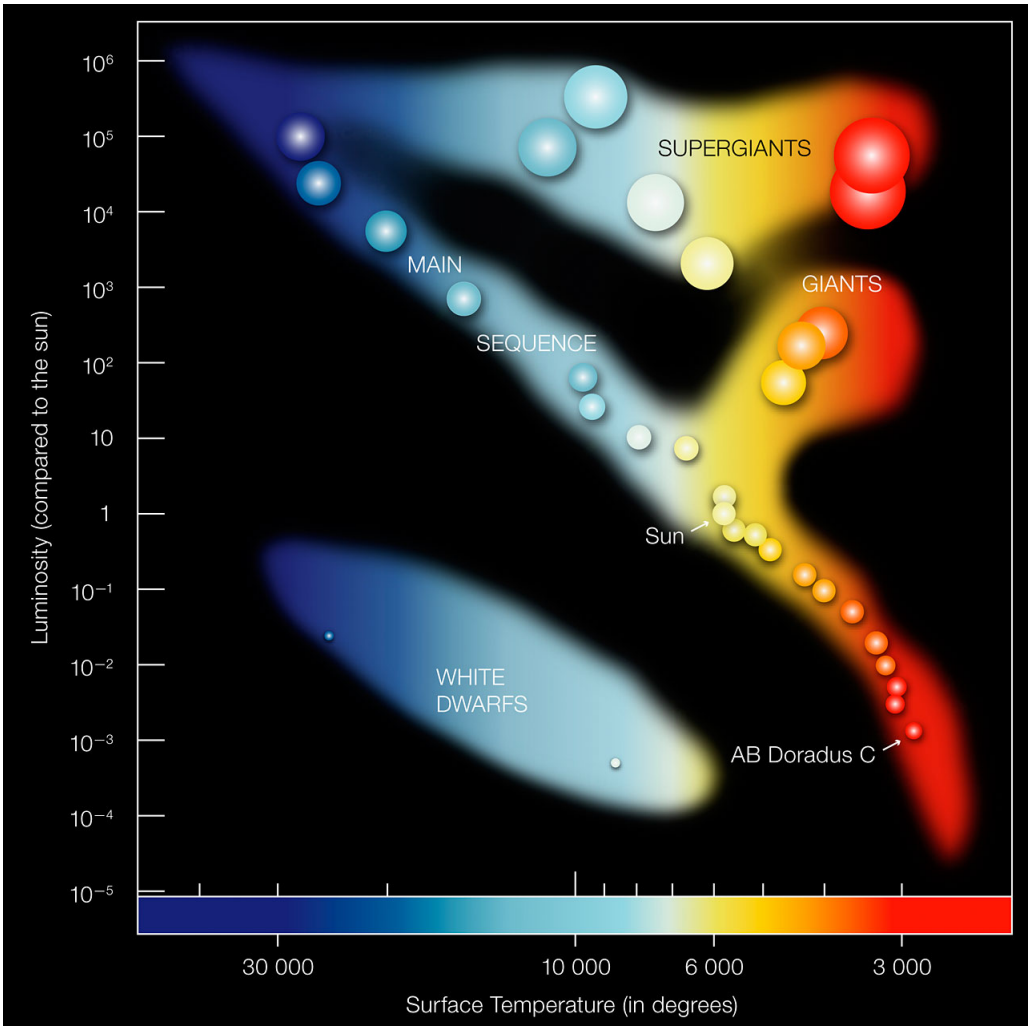

Figure 1.3: Hertzsprung–Russell diagram. Luminosity of a star is plotted against its temperature. Image credit : ESO

: the velocity at which the gravitational force cannot counterbalance the centrifugal force. This critical velocity is given by (Maeder, 2009) :

$$v_{crit} = \frac{2GM}{3R_{p,crit}} \tag{1.1}$$

where $R_{p,crit}$ is the equatorial radius.

Due to this high rotation rate, Be stars are highly flattened, like α Eridani (or Archernar) that shows an axis ratio of 0.64 (Domiciano de Souza et al., 2003). Be stars display a transient circumstellar disk named the "Be-phenomenon" (Quirrenbach et al., 1997), seemingly in Keplerian rotation (Meilland et al., 2007). There is no real understanding regarding the existence of this disc but thare are a few explanations regarding its origin : a) the high rotation would eject some matter from the star, b) a confined stellar wind that is not magnetized (Bjorkman et al., 1993; Owocki et al., 1996) or magnetized (Cassinelli et al., 2002), c) the presence of a strong magnetic field (Townsend and Owocki, 2005) and, finally, d) the non-radial pulsation (Lee and Saio, 1993; Rivinius et al., 2003,

1998, 2001, 2003; Huat et al., 2009).

There is a lot of degeneracy when confronting models with observationss (Poeckert and Marlborough, 1978) and some be start might be closer to the critical rotation than previously thought Townsend et al. (2004). This discuss the cas of highly rotating systems, possibly surrounded by a thin ring.

Red giants

A red giant is the temporary state between the life of a main-sequence star and its death. The transition from a main-sequence star to a red giant occurs when the star exhausts all the hydrogen in the core through the thermonuclear fusion and starts consuming the hydrogen in the surrounding shell (see the Schönberg-Chandrasekhar limit). As there is no more reactions in the core to sustain the hydrostatic equilibrium, the core of the star starts to shrink due to the gravitational force. For a low mass collapsing star (i.e. $0.5\mathrm{M}_\odot \leq M \leq \mathrm{M}_\odot$), pressure and heat in the core rise up and the outer layers of the star expands by absorbing the extra energy emitted (Laughlin et al., 1997). At some point, the density and temperature are high enough for the core to be degenerated and supported by electron degeneracy pressure that stops the collapse and starst the thermonuclear fusion of helium. This is always combined with a process called the helium-flash caused by the thermal runaway nuclear fusion (Hansen et al., 2004). Their surface temperature is about ~ 5000 K.

In more massive stars (whose masses range from $2\mathrm{M}_\odot$ to $8\mathrm{M}_\odot$) the core reaches a temperature sufficient to start the fusion of helium before being in a degenerated state and thus produces no helium-flash (Zeilik and Gregory, 1998). As helium is exhausted, a second red-giant phase takes place (Sackmann et al., 1993) : the core collapses to reach a state of degenerate carbon–oxygen fluid. However, a star lighter than $8\mathrm{M}_\odot$ cannot fuse such heavy elements and eject the outer layer forming a planetary nebula leaving a white dwarf at its center (Fagotto et al., 1994).

This evolution from a main-sequence (MS) star to the red giant phase has been widely investigated within the framework of the theory of figures. In a pionering article, Schönberg and Chandrasekhar (1942) studied an isothermal core embedded in a radiative envelope which set constraints on the beginning of the red-giant phase. They determine that when the core reaches 10% of the total mass, the star undergoes the transformation. Rotation plays once again an important role since it has been proved that it changes this mass limit (Maeder, 1971; Kadam et al., 2016). We will treat this question in the manuscript.

White dwarfs

White dwarfs are stellar remnants of low mass stars. In a white dwarf, the internal pressure is generated by the electron degeneracy pressure involving the Pauli exclusion principle. For a non-rotating white dwarf, this support can only occur while the mass is lower than $1.4\mathrm{M}_\odot$ which is the Chandrasekhar limit (Chandrasekhar, 1931). If by any process, the mass of the white dwarf increases, the star undergoes a supernova process known as the carbon detonation and collapses to a neutron star. Its mass is between

$0.17M_\odot$ (Kilic et al., 2007) and $1.33M_\odot$ (Kepler et al., 2007), its surface temperature is at most 100000 K and its radius lies between 0.008 to $0.02R_\odot$.

Rotation in white dwarfs exceeding the Chandrasekhar limit is a key element determining whether or not it can go into a neutron star. The rotation exerts an outward force helping the electron degeneracy pressure to counterbalance the inward-oriented gravitational force. As a consequence, awhite dwarf can have a mass higher than the Chandrasekhar limit if it is spinning fast enough (Tohline, 1984).

Neutron stars

A neutron star comes from a white dwarf exceeding the Chandrasekhar limit and going into a supernova state. As the core of the white dwarf collapses, the temperature and the pressure increase and neutrons are produced by combining protons and electrons through electron capture. The gravitational collapse is at that point prevented by the neutron degeneracy pressure once again described by the Pauli exclusion principle. Its rotation rate is even increased as the core collapses caused by the angular momentum ; the highest rotation rate of an observed neutron star is 43000 spins per minute, which corresponds to a surface velocity of 24 percent of the speed of light. The surface temperature is about 600000 K and since it is much denser than white dwarf, its typical radius is about 10km (Haensel et al., 2007)

The internal structure of a neutron star is a current challenge and can be investigated, again, in the framework of the theory of figures (New and Tohline, 1997; Hachisu et al., 1986a,b; Rasio and Shapiro, 1992, 1994) and more recently using observational means by using asterosismology applied to the stellar oscillations (Haensel et al., 2007). Actual knowledge predicts a superdense central core made of mostly neutrons with some protons and electrons. this core is coated by a solid crust composed of electrons, neutrons and atomic nuclei. The surface of a neutron stars is made of nuclei and electrons.

When a neutron star exceed another mass limit called the Tolman–Oppenheimer–Volkoff limit which is $M_{TOV} = 2 - 3M_\odot$ (Maeder, 2009), it collapses even further evolving into a black hole (Baumgarte et al., 2000)

1.2.4 Planets

Planets are byproducts of stellar formation. They are build by the aggregate of matter from the accretion disk around protostellar core. They are massive enough for the self-gravitation to overcome the star gravitational potential. Usually, planets orbit a star or a group of stars but they can be gravitationally unbounded after being ejected from their original system (rogue planets, Sumi et al., 2011; Mroz et al., 2020).

In the solar system, planets are divided in two groups : telluric planets and gaseous planets. The four closest planets of the Sun (Mercury, Venus, Earth, and Mars) are telluric : basically, they have a metallic core and a silicate mantle. Jupiter and Saturn are giant gaseous planets which are thought to have a central molten rocky or icy core surrounded by a layer of metallic hydrogen and an atmosphere of molecular hydrogen and helium (Guillot, 1999; Guillot et al., 2004; Mankovich and Fortney, 2020). Uranus and Neptune are giant icy planets : they have a core of telluric planet coated in ices chemical compounds. The internal structure of the Earth is fairly well known thanks to direct

sismology but probing the internal structure of other planets remain a great challenge to overcome. Therefore, most of the actual knowledge on internal structure of planets relies on model and inference from observations. There is a lot of ongoing work to unravel the internal structure of Jupiter and Saturn (Hubbard, 1974; Kong et al., 2016; Helled and Guillot, 2018; Mankovich and Fortney, 2020; Buccino et al., 2020) and for all types of planet (Helled and Guillot, 2018; Baraffe et al., 2014; Snellen et al., 2014; Kong et al., 2014)

Even though the planets of our solar system offer us some diversity, it is only a snapshot on the numerous other types of planets : lava planet (Pluriel et al., 2019), ocean planet, desert planet, iron planet, puffy planet or hot Jupiter. Layered spheroids are investigated in the present work.

1.2.5 Triaxial ellipsoids

When a rapidly rotating spheroid is perturbed (collisions, tidal interactions), it might adopt the shape of a triaxial ellipsoids, also called a Jacobi ellipsoid. The dwarf planet Haumea is one example of this kind of ellipsoids. Its characteristcs are derived from observations and presented in Ortiz et al. (2017). Haumea is believed to have three semi-axes equal to $a = 1161 \pm 30$, $b = 852 \pm 4$ and $c = 513 \pm 16$ km. A possible structure are presented in Dunham et al. (2019). Another example of Jacobi ellipsoids lies within barred spiral galaxies. Indeed, such galaxies display a central bar-shaped structure hosting stars. Whereas ellipsoidal dwarf planets like Haumea seems to be exotic, barred spiral galaxies represent up to two-thirds of all the spiral galaxies (Eskridge and Frogel, 1999).

Such configurations have been investigated using the theory of figures (Vandervoort, 1980). We will not deal with triaxial systems here but this would merit a complete study.

1.3 Stability, evolution and timescales

Most of the known systems (star, planet, rings, accretion disk) evolve at an apparently steady rate. Otherwise universe would be chaotic and not well arranged. Life could not jave appeared and developed as we know it. It means that any modifications of the mechanical equilibrium happening within a given body is immediatly dealt with in order to preserve this aforesaid equilibrium. The time needed by a body to adjust to a perturbation is called the dynamical timescale and noted τ_{dyn}. This first timescale has to be compared to the lifetime t_{life} of the body. If $\tau_{dyn} \ll t_{life}$, then any modification is almost instantaneous and the overall evolution is steady and the state can be regarded as a pseudo-equilibrium.

For planets and stars, we measure the dynamical timescale by estimating the time needed to collapse if all their internal pressure would suddenly disappear. Using hydrodynamical equations, we have for spheroidal systems (Maeder, 2009) :

$$\tau_{dyn} \sim \sqrt{\frac{R^3}{GM}} \sim \sqrt{G\langle\rho\rangle}^{-\frac{1}{2}}, \tag{1.2}$$

where $\langle\rho\rangle$ is the average density. For a star like the Sun, the dynamical timescale is of the order of $\tau_{dyn} \sim 30$ minutes, for a red giant $\tau_{dyn} \sim 40$ days, for a white dwarf $\tau_{dyn} \sim$ a few

seconds (Maeder, 2009) and for the Earth $\tau_{dyn} \sim 15$ minutes. This dynamical timescale has to be compared with the evolution time and lifetime of those systems. For a MS star, we can estimate the lifetime of the hydrogen burning phase t_H by comparing the amount of hydrogen available and the power it produces :

$$t_H \sim \frac{\text{fuel available}}{\text{power}} \sim \frac{\Delta M c^2}{\bar{L}} \tag{1.3}$$

For instance, in the case of the Sun, we have $t_H = 10^{10}$ years. For stars with other masses, we can derive an approximate lifetime by replacing the hydrogen available by the total mass of the star and the luminosity with the relation $\bar{L} \sim M^{\alpha}$ where the value of α lies between 3 and 3.5 for MS star. Examples for various masses are given in Tab.1.1

Mass ($M_\odot$)	t_H(yr)	Mass ($M_\odot$)	t_H(yr)
120	2.561×10^6	4	1.647×10^8
85	2.823×10^6	3	3.525×10^8
60	3.447×10^6	2.5	5.849×10^8
40	4.303×10^6	2	1.116×10^9
25	6.408×10^6	1.7	1.827×10^9
20	8.141×10^6	1.5	2.695×10^9
15	1.158×10^7	1.25	3.948×10^9
12	1.600×10^7	1.00	9.845×10^9
9	2.639×10^7	0.90	1.550×10^{10}
7	4.319×10^7	0.80	2.503×10^{10}
5	9.446×10^7		

Table 1.1: Lifetime of the hydrogen burning phase t_H for MS star. From Maeder (2009)

We see that $\tau_{dyn} \ll t_H$ and it is only the time for a star to burn its hydrogen which represent only a small part of its life. In the light of that, it is opportune to treat a MS star as equilibrium.

For rings and accretions disks, the dynamical scale is simply given by the orbital timescale, i.e. the time it takes to do a complete revolution around the central mass. It is given by :

$$\tau_{dyn} \sim \Omega^{-1} \tag{1.4}$$

where Ω is the angular velocity. For a Keplerian non-self-gravitating disk, the square of the angular velocity is given by $\Omega^2 = \frac{GM}{R^3}$ where M is the mass of the central object and R is the radius of the disk. Therefore, the dynamical timescale of a disk is given by Montesinos (2012) :

$$\tau_{dyn} \sim \sqrt{\frac{R^3}{GM}} \tag{1.5}$$

The typical dynamical timescale of a disk is of the order of a few hundres years.

The lifetime of a disk is driven by its larger time scale : the viscous timescale which gives the timescale of the matter being diffused in the disk over the distance R. It is given by (Montesinos, 2012) :

$$\tau_{vis} = \frac{R^2}{\nu} \tag{1.6}$$

where ν is the kinematical viscosity of the disk. Accretion disks around young stars last for ~ 10 millions (Mamajek et al., 2004; Mamajek, 2009) years up to ~ 25 millions years (White and Hillenbrand, 2005). For an accretion disk, we therefore have :

$$\tau_{dyn} \ll \tau_{vis} \tag{1.7}$$

For planetary rings, we have the example of the saturn's rings. The dynamical timescale is given by the same expression as for accretion disk. In the case of Saturn's rings, we have :

$$\tau_{dyn} \sim 5000s \tag{1.8}$$

The lifetime of Saturn's ring is believed to be of the order of 300 millions years (O'Donoghue et al., 2019). In this thesis, we will talk about close and massive rings.

1.4 Applications to other fields

The theory of figures can be applied in other field of Science as long as we can find any cohesive interaction analogous to gravity.

In fluid mechanics, the theory can be used to study rotating liquid drops by considering the surface tension (Cohen et al., 1974; Cardoso, 2008; Hill and Eaves, 2008). First attempt were made by suspending olive oil in a mixture of water and alcohol to counterbalance the undesired effect of gravity (Maxwell, 1874). Hill and Eaves (2008) designed an ingenious way for making droplets levitate : diamagnetic levitation. They proceed to make the droplets spins and they generated nonaxisymmetric shapes shown in Fig.1.4.

There are a few applications on biology. Chavanis and Sire (2008) have linked the critical size of bacterial populations to the Chandrasekhar limit on the mass of white dwarfs. Prouteau et al. (2017) reported a torus-shaped protein called TOROID (TORC1 organized in inhibited domains), shown in Fig.1.5.

Since there is a certain analogy between the gravitational potential and the nuclear potential, one might assumes that the theory of figures can be applied to nuclear physics. Rapidly rotating nuclei has been investigated over the year and it was demonstrated that a rotating nuclei can adopt, as self-gravitating bodies do, spheroidal or ellipsoidal shapes (Cohen et al., 1974; Bohr and Mottelson, 1979).

1.5 Motivations and outline of the thesis

As a matter of fact, the internal structure of objects is mostly unknown. We have a rather good idea of the internal structure of the Earth and our Sun but there is a lack of knowledge and a great uncertainty for other celestial bodies, even as close as Jupiter or Venus.

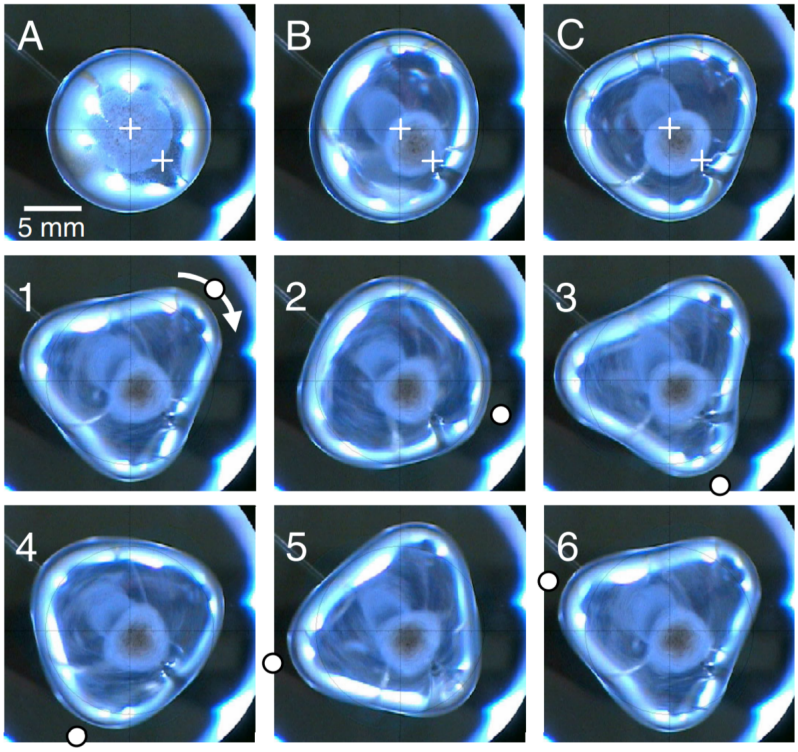

Figure 1.4: A levitating 1.5 ml droplet. (a) Not rotating. (b) Liquid rotating at $\Omega/2\pi = 2.00$ rps: the droplet's equator has an elliptical outline. (c) 2.5 rps: the equator has the symmetry of an equilateral triangle. In (b),(c) the outline is not rotating with the fluid. Crosses show the electrode positions. (1)– (6) Consecutive movie frames, 40 ms apart; here, the triangular outline is rotating with the fluid in the arrow's direction at $\Omega/2\pi = 3:33$ rps. White circles follow one corner

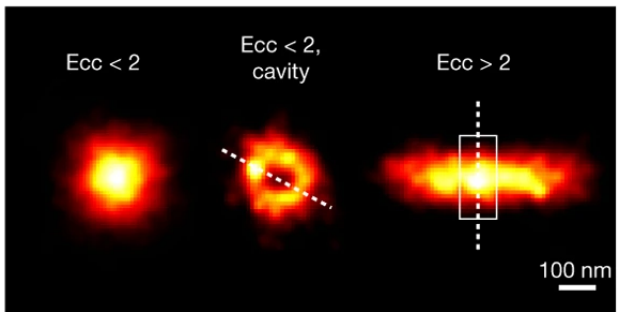

Figure 1.5: Averaged images of aligned clusters

Researchers constraint models of internal structure of stars and planets with observables like the mass, the radius, the luminosity, the rotation rate and, if accessible, the shape of the gravitational potential generated by the aforesaid bodies. The first question that we can ask ourselves is : is there some degree of degenerecy of models, i.e. various internal structures leading to the same set of observables ?

This thesis is devoted to the study of self-gravitating systems in differential rotation. We develop a global understanding on massive bodies : we did not dig into details of

chemistry composition, cloud dynamics in the atmospheres, planetary relief or sporadic process. We study object as a whole in order to acquire general knowledge about them. We bring new contribution to the theory of figures with axisymmetrical equilibrium composed by several multi-layer bodies. We developped a scale-free approach that provides us with new theoretical and numerical diagnostic tools enabling to better understand the internal structure of astrophysical objects such as planets, exoplanets, stars and rings.

In this manuscript, a presentation of the mathematical and physical formalisms is presented in Chap. 2. We introduce the hypothesis and the equations of the problem. In Chap. 3, we present the version of the `DROP` code as it was when the thesis started (Huré and Hersant, 2017; Huré et al., 2018). It is based upon a Self-Consistent Field algorithm that solves the Bernoulli equation together with the Poisson's equation for polytropic fluids. **Multibody configurations** and modifications to the `DROP` code are presented in Chap. 4. We focus on two-body configurations made of a central spheroid and a surrounding ring. We deal with both incompressible and compressible fluids and show how they populate the rotation rate - angular momentum reference diagram. In particular, we report the existence of a maximum rotation rate for the permitted equilibria. We report multiple connections between the Maclaurin sequence and the One-Ring sequence. At last, we present multibody systems for further investigations such as the study of Be-stars, accretion disks and young protoplanetary systems. **Multi-layered configurations** and new implementations to the `DROP` code are presented in Chap. 5. We discuss that different internal structures can lead to the same mass-radius and mass-radius-surface velocity relationship. We highlight the critical effect of a density jump paired with a rotation discontinuity at each layer interface. We investigate the effect of a differential rotation and an external gravitational potential on the internal structure of a two-layer system. It is directly linked to the Schönberg-Chandrasekhar limit and the red giant phase and we corroborate that this aforementionned limit is indeed reduced by differential rotation. However, we show that this limit is increased in the presence of a massive companion. In Chap. 6, we present the results on toroidal systems. Analytical developments on the gravitational potential of toroids are derived and shortly compared to an historical work reported in Wong (1973). The internal structure of the observed system GG Tau is studied and we show the effect of the rotation profile and the equation-of-state on its internal structure. We give some constraints on the internal structure reproducing observational data. Main conclusions of the PhD Thesis are reported in Chap. 7. We also give some persepectives for future works such as the computation of 3D equilibrium and the current investigation of the internal structure of Jupiter and Saturn with two-and-three-layer systems. We are aware that many part of this thesis would merit further development but this is a wide topic which is difficult to master in a few years only, for further readings on polytropes and figures of equilibrium see Horedt (2004) and the VisTrails of Joel E. Tohline

Chapter 2

Theory of figures

Contents

2.1 Lane-Emden equation

The Lane-Emden equation describes the structure of a fluid under the only forces of gravity and internal pressure for non-rotating systems and beyond (see Sect.2.2and Sect.2.3 for rotation, see also Sect.2.1.4 for a discussion for the isothermal case). This equation was found by Jonathan Lane in Lane (1870) and was solved independantly by Schuster (1883) and Emden (1907). It is the first equation aiming at studying the internal structure of a star. It is a simple model due to a number of hypothesis : non-rotating star, polytropic equation-of-state, only two forces taken into account, central symmetry and steady state.

2.1.1 Framework

The Lane-Emden equation can be derived from the hydrostatic equilibrium of a piece of fluid under several hypothesis :

- No rotation and the star is perfectly spherical : point reflection
- An equation-of-state :

$$P = P(\rho, T, ...) \tag{2.1}$$

Balance between the pressure forces $\vec{\nabla}P$ and the gravitational force $-\rho\vec{\nabla}\Psi$:

$$\vec{\nabla}P = -\rho\vec{\nabla}\Psi \tag{2.2}$$

The equation-of-state (EOS) is a function that links the pressure to the density, the temperature, the volume or other state variables.

A special case of matter whose EOS is only a function of pressure P and density ρ is called a barotrope, i.e. $f(P, \rho) = 0$. An special kind of barotrope is the polytrope whose equation-of-state explicitly reads :

$$P = K\rho^{\gamma} \tag{2.3}$$

where γ is the adiabatic index and $K \leq 0$ is the polytropic constant. The adiabatic index is linked to the polytropic index n :

$$\gamma = 1 + \frac{1}{n} \tag{2.4}$$

This EOS is used in the thesis throughout.

Polytropes are widely used in the astrophysical context due to their versatility of applications. Depending on the value of γ or n, the EOS models different physical processes (see table 2.1). For instance, a polytrope can describe the core of a non-relativistic star (ideal gas in an isothermal condition) when $n = \infty$, the convective layer of a non-relativistic star when $n = 1.5$ or a neutron star when $n = 3$. The use of polytropes is fundamental in astrophysics because it can help in understanding the internal structure, the formation and the evolution of astrophysical bodies without considering microphysics (planets and moons, stars, neutron stars, black holes, galaxies, interstellar clouds and cosmic filaments).

The gravitational potential Ψ is obtained through the Poisson's equation :

$$\Delta\Psi = 4\pi\rho G \tag{2.5}$$

n	γ	Description
0	—	Incompressible gas; constant density
0.42857	10/3	Thomas-Fermi EOS
1	2	analytic solution to Lane-Emden equqation; constant R_*
1.5	5/3	ideal monatomic gas EOS; convective; non-relativistic degenerate
2	3/2	Holzer & Axford's maximum γ for an accelerating solar wind
2.5	7/5	ideal diatomic gas EOS
3	4/3	Eddington's standard model; ultra-relativistic degenerate; constant M_*
3.25	17/13	Chandrasekhar's constant-ϵ Kramers model
5	6/5	Schuster sphere of infinite radius
∞	1	Isothermal gas; Bonnor-Ebert sphere

Table 2.1: Few examples of physical processes described by various polytropic indices

Introducing the polytropic equation Eq.(2.3) in Eq.(2.2), we have :

$$\frac{1}{\rho}\vec{\nabla}\left(K\rho^{\gamma}\right) = -\vec{\nabla}\Psi \tag{2.6}$$

We can rewrite the left side of Eq.(2.6) in terms of the gradient of a scalar field :

$$\frac{1}{\rho}\vec{\nabla}\left(K\rho^{\gamma}\right) \equiv \vec{\nabla}H, \tag{2.7}$$

where H is called the enthalpy, and can be obtained from :

$$H = K\int \frac{1}{\rho}\frac{d(\rho^{\gamma})}{dr}dr \tag{2.8}$$

When $\gamma \neq 1$, it can be written in the form of :

$$H = K\frac{\gamma}{\gamma-1}\rho^{\gamma-1} + C, \tag{2.9}$$

and, if $\gamma = 1$, it can be written as :

$$H = K\ln\frac{\rho}{\rho_0} + C. \tag{2.10}$$

Since we have $\vec{\nabla}\left(H+\Psi\right) = \vec{0}$, the hydrostatic equilibrium (2.2) can be rewritten as :

$$H + \Psi = C \tag{2.11}$$

Then by replacing Ψ by $-H$ in the Poisson equation (2.5) and from the Laplacian in spherical coordinates, we have :

$$\Delta(-H) = -\frac{1}{r^2}\frac{d}{dr}\left(r^2\frac{dH}{dr}\right) = 4\pi\rho G \tag{2.12}$$

We can rewrite this equation using dimensionless variables. We use a physical length L to build the dimensionless radius ξ :

$$r = L\xi \tag{2.13}$$

For the enthalpy H and the density ρ, we have :

$$\rho = \rho_0 \hat{\rho}, \tag{2.14a}$$

$$H = H_0 \hat{H}. \tag{2.14b}$$

where $\hat{x}$ is the dimensionless variable, x_0 is the typical variable scale which also contains the physical units of a variable x. For $\gamma \neq 1$, we have :

$$H_0 = K(n+1)\hat{\rho}_0^{\frac{1}{n}}, \tag{2.15}$$

and we see that :

$$\hat{H} = \hat{\rho}^{\frac{1}{n}}. \tag{2.16}$$

For $\gamma = 1$, see Sect.(2.1.4)

By using these definitions, Eq.(2.12) becomes :

$$\frac{H_0}{4\pi G \rho_0} \frac{1}{\xi^2} \frac{d}{d\xi} \left(\xi^2 \frac{d\hat{H}}{d\xi} \right) + \hat{\rho} = 0 \tag{2.17}$$

We see that :

$$\frac{H_0}{4\pi G \rho_0} = \frac{K(n+1)\rho_0^{\frac{1}{n}-1}}{4\pi G} \tag{2.18}$$

and this term has the dimension of a squared length, so we can set :

$$L^2 \equiv \frac{H_0}{4\pi G \rho_0 L^2} \tag{2.19}$$

Finally, we obtain the Lane-Emden equation :

$$\frac{1}{\xi^2} \frac{d}{d\xi} \left(\xi^2 \frac{d\hat{H}}{d\xi} \right) = -\hat{H}^n. \tag{2.20}$$

It is a 2nd-order non-linear differential equation. To solve it for $\hat{H}$, we need two boundary conditions. This equation is investigated by mathematicians for long (Emden, 1907; Srivastava, 1962; Medvedev and Rybicki, 2001; Horedt, 2004; Mach, 2012). For physically relevant solutions, only positive value of $\hat{H}$ are of interest. Besides $\rho(\xi = 0) = \rho_0$ therefore $\hat{H}(\xi = 0) = 1$. Moreover, symmetry implies $\frac{dP}{dr}\big|_{r=0} = 0$ thus $\frac{d\hat{H}}{d\xi}\Big|_{\xi=0} = 0$. The two boundary conditions usually employed to solve the Lane-Emden equation are :

$$\hat{H}(0) = 1, \tag{2.21a}$$

$$\left. \frac{d\hat{H}}{d\xi} \right|_{\xi=0} = 0. \tag{2.21b}$$

2.1.2 Analytical solutions of the Lane-Emden equation

The Lane-Emden equation has no trivial solution. Medvedev and Rybicki (2001) proved that this equation was nonintegrable in a closed form. For the most part, solutions are found numerically using a solver. However, a few analytical solutions are known for some well-chosen polytropic indices, namely for $n = 0$, $n = 1$ and $n = 5$.

Solution for $n = 0$.

By integrating two times and using the boundary values, we obtain a solution for $\hat{H}$:

$$\hat{H}(\xi) = 1 - \frac{1}{6}\xi^2 \tag{2.22}$$

This solution is a monotonous decreasing function and its only root is for $\xi_1 = \sqrt{6}$

Solution for $n = 1$.

This is a Bessel's differential equation and we van write a general solution in the form of $\hat{H}(\xi) = C\frac{\sin\xi}{\xi} + C'\frac{\cos\xi}{\xi}$. Given the boundary conditions, we find that $C = 1$ and $C' = 0$:

$$\hat{H}(\xi) = \frac{\sin\xi}{\xi} \tag{2.23}$$

This solution is an even oscillating function and its first root happens for $\xi_1 = \pi$.

Solutions for $n = 5$.

All solutions for $n = 5$ have been reported in Mach (2012) using an autonomous form of Eq.(2.20). We transform this equation by using $H = \frac{z}{\sqrt{2\xi}}$ and $t = -\ln\xi$, it can be written in the form of

$$\frac{d^2z}{dt^2} = \frac{1}{4}z(1 - z^4) \tag{2.24}$$

and its integration yields (Mach, 2012) :

$$\left(\frac{dz}{dt}\right)^2 = \frac{1}{12}\left(-z^6 + 3z^2 + C\right) \tag{2.25}$$

The solution depends on the value of the constant C. The usual solution of the Lane-Emden equation is obtained with $C = 0$ and we have :

$$\hat{H}(\xi) = \frac{1}{\sqrt{1 + \frac{\xi^2}{3}}}. \tag{2.26}$$

The first root of $\hat{H}(\xi)$ happens for $\xi_1 = +\infty$ which means that this solution presents an infinite radial extent. Nonetheless, quantities such as the mass can be calculated and are finite. Even though there is no known solution, we know that all solutions for $n \geq 5$ present a first root for $\xi_1 = +\infty$.

Solution for $n = 5$ **found by Srivastava**:

Another solution of $\hat{H}$ was found by Srivastava (1962). This solution is :

$$\hat{H}(\xi) = \frac{\sin(\ln\sqrt{\xi})}{\sqrt{\xi}\left(3 - 2\sin^2(\ln\sqrt{\xi})\right.} \tag{2.27}$$

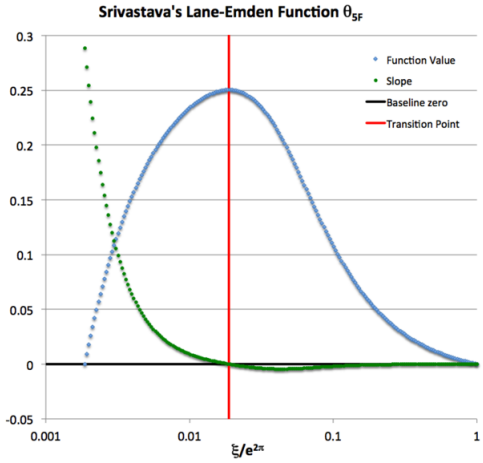

Table 2.2: Solution of the Lane-Emden reported in Srivastava (1962) for $n = 5$. From the VisTrails of Joel E. Tohline.

However, it does not fulfill the standard boundary values, but it can be used to generate more complex objects like stars with multiple layers where each layer has a specific polytropic index. Such models are called "composite stellar" or "bipolytropic" models, see Chap.5 and Murphy (1980, 1983).

2.1.3 Numerical solutions of the Lane-Emden equation

When using a solver, we can find the solution to the Lane-Emden equation for any $n \geq 0$. Usually, it is done in the real plane. Although a complex plane strategy was developed in Geroyannis (1993) in order to constraint the polytropic index of the Sun. It was later applied to the jovian system (Geroyannis and Dallas, 1994; Geroyannis and Valvi, 1994).

Some examples of solutions are given on in Fig.2.1.

2.1.4 Isothermal case : the Emden–Chandrasekhar equation

The Emden–Chandrasekhar equation is a special case of the Lane-Emden equation when considering an isothermal EOS when we have $n = +\infty$ or $\gamma = 1$. We see from Eq.(2.10) that the enthalpy takes the following form :

$$H = K \ln\left(\frac{\rho}{\rho_0}\right) + C. \tag{2.28}$$

Instead of Eq.(2.15), the definition of the dimensionless enthalpy $\hat{H}$ is now :

$$H = H_0 \hat{H} = K \ln\left(\frac{\rho}{\rho_0}\right) + C, \tag{2.29}$$

and,

$$H_0 = K, \tag{2.30a}$$

$$\hat{H} = \ln \hat{\rho}. \tag{2.30b}$$

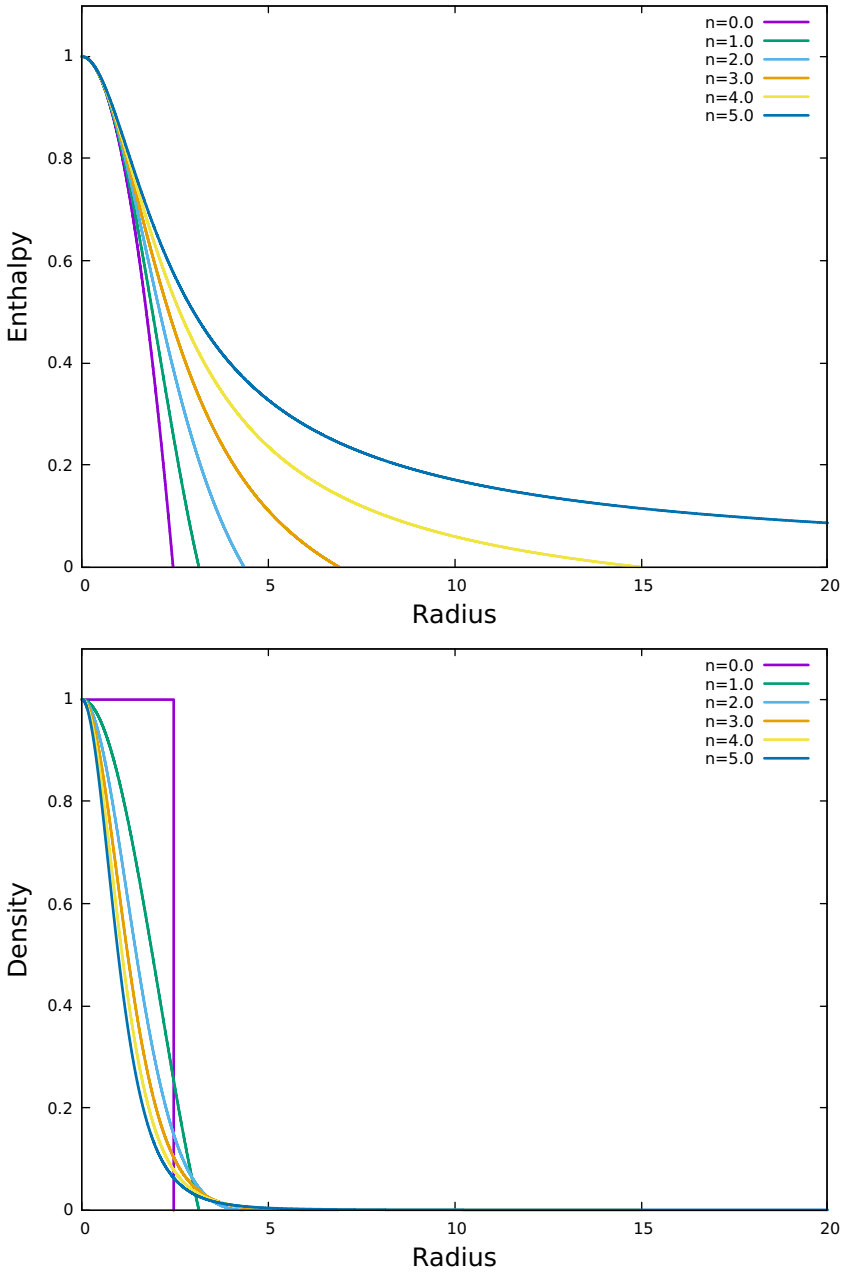

Figure 2.1: Numerical solutions of the Lane-Emden equation for various value of the polytropic index using a a Runge-Kutta of the fourth order integrator. (Top) Enthalpy. (Bottom) Density.

so the Emden-Chandrasekhar equation writes :

$$\frac{1}{\xi^2}\frac{d}{d\xi}\left(\xi^2\frac{d\hat{H}}{d\xi}\right) = -e^{\hat{H}} \tag{2.31}$$

with the boundary conditions :

$$\hat{H}(0) = 0 \tag{2.32a}$$

$$\left.\frac{d\hat{H}}{d\xi}\right|_{\xi=0} = 0 \tag{2.32b}$$

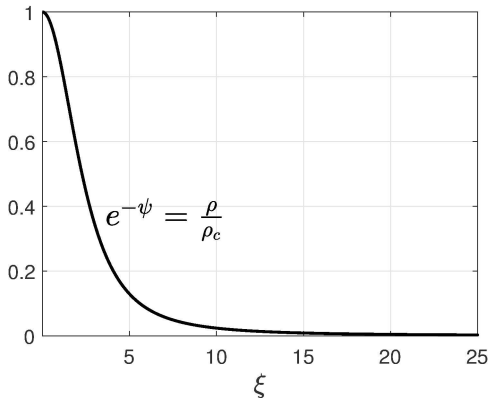

Figure 2.2: Numerical solution of the Emden-Chandrasekhar equation obtained by using a solver.

There is no common solution to this equation and the only way of solving it is numerically, see Fig.2.2. One application of the isothermal case is the properties and stability of Bonnor-Ebert spheres.

2.1.5 Polytropic slabs and cylinders

In fact, there is an extension of the Lane-Emden equation in a N-dimension space, namely :

$$\frac{1}{\xi^{N-1}}\frac{d}{d\xi}\left(\xi^{N-1}\frac{d\hat{H}}{d\xi}\right) = -\hat{H}^n. \tag{2.33}$$

The polytropic cylinders, which can be considered by setting $N = 2$, are, in a first approximation, a good representation of interstellar filaments. Early works were only theoretical in order to comprehend the properties and stability of incompressible cylinders (Chandrasekhar and Fermi, 1953) and compressible cylinders (Stodólkiewicz, 1963; Ostriker, 1964). Recent observations of filaments captured by the Herschel Space Observatory gave insight on such objects and their complexity (Molinari et al., 2010; André et al., 2014; Moeckel and Burkert, 2015). More recent theoretical works have been done analytically supported by numerical means in order to study the various instabilities and gravitationnal collapses occuring in these filaments (Toci and Galli, 2015a,b; Lou and Hu, 2017; Coughlin and Nixon, 2020). Note that this objects are oftenly irradiated and negative polytropic indices n are widely used to characterized external pressure.

2.1.6 Properties of non-rotating polytropes

It is of great interest to determine some characteristics of non-rotating polytropes such as the mass M, the maximal physical radius L, the central pressure P_c, the average density $\langle\rho\rangle$, the gravitational energy W and the internal energy U.

By definition, we have $\xi = \frac{r}{L}$ and thus we have $R = L\xi_1$, where ξ_1 is the first root of $\hat{H}$. In other terms :

$$L = \sqrt{\frac{\kappa(n+1) + \rho_c^{\frac{1}{n}-1}}{4\pi G}}\xi_1 \tag{2.34}$$

The mass is defined by :

$$\begin{aligned} M &= \int_0^R 4\pi r^2 \rho dr \\ &= 4\pi L^3 \rho_c \int_0^{\xi_1} \xi^2 H^n d\xi \\ &= 4\pi L^3 \rho_c \left[-\xi^2 \frac{dH}{d\xi}\right]_{\xi_1} \\ &= M_0 \tilde{M} \end{aligned} \tag{2.35}$$

where $M_0 = 4\pi L^3 \rho_c$ is the magnitude of the mass. We can define the average density $\langle\rho\rangle$. As we have spheres, it reads :

$$\begin{aligned} \langle\rho\rangle &= \frac{M}{\frac{4\pi R^3}{3}} \\ &= \frac{3\rho_c}{\xi_1^3}\left[-\xi^2 \frac{dH}{d\xi}\right]_{\xi_1} \\ &= \frac{3\rho_c}{\xi_1^3}\tilde{M}_1 \end{aligned} \tag{2.36}$$

To obtain the gravitational energy, we need to integrate :

$$W = -\frac{GM_0^2}{L}\int_0^{\xi_1} \tilde{M}(\xi)\xi\hat{H}^n d\xi, \tag{2.37}$$

rewriting the various terms in the integral, integrating by parts and introducing temporary variables, the procedure is detailed for instance in Poisson and Will (2014). We obtain :

$$W = -\frac{3}{5-n}\frac{GM_0^2 \tilde{M_1}^2}{\alpha\xi_1} = -\frac{3}{5-n}\frac{GM^2}{L}. \tag{2.38}$$

Using the scalar virial theorem in the static case gives us direclty the internal energy :

$$U + W = 0 \tag{2.39}$$

2.2 Slowly rotating polytropes

As stated earlier, the Lane-Emden equation is a basic equation to study non-rotating bodies. One ubiquitous feature in the astrophysical context is the presence of rotation.

n	ξ_1	$\hat{H}(\xi_1)$	$\left.\frac{dH}{d\xi}\right\|_{\xi_1}$	$\left[-\xi^2\frac{dH}{d\xi}\right]_{\xi_1}$
–0.5	2.208E+00	0.000E+00	-0.521E+00	7.421E+00
0.0	2.449E+00	0.000E+00	-8.150E-01	4.899E+00
1.0	3.142E+00	0.000E+00	-3.183E-01	3.142E+00
1.5	3.654E+00	0.000E+00	-2.033E-01	2.714E+00
3.0	6.897E+00	0.000E+00	-4.243E-02	2.018E+00
4.0	1.497E+01	0.000E+00	-8.018E-03	1.797E+00
5.0	∞	0.000E+00	0.000E+00	1.732E+00
$+\infty$	∞	∞	0.000E+00	∞

Table 2.3: Properties of polytropes for various n. From Horedt (2004).

When considering rotation, the equation set can be written in an extended form of the Lane-Emden equation. It can only be solved exactly, for now, for a rigidly rotating incompressible ellipsoid (See Sect.2.3). For other cases, there are two kinds of methods allowing the study of rotating polytropes : analytical developments in the slow rotation regime and computations with modern means (See Chap.3).

The equilibrium of slowly rotating polytrope was investigated by Chandrasekhar (1933a,b) using a first-order perturbative method following the early works by Milne (1923) and von Zeipel (1924). These rotating polytropes were also studied through variational methods (Roberts, 1963a,b) but gave poor results since his equidensity surface hypothesis is not verified when considering rotation. New pertubative calculations around the Lane-Emden equation (Bender et al., 1989; Ramos, 2008) using the homotopy theorem (Hu, 1959; He, 1999) are under investigation and development.

Here, we present the perturbative approach reported in Chandrasekhar (1933a). When considering rotation, there is centrifugal force to add to the hydrostatic equilibrium Eq.(2.2). In spherical coordinates (r, θ, ϕ) :

$$\vec{e}_r : \frac{\partial P}{\partial r} = -\rho\frac{\partial \Psi}{\partial r} + r\sin^2\theta\Omega_0^2\rho, \tag{2.40}$$

$$\vec{e}_\theta : \frac{\partial P}{\partial \theta} = -\rho\frac{\partial \Psi}{\partial \theta} + r^2\sin\theta\cos\theta\Omega_0^2\rho. \tag{2.41}$$

Early work on this subject assumed a solid rotation, i.e. $\Omega_0 = \dot{\phi} = cst$ in space and time. Eqs.(2.40) and (2.41) can be written in the form of :

$$\vec{e}_r : \frac{\partial P}{\partial r} = -\rho\frac{\partial \Psi}{\partial r} + r(1-\mu^2)\Omega_0^2\rho, \tag{2.42}$$

$$\vec{e}_\theta : \frac{\partial P}{\partial \mu} = -\rho\frac{\partial \Psi}{\partial \mu} - r^2\mu\Omega_0^2\rho, \tag{2.43}$$

where $\mu = \cos\theta$. The Poisson equation is expressed as :

$$\frac{1}{r^2}\frac{\partial}{\partial r}\left(r^2\frac{\partial \Psi}{\partial r}\right) + \frac{1}{r^2}\frac{\partial}{\partial \mu}\left((1-\mu^2)\frac{\partial \Psi}{\partial \mu}\right) = 4\pi\rho G \tag{2.44}$$

By using Eq.(2.42), (2.43) and (2.44), we obtain what Chandrasekhar (1933a) calls the "fundamental equation of the problem" :

$$\frac{1}{r^2}\frac{\partial}{\partial r}\left(\frac{r^2}{\rho}\frac{\partial P}{\partial r}\right)+\frac{1}{r^2}\frac{\partial}{\partial \mu}\left(\frac{1-\mu^2}{\rho}\frac{\partial P}{\partial \mu}\right)=-4\pi\rho G+2\Omega_0^2 \tag{2.45}$$

Introducing the same dimensionless functions as for the non-rotating case (the dimensionless enthalpy $\hat{H}$ and the dimensionless radius ξ), the fundamental equation of the problem becomes :

$$\frac{1}{r^2}\frac{\partial}{\partial \xi}\left[\xi^2\frac{\partial \hat{H}}{\partial \xi}\right]+\frac{1}{r^2}\frac{\partial}{\partial \mu}\left[(1-\mu^2)\frac{\partial \hat{H}}{\partial \mu}\right]=-\hat{H}^n+\hat{\omega} \tag{2.46}$$

with $\hat{\omega}$ being the dimensionless rotation rate defined as :

$$\hat{\omega}\equiv\frac{\Omega_0^2}{2\pi\rho_c G} \tag{2.47}$$

We recover the Lane-Emden when considering a null rotation ($\hat{\omega}=0$).

If we assume a slow rotation, i.e. the term in Ω_0^4 can be neglected. We can express $\hat{H}$ as a perturbated function solution of the non-rotating case :

$$\hat{H}\approx\hat{H}(\omega_0=0)+\hat{\omega}\delta\hat{H} \tag{2.48}$$

We search for an expression of $\hat{H}_1$ in the form :

$$\delta\hat{H}=\sum_{j=0}^{+\infty}A_j\hat{h_j}P_j(\mu) \tag{2.49}$$

where $P_j(\mu)$ is the Legendre function of index j satisfying the following differential equation :

$$\frac{\partial}{\partial \mu}\left[(1-\mu^2)\frac{\partial P_j}{\partial \mu}\right]+j(j+1)=0 \tag{2.50}$$

and it follows that :

$$\hat{H}=\hat{H}_{\hat{\omega}=0}+\hat{\omega}\left(\hat{h}_0(\xi)-\frac{5}{6}\frac{\xi_1^2}{3\hat{h}_2(\xi_1)+\xi_1\hat{h'}_2(\xi_1}\hat{h}_2(\xi)P_2(\mu)\right) \tag{2.51}$$

where ξ_1 is the first root of $\hat{H}(\hat{\omega}=0)$, as already introduced earlier. The two functions $\hat{h}_0$ and $\hat{h}_2$ are the solution of the differential equations :

$$\frac{1}{\xi^2}\frac{d}{d\xi}\left(\xi^2\frac{d\hat{h}_0}{d\xi}\right)=-n\hat{H}_{\Omega_0=0}^{n-1}\hat{h}_0+1 \tag{2.52}$$

$$\frac{1}{\xi^2}\frac{d}{d\xi}\left(\xi^2\frac{d\hat{h}_2}{d\xi}\right)=\left(-n\hat{H}_{\Omega_0=0}^{n-1}+\frac{6}{\xi^2}\right)\hat{h}_2 \tag{2.53}$$

The boundary of the slowly rotating polytrope can be found by solving $\hat{H} = 0$. We have :

$$\xi_1(\hat{\omega}) = \xi_1(\hat{\omega} = 0) + \frac{\hat{\omega}}{|\hat{H}_{\Omega_0=0}(\xi_1)'|}\left(\hat{h}_0(\xi_1) - \frac{5}{6}\frac{\xi_1^2\hat{h}_2(\xi_1)P_2(\mu)}{3\hat{h}_2(\xi_1) + \xi_1\hat{h}_2'(\xi_1)}\right) \tag{2.54}$$

We see that the surface of a rotation polytrope is a deformed ellipsoid due to $P_2(\mu)$ describing an ellipsoid and is slightly modified by the other terms.

In absence of rotation ($\hat{\omega} = 0$), the radius of the boundary is always at $\xi = \xi_1$ and is a perfect sphere. When $\hat{\omega} \neq 0$, the radius of the boundary varies with respect to μ. Since $P_2(\mu) = 1$ at the poles and $P_2(\mu) = -0.5$ at the equator, we see that the equatorial radius is greater than the polar radius and a rotating polytrope adopt an oblate form. Moreover, it means that for a fixed equatorial radius, the volume and the mass of a rotating body are lower than for a non-rotating one.

2.3 Exact solution at high rotations

In the simplest case of a solid rotation and a incompressible polytrope, an exact solution can be found. The first calculus were made by Maclaurin (1742), generalizing the discovery by Newton to any rotation for axisymmetrical ellipsoids. He found that, for any rotation, a hydrostatic equilibrium was reachable. It was noticed a year later that a maximum rotation rate arises from the equations and that there is not one but, in fact, two possible equilibria for a given rotation rate below this maximal value.

Later on, Jacobi (1834) found that, when breaking the axisymmetry, a triaxal ellipsoid could also be a solution to the equation of a rotating incompressible body. Unlike the Maclaurin spheroids, there is only one rotation rate possible for a given eccentricity.

2.3.1 The sequence of incompressible equilibria

Over the years, a way of craftily representing and comparing equilibrium is to plot them in a reference diagram called the $\omega^2 - j^2$ diagram where ω is the dimensionless rotation rate and the j is the dimensionless angular momentum defined as :

$$\omega^2 = \frac{\Omega^2}{4\pi G\langle\rho\rangle}, \tag{2.55a}$$

$$j^2 = \frac{J^2}{4\pi G M^{10/3}\langle\rho\rangle^{-1/3}}. \tag{2.55b}$$

Sequences of equilibrium are generated by calculating a continuous set of equilibrium by varying smoothly a control parameter, typically the geometrical properties (axis ratio, eccentricity).

An exemple of a few sequences in the incompressible assumption are given in Fig.2.3 : the Maclaurin sequence, the Jacobi sequence, the hamburger and one-ring sequence. We can see that the sequence of Maclaurin starts at the origin ($\omega^2 = 0, j^2 = 0$), i.e. no rotation and no angular momentum (see Fig.2.4 *Top left panel*). As we go along the

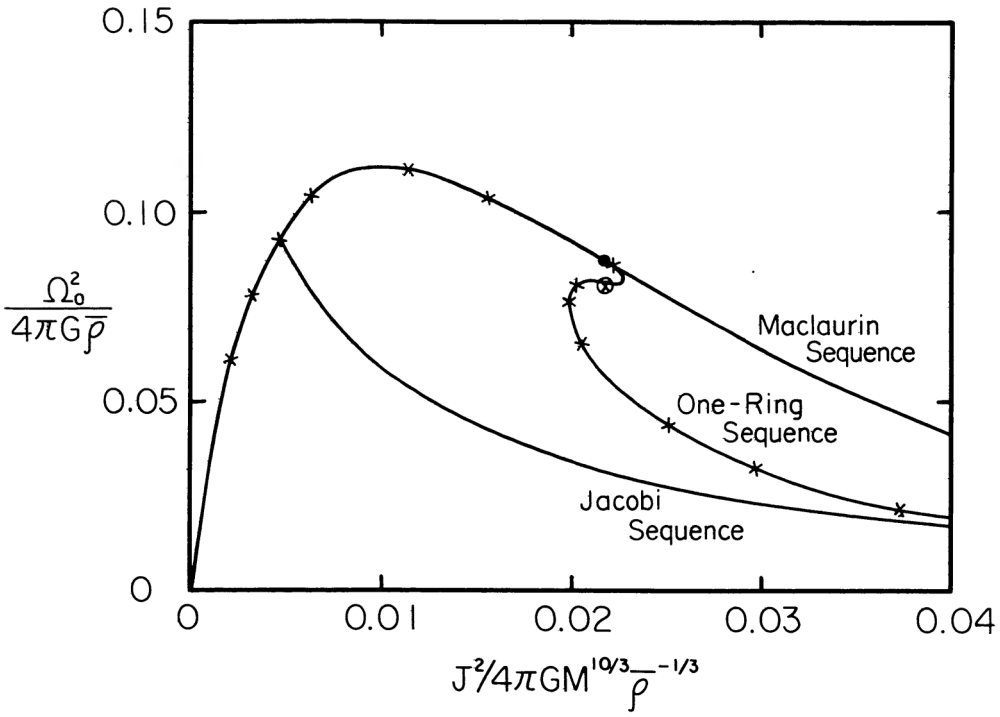

Figure 2.3: Dimensionless angular momentum as a function of the dimensionless angular momentum for a j-constant rotation law. From Hachisu (1986).

sequence, the dimensionless rotation rate increases up to a maximum of $\omega^2_{max} = 0.1123$ and then manages to decrease back to, asymptotically, 0. As we follow this sequence, the ellipsoid is flatter and flatter (see Fig.2.4 *Top right panel*) and the dimensionless the angular momentum does not stop increasing. At $(\infty, 0)$, the solution is an infinitly thin disk.

The Jacobi sequence is obtained by varying the principal semi-axes of the ellipsoid (a_1,a_2 and a_3). When two principal semi-axes are fixed, the third one is not free, i.e. there is only one equilibrium with a given ratio $\frac{a_2}{a_1}$ or $\frac{a_3}{a_1}$. As opposed to the Maclaurin sequence, the Jacobi sequence is monotonous and decreases. The Jacobi sequence branches off of the Maclaurin sequence for a dimensioless rotation rate of $\omega^2 = 0.09356$ ($e = 0.5827$).

This kind of object can for instance be used to study the galactic bars in barred spiral galaxies (Vandervoort, 1980).

Objects that can also be found in the $\omega^2 - j^2$ are the rings (or tori). The sequence is obtained after another bifurcation from the Maclaurin sequence. There is a specific kind of equilibrium between the Maclaurin ellipsoid and the ring : the "hamburger" shaped bodies (see Fig.2.4 *bottom left panel*). It is a transition state where the density along the semi-minor axis of the ellipsoid drops (Hachisu, 1986). The point connecting the hamburger sequence and the one-ring sequence is a specific state of torus called the horn torus (the vertical axis is in contact with the tore on the origin).

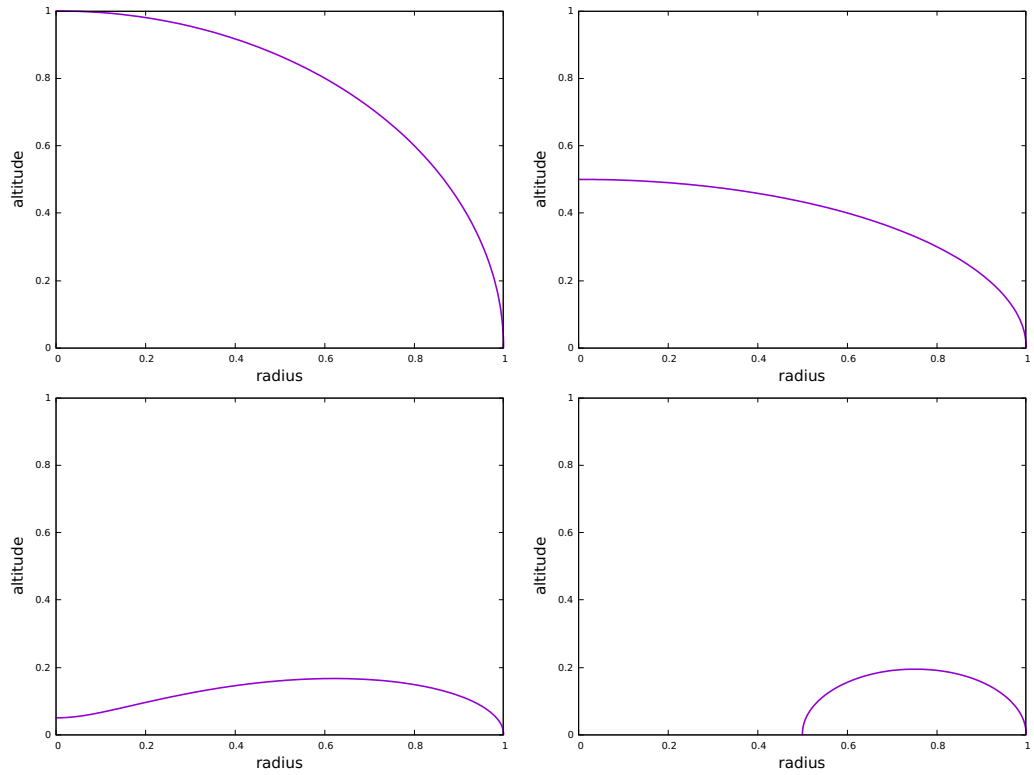

Figure 2.4: Different states of equilibrium in the incompressible case $n = 0$ computed with the `DROP` *code. (Top left) A non-rotating Maclaurin ellipsoid. (Top Right) A rotating Maclaurin ellipsoid. (Bottom left) A dumb-bell equilibrium). (Bottom right) A ring.*

2.3.2 Stability of Maclaurin spheroids

The stability of the equilibrium of polytropes can be investigated through analytical means to determine whether or not a configuration is stable or tends towards another one if disturbed. There is a lot of instabilities that can be investigated. Usually, instabilities are investigated with respect to the kinetic energy-to-gravitational energy ratio $\frac{T}{|W|}$ and is linked to the axis ratio or eccentricity. As shown earlier, the Maclaurin ellipsoid is one possible solution to the so called "compatibility condition", i.e. an equation giving the conditions for a rotation ellipsoid. Another solution is the Jacobi ellipsoid whom sequence branches off the Maclaurin sequence as seen in Sect.2.3.1. At the specific point of the bifurcation ($e = 0.5827$, $\omega^2 = 0.09356$ and $\frac{T}{|W|} = 0.1375$), the Maclaurin and Jacobi are both solution to this compatibility equation. For any higher eccentricity and for a given angular momentum, the total energy of the Jacobi is smaller than the one of the Maclaurin which means that in the presence of a perturbation, the Maclaurin might develop instabilities that leads it towards a Jacobi shape. After performing a stability analysis (Chandrasekhar, 1969; Horedt, 2004; Poisson and Will, 2014), the Maclaurin is concluded to be stable if its eccentricity is lower than 0.8126 (its axis ratio is higher than 0.5827).

If the Maclaurin's eccentricity is greater than 0.8126 but lower than 0.9523 and has a mean of dissipating energy (viscosity, tidal dissipation), if perturbed, the ellipsoid breaks its axisymmetry and evolves into a Jacobi ellipsoid. The Maclaurin dissipates its en-

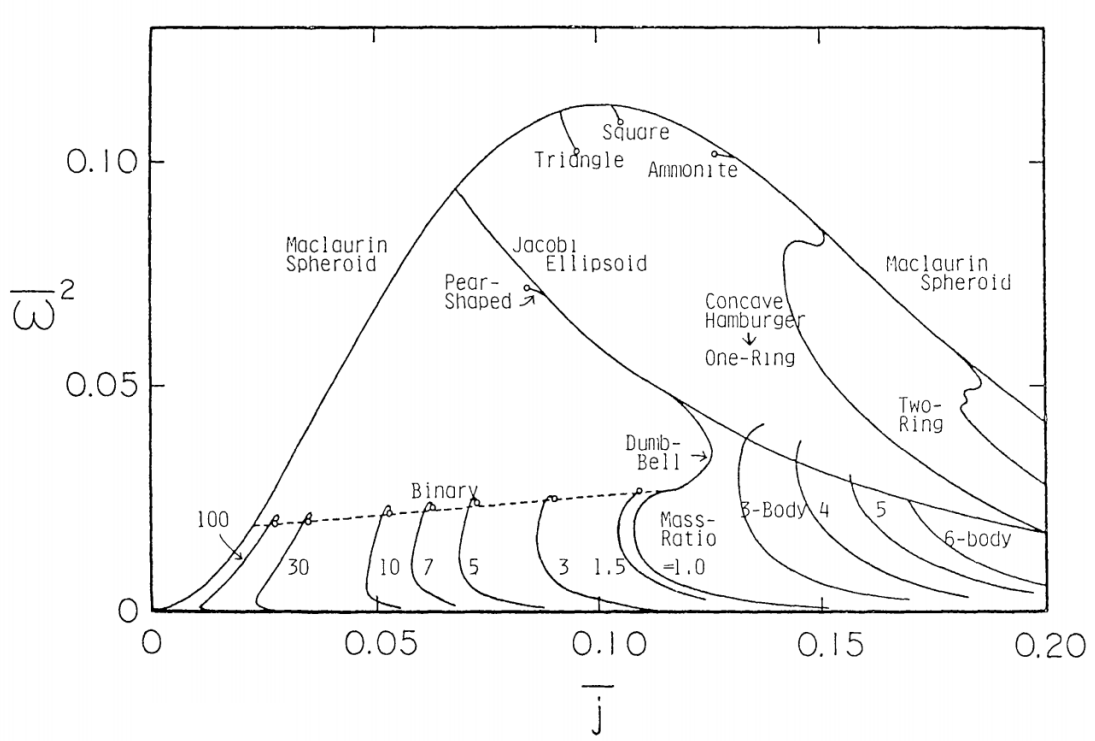

Figure 2.5: Squared dimensionless rotation rate as a function of the dimensionless angular momentum for homogenous configurations. Many sequences and bifurcations are shown. From Hachisu and Eriguchi (1984b).

ergy while it undergoes the transformation. This is called the secular instability. If the Maclaurin has no dissipation mechanism, it stays in a Maclaurin form. This is called the ordinary or dynamical stability.

If the Maclaurin's eccentricity is greater than 0.9523, it is always unstable and go into a Jacobi if perturbed, with or without dissipation mechanism. This is called the dynamical instability.

2.4 Fission sequences

The theory of figures can be applied to the "fission" process through bifurcations and sequences. In the incompressible case, a large amount of new sequences were unveiled in Hachisu and Eriguchi (1984b). They are presented in Fig.2.5 and the 3D equilibria constituting these sequences are shown in Fig.2.6. A fission scenario involves a Jacobi ellipsoid evolving quasi-steadily into a binary with a transitory shape called a "dumb-bell". Similar scenarii are presented for 3-and-more-body systems starting from a triangle, square or ammonite equilibrium.

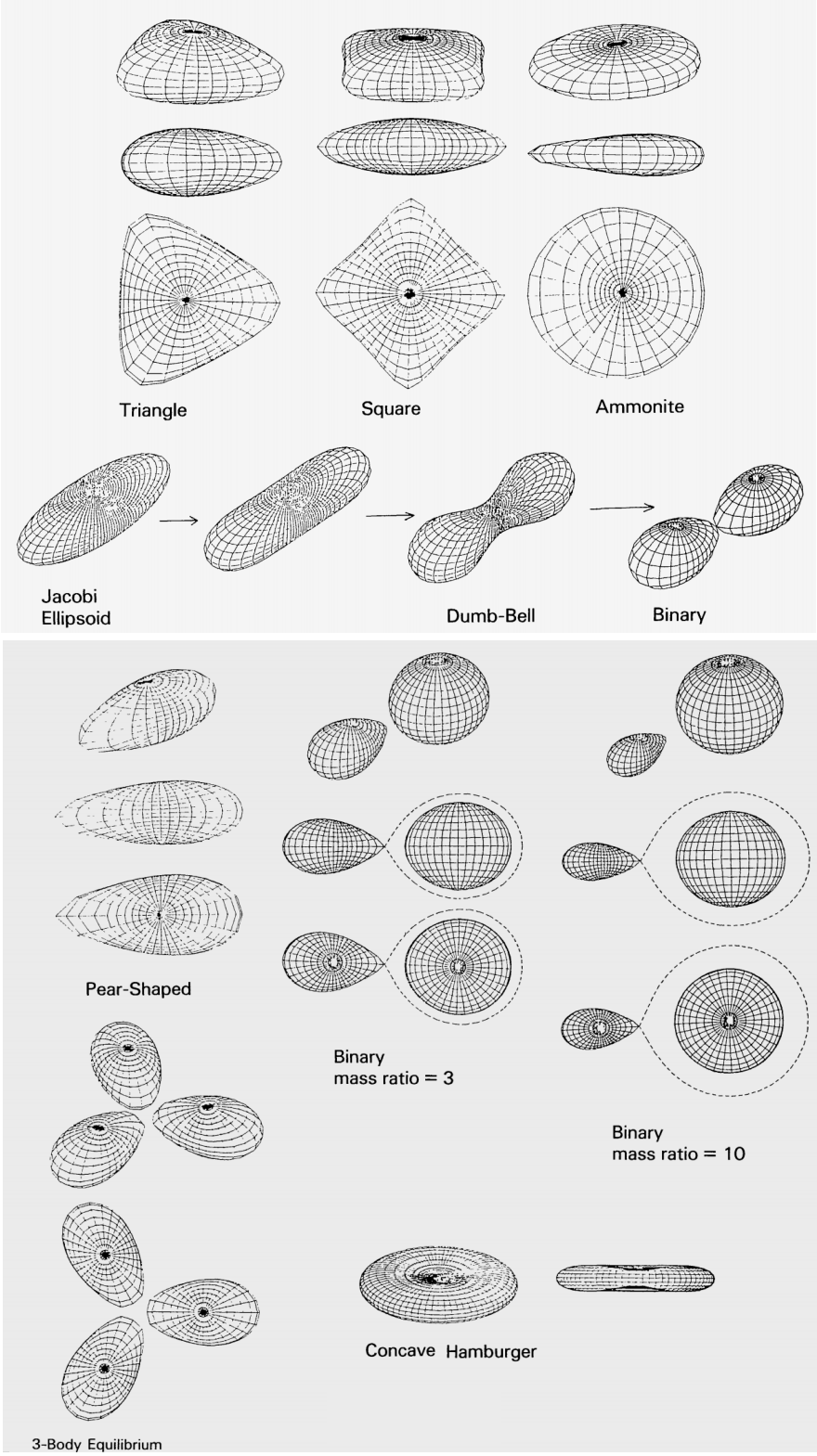

Figure 2.6: 3D representations of the equilibrium displayed in Fig.2.5. From Hachisu and Eriguchi (1984b).

Chapter 3

Figures of equilibrium with rotation

Contents

When leaving the slow and rigid rotation hypothesis, we cannot analytically solve the *fundamental equation of the problem* in general (see Sect.2.2). We have to use numerical means to solve this equation and generate equilibria.

The first computations on rotating polytropes were obtained by James (1964). But in the 70's, a new way of solving this problem was brought up to light by Ostriker and Mark (1968) thanks to an iterative algorithm : a Self-Consistant Field method. However, this first version suffered from a "drift" problem. This problem was overcome a decade later by Hachisu (1986) doing a self-normalization of the solution, and avoiding the aforementionned drift. This latest paper is a cornerstone in the numerical work on figures of equilibrium and constitutes an unavoidable rudiment for the developments of numerical codes based on this principle. This new method by Hachisu (1986) is efficient and accurate for any polytropic index and any given rotation.

Since we consider all kind of rotation profile which can lead to highly flattened bodies, the use of spherical coordinates does not seem to be the wisest choice. We use instead cylindrical coordinates from now on.

3.1 Equation set

When considering rotation, we need to reconsider the point reflection and use a axis symmetry instead. A centrifugal term is added to the hydrostatic equilibrium. From the Schwarz condition, the angular momentum and the rotation rate only depend on the radius R (Amendt et al., 1989). The circular velocity is defined as :

$$\vec{v} = \Omega(R) R \vec{e}_\Phi \tag{3.1}$$

and the hydrostatic equilibrium can be written like :

$$-\frac{v^2}{R}\vec{e_\phi} = -\frac{1}{\rho}\vec{\nabla}P - \vec{\nabla}\Psi \tag{3.2}$$

We can introduce the centrifugal potentiel :

$$\Phi = -\int \Omega^2(R) R dR < 0 \tag{3.3}$$

Provided the polytropic EOS, the enthalpy can be expressed as :

$$H = K\frac{\gamma}{\gamma - 1}\rho^{\gamma - 1} + cst, \tag{3.4}$$

and we can rewrite Eq.(3.2) as :

$$\vec{\nabla}\left(H + \Psi + \Phi\right) = \vec{0}. \tag{3.5}$$

Finally, our equation set reads, with the Poisson equation :

$$\begin{cases} H + \Psi + \Phi = C, \\ H = K(n+1)\rho^{\frac{1}{n}}, \rho > 0, \\ \Delta\Psi = 4\pi\rho G \end{cases} \tag{3.6}$$

3.1.1 Rotation law

As outlined in the introduction, the rotation profile are generally the result of evolution process and mechanism at work. It is generally not very well constrained. It is customary to consider some ad hoc rotation laws based on physical arguments : rigid rotation (rocky planets, core of the sun), v-constant rotation (galactic profile, Sofue (2013)) ,j-constant rotation (relaxed system) and Keplerian rotation (matter around central mass).

In those differents cases, the centrifugal potential Φ and the squared angular velocity Ω^2 can be expressed as follow :

$$\begin{cases} \text{Rigid rotation :} \\ \Phi(R) = -\frac{R^2}{2} \quad \text{and} \quad \Omega^2 = \Omega_0^2 = Const, \\ \\ v\text{-constant rotation :} \\ \Phi(R) = -\frac{1}{2}\ln(R^2+d^2) \quad \text{and} \quad \Omega^2 = \frac{v_0^2}{R^2+d^2}, \\ \\ j\text{-constant rotation :} \\ \Phi(R) = -\frac{1}{2}\frac{1}{R^2+d^2} \quad \text{and} \quad \Omega^2 = \frac{j_0^2}{R^2+d^2}, \\ \\ \text{Keplerian rotation due to a central point mass :} \\ \Phi(R) = \frac{1}{R} \quad \text{and} \quad \Omega^2 = \frac{GM_0}{R^3}, \end{cases} \tag{3.7}$$

where d is a parameter set to a small value in order to avoid the divergence at $R = 0$.

In the case of an isolated single body, there is no point of using a keplerian law. It will however be used in the following chapters and in particular in Chap.6

3.1.2 Dimensionless set

In order to solve this problem numerically, we change the physical equation set for a dimensionless one. This transformation has three advantages. The first one is it gives us a scale free problem which means that we can study bodies of all sizes : black holes, neutron stars, main-sequence stars, planet or even moons. The second one is that we can have similarities through coefficients (in a fashion similar to the Reynolds number) : systems at different scales can have the same behaviour and it allows generical studies. The third one is that we are dealing only with dimensionless quantities of the order of unity. It is convenient for our numerical approach since performing computations with low and large value can be tricky and bring his share of problems such as calculation errors.

To express dimensionless variables as physical ones, we need to normalize regarding the physical scales of the problem : L for the length, ρ_0 for the density and Ω_0 for the rotation rate.

The dimensionless length writes

$$\begin{cases} \hat{R} = \frac{R}{L} \\ \hat{Z} = \frac{Z}{L} \end{cases} \tag{3.8}$$

We can proceed in a similar way for the other dimensionless quantities such as density, pressure, rotation rate, gravitationnal potential, enthalpy and centrifugal potential :

$$\begin{cases} \hat{\rho} = \frac{\rho}{\rho_0} \\ \hat{P} = \frac{P}{P_0} \\ \hat{\Omega} = \frac{\Omega}{\Omega_0} \\ \hat{\Psi} = \frac{\Psi}{\Psi_0} \\ \hat{H} = \frac{H}{H_0} \\ \hat{\Phi} = \frac{\Phi}{\Phi_0} \end{cases} \tag{3.9}$$

where

$$\begin{cases} P_0 = K\rho^\gamma, \\ \Psi_0 = G\rho_0 L^2, \\ H_0 = K(n+1)\rho_0^{1/n}, \\ \Phi_0 = \Omega_0 L^2. \end{cases} \tag{3.10}$$

So the equation set (3.6) becomes

$$\begin{cases} C_1\hat{H} + C_2\hat{\Phi} + \hat{\Psi} = C_3, \\ \hat{\rho}^{1/n} = \sup(\hat{H}, 0), \\ \Delta\hat{\Psi} = 4\pi\hat{\rho}, \end{cases} \tag{3.11}$$

with

$$\hat{\Phi} = -\int \hat{\Omega}^2(\hat{R})\hat{R}d\hat{R} \tag{3.12}$$

The constants C_1 and C_2 are defined as follow when n is finite :

$$\begin{cases} C_1 = \frac{H_0}{\Psi_0} = \frac{K(n+1)\rho_0^{\gamma-2}}{GL^2}, \\ C_2 = \frac{\Phi_0}{\Psi_0} = \frac{\Omega_0^2}{G\rho_0}. \end{cases} \tag{3.13}$$

When $n = \infty$, i.e. $\gamma = 1$, we must adapt our system :

$$\begin{cases} H_0 = K, \\ \hat{\rho} = e^{\hat{H}}, \\ C_1 = \frac{H_0}{\Psi_0} = \frac{K(n+1)\rho_0^{\gamma-2}}{GL^2}. \end{cases} \tag{3.14}$$

3.2 The Self-Consistent Field method and the DROP-code for a single body

In this section, we describe the numerical code DROP as it was when the thesis started. It is deeply inspired by the code reported in Hachisu (1986) but brings new significant improvements regarding : a) the treatment of the Poisson equation, b) the consideration of the fluid boundary and c) the convergence of the SCF is improved from a preconditionner. The version presented here was reported in Huré and Hersant (2017) and Huré et al. (2018).

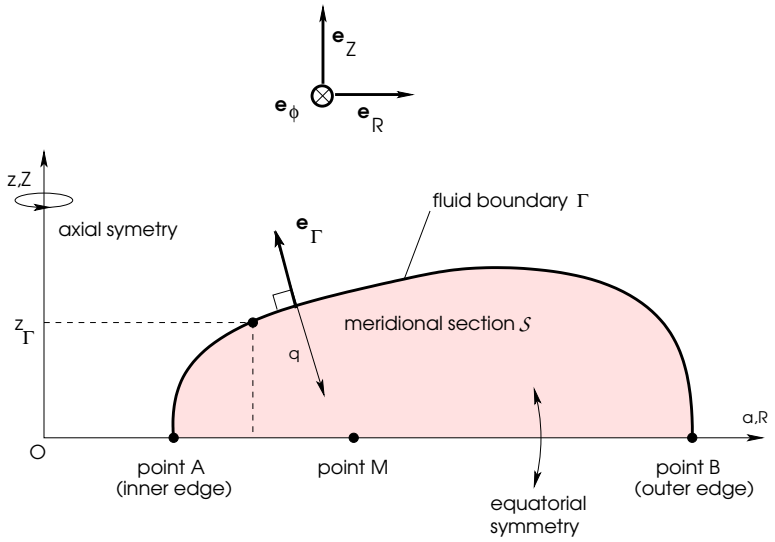

Figure 3.1: Typical configuration for a self-gravitating body. The SCF-method relies on two reference points A and B selected along the fluid boundary Γ (bold line) and a third, floating point M where enthalpy is maximum.

3.2.1 The Self-Consistent Field method

The Self-Consistent Field method is an iterative method that was first used in quantum physics to determine wave-functions (Hartree, 1928; Fock, 1930) by solving the Schrödinger equation for a given number of nuclei and atoms. It was first called the Hartree-Fock method for its only application in wave mechanics.

The idea is pretty simple : we choose a control parameter that is to be fine-tuned after solving the set of equations several times until convergence. For instance, in quantum mechanics it is the wavefunction that is fine-tuned through the Schrödinger equation solving until the energy of the system converges. In the astrophysics context and more specifically in the figures of equilibrium framework, the enthalpy is the field that is fine-tuned (Ostriker and Mark, 1968; Hachisu, 1986).

3.2.2 The SCF cycle

To start the iterative procedure, we need an initial enthalpy field. In our case, we use a paraboloid as our guessed enthalpy field. At the fluid boundary, because of the absence of external pressure, we have $\hat{H} = 0$ and in particular at the two specific points A and B. Since we have three constants to determine, we need a third equation : the point of maximum enthalpy M is chosen. Eq.(3.11)a evaluated at those points gives :

$$\begin{cases} C_2\hat{\Phi}_A + \hat{\Psi}_A = C_3 \\ C_2\hat{\Phi}_B + \hat{\Psi}_B = C_3 \\ C_1\hat{H}_M + C_2\hat{\Phi}_M + \hat{\Psi}_M = C_3 \end{cases} \tag{3.15}$$

By substracting Eq.(3.15)a to Eq.(3.15)b, we get C_2. Then, we can inject this expression of C_2 in one of the previous equations yielding C_3. And lastly, we inject the expression of C_2 and C_3 in Eq.(3.15c) to have C_1 which yields :

step	operation
1	$\hat{\rho}$ is computed from the polytropic assumption Eq.(3.11b); only positive parts of the enthalpy is retained,
2	$\hat{\Psi}$ is computed from the Poisson equation, i.e. Eq.(3.11c),
3	values of $\hat{\Psi}$ at the 2 reference points A and B are deduced, i.e. $\hat{\Psi}_A$ and $\hat{\Psi}_B$,
4	C_2 is obtained from Eq.(3.16b),
5	C_3 is deduced from Eq.(3.16c),
6	$C_1\hat{H}$ is computed from the Bernoulli equation, i.e. Eq. (3.11a)
7	the point M where $C_1\hat{H}$ is maximum is localized,
8	a new $\hat{H}$ is computed with $\hat{H} = \frac{C_1\hat{H}}{C_1}$

Table 3.1: Main steps of the SCF-method for a polytropic star. The loop starts for a guessed value of the enthalpy $\hat{H}$.

$$\begin{cases} C_1 = -\frac{\hat{\Psi}_M\Delta\hat{\Phi}_{AB}+\hat{\Psi}_A\Delta\hat{\Phi}_{BM}+\hat{\Psi}_B\Delta\hat{\Phi}_{MA}}{\hat{H}_M\Delta\hat{\Phi}_{AB}}, \\ C_2 = -\frac{\Delta\hat{\Psi}_{AB}}{\Delta\hat{\Phi}_{AB}}, \\ C_3 = \frac{\hat{\Psi}_B\hat{\Phi}_A-\hat{\Phi}_B\hat{\Psi}_A}{\Delta\hat{\Phi}_{AB}}, \end{cases} \tag{3.16}$$

where $\Delta\hat{\Phi}_{XY} = \hat{\Phi}_X - \hat{\Phi}_Y$ and $\Delta\hat{\Psi}_{XY} = \hat{\Psi}_X - \hat{\Psi}_Y$. In the method presented by Hachisu (1986), $\hat{H}$ is normalized by imposing $\hat{H}_M = 1$ which imply that, in practical, C_1 is found at each iteration t by doing :

$$C_1^{(t+1)} = \max(\hat{H}^{(t+1)}) = \max\left(C_3^{(t)} - C_2^{(t)}\hat{\Phi}^{(t)} - \hat{\Psi}^{(t)}\right) = \hat{H}_M^{(t+1)}. \tag{3.17}$$

The SCF cycle is described in Tab.3.1 and in Fig.3.2

3.2.3 Normalization

Under an angular symmetry, the only two relevant coordinates are (R, Z), in the dimensionless space $(\hat{R}, \hat{Z})$. In this version of the DROP-code, the equatorial symmetry is not used to reduce the computational box to the upper plane because the Neumann boundary conditions can be avoided and there are less Dirichlet boundary conditions to be calculated : the upper condition values are reproduced onto the lower plane.

The most numerical intensive part in the DROP-code is the determination of the gravitational potential through the Poisson equation Eq.(3.11)c. This potential needs to be computed at every step since the enthalpy and therefore the density varies from one step to another. The easiest way to compute this equation is to integrate it over space but it has the flaw of being really slow. In the DROP code, this equation is solved using multigrid. It is a very efficient method when it comes to solving partial differential equations since it uses nested grids mixed with relaxation (Briggs et al., 2000; Gheller et al., 2004; Guillet and Teyssier, 2011; Braess, 1981). The relaxation process on a highly resolute grid tends to fastly kills short wavelengths but struggles to make long wavelengths disappear. To bypass this problem, the resolution of the initial grid is downgraded a given number of times to obtain coarser grid in which the high frequencies from the highly resolute grid are transformed into low frenquecies allowing the relaxation to perform well on long

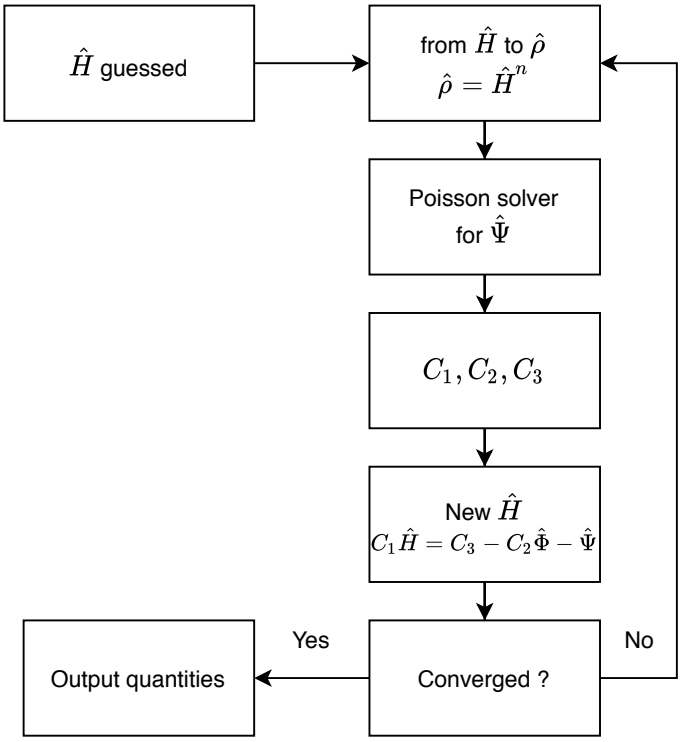

Figure 3.2: SCF-Cycle repeated as long as necessary to obtain a converged solution. It is achieved when $\frac{1}{N^2}\sum_{i,j=0}^{N}|\hat{H}_{i,j}^{(t+1)} - \hat{H}_{i,j}^{(t)}| \leq \epsilon$*, with* ϵ *being the convergence criterion, typically a small number.*

wavelengths aswell. The transition between all the grids are possible using restriction and prolongation operators which permit to have the discretization of the equations on the values of the fields on any given grid and nodes.

The multigrid techniques requires that the number of intervals in $\hat{R}$ and $\hat{Z}$ is a power of 2 (there are some methods using power of 3). The highest resolution is the resolution of the regular grid and is defined by an integer denoted l. The finest grid then posseses 2^l intervals and $N = 2^l + 1$ computational nodes, per direction. The multigrid performed best when the nodes of the grids are regularly spaced which is why computations are made on a square grid $[\hat{R}_0, \hat{R}_N] \times [\hat{Z}_0, \hat{Z}_N]$.

The numerical resolution is defined by :

$$\hat{h} = \frac{\hat{R}_N - \hat{R}_0}{N} = \frac{\hat{Z}_N - \hat{Z}_0}{N} \tag{3.18}$$

and each nodes are calculated by :

$$\begin{cases} \hat{R}_i = \hat{R}_0 + i\hat{h}, & i \in [0, N], \\ \hat{Z}_i = \hat{Z}_0 + j\hat{h}, & j \in [0, N]. \end{cases} \tag{3.19}$$

To go from a l level to the $l-1$ level of multigrid, the only nodes that are kept are the $2i$ and $2j$ nodes.

When discretizing the cylindrical Poisson equation Eq.(3.11c), the laplacian writes :

$$\Delta\hat{\Psi}_{i,j} = \left(\delta^2_{\hat{R}\hat{R}} + \frac{1}{\hat{R}_i}\delta_{\hat{r}} + \delta^2_{\hat{Z}\hat{Z}}\right)\hat{\Psi}_{i,j} + O(h^2) \tag{3.20}$$

and the second member is :

$$s_{i,j} = 4\pi\hat{\rho}_{i,j} \tag{3.21}$$

When using central second-order scheme, we finally have :

$$\hat{\Psi}_{i,j} = \frac{1}{4}\Big(C_+\hat{\Psi}_{i+1,j} + C_-\hat{\Psi}_{i-1,j} \tag{3.22}$$

$$+\hat{\Psi}_{i,j+1} + \hat{\Psi}_{i,j-1} - 4\pi\hat{\rho}_{i,j}\hat{h}^2\Big), \tag{3.23}$$

where

$$\begin{cases} C_+ = 1 + \frac{\hat{h}}{2\hat{r}_i}, \\ C_- = 1 - \frac{\hat{h}}{2\hat{r}_i}. \end{cases} \tag{3.24}$$

Dirichlet boundary conditions

The Dirichlet boundary condition brings a constraint on the value of the field at specific points. In our case, those points are at the edges of the computational box. Under axial and equatorial symmetries, these boundary values are determined numerically by evaluating the dimensionless potential takes the form Durand (1953); Kellog (1929) :

$$\hat{\Psi} = \iint_{\mathcal{S}} \hat{\rho}\kappa d\hat{z}d\hat{a}, \tag{3.25}$$

where

$$\begin{cases} \hat{a} \equiv \frac{a}{L}, \\ \hat{z} \equiv \frac{z}{L}, \end{cases} \tag{3.26}$$

$$\kappa = -2\sqrt{\frac{\hat{a}}{\hat{R}}}\left[k_+\mathbf{K}(k_+) + k_-\mathbf{K}(k_-)\right], \tag{3.27}$$

$$\mathbf{K}(k) = \int_0^{\pi/2} \frac{d\phi}{\sqrt{1 - k^2\sin^2\phi}}, \tag{3.28}$$

is the complete elliptic integral of the first kind,

$$k_\pm = \frac{2\sqrt{\hat{a}\hat{R}}}{\sqrt{(\hat{a}+\hat{R})^2 + \hat{\zeta}^2_\pm}}, \tag{3.29}$$

is the modulus, $\hat{\zeta}_+ = \hat{Z} - \hat{z}$ and $\hat{\zeta}_- = \hat{Z} + \hat{z}$. κ diverges logarithmically when $k \to 1$ making the computation of Ψ inaccurate. This divergence is avoided as long as we do not calculate Ψ inside the source. The fluid boundary stays strictly out of the grid boundary where the Dirichlet condition is applied.

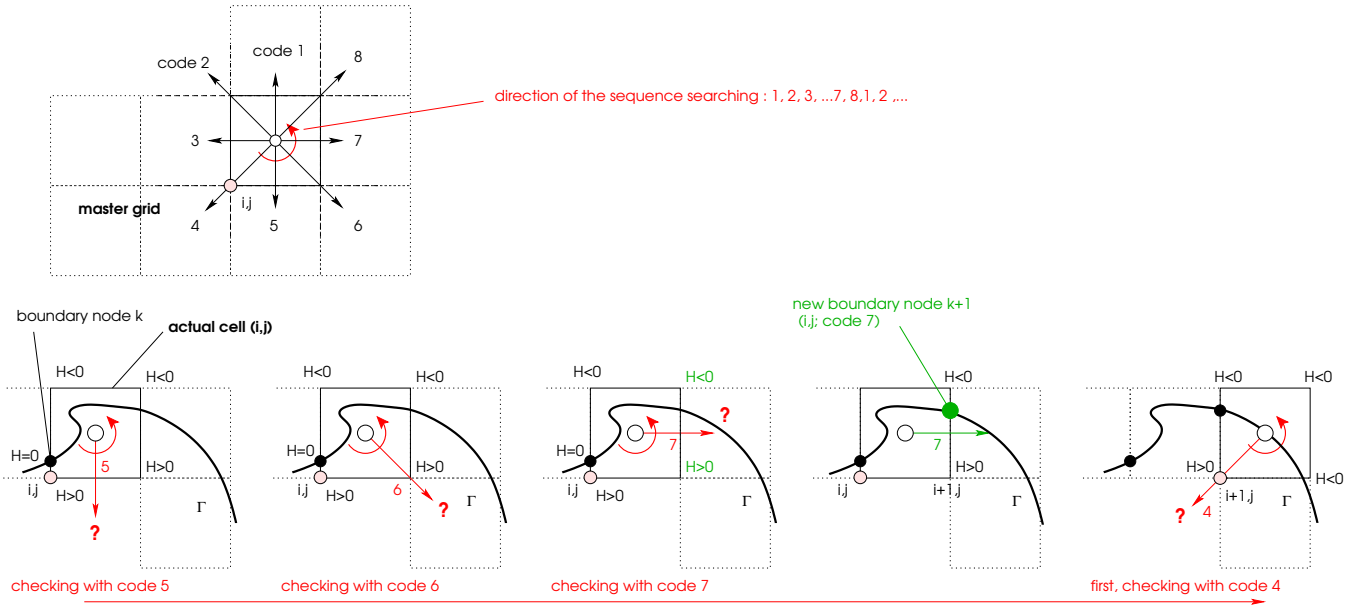

Figure 3.3: The determination of the fluid boundary Γ resides on the 8-point directional Freeman chain code. The curve is gradually unveilled by searching for the edge of the actual cell where the enthalpy vanishes. The signs of $\hat{H}$ at successive pairs of grid nodes is checked. The new boundary node is then estimated by a quadratic formula. Edges and corners are visited following a unique sequence, and the selected edge is given a code $c \in [1, 8]$.

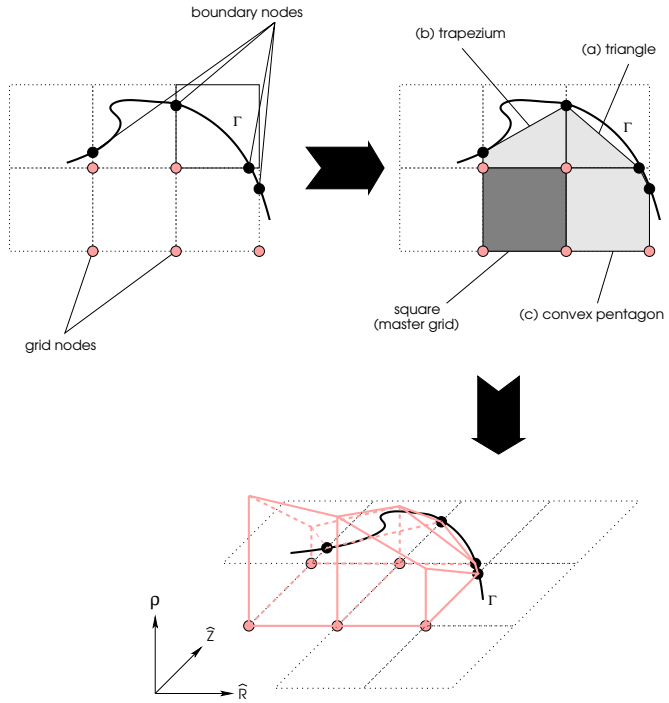

Figure 3.4: From the coordinates of boundary and grid nodes, three types of boundary cells can be generated depending on their base : triangular cells (a), trapezoidal cells (b) and pentahedral cells (c). The volume of the corresponding polyhedra are then computed using known formula.

3.2.4 Detection of the fluid boundary

In order to have the better accuracy possible, we can refine as much as we can the quality of the global quantities such as the boundary value of the gravitational potential for the Poisson equation or the various integrals needed to calculate output like the mass, the volume and other properties. Huré and Hersant (2017) shows that the accuracy on the solutions is improved when taking into account the fluid boundaries properly. The closer to 0 the polytropic index, the sharper the transition between the fluid and the free space. Therefore, a high precision on the boundary is needed.

When considering isolated system without any external source of pressure, the fluid boundary is defined by $\hat{H} = 0$. This boundary is a line that almost never cross the nodes of the grid. In every step of the SCF procedure, we determine the fluid boundary Γ by using a 8-point directional Freeman chain code (Freeman, 1961). We start on a reference point, usually this point is on the Z-axis and we detect all the cells where the boundary is up to the moment when we are on the R-axis. Fig.3.3 depicts the process in our code. The Freeman routine catalogues every nodes where the boundary crosses the edge of a cell, those nodes are identified by $(\hat{R}_k, \hat{Z}_k)$. All of the boundary nodes $(\hat{R}_k, \hat{Z}_k)$ paired with the surrounding natural grid nodes $(\hat{R}_i, \hat{Z}_j)$ forms three types of volume : triangle, trapezium and a pentagon (see Fig. 3.4).

3.2.5 Virial test

The Virial theorem is an energy equation that links the kinetic energy, the internal energy and the gravitational energy and shows how they are spatially shared. It is easily obtain by integrating the dot product of equation Eq.(3.6a) over the mass $m = \rho dV$. Given the stationnary nature of our problem , the virial theorem reads in the physical space :

$$W + 2T + U = 0, \tag{3.30}$$

where

$$\begin{cases} W = \frac{1}{2}\iiint \Psi dm, \\ T = \frac{1}{2}\iiint v^2 dm, \\ U = 3\Pi, \\ \Pi = \iiint \frac{P}{\rho} dm. \end{cases} \tag{3.31}$$

It writes, for finite indices, in dimensionless form :

$$\hat{W} + \frac{C_1}{n+1}\hat{U} + 2C_2\hat{T} = 0. \tag{3.32}$$

For $n = +\infty$, we have :

$$\hat{W} + C_1\hat{U} + 2C_2\hat{T} = 0, \tag{3.33}$$

$$\begin{cases} W = GL^5\rho_0^2\hat{w}, \\ \Pi = P_0L^3\hat{\Pi}, \\ T = L^5\rho_0\hat{\Omega}_0^2\hat{T}, \end{cases} \tag{3.34}$$

and

$$\begin{cases} \hat{W} = \pi \int\int_{\mathcal{S}} \hat{\Psi}\hat{\rho}\hat{a}d\hat{a}d\hat{z}, \\ \hat{U} = 3\hat{\Pi}, \\ \hat{\Pi} = 2\pi \int\int_{\mathcal{S}} \hat{P}\hat{a}d\hat{a}d\hat{z}, \\ \hat{T} = \pi \int\int_{\mathcal{S}} \hat{\Omega}^2\hat{\rho}\hat{a}^3 d\hat{a}d\hat{z}. \end{cases} \tag{3.35}$$

When the SCF method has converged towards an equilibrium, it means that Eq.(3.11) is solved and that Eq.(3.32) should be satisfied. But numerical techniques are only as precise as the algorithm used and they bring their share of errors. So the virial parameter VP defined as

$$VP = \frac{1}{|\hat{W}|}\left(\hat{W} + \frac{C_1}{n+1}\hat{U} + 2C_2\hat{T}\right) \tag{3.36}$$

should be as closed as possible to 0. Usually, and depending on the resolution of our grid, this parameter is of the order of $10^{-2} \sim 10^{-4}$.

3.3 Sequence of compressible equilibrium

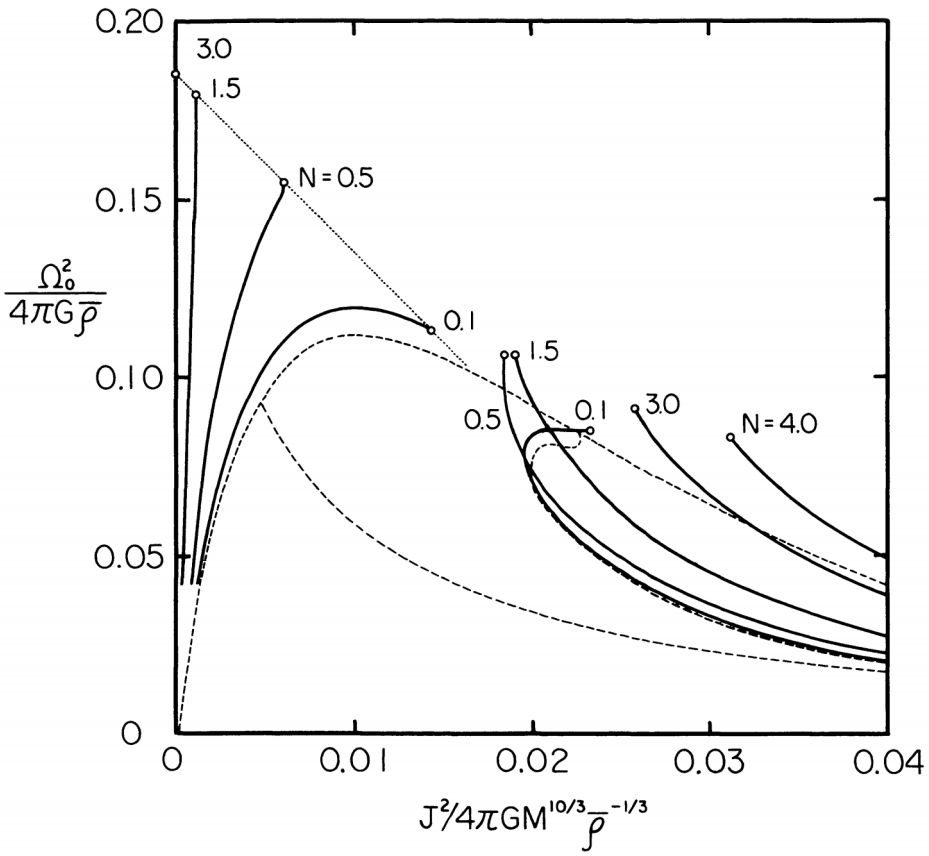

Figure 3.5: Dimensionless angular momentum as a function of the dimensionless angular momentum for a solid rotation law. From Hachisu (1986).

					n=0						
z_A	ω_0^2	M	V	J	T	$-W$	3Π	P_{max}	j^2	ω^2	VP
1.000	0.0000	4.1904	4.1904	0.0145	0.0000	10.533	10.525	2.0942	0.0000	0.0000	-3.13
0.500	1.3147	2.0953	2.0953	0.9613	0.5511	3.1845	2.0808	0.8281	0.0062	0.1046	-3.33
0.333	1.4039	1.3957	1.3957	0.6618	0.3921	1.5259	0.7413	0.4429	0.0115	0.1117	-3.54
0.250	1.3099	1.0482	1.0482	0.4801	0.2747	0.8971	0.3475	0.2764	0.0157	0.1042	-3.82
0.167	1.0819	0.7011	0.7011	0.2919	0.1518	0.4194	0.1158	0.1376	0.0222	0.0861	-4.61
-0.333	0.8268	0.9235	0.9235	0.4448	0.2022	0.6433	0.2383	0.1729	0.0205	0.0658	-3.09
-0.417	0.6908	0.8432	0.8432	0.3973	0.1651	0.5312	0.2006	0.1593	0.0222	0.0550	-3.12
-0.500	0.5474	0.7195	0.7195	0.3246	0.1201	0.3858	0.1455	0.1353	0.0251	0.0436	-3.77
-0.583	0.4078	0.5703	0.5703	0.2401	0.0767	0.2435	0.0902	0.1057	0.0298	0.0325	-3.97
-0.667	0.2783	0.4076	0.4076	0.1539	0.0406	0.1262	0.0451	0.0739	0.0375	0.0221	-4.21
-0.750	0.1683	0.2526	0.2526	0.0806	0.0165	0.0499	0.0169	0.0446	0.0507	0.0134	-3.33
					n=3.0						
1.000	0.0000	0.0772	4.1910	3.36e-6	0.0000	0.0090	0.0090	0.0660	0.0000	0.0000	-3.84
0.917	0.0111	0.0628	3.8254	4.46e-4	2.35e-5	0.0063	0.0063	0.0571	4.08e-5	0.0537	-3.79
0.833	0.0192	0.0490	3.4096	3.97e-4	2.76e-5	0.0042	0.0041	0.0481	7.09e-5	0.1064	-3.74
0.750	0.0240	0.0367	2.9273	2.78e-4	2.15e-5	0.0026	0.0025	0.0395	8.71e-5	0.1525	-3.67
0.667	0.0256	0.0260	2.2983	1.63e-4	1.30e-5	0.0014	0.0014	0.0314	9.09e-5	0.1801	-3.59
*0.662	0.0256	0.0254	2.2496	1.57e-4	1.25e-5	0.0014	0.0014	0.0309	9.08e-5	0.1803	-3.59
*-0.442	0.0984	0.0634	0.6977	0.0086	0.0014	0.0041	0.0014	0.0101	0.0263	0.0862	-3.96
-0.458	0.0969	0.0681	0.7355	0.0098	0.0015	0.0046	0.0016	0.0105	0.0268	0.0832	-4.03
-0.500	0.0873	0.0710	0.7226	0.0108	0.0016	0.0048	0.0016	0.0104	0.0290	0.0707	-4.13
-0.583	0.0642	0.0621	0.5889	0.0095	0.0012	0.0036	0.0012	0.0085	0.0356	0.0485	-4.23
-0.667	0.0426	0.0461	0.4195	0.0065	0.0007	0.0019	0.0006	0.0060	0.0456	0.0308	-4.28
-0.750	0.0250	0.0291	0.2580	0.0035	0.0003	0.0008	0.0002	0.0036	0.0618	0.0176	-4.31

*Table 3.2: Various output quantities of rotating polytropes for a rigid rotation for several given polytropic index n. Spheroids are when $z_A \geq 0$ and toroids are when $z_A \leq 0$. The * denotes the critical rotation.*

Sequences are produced in the same fashion as for the incompressible case : by varying the geometrical properties (i.e. the rotation) of the polytrope. A few examples of compressible sequences are given in Fig.2.3 for several values of the polytropic index. The first noticeable change from the compressible case is the opening of the Maclaurin sequence. This is caused by the lack of equilibrium for some axis ratio and it creates a "forbidden gap" between the ellipsoid and ring sequences.

The last equilibrium found on the ellipsoid sequence and the ring sequence on each side of the gap is called a critical rotation, it is the last axis ratio possible that yields an equilibrium. Those state are rather special because they adopt a very specific shape (see Fig.2.4 *top right panel* and *bottom right panel*). Whereas in the incompressible case and far from the critical rotation in the compressible case, the derivative of the fluid boundary in point B is continuous from the upper plan to the lower plan (see Fig2.4 *top left panel* and *bottom left panel*), near the critical rotation, this derivative is no longer continuous and the fluid boundary forms a kind of a beak. We do not know exactly the reason behind the existence of such limit but physically it means that in the compressible case, the three forces we takes into account cannot manage to counterbalance each other.

As an example, we give output properties of incompressible ($n = 0$) and incompressible

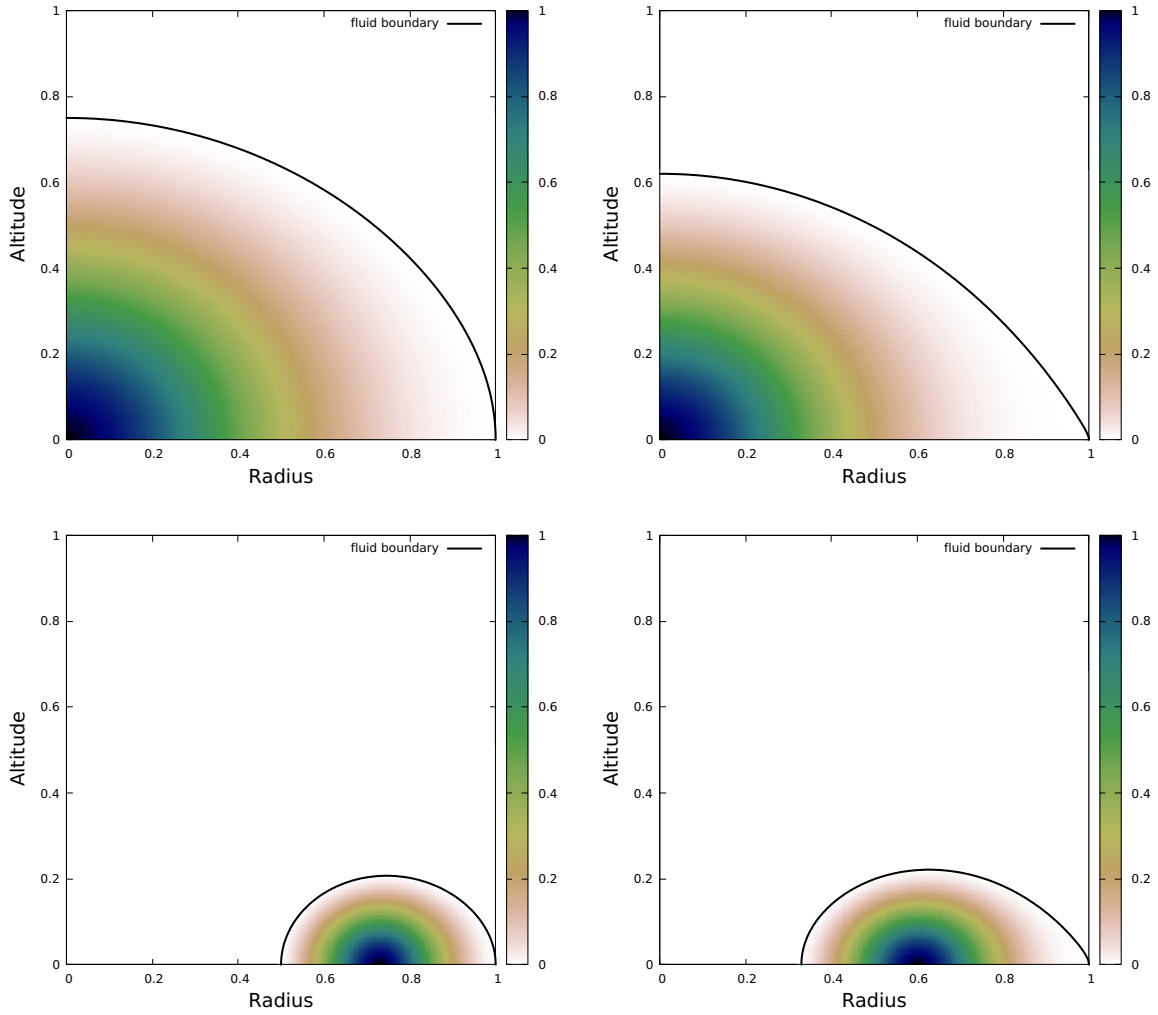

Figure 3.6: Different states of equilibrium in the compressible case $n = 1.5$. (Top left) A spheroid far from the critical rotation. (Top Right) Critical rotation of an spheroid. (Bottom left) A ring far from the critical rotation. (Bottom right) Critical rotation of a ring.

($n = 3$) isolated polytropes for various axis ratios on Tab.3.2. It compares very well to the tables given in Hachisu (1986) and insure that the DROP-code computes accuratly equilibrium. One should note that there is no big difference in the values for low polytropic indices ($n \leq 1.5$) but for higher polytropic indices such as $n = 3$ or $n = 4$, some overall discrepancies of a few percents start to appear for all the output quantities. This was already noticed by Trova (2013) (private communication).

3.4 influence of the rotation law

As seen in Sect.3.1.1, several law can be prescribed. Let us give a few examples of sequences of equilibrium in the compressible and incompressible case for a v-constant rotation and j-constant rotation laws.

3.4.1 The v-constant rotation

Hachisu (1986) computed sequences with a v-constant rotation law for three polytropic indices : $n = 0$, $n = 1.5$ and $n = 3$. He set the d^2 parameter in Eq.(3.7) to $d^2 = 0.01$. Sequences are shown in Fig.3.7. We can see that the sequences behave very differently for the solid rotation case : the maximum ω^2 reachable is lower by a factor ~ 3 for $n = 0$ and $n = 1.5$ and there is continuous sequence for compressibles cases. Some similarities are nonetheless present like the opening of sequence when n is high enough, here it is $n = 3$ but the true threshold is probably is bit lower. There is also spheroid configurations for low j^2 and ring configurations for high j^2.

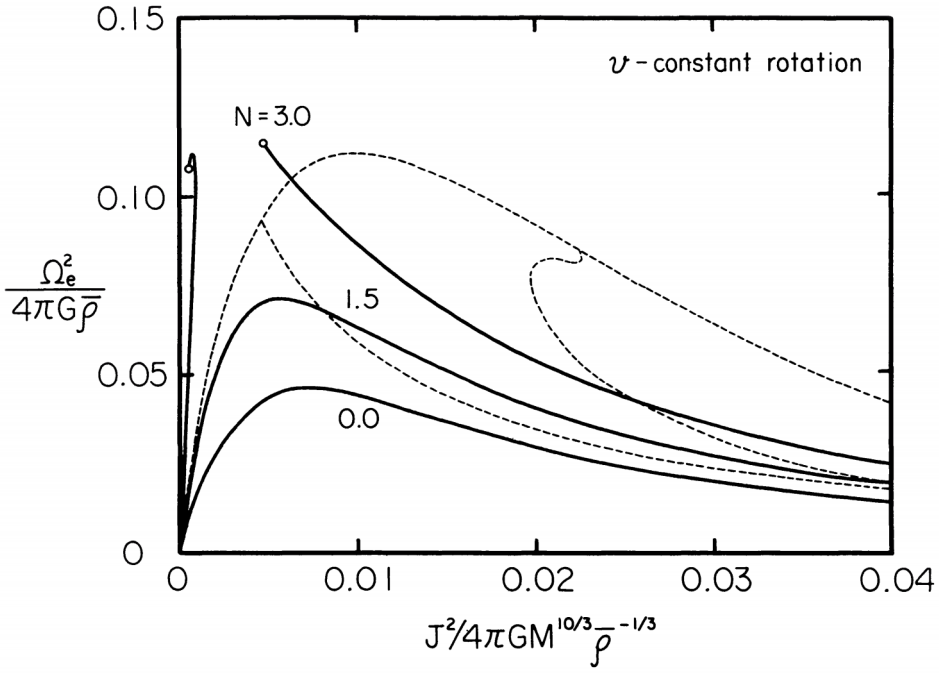

Figure 3.7: Dimensionless angular momentum as a function of the dimensionless angular momentum for a v-constant rotation law. From Hachisu (1986)

3.4.2 The j-constant rotation

Sequences for a j-constant rotation law were also computed by Hachisu (1986) in the same computation condition (same value of n and d^2). Sequences are shown in Fig.3.8. In this case, the maximum rotation rate is even lower than for the v-constant rotation law and there is no more opened sequence. As a consequence, any axis ratio of spheroid or ring leads to an equilibrium. The hamburger shape observed for the incompressible case in solid rotation at high rotation rate appears at low rotation rate for the j-constant rotation law.

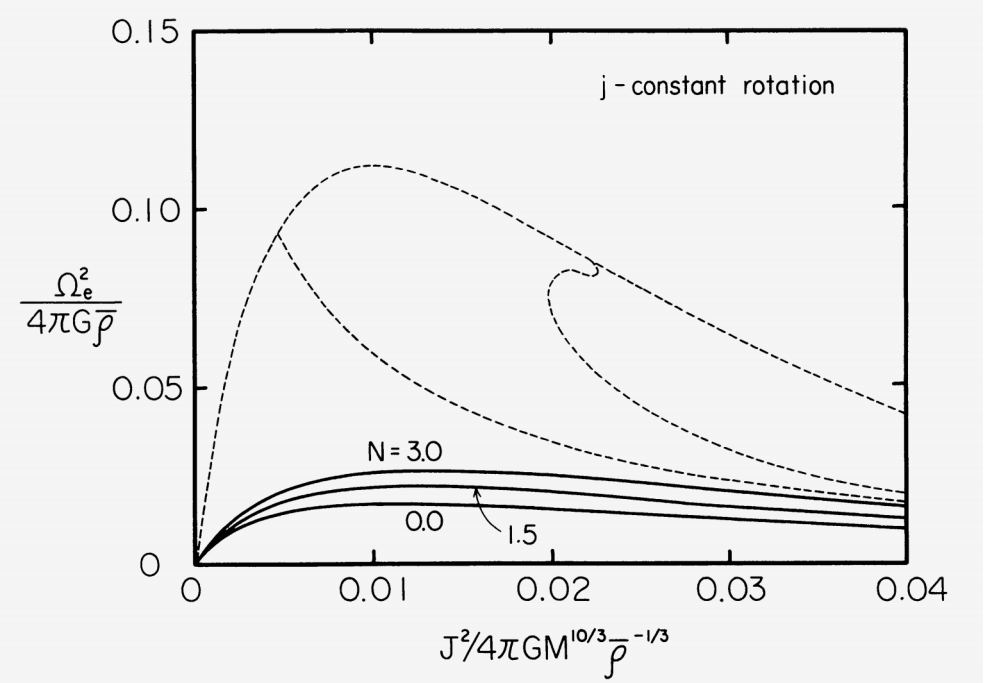

Figure 3.8: Dimensionless angular momentum as a function of the dimensionless angular momentum for a j-constant rotation law. From Hachisu (1986)

Chapter 4

Multibody configurations

Contents

As mentionned earlier, there is a large number of publications devoted to single body configurations. Research on two bodies and more equilibrium is still poorly documented. There is only a handful of publications (Eriguchi and Hachisu, 1983; Hachisu et al., 1986b; Taniguchi and Nakamura, 2000; Caimmi, 2016) that aim to study the stellar structure and the effect of the tidal force in binary systems. However, studies for more than two bodies are less usual for the obvious reason of complexity, yet such configurations are really interesting and should unravel some amazing features.

The work from Hachisu and Eriguchi (1983) studied the conditions for "core-ring" and especially "ring-ring" equilibria and their position in the classical ω^2-j^2 diagram. A striking feature they showed is the existence of a maximum rotation rate for core-ring states in rigid rotation. A recent paper from Ansorg et al. (2003) observed the bifurcations that undergo a pinched Maclaurin using a spectral decomposition of the fluid boundary. Those bifurcations happen in the descending part of the Maclaurin sequence (MLS) after its maximum rotation rate and their end-point is positionned between the one-ring sequence (ORS) and the MLS, see Fig.4.1. They studied axisymmetrical ellipsoids pinched on one or several points, denoted $\varepsilon_{k\geq 2}$. When k is an even number, $\frac{k}{2}$ pinchings are present and the ellipsoid is on the verge of splitting into a central component and $\frac{k}{2}$ ring(s) at the end-point of the given sequence, an exemple is given for $k = 2$ on the left panel of Fig. 4.2. When k is an odd number, the ellipsoid first changes to a highly flattened ring by removing all matter along the polar axis before showing $\frac{k-1}{2}$ pinchings, an exemple is given for $k = 3$ on the right panel of Fig.4.2. Those two papers offered solid rudiments for the 2-body incompressible equilibria gave us food for thought : what if a unique body could split into several bodies ?

For the $k = 2$ case, a significant work has been done to determine which states of 2-body system can really exist beyond the sequence ending. This work has been reported in Basillais and Huré (2019). This kind of configuration is important for the physics of accretion disks and tori around normal and compact stars Masuda et al. (1998); Abramowicz et al. (1998), mass-transfer, rotation and angular momentum exchange between the two components.

We improved the `DROP` code to be able to make layered m-body simulations where the number of layer was initially one or two and the m was could go up to 7 (Boutin-Basillais and Huré, 2018). We started to study axisymmetrical systems made of a central spheroid and a surrounding torus and we then moved to more bodies in order to shed some light on protoplanetary systems such as HL Tau.

4.1 Equation set for multibody systems

Each fluid is characterized by an Euler equation. The integration yields one Bernoulli equation per body. So we can make a more general use of Eq.(3.11) with one equation set per body and each body having a different set of constants. This is true when bodies are not in contact and fully detached because there is not condition on the continuity of fields. For fluid number f, still assuming a polytropic EOS, we have in dimensionless

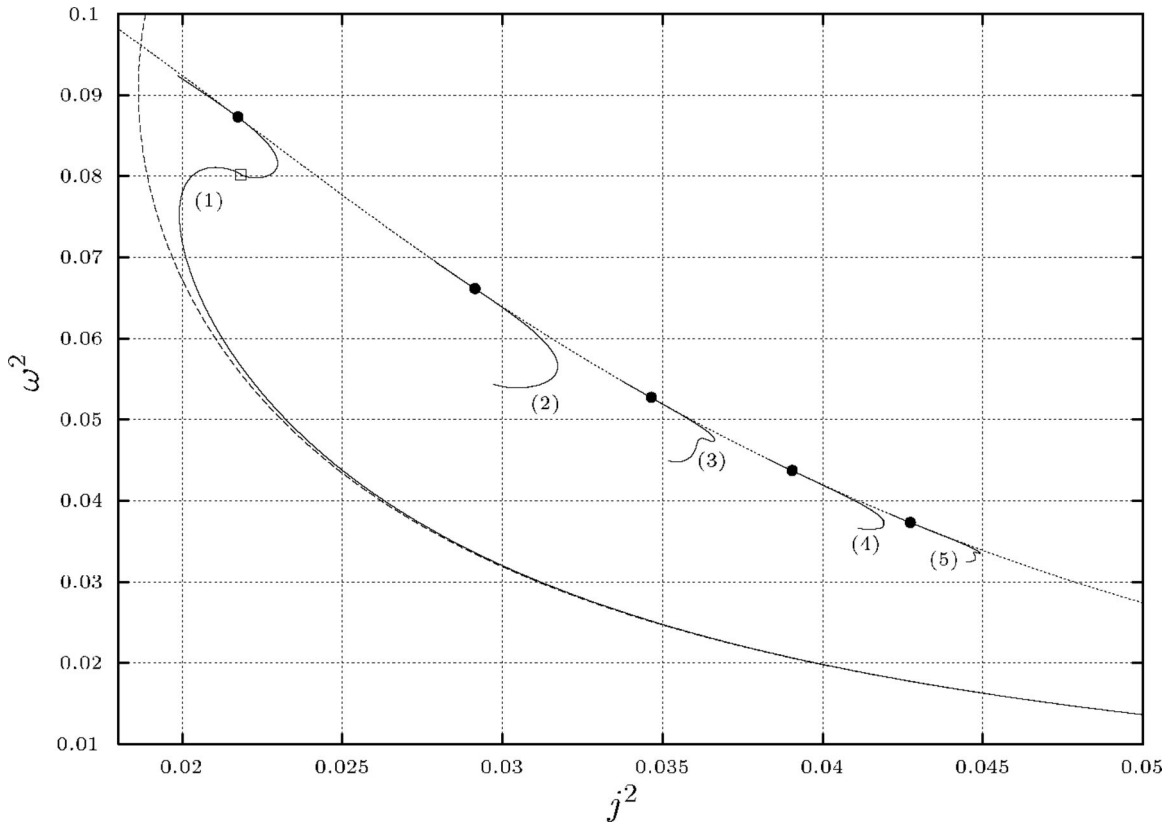

Figure 4.1: Zoom on the descending part of the Maclaurin sequence which is the siege of numerous bifurcations leading to the ε_k. Particular attention should be given to the ε_2. From Ansorg et al. (2003).

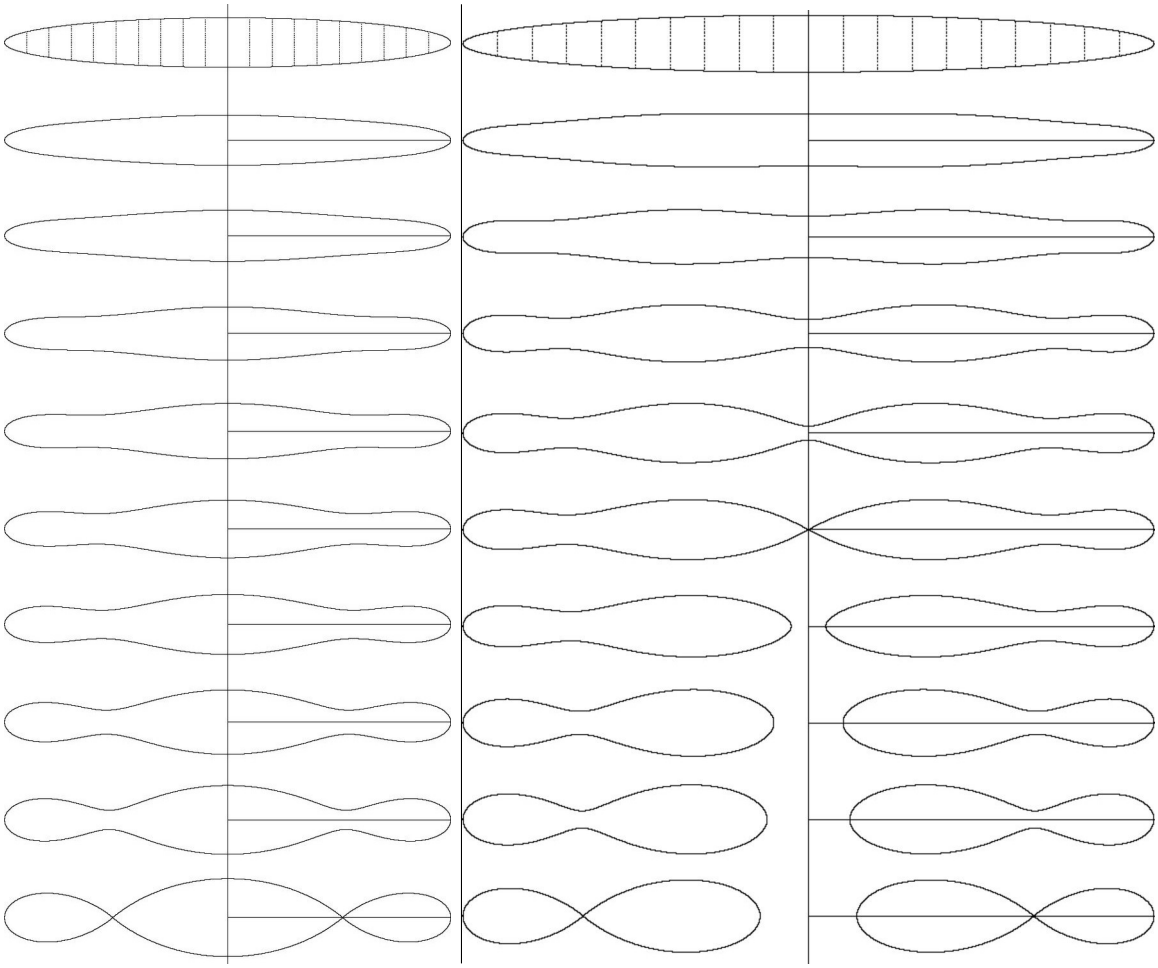

Figure 4.2: (left) : snapshots of equilibrium along the ε_2-sequence.(right) : snapshots of equilibrium along the $\varepsilon_3$sequence.
The last equilibrium are the end-point of the given sequence. From Ansorg et al. (2003)

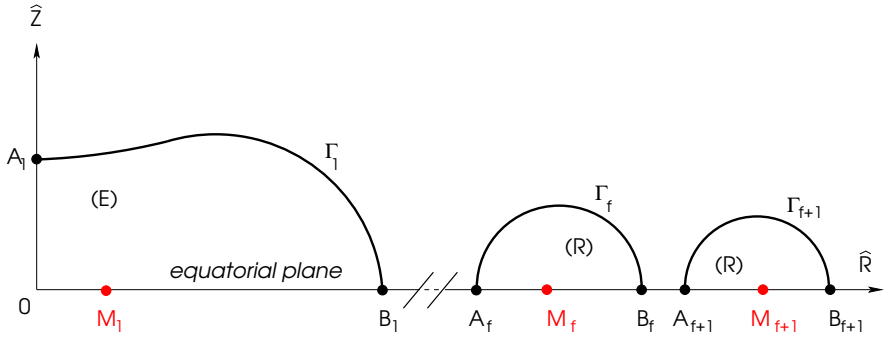

Figure 4.3: Typical configuration for a m-body self-gravitating system made of an optional spheroid (E) and concentric rings (R). The SCF-method relies on two reference points A and B selected along each fluid boundary Γ (bold line) and a third, floating point M where enthalpy is maximum (one triplet per body). Accuracy is optimized by using individual computational boxes.

variables :

$$\begin{cases} \hat{\Psi}_f + C_{1f}\hat{H}_f + C_{2f}\hat{\Phi}_f = C_{3f}, \\ \hat{\rho}^{1/n_f} = \sup(\hat{H}_f, 0), \\ \Delta\hat{\Psi}_{f,tot} = 4\pi\hat{\rho}_f, \end{cases} \tag{4.1}$$

where

$$C_{1f} = \frac{K(n_f+1)\rho_{0f}^{1/n_f-1}}{GL^2}, \tag{4.2}$$

$$C_{2f} = \frac{\Omega_{0f}^2}{G\rho_{0f}}, \tag{4.3}$$

for any $f \in [1, m]$ where m is the total number of interacting bodies. As indicated through the presence of C_{1f} and C_{2f}, we normalize the mass density of each fluid by a specific value ρ_{0f}. This is especially convenient from a numerical point of view when one uses one computational box per body (see Sect. 4.2.2). So, if ρ_{0f} is typically the maximum local value, all second members in Eq.(4.1c) (there is one Poisson equation to solve per body) have the same order of magnitude. For a m-body system, $f \in [1, m]$ in Eq.(4.1), this leaves $3m$ equations in total. Note that, in fact, all the Poisson equation are equivalent. The coupling between all bodies operates through mutual gravitational interactions. The gravitatinal potential felt by fluid f is the sum of its own potential $\Psi_{f\to f}$ and of the potential due to other bodies $\Psi_{f'\to f}$. We thus have

$$\Psi_{f,tot} = \Psi_{f\to f} + \sum_{f'\neq f} \Psi_{f'\to f}, \tag{4.4}$$

which equation, in the dimensionless space, becomes

$$\hat{\Psi}_{f,tot} = \sum_{f'} \eta_{f'f}\hat{\Psi}_{f'\to f}, \tag{4.5}$$

where we have introduced the mass density contrast

$$\eta_{ff'} = \frac{\hat{\rho}_{0f}}{\hat{\rho}_{0f'}}. \tag{4.6}$$

An additional degree of freedom is possible regarding the reference rotation rate Ω_0 which can differ from one fluid to another. In this work, all bodies share the same rotation profile and Ω_0 and so :

$$C_{2f}\rho_{0f} = const. \tag{4.7}$$

Density contrasts are therefore given by the following relations

$$\eta_{ff'} = \frac{C_{2f'}}{C_{2f}}. \tag{4.8}$$

step	operation
1	$\hat{\rho}_f$ are computed from the polytropic assumption; only positive parts of the enthalpy is reta
2	$\psi_{f,tot}$ is computed from Poisson equation, i.e. Eq.(eq:esetfc)
3	values of $\hat{\Psi}_f$ at the 3 reference points A_f, B_f and M_f are deduced, i.e. $\hat{\Psi}_{Af}$, $\hat{\Psi}_{Bf}$ and $\hat{\Psi}_{Mf}$
4	C_{2f} is obtained from Eq.(4.9),
5	C_{3f} is deduced from Eq.(4.9c),
6	$C_{1f}\hat{H}_{Mf} = C_{3f} - C_{2f}\hat{\Phi}_{Mf} - \hat{\Psi}_{Mf}$
7	$C_{1f} = \max(H_f)$,
8	$\eta_{ff'}$ is computed from Eq.(4.8)

Table 4.1: Main steps of the SCF-method for a multibody configuration. The loop starts for a given value of η and m enthalpies H_f.

4.2 The DROP-code for multibody systems

4.2.1 Modified SCF cycle

We can capture the numerical solutions of this m-body configuration by modifying the SCF method for a single body. We need a set of $2m-1$ input parameters (see Sect.4.2.5) and we start from a guess on the enthalpy for each body. Then we cycle through the equation set (4.1) until convergence. An iteration step is as follows : $\hat{H}_f$ yields $\hat{\rho}_f$ from Eq.(4.1b) and then $\hat{\Psi}_{f,tot}$ is deduced from Eq.(4.1c). From the reference points A_f, B_f, and M_f belonging to the fluid (one triplet for each body), as indicated in Fig. 4.3, we can solve for the 3 constants using the same formulae, namely :

$$\begin{cases} C_{1f} = -\frac{\hat{\Psi}_{Mf}\Delta\hat{\Phi}_{ABf}+\hat{\Psi}_{Af}\Delta\hat{\Phi}_{BMf}+\hat{\Psi}_{Bf}\Delta\hat{\Phi}_{MAf}}{\hat{H}_{Mf}\Delta\hat{\Phi}_{ABf}}, \\ C_{2f} = -\frac{\Delta\hat{\Psi}_{ABf}}{\Delta\hat{\Phi}_{ABf}}, \\ C_{3f} = \frac{\hat{\Psi}_{Bf}\hat{\Phi}_{Af}-\hat{\Phi}_{Bf}\hat{\Psi}_{Af}}{\Delta\hat{\Phi}_{ABf}}, \end{cases} \tag{4.9}$$

where points A_f and B_f are selected along the boundary Γ_f where $\hat{H}_f = 0$. This step provides us with the $3m$ constants C_{1f}, C_{2f} and C_{3f}. Then we can compute a new enthalpy field at step $t+1$, namely :

$$\hat{H}_f(t+1) = \frac{C_{3f}(t) - \hat{\Psi}_f(t) - C_{2f}(t)\hat{\Phi}_f(t)}{C_{1f}(t)}. \tag{4.10}$$

If $\hat{H}_f(t+1) \neq \hat{H}_f(t)$, we proceed to a next iteration otherwise the algorithm is stopped and the solution is obtained.

4.2.2 Computational grids and grid stretching

We restrict the computations to the upper half-plane, i.e. $\hat{Z} \geq 0$. We use an individual grid per body rather than a unique grid encompassing all the bodies. This does not needs more technical efforts, and the quality of results is better because the covering factor for every body is optimized : the fluids are better resolved. This is especially true when the

fluids occupy very different volumes, or if these are relatively distant to each other. On this basis, the fluid with number f has grid $\mathcal{G}_f$ with inner and outer radii $\hat{R}_{f,0}$ and $\hat{R}_{f,N}$, and bottom and top altitudes $\hat{Z}_{f,0} = 0$ and $\hat{Z}_{f,N}$. Finally, all Poisson equations are solved in the unit square grid $\varpi \in [0,1] \times \xi \in [0,1]$, whatever the configuration, spheroidal or toroidal. This unit grid is easily connected to each individual grid $\mathcal{G}_f$ through the same linear transformation we use for a single body :

$$\begin{cases} \hat{R}_f = a_f \varpi + b_f, \\ \hat{Z}_f = c_f \xi + d_f, \end{cases} \tag{4.11}$$

where a_f and c_f are compression/dilatation factors, and coefficients b_f and d_f are shifts of the body f. Those fours numbers are parameters depending on our initial geometrical parameters. This is summarized in Fig. 4.4. To our knowledge, *this kind of stretching has never been done before*. This is very convenient for rotating polytropes which are rather oblate (Hachisu, 1986). This enables to maximize the covering factor (the fluid section-to-grid area ratio), each individual grid $\mathcal{G}_f$ is not a square and the spacing in both direction are not the same. The radius $\hat{R}_f \in [\hat{R}_{f,0}, \hat{R}_{f,N}]$ and the altitude $\hat{Z}_f \in [\hat{Z}_{f,0}, \hat{Z}_{f,N}]$.

The resolution of the finest grid is defined by :

$$\begin{cases} \hat{h}_{\hat{R}f} = \frac{\hat{R}_{f,N} - \hat{R}_{f,0}}{N}, \\ \hat{h}_{\hat{Z}f} = \frac{\hat{Z}_{f,N} - \hat{Z}_{f,0}}{N} \end{cases} \tag{4.12}$$

To go from the finest grid to the coarser grid at level $l-1$, we double the mesh size of the grid at level l. In pratical, it is done by keeping every two nodes. In the coarsest grid, i.e. level 1 we only have 3 nodes in each direction and 9 nodes in total.

In the new coordinate system (ϖ, ξ), the cylindrical Poisson equation $\Delta\hat{\Psi} = s$ becomes for every body f in each computational boxes :

$$\left(\partial^2_{\varpi\varpi} + \frac{D_f}{\varpi} \partial_\varpi + Q_f \partial^2_{\xi\xi} \right) \hat{\Psi} = s a_f^2, \tag{4.13}$$

where

$$\begin{cases} D_f(\varpi) = \frac{a_f \varpi}{a_f \varpi + b_f}, \\ Q_f = \left(\frac{a_f}{c_f} \right)^2 \\ s a_f^2 = 4\pi \hat{\rho}_f a_f^2. \end{cases} \tag{4.14}$$

4.2.3 Poisson solver and associated 2nd-order finite difference scheme

As quoted above, the (ϖ, ξ)-grid is the unit square grid with $N+1$ nodes and regular spacing h in both directions. It is defined as follows :

$$\begin{cases} \varpi \in [\varpi_0, \varpi_N], \\ \qquad \text{with} \;\; \varpi_N - \varpi_0 = N\hat{h}, \\ \xi \in [\xi_0, \xi_N], \\ \qquad \text{with} \;\; \xi_N - \xi_0 = N\hat{h}. \\ \varpi_N - \varpi_0 == 1, \end{cases} \tag{4.15}$$

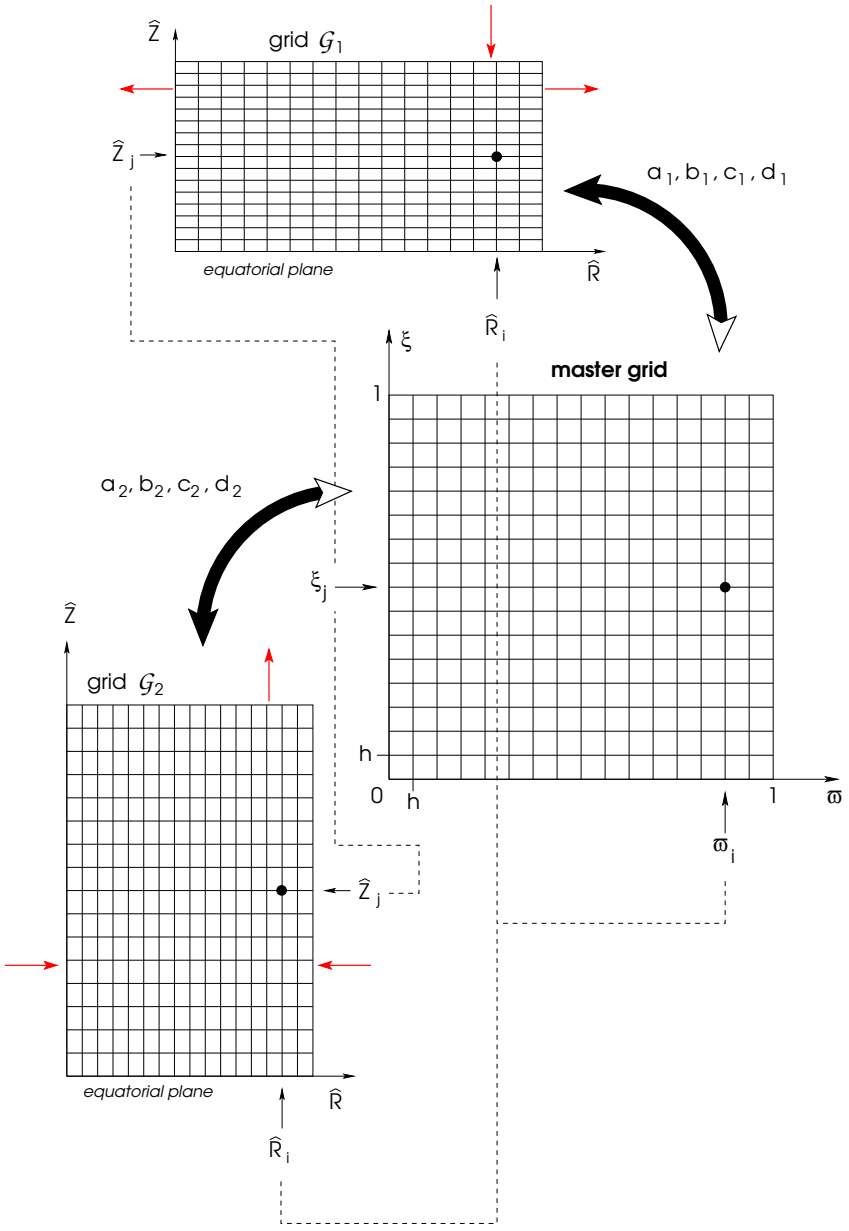

Figure 4.4: Each fluid f carries its own numerical grid G_f, but the Poisson equations are solved on a unique unit grid (ϖ, ξ) which is a unit square box $[0,1] \times [0,1]$. Radial grid stretching (red arrows) appropriate for oblate/prolate structures is also incorporated. The mapping being linear, only 4 coefficients (a_f, b_f, c_f, d_f) are necessary to jump from one grid to the other throug Eq.(4.11).

where the value of ϖ_0 and ξ_0 are usually set to 0). From Eq.(4.11), we have

$$\begin{cases} a_f = \frac{\hat{R}_{f,N} - \hat{R}_{f,0}}{Nh} \\ c_f = \frac{\hat{Z}_{f,N} - \hat{Z}_{f,0}}{Nh} \\ b_f = \frac{\varpi_N \hat{R}_{f,0} - \varpi_0 \hat{R}_{f,N}}{Nh} \\ d_f = \frac{\xi_N \hat{Z}_{f,0} - \xi_0 \hat{Z}_{f,N}}{Nh}. \end{cases} \tag{4.16}$$

When a partial derivative ∂ is replaced by a second-order finite difference δ, the Laplacian becomes

$$\Delta\hat{\Psi} = \left(\delta^2_{\varpi\varpi} + \frac{D}{\varpi}\delta_{\varpi} + Q\delta^2_{\xi\xi}\right)\hat{\Psi} + O(\hat{h}^2). \tag{4.17}$$

With central second-order schemes, we are led to the algebraic equation

$$\begin{aligned} &C_+\hat{\Psi}_{i+1,j} + C_-\hat{\Psi}_{i-1,j} \\ &\quad + Q(\hat{\Psi}_{i,j+1} + \hat{\Psi}_{i,j-1}) - 2(1+Q)\hat{\Psi}_{i,j} - 4\pi\rho_{i,j}\hat{h}^2 = 0, \end{aligned} \tag{4.18}$$

with

$$\begin{cases} C_+ = 1 + D_{i,j}\frac{h}{2\varpi_{ij}}, \\ C_- = 1 - D_{i,j}\frac{h}{2\varpi_{ij}}. \end{cases} \tag{4.19}$$

This formula is easy solved for the value at central node $u_{i,j}$. There are $(N-1)^2$ equations of this kind with $i \in [1, N-1]$ and $j \in [1, N-1]$, $u_{i,j}$. Values all along the grid boundary remains to be prescribed with either Dirichlet or Neumann boundary values. For a spheroid, Dirichlet boundary conditions are applied on the top and right edges of the box and for a ring on the left, top and right edges.

4.2.4 Neumann condition with stretching factor

The Neumann condition brings a constraint on the derivative of the field at specific points. Along the polar axis, the symmetry imposes $\partial_R\Psi = 0$ while equatorial symmetry means $\partial_Z\Psi = 0$. The use of Neuman boundary conditions is appropriate for the left and bottom edges of the grid in the case of an ellipsoid and for the bottom edge only in the case of a toroid. In variables ϖ and ξ, these conditions of null derivative become $\partial_\varpi\hat{\Psi} = 0$ and $\partial_\xi\hat{\Psi} = 0$. By using a forward, second-order finite difference on the unit grid, the axial symmetry yields

$$-3\hat{\Psi}_{0,j} + 4\hat{\Psi}_{1,j} - \hat{\Psi}_{2,j} = 0, \tag{4.20}$$

for $j \in [0, N]$. This constraint, together with Eq.(3.23) enables to determine both $\hat{\Psi}_{0,j}$ and $\hat{\Psi}_{1,j}$ for any $j \in [1, N-1]$. We find

$$\hat{\Psi}_{1,j} = \frac{(3C_+ - C_-)\hat{\Psi}_{2,j} + 3Q(\hat{\Psi}_{1,j-1} + \hat{\Psi}_{1,j+1}) - 3s_{1,j}\hat{h}}{6(1+Q) - 4C_-}, \tag{4.21}$$

where Q is the stretching factor introduced in order to maximize the covering factor. For spheroids, this schemes is used instead of Eq.(3.23) at $i = 1$, and left-side values $\hat{\Psi}_{0,j}$ follow from Eq.(4.20).

In a similar manner, equatorial symmetry leads to

$$-3\hat{\Psi}_{i,0} + 4\hat{\Psi}_{i,1} - \hat{\Psi}_{i,2} = 0, \tag{4.22}$$

which yields $\hat{\Psi}_{i,1}$ when combined with Eq.(4.18). We have

$$\hat{\Psi}_{i,1} = \frac{3C_+\hat{\Psi}_{i+1,1} + 3C_-\hat{\Psi}_{i-1,1} + 2Q\hat{\Psi}_{i,2} - 3s_{i,1}h^2}{2(3+Q)}, \tag{4.23}$$

valid for $i = 1, N-1$. This schemes replaces Eq.(4.18) at $j = 1$, and bottom-side values $u_{i,0}$ follow from Eq.(4.22). Both ellipsoids and toroids are concerned. For ellipsoids however, Eqs.(4.21) and (4.23) must combined together at the unique node $(i, j) = (1, 1)$. We find

$$\hat{\Psi}_{1,1} = \frac{(3C_+ - C_-)\hat{\Psi}_{2,1} + 2Q\hat{\Psi}_{1,2} - 3s_{1,1}h^2}{2(3+Q) - 4C_-}, \tag{4.24}$$

and the value at the origin of coordinates is then deduced from Eq.(4.20) or (4.22).

Note that if we consider a square grid without any stretching, we have :

$$a_f = c_f = 1 \tag{4.25}$$

this, we have :

$$Q = 1 \tag{4.26}$$

and we find the usual Neumann scheme. This holds for any fluid f (for clarity, we omitted the f subscript).

4.2.5 Control Parameter

For a single body, reference points A and B are set once and for all, while M is the point of maximum enthalpy and its location varies during the cycle, especially at the beginning. This procedure leads to self-normalized solutions. For a m-body system, we can proceed in the same way and fix the reference points A_f and B_f for the run. In doing so, however, we do not have any control on the density contrasts $\eta_{ff'}$ and they are output quantities. Another way to proceed is to impose the density contrasts and to set free some points (the number of input parameters must be conserved). For instance, in the 2-body case, we can set the density contrast to any value we want and free the A_1 point.

As for a single body, convergence of the SCF-method for $m > 1$ is capable to reach any accuracy level at convergence, e.g. the computer precision.

4.3 2-body systems with a constant density contrast

4.3.1 Main results for incompressible case n=0

The first and most simple case we can consider is the incompressible case. We use the `DROP`-code to generate systems with 2 detached bodies in gravitational interaction in order to perform a wide parameter-survey (see Sect.4.2 for a technical and numerical review).

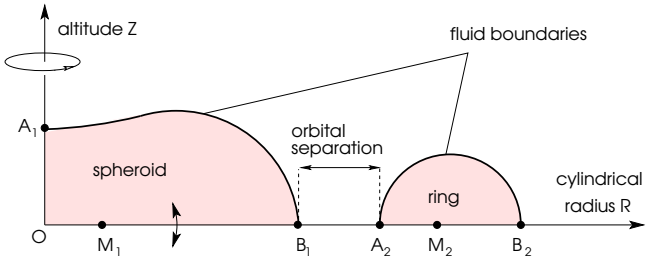

Figure 4.5: Configuration for a spheroid-ring system. The relative separation is $s = B_1A_2/OB_1$ and the axis ratios are $e_i = OA_i/OB_i$ $(i = 1, 2)$. Points M refer to the maximum enthalpy.

Set of parameters

When considering a 2 body system, we have two possible sets of three parameters (see the discussion in sect.4.2.5). The first set is composed of (see Fig. 4.5) :

- the axis ratio of the ellipsoid $e_1 = \mathrm{OA_1/OB_1}$
- the axis ratio of the ring $e_2 = \mathrm{OA_2/OB_2}$
- the orbital separation $s = \mathrm{B_2A_1/OB_1}$

The second set is composed of :

- the axis ratio of the ring e_2
- the orbital separation s
- and the density contrast $\eta = \eta_{21} = \frac{\rho_{02}}{\rho_{01}}$

In our case, we need to have a denstity contrast η equals to 1 to be in the same conditions as Hachisu and Eriguchi (1983) and Ansorg et al. (2003). Our set of parameters is then ($\eta = 1$,e_2,s) and the axis ratio of the ellipsoid e_1 is regarded as an output quantity. For this work, we used a multrigrid level $l = 7$ which represents a numerical grid of 129×129. The typical range of error is of the order of $1/N^2 \sim 10^{-4}$ at most.

Survey of the parameter space

The equilibrium at the end-point of the ε_2-sequence computed in Ansorg et al. (2003) is special. It is the state of a single body on the verge of splitting into two, the orbital separation is strictly 0. It is shown in Fig.4.2 (*left panel*). Our code is not able to work with $s = 0$ by construction. However we tried to reproduce this state. We have generated a 2-body equilibrium with an orbital separation as low as $s = 0.0051$ shown in Fig. 4.6 (*right panel*). All output quantities are displayed in Tab. 4.2 (rows 1 and 2).

We then have explored the parameter space (e_2, s) by generation a large amount of equilibrium (~ 30000) for various axis ratio e_2 of the ring and various orbital separation s. All sets of parameters leading to an equilibrium are shown in Fig.4.8. Every equilibrium found are such that $e_1 \gtrsim 0.33$ and $e_2 \gtrsim 0.51$. Any type of configurations is possible, from a dominant spheroid to a dominant ring, i.e. $\hat{M}_1/\hat{M}_2 \in [0, \infty[$. There is no constraint on

input parameters							
e_2	s	M	M_1/M_2	j^2	ω^2	e_1	comment/ref.
0.5162*	0.0000		0.4105	0.02972	0.05433	0.3413	Ansorg et al. (2003)
0.5162*	0.0051	8.8511	0.4095	0.02973	0.05419	0.3413	configuration a, Fig. 4.6
0.9900	1.1204	3.6708	1026.8	0.00088	0.03107	0.8807	configuration b, Fig. 4.7
0.6380	0.3516	4.7567	1.0632	0.02056	0.05470	0.6092	configuration c, Fig. 4.7
0.9000	1.9118	5.3008	2.7043	0.01148	0.01318	0.9304	configuration d, Fig. 4.7
0.6000	5.0000	5.3798	0.0042	0.03109	0.03055	0.5548	configuration e, Fig. 4.7
0.7100	1.2021	11.558	0.3472	0.03257	0.02883	0.7240	configuration f, Fig. 4.7
0.6200	3.0844	143.49	0.0174	0.03260	0.02881	0.5926	configuration g, Fig. 4.7
0.9990	0.6910	3.2874	3×10^5	0.00170	0.05306	0.7906	critical point C, 4.8

*Table 4.2: Values obtained for the equilibria shown in Figs. 4.6 and 4.7 (see text for the numerical setup); *end-point of the ε_2-sequence. Columns 1 and 2 are input parameters. See also Fig. 4.8.*

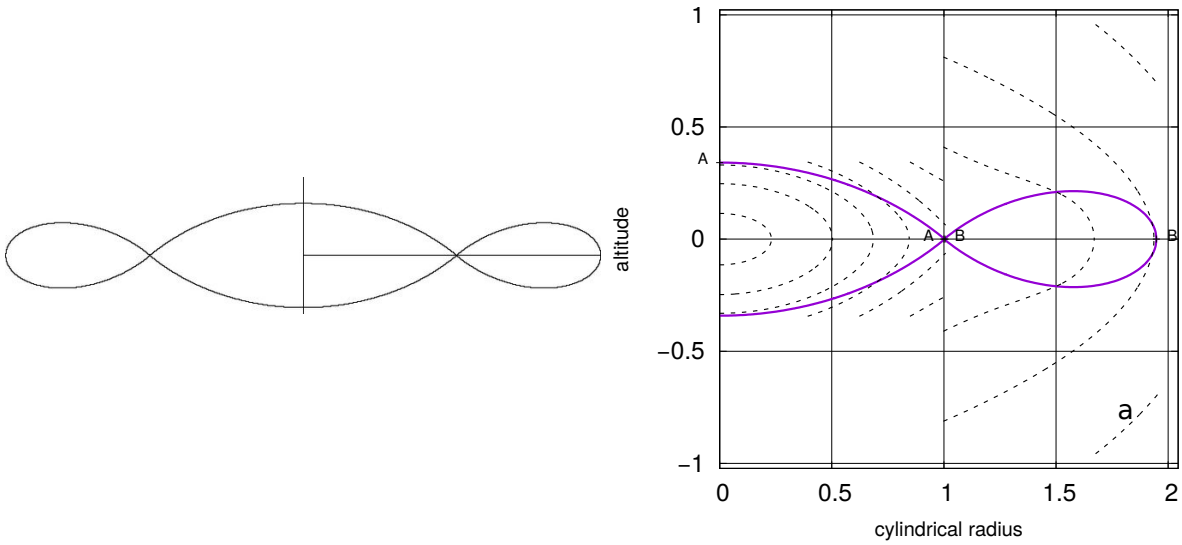

Figure 4.6: (left) : Equilibrium state at the end-point of the ε_2-sequence computed from Ansorg et al. (2003). (right) : Equilibrium computed with the DROP code using a 2-body configuration and a very low orbital separation. Colors stand for the fluid boundary where the enthalpy vanishes (bold pink), and a few isopotential lines are given (dashed black). The positions of the maximum enthalpy is indicated (red dot); see also Fig. 4.5 and Tab. 4.2. From Basillais and Huré (2019)

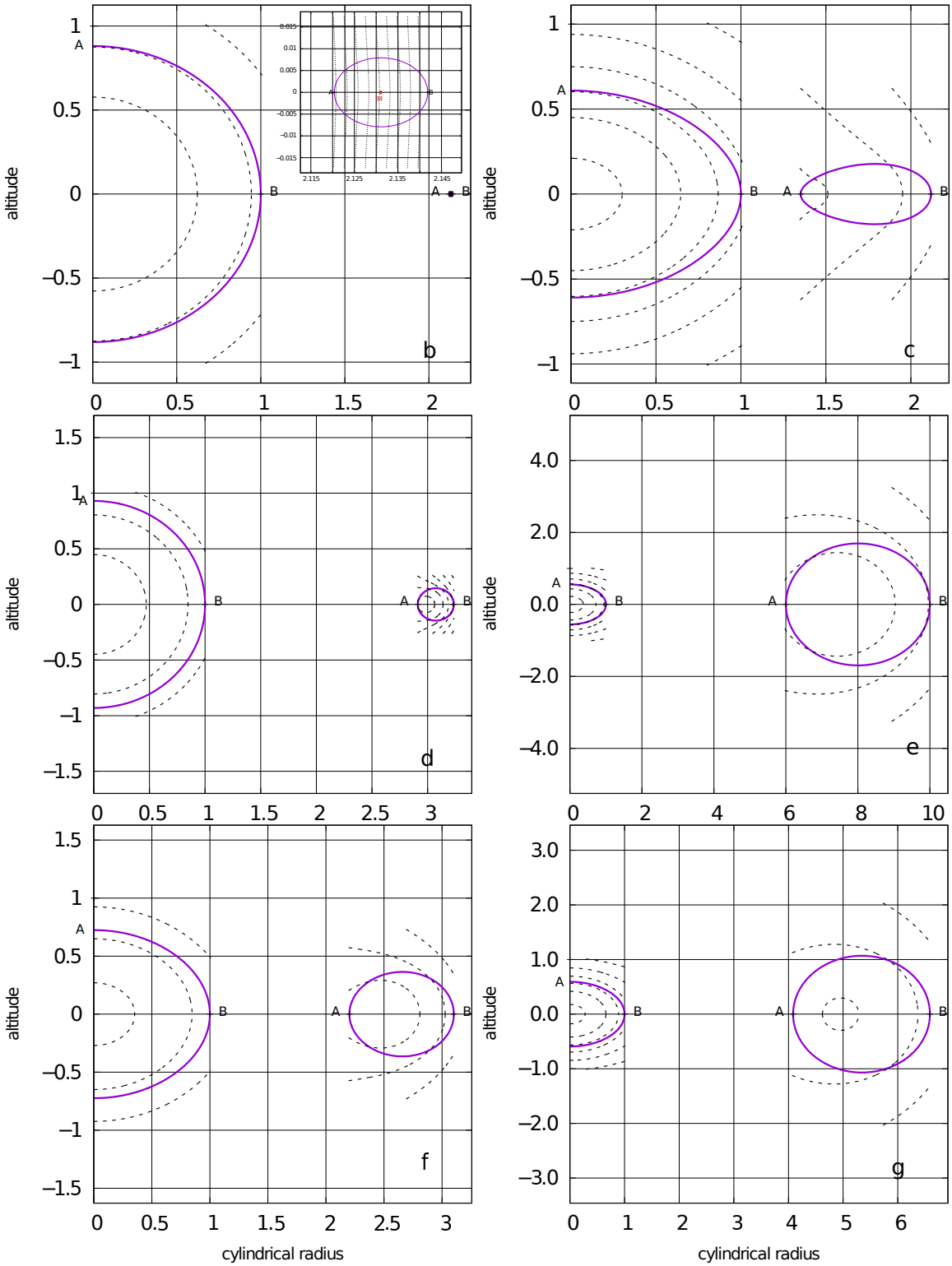

Figure 4.7: Same legend as for Fig. 4.6 but for 6 equilibria among the many runs performed (see Tab. 4.2 for associated key quantities) For panel b, the details of ring structure are given in the inset.

the orbital separation s either that ranges from 0 to ∞. A few examples of converged structures are given in Fig. 4.7. Associated data are listed in Tab. 4.2 (rows 3 to 9). The effect of binarity tends to modified the shape with respect to single body figures. The central body is slightly under elliptic and the ring is substantially flatter. As a consequence, the volume and therefore the mass of each fluid is reduced compared their isolated counterparts.

Figure 4.8 shows the results plotted in the ω^2-j^2 diagram. For a $m-body$ system, ω and j are defined by :

$$\begin{cases} \omega^2 = \frac{\Omega_0^2}{4\pi G\hat{\rho}}, \\ j^2 = \frac{\hat{J}^2}{4\pi G\hat{M}^{10/3}\hat{\rho}^{-1/3}}, \end{cases} \tag{4.27}$$

where M is the total mass. For $m = 2$, $M = M_1 + M_2$. We clearly see that all solutions are concentrated between the ascending part of the MLS and a *first limit curve* (hereafter, the "high-ω limit"), which meets the MLS at the critical point C $(0.00171, 0.05306)$ where the axis ratio of the primary is $e_1 \approx 0.791$ and the orbital separation is $s \approx 0.691$. There is *no solution for* $\omega \gtrsim \omega_l(j)$. An analog is known for binary stars (Hachisu and Eriguchi, 1984a). For $j^2 \leq 0.025$, this high-ω limit follows a linear equation given by :

$$\omega_l^2(j) \approx 0.0536 + 0.09j^2. \tag{4.28}$$

The right-part of it is slightly bended and meets the end-point of the ε_2-branch where $e_1 \approx 0.341$. This is due to the critical rotation (see Fig. 4.7c). The configurations located close to the MLS consist in a prominent central body and a small ring (Fig. 4.7b). The orbital separations are moderate to large, but non-zero. For points in between the MLS and the ORS (Fig. 4.7d), the two bodies are comparable in size and mass. The solutions overtake the ORS, and reach a *second limit curve* (hereafter, the "high-j limit"), which asymptotically merges with the ORS for large values of j, and attains the end-point of the ε_2-sequence where $j^2 \sim 0.03$. For a given value of ω, there is a maximal allowed value for j where no equilibrium is found beyond. These maximal values tend to ∞ when $\omega \to 0$. Another interesting point is the presence of *a zone of degeneracy* located between the ORS and the high j-limit (Fig. 4.7f and g), where two different configurations correspond to a single pair (j^2, ω^2). A point located close to the ORS can correspond to two very different configurations. Either the spheroid has a small size and relative mass, the ring dominates and the orbital separation s is large (Fig. 4.7e and g). Then the ring resembles very much the single ring, or the spheroid and the ring have comparable mass and size. In this case, the ring (in particular, its axis ratio) is very different from the single ring equilibrium (Fig. 4.7f). In this region where the rings are among the largest in size, the convergence of the SCF method is tricky (the number of SCF iterations rises, and the Virial parameter deteriorates).

Effect of the denstity contrast $\eta \neq 1$

After a survey for $\eta = 1$, it is interesting to know how the denstity contrast affects the main features : the maximum rotation rate, the degeneracy zone and the distribution of equilibria.

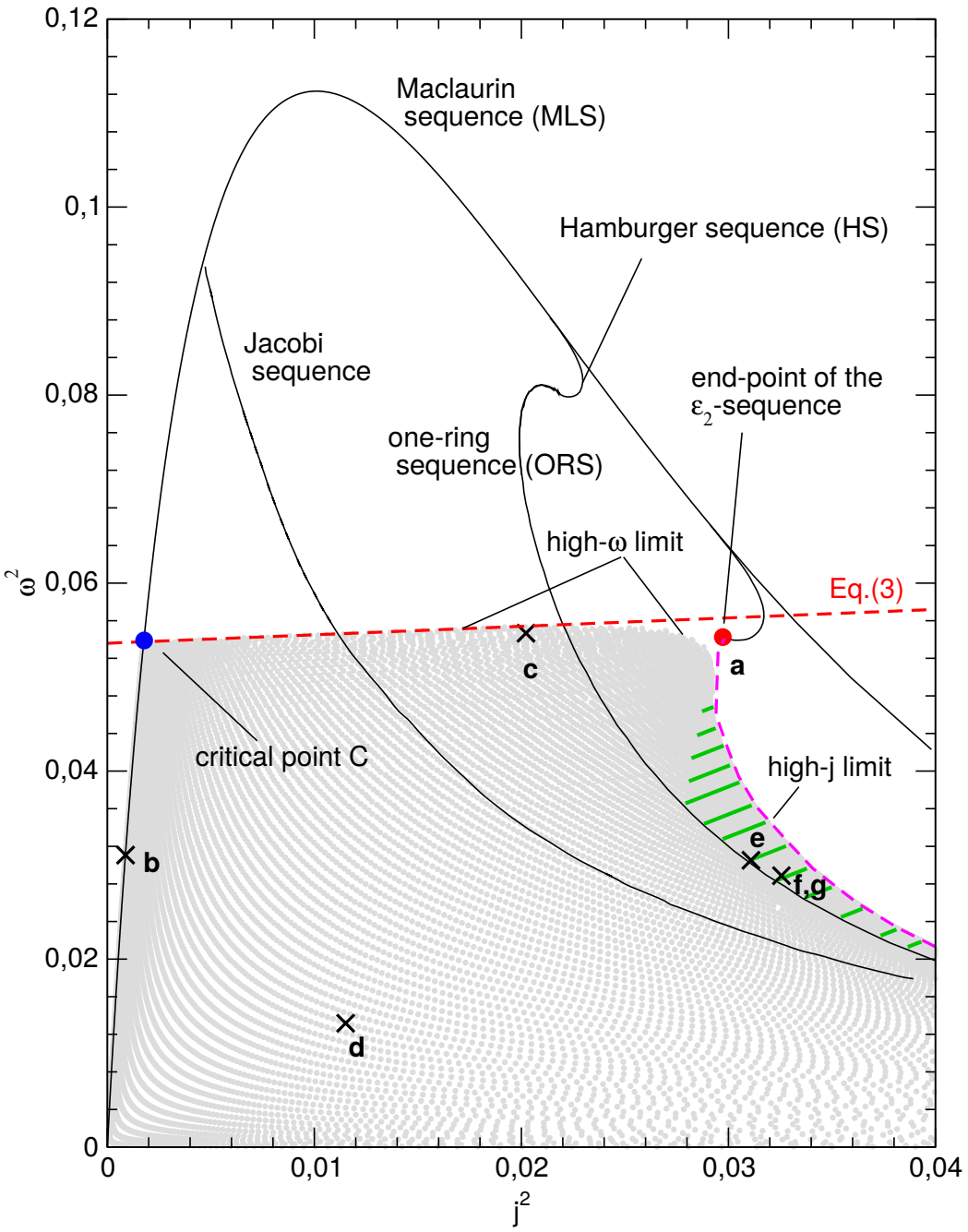

Figure 4.8: The spheroid-ring solutions (gray dots) populate the ω^2-j^2 diagram in between the MLS, the high-ω limit and the high-j limit (see text for explanations). The MLS, ORS, Jacobi-sequence, Hamburger-sequence and ε_2 sequence are also shown (plain lines). Points labelled a to f (cross) correspond to equilibria shown in Fig. 4.7; see also Tab. 4.2. There is a band of degeneracy rightward to the ORS (green dashed zone).

We perform a new parameter survey for $\eta = 0.2, 0.5, 2, 5$ that are shown in Fig.4.9. One main aspect in changing η is the alteration of the maximum rotation rate : the higher the density contrast, the higher the rotation rate. It can be understood from the Bernoulli equation :

$$\Phi + H + \Psi = const.$$

To sustain a higher rotation rate, the body needs to be either more massive to increase H or to create a deeper gravitational well Ψ. By increasing η, both changes are happening which allow the system to rotate faster.

Another effect in changing η is the modification of axis ratio for both bodies. While for $\eta = 1$, $e_1 \in [0.32, 1.00]$ and $e_2 \in [0.51, 1.00]$, we have :

- for $\eta = 0.2$: $e_1 \in [0.68, 1.00]$ and $e_2 \in [0.28, 1.00]$
- for $\eta = 0.5$: $e_1 \in [0.30, 1.00]$ and $e_2 \in [0.34, 1.00]$
- for $\eta = 2$: $e_1 \in [0.28, 1.00]$ and $e_2 \in [0.67, 1.00]$
- for $\eta = 5$: $e_1 \in [0.25, 1.00]$ and $e_2 \in [0.79, 1.00]$

4.3.2 Main results for the compressible case $n > 0$

A polytropic index n greater than 0 results in the opening of the well known Maclaurin sequence thus creating a forbidden gap where no equilibrium is found between the ellipsoidal sequence and the one-ring sequence (see Sect.3.3). As shown in the previous section, there is always a 2-body equilibrium in the incompressible case for a given j^2 while this is not true for ω^2. Can the same characteristic exist when considering the compressible case ?

In this purpose, we have performed the same parameter survey as before using a polytropic index of $n = 1.5$ and $\eta = 0.2, 0.5, 1, 2, 5$. For $\eta = 1$, the results are shown in Fig.4.10 and, for the other density contrasts, results are shown in Fig.4.11. We can see that, as for the incompressible case, the 2-body equilibria populate the diagram for any given angular momentum j, from the spheoird sequence to the ring sequence. As for $n = 0$, we find the same kind of equilibrium ranging from the dominant ellipsoid to the dominant ring. in contr incompressible case, we were able to generate equilibria where the two bodies are in contact : the higher the density contrast is, the more leeway we have on both axis ratio to generate an equilibrium. We even found contact equilibrium with a tiny ring. However we cannot connect directly the critical rotation of the spheroid to the critical rotation of the ring. As for the incompressible case, equilibrium composed of spheroid and a distant massless loop can be obtained for any given η.

Within the numerous equilibria generated, some display an spheroid flatter that it would be possible if isolated, i.e. the axis ratio of the spheroid is smaller than the axis ratio of the critical rotation for an isolated spheroid. For $\eta = 1$, we find equilibrium where $e_1 \sim 0.55$ and $e_1 \sim$for $\eta = 5$. The same features was not found for the rings when $\eta \geq 1$. It is in fact the opposite : the higher the denstity contrast is, the lesser possible axis ratios of the ring are found. For instance, the lower axis ratio of the ring found for $\eta = 1$ is $e_2 \sim 0.65$ and for $\eta = 5$, it is $e_2 \sim 0.65$. Those properties are inverted when going well

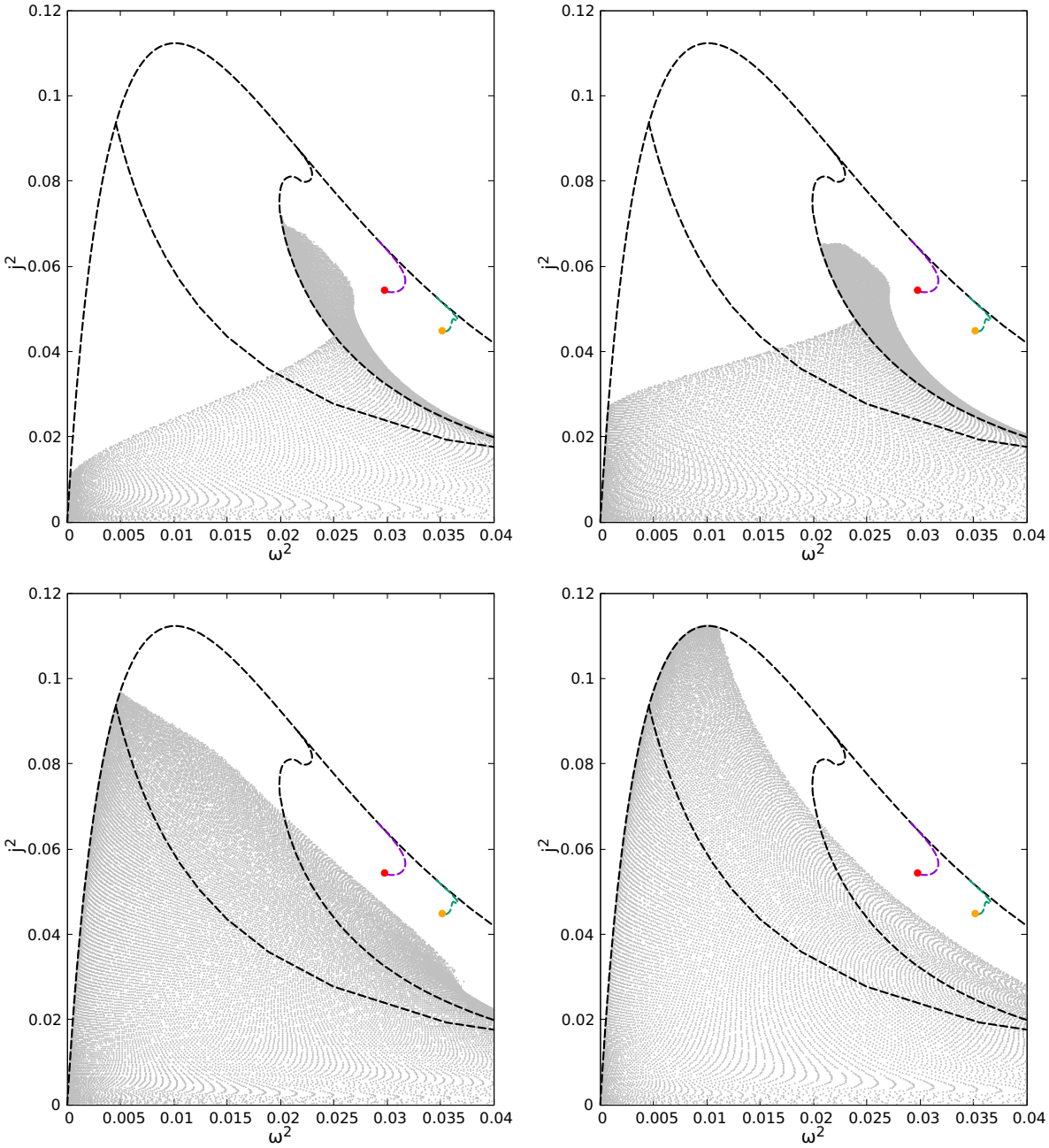

Figure 4.9: The spheroid-ring solutions (gray dots) in ω^2-j^2 diagram forfrom top-left to bottom-right, $\eta = 0.2, 0.5, 2, 5$ (from top-left to bottom-right) in the incompressible case $n = 0$. The MLS, ORS, Jacobi-sequence, Hamburger-sequence and ε_2 sequence are also shown (plain lines).

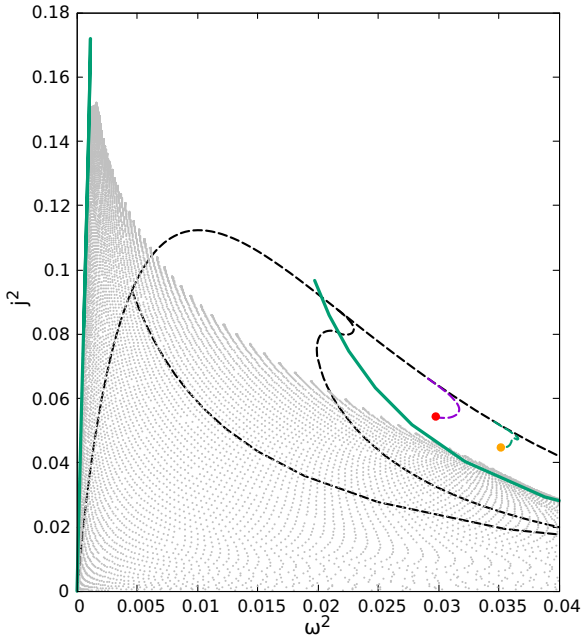

Figure 4.10: The spheroid-ring solutions (gray dots) in ω^2-j^2 diagram for $\eta = 1$ and $n = 1.5$. The MLS, ORS, Jacobi-sequence, Hamburger-sequence and ε_2 sequence are also shown.

under $\eta = 1$. For $\eta = 0.2$, we find rings with an axis ratio of $e_2 \sim 0.33$ and axis ratio of the ellipsoid not lower than $e_1 \sim 0.71$.

4.4 Sequences with a free density contrast for n=0

We can release the constraint on the density contrast and change the set of input parameters. We then take as input the geometrical parameters : the axis ratio of bodies and their orbital separation. In doing so, it brings a whole new set of equilibrium where the density contrast can vary between ~ 0 to $+\infty$. We have all kind of equilibria : dominant spheroid and dominant ring. We can multiple contact configurations and we discovered new routes to go from the end-point of the ε_2-sequence to the MLS or the ORS.

4.4.1 Connections to the end-point of the ε_2-sequence

We find various families of sequences starting from the end-point of the ε_2-sequence computed by Ansorg et al. (2003). When keeping e_1 and/or e_2 constant, three kinds of sequences can be considered :

- ERa : the axis ratios are held constant while the inner edge of the ring increases.
- ERb : the axis ratio of the spheroid and the orbital separation are held constant while the outer edge of the ring decreases (in other words the ring "vanishes" in contact of the central spheroid).

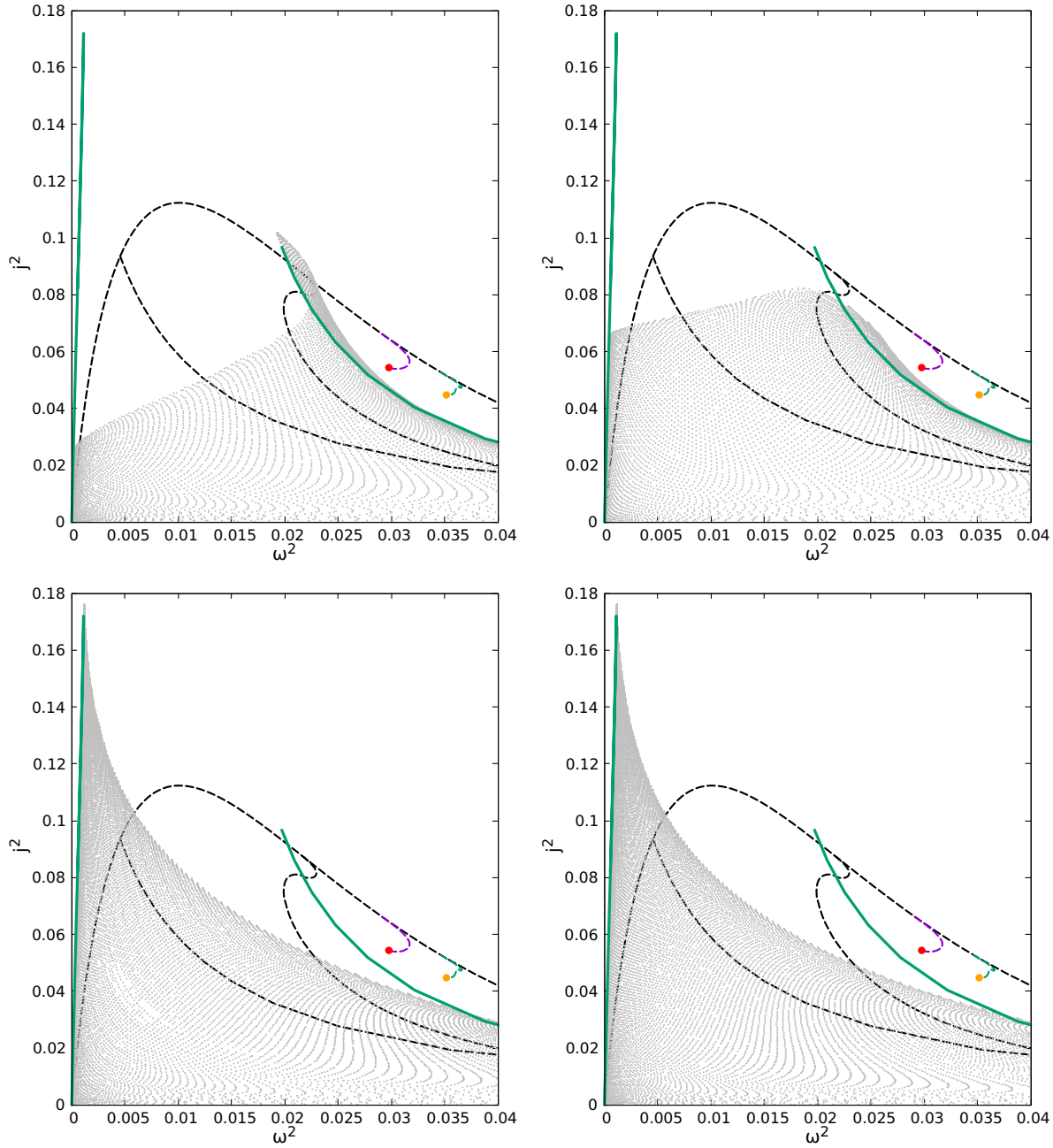

Figure 4.11: The spheroid-ring solutions (gray dots) in ω^2-j^2 diagram for, from top-left to bottom-right, $\eta = 0.2, 0.5, 2, 5$ and $n = 1.5$. The MLS, ORS, Jacobi-sequence, Hamburger-sequence and ε_2 sequence are also shown.

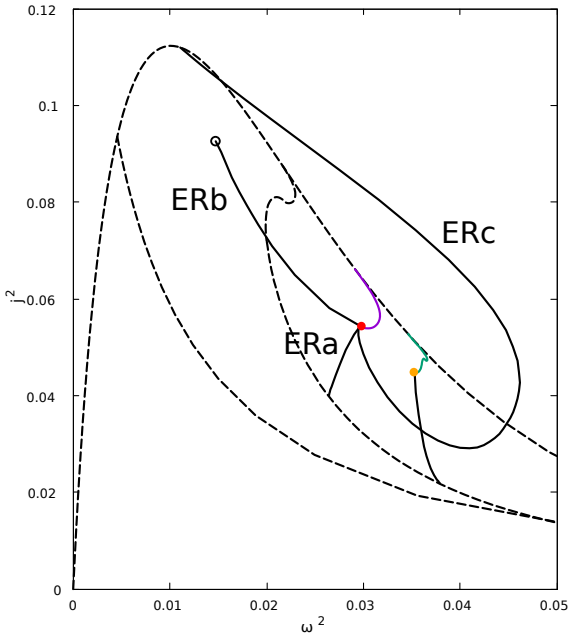

Figure 4.12: Sequences in the ω^2-j^2 diagram obtained by : sending the tore away linking the end-point of the ε_2 sequence to the ORS (ERa), shrinking the ring in contact of the central spheroid (ERb) and shrinking the ring towards its point of maximum enthalpy linking the end-point of the ε_2 sequence to the MLS (ERc).

- ERc : the axis ratio of the spheroid is held constant while the ring shrink towards its point of maximum enthalpy.

These three sequences are displayed in Fig.4.12. We can see that the ERa sequence connects directly the end-point of the ε_2 to the ORS where $e_2 = 0.51$. The variations of the density contrast in this sequence are rather small : starting with $\eta \sim 1$ and ending on the ORS with $\eta = 0.975$. While "sending away" the ring (increasing the orbital separation s), its relative mass grows until the contribution of the spheroid becomes negligible. The ERb sequence is cut before reaching the MLS, the last configuration obtain is showed by a circle. As a consequence, we cannot have a infinitly thin ring in contact with the central body in the incompressible assumption. One should note that by slightly increasing the orbital separation, typically a few percent of the radius of the spheroid, the connection between the end-point of the ε_2 and the MLS is easily achieved. The last sequence generated is the ERc sequence that connects the end-point of the ε_2 to the MLS where $e_1 = 0.3413$. This sequence presents an immense variation in the density contrast. Starting with $\eta \sim 1$, it reaches $\eta \sim 10$ at the point of maximum j^2. The rapid growth of the denstity contrast overwhelms the diminution of the ring size. As a result, in the first part of the sequence, it goes toward the ORS. But at some point, the growth of the density contrast is not enough to counterbalance its vanishing and the sequence tends to the MLS. When reaching it, we have $\eta \sim 10^9$. Even though reaching high rotation rate, this sequence does not exceed the limit of $\omega^2_{max} = 0.1123$ (see Sect.2.3.1).

After generating sequences conserving at least one geometrical properties, we generated tweaked version or the ERa and ERc sequences to connect the end-point of the ε_2

to various points of the ORS and MLS. Results are shown in Fig.4.13.

4.4.2 Connections to the end-point of the ε_3-sequence

The ε_3 sequence is the sequence starting from a Maclaurin ellipsoid and turning into a mono ring system on the verge of splitting into two rings. We have also investigated the connection between the end-point of this sequence and the ORS. There are actually two possible routes while keeping at least one ring geometrically intact. The first one is generated by increasing the orbitale separation s, this sequence connects the ORS at $e \sim 0.6524$. The second one is generated by shrinking the outer ring around its point of maximum enthalpy, this sequence connects the ORS at $e \sim 0.2124$. Another route departing from the end-point of the ε_3-sequence and connecting to the end-point of the ε_2-sequence can be considered by turning the central ring into a central spheroid. We note that the convergence of the SCF algorithm for such configurations is highly unstable when the two bodies are close from one another, $s \leq OA_1$.

4.5 Summary for the 2-body case and perspectives for $m \geq 2$

This survey shows some interesting features summarized as follow (Basillais and Huré, 2019) :

- no contact binary other than the one reported in Ansorg et al. (2003) is detected
- the 2-body equilbria only populate a specific section between the MLS and the ORS in the $\omega^2 - j^2$ diagram with the existence of a maximum rotation rate already reported in Hachisu and Eriguchi (1983)
- near the ORS there is an area of degenerecy where two different equilibria can display the same rotation rate ω and the same angular momentum j
- new bifurcations from the ascending part of the Maclauring towards the ORS where found for ellipsoid having an eccentricity lower than ≈ 0.612

This new version of the `DROP`-code is able to generate configurations with, theoretically, as much bodies as wanted. The only drawback is the computation time : more bodies means more Poisson equations to solve and it slows drastically the time needed to do one SCF iteration. All the following configurations were obtained with a polytropic index $n = 1.5$ and a solid rotation law. In Fig.4.14 are presented two configurations. The first one is for $m = 2$ composed of a central spheroid and a close and tiny ring (one equilibrium obtain in the space-parameter survey for $n = 1.5$). As seen earlier, we can find equilibrium composed of a massive spheroid and a tiny ring in contact. Such configurations could be useful for the study of Be stars : a highly flattened central spheroid surrounded by a tiny transient ring. This kind of configurations could be use to unravel the internal structure of fast rotator. For example, it can be applied to the Be star Achernar which present a strong oblatness with an axis ratio of ~ 0.64. Achernar displays a transient circumstellar

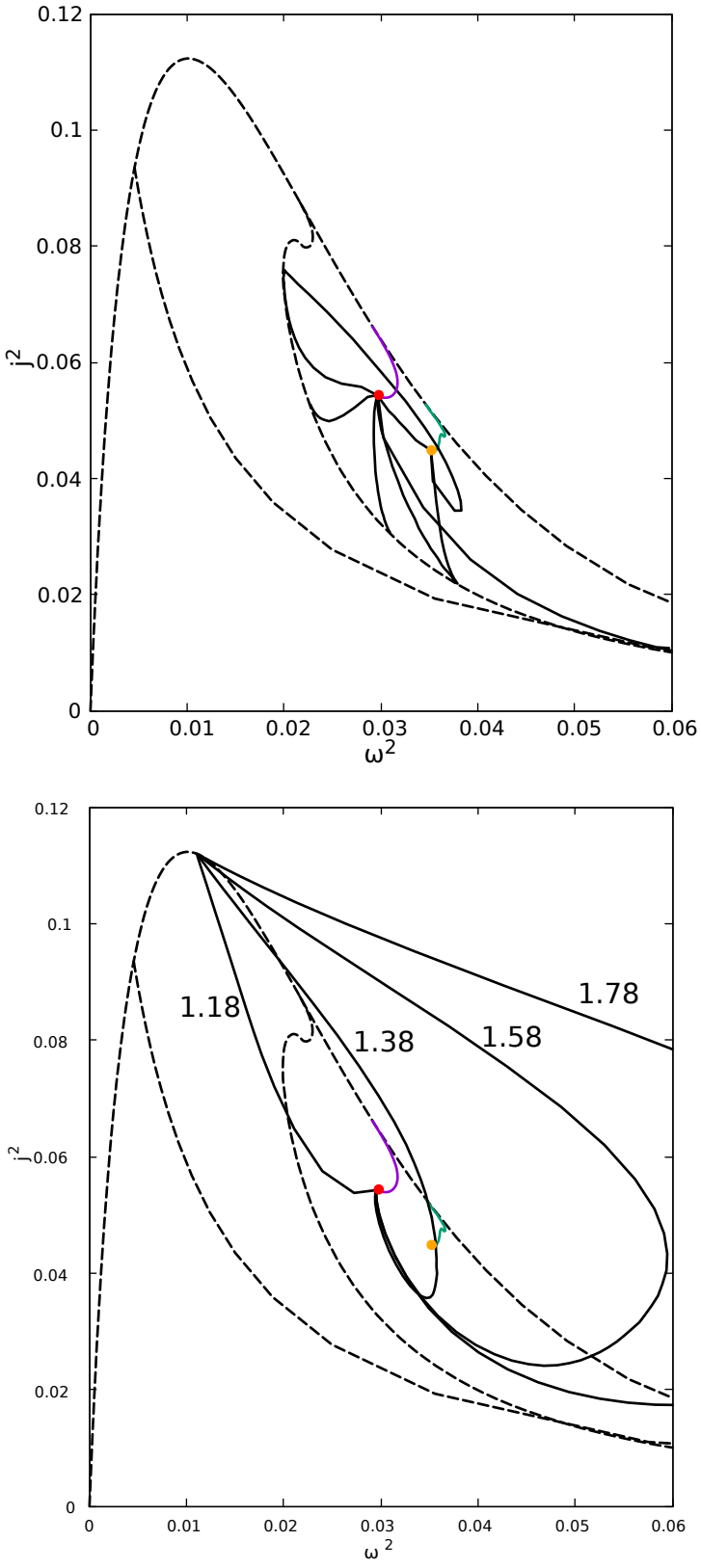

Figure 4.13: (top) : sequences linking the end-points of the ε_2 and ε_3 sequences to the ORS for various axis ratio of the outer ring.
(bottom) : sequences linking the end-points of the ε_2 sequence to the MLS by shrinking the ring on various points.

disk on its equatorial plane (Rivinius et al., 2016; Dalla Vedova et al., 2017). Two figures are presented in Fig.4.15 with $m = 4$ and $m = 5$. This kind of configurations can be used in order to investigate ringed accretion around massive bodies. It is usually used in the general relativity framework to study accretion of massive disks around black hole (Pugliese and Stuchlík, 2015, 2017; Pugliese and Stuchlik, 2019). Typical ringed accretion displays several tores corotating or counterrotating. This ringed accretion could also take place around less massive body like dwarf stars or neutron stars and can be investigated with the classical theory of figures. The geometry of the system and the internal structure of the tori can be derived. In Fig.4.14(*bottom panel*) is presented a configuration with $m = 7$ where the geometrical parameters (size and orbital separation of the ring) are the same as the protoplanetary system HL Tau (Carrasco-González et al., 2016, 2019). In the hyposthesis where the rings are self-gravitating, we need to reconsider the solid rotation in order to properly model HL Tau.

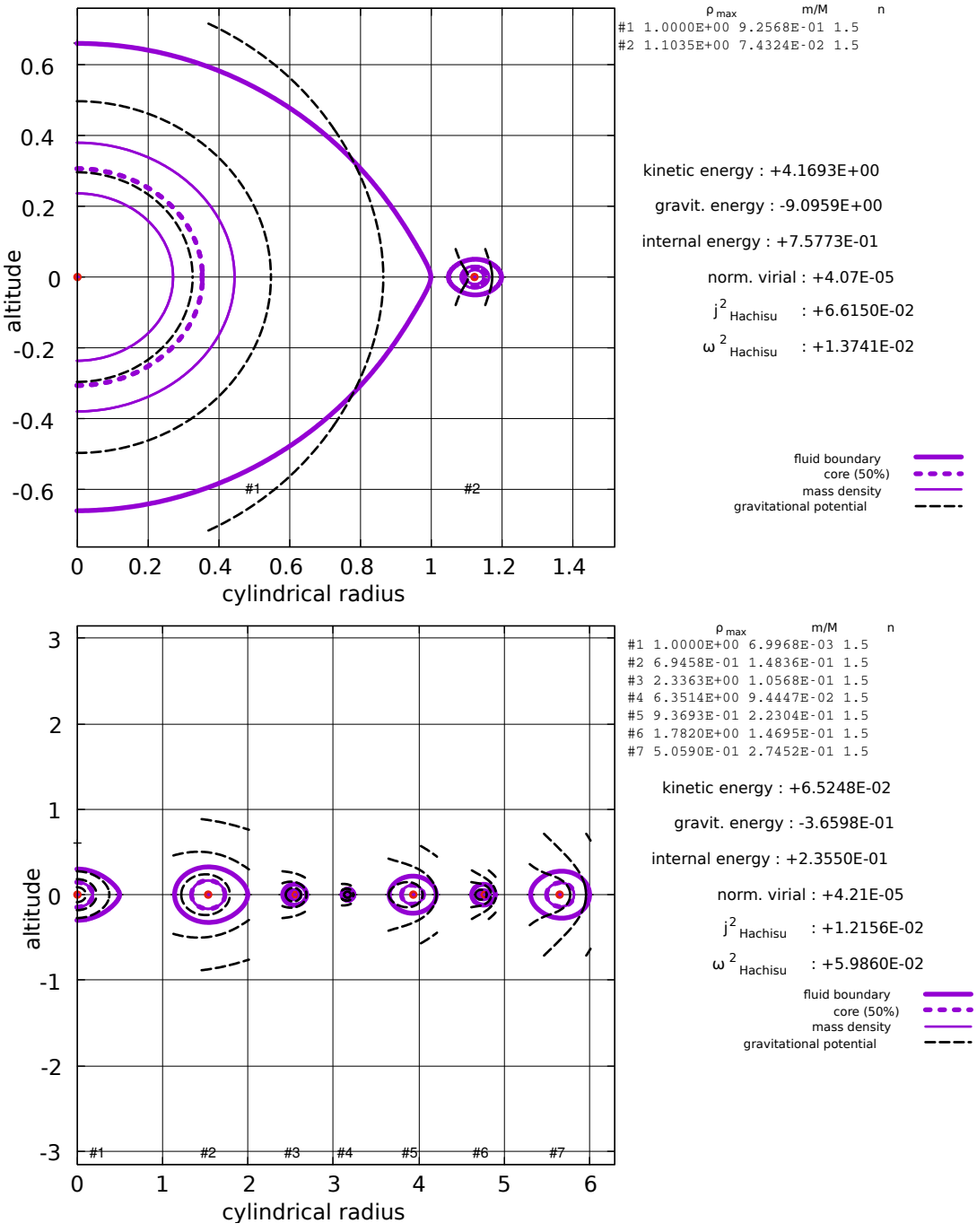

Figure 4.14: (top) : configuration with $m = 2$. (bottom) : configuration with $m = 7$.

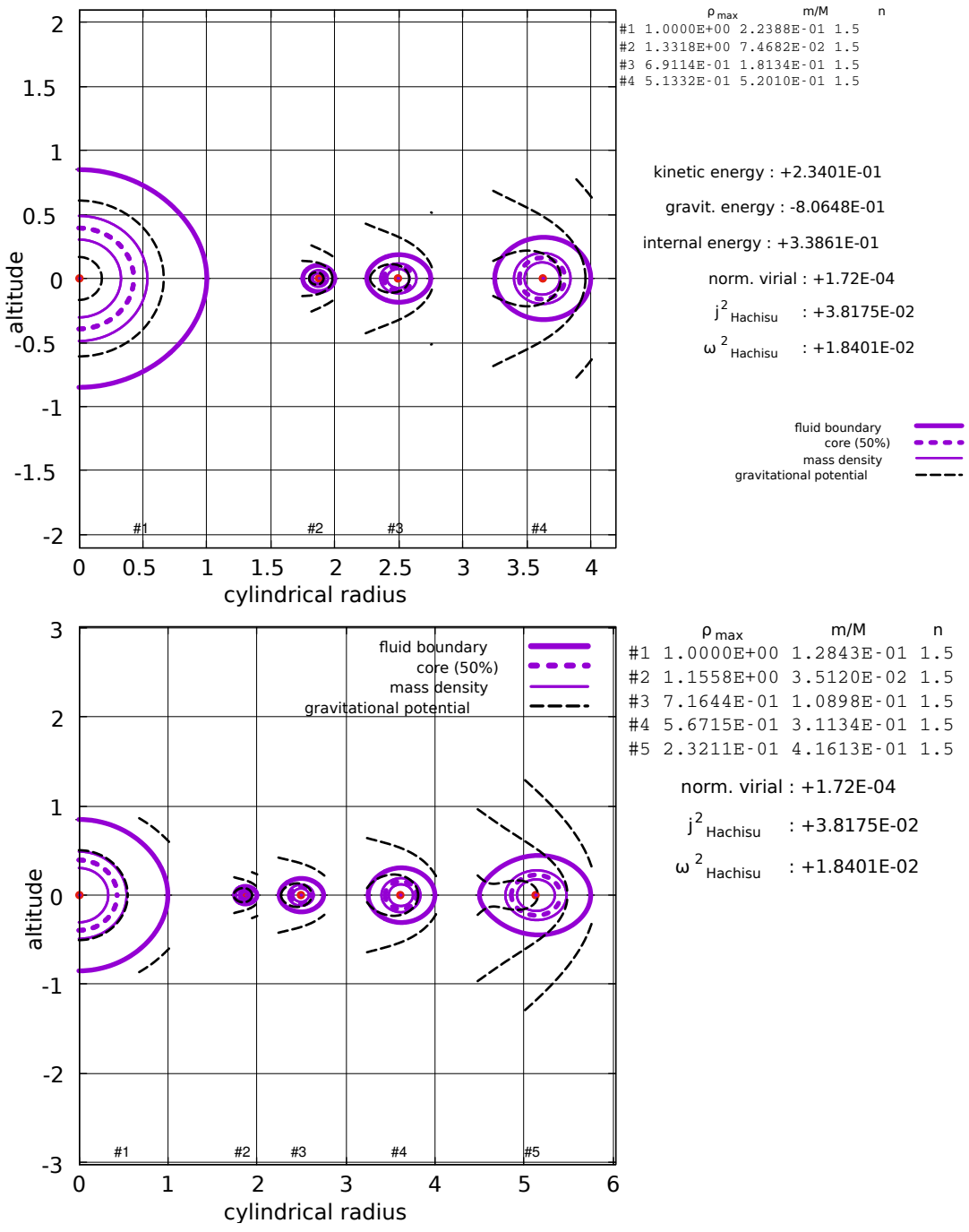

Figure 4.15: (top) : configuration with $m = 4$.
(bottom) : configuration with $m = 5$.

Chapter 5

Multi-layer configurations

Contents

In this chapter, we introduce a more complex model for rotating bodies based on another use of the Bernoulli equation : multi-layer bodies. We consider a rotating body with several layers and each layer can have a different EOS. We start off with the most simple case of multi-layered configurations : a two-layer body before moving on a multilayered system. Such layered configurations are of high interest in the understanding of internal structure of MS stars (helium core and hydrogen envelope), rocky planets (rocky core surrounded by an ocean or atmosphere) and gas planets (rocky or icy core, atomic hydrogen mantle and molecular hydrogen atmosphere). Some publications adressed this matter but are rather uncommon when considering all the scientific research on figures of equilibrium and polytropes (Caimmi, 1986; Rucinski, 1988; Curry and McKee, 2000; Dullemond and Natta, 2003; Kiuchi et al., 2010) More importantly, in this thesis, we introduce a *density jump* and a *rotational discontinuity* at each interface between layers. Although this problem was adressed (e.g. Kiuchi et al., 2010), we proceed to a more thorough investigation. For instance, in the Sun, the rotation profile in the core (solid rotation) is not the same that the rotation in the envelope (shellular rotation at the pole and cylindrical rotation at the equator). For planets, the core and the atmosphere can spin at different rates.

5.1 The case of a two-layer body : bipolytrope

5.1.1 Introduction

Using a single polytropic EOS and solving the Lane-Emden equation to study self-gravitating non-rotating spheres is useful to understand stars, planets and torus in their entirety but is a rather crude approach and is lacking details about their internal structure. In a star or a planet, the gradient of density can vary quite steeply : nuclear core, radiative layer and convective surface. A single EOS can not replicate precisely high density region in the center of the star and low density region in the outer part of the star at the same time because different physical mechanisms are at work. Milne (1930) was one the first to propose a more advanced model using two EOS and building a composite polytrope that is nowadays called a bipolytrope (core and photosphere). Each EOS describes a specific region, or layer, of the star : one describes the center of the star and the other describes the outer part.

5.1.2 The Schönberg-Chandrasekhar limit

The evolution of a main-sequence star into a red giant is a known process since the study of embedded polytropes. Schönberg and Chandrasekhar (1942) found that, for a non-rotating star, if an isothermal core (i.e. $n_c = \infty$) is embedded in an external radiative envelope with a polytropic index of 3, there is an upper limit on the core's mass. If the core is less massive than this limit, the equilibrium exists and the star remains in the main-sequence. But if the core is more massive, the equilibrium cannot exist anymore and the core begins to contract and as a consequence the star leaves the main-sequence and evolve into a red giant. This upper limit is called the Schönberg-Chandrasekhar limit (hereafter the SC-limit). In Schönberg and Chandrasekhar (1942), this limit is defined as

:

$$\frac{M_{core}}{M_{envelope}} = 0.37 \frac{\mu_{envelope}}{\mu_{core}} \tag{5.1}$$

where μ is the mean molecular weight.

After this initial work on the subject, several others have studied the SC-limit to better understand and constraint when and how the star evolves into a red giant. The density gradient between the core and the envelope is a key factor for the evolution into a red giant Beech (1988). Eggleton et al. (1998) showed that in the analytical case where the polytropic index of the core is 5 and the polytropic index of the envelope is 1, then an SC-like-limit exists if the core is four time denser than the envelope at the interface. Using Milne's variable, Ball et al. (2012) demonstrated that there is an SC-like-limit if the polytropic index of the core is larger than 5.

The case where the polytropic index of the the core is $n_c = 5$, the polytropic index of the the envelope $n_e = 1$ and the density jump between the two layers is $\alpha = 4$ is of a great interest for two reasons : it is an analytical case and this value of α is relevant in stellar context because it is the ratio between the molecular weight of the helium in the core and the molecular weight of the hydrogen in the envelope of a star.

5.1.3 Equation set in the non-rotating case

When studying a body composed by two layers, we commonly call *core* the deepest layer *envelope* the outside one, see fig 5.1. Each layer is described by a specific EOS. We set

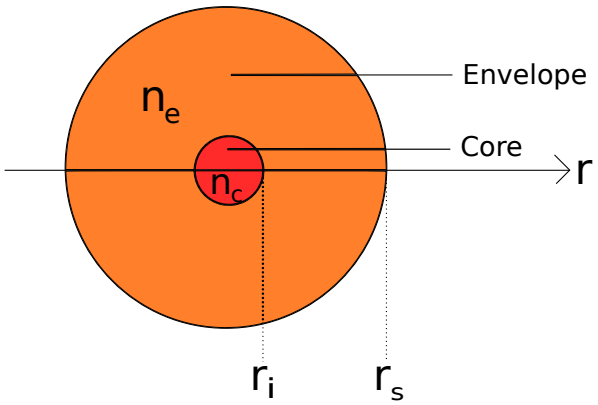

Figure 5.1: Typical configuration for a two-layered body. The core and the envelope can have different EOS, different rotation law and possibly a mass density jump at the core-envelope interface.

n_c as the polytropic index of the core and n_e as the polytropic index of the envelope. As seen in Eq.(2.20), the dimensionless equation of Lane-Emden writes :

$$\frac{1}{\xi^2}\frac{d}{d\xi}\left(\xi^2 \frac{d\hat{H}}{d\xi}\right) = -\hat{H}^n \tag{5.2}$$

where $\xi = \frac{r}{L}$ with $L = \sqrt{\frac{\kappa(n+1)+\rho_c^{\frac{1}{n}-1}}{4\pi G}}$.

5.1.4 An analytical case : $n_c = 5$ and $n_e = 1$

The Lane-Emden equation has analytical solutions in case of $n = 1$: $\hat{H} = \frac{\sin(\delta\xi - B)}{\xi}$ with $\delta = \pm 1$ and in case of $n = 5$: $\hat{H} = \frac{1}{\sqrt{1+\frac{\xi^2}{3}}}$. The SC-limit corresponds to an isothermal core and a convective envelope, the analytical solutions closest to this configuration is obtained for a core with a polytropic index of 5 and an envelope with a polytropic index of 1.

The solution for the envelope is H_e whereas the solution for the core is H_c and from now on, ξ is the dimentionless radius of the core and η is the dimentionless radius of the envelope. We use a scaling factor to link both dimentionless space of solution. We define it as $f = \frac{L_e}{L_c}$ From Eq.(2.19), we have :

$$L_c^2 = \frac{(n_c+1)K_c\rho_c^{\gamma_c-2}}{4\pi G} \text{ and } L_e^2 = \frac{(n_e+1)K_e\rho_e^{\gamma_e-2}}{4\pi G},$$

which leads to :

$$f = \frac{L_e}{L_c} = \frac{\alpha}{\sqrt{3}}(1 + \frac{\xi_i^2}{3}). \tag{5.3}$$

where α is the density jump and is defined as :

$$\alpha = \frac{\rho_i^c}{\rho_i^e} \tag{5.4}$$

In the physical domain, the pressure is continuous at the interface, i.e. at $r = r_i$, which is expressed as $P_{c_i} = P_{e_i}$. Using the polytropic EOS, we have :

$$\frac{K_c}{K_e} = \frac{\rho_{e_i}^2}{\rho_{c_i}^{\frac{6}{5}}}. \tag{5.5}$$

At the interface $r = r_i$ the enthalpy gradient is continous, i.e. $\nabla H_{c_i} = \nabla H_{e_i}$. Using dimensionless variables, it yields :

$$\nabla\tilde{H}_{c_i}\frac{H_{c_0}}{L_c} = \nabla\tilde{H}_{e_i}\frac{H_{e_0}}{L_e}. \tag{5.6}$$

We know that :

$$
\begin{aligned}
\nabla \tilde{H}_{c_i} &= -\frac{\xi_i \sqrt{3}}{(\xi_i^2+3)^{\frac{3}{2}}}, \\
H_{c_i} &= H_{c_0}\left(1+\frac{\xi_i^2}{3}\right)^{-\frac{1}{2}} = 6K_c\rho_{c_i}^{\frac{1}{5}}, \\
\nabla \tilde{H}_{e_i} &= \frac{\delta\cos(\delta\eta_i - B) - \sin(\delta\eta_i - B)}{\eta_i^2}, \\
H_{e_i} &= H_{e_0}\frac{\sin(\delta\eta_i - B)}{\eta_i} = 2K_e\rho_{e_i}, \\
\text{And : } \frac{K_c}{K_e} &= \frac{\rho_{e_i}^2}{\rho_{c_i}^{\frac{6}{5}}},
\end{aligned}
$$

which leads to :

$$\delta\cot(\delta\eta_i - B) = \delta\cot(\phi_i) = \frac{\alpha - \xi_i^2\left(1-\frac{\alpha}{3}\right)}{\xi_i\sqrt{3}}. \tag{5.7}$$

At the fluid boundary, the pressure goes to 0 and therefore the enthalpy of the envelope is 0 at the surface $r = r_s$. So we have :

$$H_{e_s} = \frac{\sin(\delta\eta_s - B)}{\eta_s} = 0 \tag{5.8}$$

which leads to :

$$\eta_s = \frac{\pi + B}{\delta} \tag{5.9}$$

Mass

The mass of the core is obtained by :

$$
\begin{aligned}
m_c &= \int_0^{r_i} \rho_c r^2 \sin(\theta) d\theta d\phi \\
&= 4\pi R_{c_0}^3 \rho_{c_0} \int_0^{\xi_i} \frac{\xi^2}{(\xi^2+3)^{\frac{5}{2}}} d\xi \\
&= 4\pi R_{c_0}^3 \rho_{c_0} \frac{\xi_i^3\sqrt{(3)}}{(3+\xi_i^2)^{\frac{3}{2}}}
\end{aligned} \tag{5.10}
$$

and the mass of the envelope by :

$$
\begin{aligned}
m_e &= \int_{r_i}^{r_s} \rho_e r^2 \sin(\theta) d\theta d\phi \\
&= 4\pi R_{e_0}^3 \rho_{e_0} \int_{\eta_i}^{\eta_s} \eta \sin(\delta\eta - B) d\xi \\
&= 4\pi R_{e_0}^3 \rho_{e_0} \left(\pi + B - \sin(\delta\eta_i - B) + \delta\eta_i\cos(\delta\eta_i - B)\right)
\end{aligned} \tag{5.11}
$$

core mass fraction as a function of core radius fraction

The core mass fraction is set as :

$$\nu = \frac{m_c}{m_c + m_e} = \frac{1}{1 + \frac{m_e}{m_c}} \tag{5.12}$$

with :

$$\frac{m_e}{m_c} = \alpha \left(1 + \frac{\xi_i^2}{3}\right) \frac{1}{\xi_i^2} \left(\frac{\pi + B}{\sin \delta\eta_i - B} - 1 + \delta\eta_i \cot(\delta\eta_i - B)\right). \tag{5.13}$$

The core radius fraction is set as :

$$q = \frac{r_i}{r_s} = \frac{\eta_i}{\eta_s} \tag{5.14}$$

We can now determine the diagram $\nu = f(q)$. To do so we follow a simple process :

$$1 : \text{We choose a } \xi_i \tag{5.15}$$

$$2 : \text{We now have our scaling factor : } f = \frac{\alpha}{\sqrt{3}} \left(1 + \frac{\xi_i^2}{3}\right) \tag{5.16}$$

$$3 : \text{We determine } \cot(\phi_i) \text{ with Eq.(5.7)} \tag{5.17}$$

$$4 : \text{We calculate } \phi_i = \arctan^{-1}\left(\frac{1}{\cot(\phi_i)}\right) \tag{5.18}$$

$$5 : \text{We calculate } B \text{ with } B = \delta\eta_i - \phi_i \tag{5.19}$$

$$6 : \text{We can have } \eta_s = \frac{\pi + B}{\delta} \tag{5.20}$$

$$7 : \text{We can determine the core radius fraction : } q = \frac{\eta_i}{\eta_s} \tag{5.21}$$

$$8 : \text{Finally we determine } \frac{m_e}{m_c} \tag{5.22}$$

The core mass fraction as a function of core radius fraction is plotted in Fig.5.2 for various density jumps α. We can see that as α increases, the maximum relative size of the core decreases and there is no mass limit of the core. Moreover, for $\alpha = 2$, there is only one core mass fraction for a given core radius fraction. For a specific value of $\alpha_{2\nu} \in [2, 2.9]$, a second value of the core mass fraction appears for the same q and two ν can be obtained for the same q when $\alpha \geq \alpha_{2\nu}$. A mass limit of the core appears when $\alpha \geq 3$. A density jump of great interest is $\alpha = 4$ because it corresponds to the density jump at the interface of the core and the envelope in a main-sequence star burning hydrogen into helium. We can see that, with this analytical model, a maximum q and a maximum ν are predicted. As a consequence, there is an analog of the SC-limit for this case where $n_c = 5$, $n_e = 1$. This analog limit called the SC-like-limit.

A space parameter survey has been conducted for various polytropic index of the core n_c, polytropic index of the envelope n_e and density jump α using a numerical integrator in the non-rotating case. It was the first investigation on the subject of the SC-limit in order to do the spadework for the computations with the `DROP` code. With this preliminary work, we confirm that there is no SC-like-limit if $n_c < 5$, that there can be a SC-like-limit if $n_c = 5$ and that there is always a SC-like-limit if $n_c > 5$.

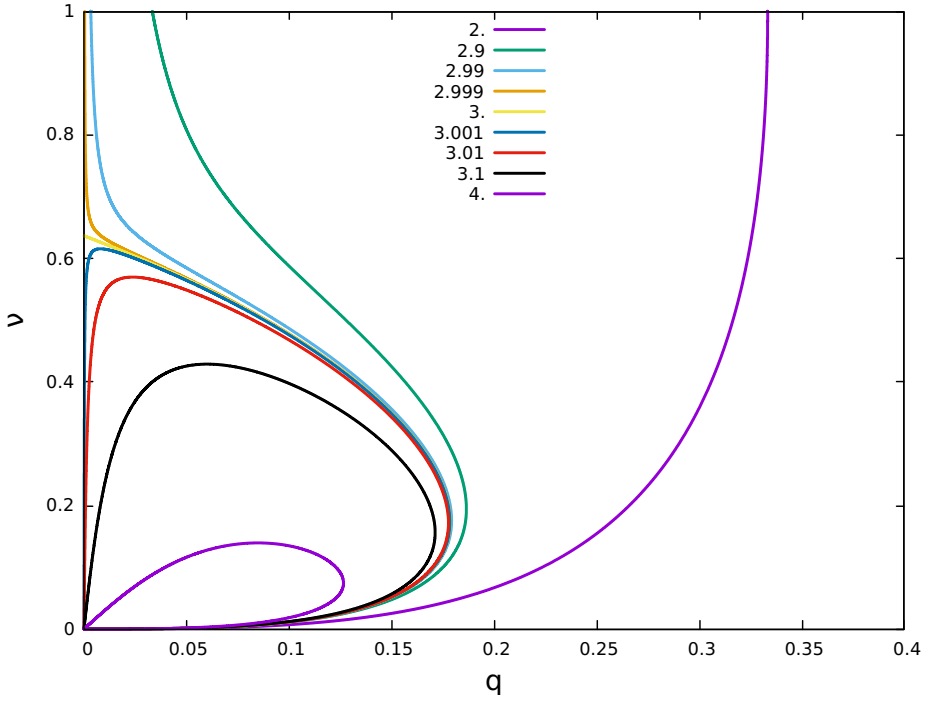

Figure 5.2: Core mass fraction ν as a function of the core mass radius q for various density jumps α. Core and envelope are rigidly rotating

5.2 Equation set in the rotating case

In this section, we present the improvements implemented to the DROP code to take into account multi-layered polytrope. We will present the simpliest case of a rotating bipolytrope in Sect.5.2.1. A general algorithm to generate multi-layer polytrope is presented in Sect.5.9.

5.2.1 Case of a 2-layered polytrope : bipolytrope

The equation set for a two-layer polytrope is derived from the equation set of a single-layered polytrope which is :

$$\begin{cases} C_1\hat{H} + C_2\hat{\Phi} + \hat{\Psi} = C_3 \\ \hat{\rho}^{1/n} = \sup(\hat{H}, 0) \\ \Delta\hat{\Psi} = 4\pi\hat{\rho} \end{cases} \tag{5.23}$$

where C_1 and C_2 are defined by :

$$\begin{cases} C_1 = \frac{K(n+1)\rho_0^{\gamma-2}}{GL^2} \\ C_2 = \frac{\Omega_0^2}{G\rho_0} \end{cases} \tag{5.24}$$

The equation set Eq.(5.23) is reproduced for each layer. There is a constraint on the pressure : *it is continuous at any interface*. As shown above, we have :

$$K^c\rho_i^c = K^e\rho_i^e \tag{5.25}$$

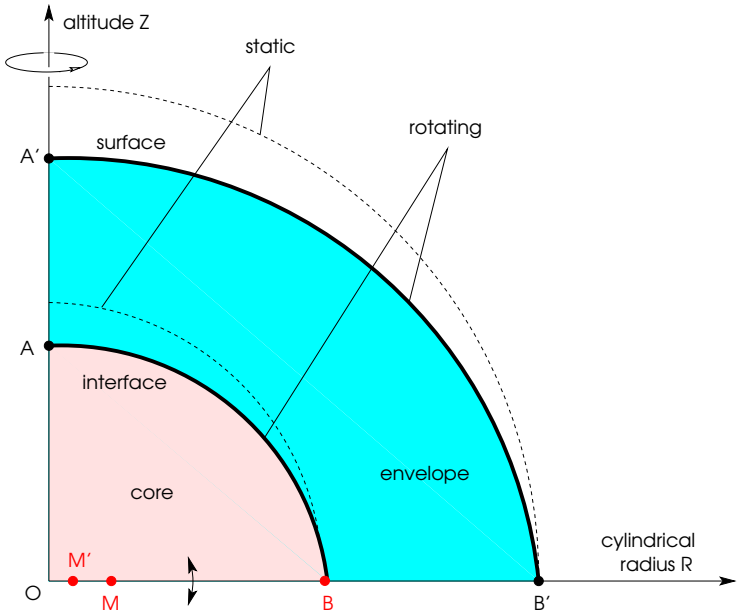

Figure 5.3: Typical configuration for a m-body self-gravitating system made of an optional ellipsoid (E) and concentric rings (R). The SCF-method relies on two reference points A and B selected along each fluid boundary Γ *(bold line) and a third, floating point M where enthalpy is maximum (one triplet per body). Accuracy is optimized by using individual computational boxes.*

Whereas the pressure is continuous at the interface, the density is not and we can quantified the discontinuity with the density jump α such as :

$$\alpha = \frac{\rho_i^c}{\rho_i^e} \tag{5.26}$$

We choose to decouple in term of density scale each layer in order to avoid a lot of numerical problem due to the discontinuity at the interface and potential magnitude problem between dense and diffuse regions. By doing this, we solve the system by taking into account the discontinuity accuratly rather than leaving it to the Poisson solver to manage as it was done earlier in Kiuchi et al. (2010); Kadam et al. (2016). We set ρ^c for the core and ρ^e for the envelope. The total gravitational potential is written as :

$$\Psi_{tot} = \Psi^c + \Psi^e. \tag{5.27}$$

The dimensionless gravitational potential in the core space is $\hat{\Psi}^c_{tot} = \hat{\Psi}^c + \beta\hat{\Psi}^e$ and in the envelope space is $\hat{\Psi}^e_{tot} = \frac{1}{\beta}\hat{\Psi}^c + \hat{\Psi}^e$ where

$$\beta = \frac{\rho_0^e}{\rho_0^c}, \tag{5.28}$$

is the envelope-to-core mass density ratio. Using Eq.(5.24b) applied to core and the envelope, we see that :

$$\beta\omega_{ec}C_2^e = C_2^c, \tag{5.29}$$

where ω_{ec} is the parameter describing the *rotational discontinuity* defined by :

$$\sqrt{\omega_{ec}} = \frac{\Omega_0^c}{\Omega_0^e} > 0. \tag{5.30}$$

Actually, in contrast to studies where a global rotation is assumed, we can introduce a different rotation for the core and for the envelope. When $\omega_{ec} < 1$, the core rotates slower than the envelope, if $\omega_{ec} = 1$, both the core and the envelope rotate at the same speed and if $\omega_{ec} > 1$, the core rotates faster than the envelope. For the main results in this chapter, ω_{ec} will be set to 1 if not specified otherwise. The importance of this parameter is discused in Sect.5.2.2.

The general equation set for a bipolytrope is :

$$\begin{cases} C_1^c \hat{H}^c + C_2^c \hat{\Phi}_{tot}^c + \hat{\Psi}^c = C_3^c \\ \hat{\rho}^c = \hat{H}^{c^{n_c}} \\ \Delta \hat{\Psi}_{tot}^c = 4\pi \left(\hat{\rho}^c + \beta \hat{\rho}^c\right) \\ C_1 \hat{H}^e + C_2^e \hat{\Phi}_{tot}^e + \hat{\Psi}^e = C_3^e \\ \hat{\rho}^e = \hat{H}^{e^{n_e}} \\ \Delta \hat{\Psi}_{tot}^e = 4\pi \left(\hat{\rho}^e + \beta \hat{\rho}^e\right) \\ \bar{\alpha} C_1^c \hat{H}_i^c = \beta C_1^e \hat{H}_i^e \\ \alpha\beta \hat{\rho}_i^e = \hat{\rho}_i^c \\ \beta \omega_{ec} C_2^e = C_2^c \end{cases} \tag{5.31}$$

where $\bar{\alpha} = \alpha \frac{1+n_e}{1+n_c}$.

We solve these equations with the SCF method using a modified cycle from the one described for a simple polytrope. In this case, again, we use two points one the surface (Γ_e) of the envelope A' and B' and another third point A at the interface (Γ_c) that belongs to the core and the envelope :

$$\begin{cases} (a): & \frac{1}{\beta}\hat{\Psi}_{A'}^c + \hat{\Psi}_{A'}^e + C_2^e \hat{\Phi}_{A'} = C_3^e \\ & \text{A' belongs to the surface so } \hat{H}_{A'}^c = 0, \\ (b): & \frac{1}{\beta}\hat{\Psi}_{B'}^c + \hat{\Psi}_{B'}^e + C_2^e \hat{\Phi}_{B'} = C_3^e \\ & \text{B' belongs to the surface so } \hat{H}_{B'}^c = 0, \\ (c): & \beta C_1^e = \max\left(\beta C_1^e \hat{H}^e\right) \\ & \text{normalization of the enthalpy,} \\ (d): & C_1^e \hat{H}_A^e + \frac{1}{\beta}\hat{\Psi}_A^c + \hat{\Psi}_A^e + C_2^e \hat{\Phi}_A = C_3^e \\ & \text{A belongs to the envelope,} \\ (e): & \bar{\alpha} C_1^c \hat{H}_A^c(\Gamma_c) = \beta C_1^e \hat{H}_A^e(\Gamma_c) \\ & \text{pressure balance at the interface,} \\ (f): & \beta \omega_{ec} C_2^e = C_2^c \\ & \text{scaling condition,} \\ (g): & C_1^c \hat{H}_A^c + \hat{\Psi}_A^c + \beta \hat{\Psi}_A^e + C_2^c \hat{\Phi}_A = C_3^c \\ & \text{A belongs to the core,} \\ (h): & C_1^c = \max\left(C_1^c \hat{H}^c\right) \\ & \text{normalisation of the enthalpy,} \\ (i): & \alpha\beta \hat{H}_A^e(\Gamma_c)^{n_e} = \hat{H}_A^{c\,n_c}(\Gamma_c) \\ & \text{mass density jump at the interface} \end{cases} \tag{5.32}$$

step	operation
1	$\hat{\rho}^c$ and $\hat{\rho}^e$ are computed from the polytropic assumption; only positive parts of the enthalpy is retained
2	$\hat{\Psi}^c$ and $\hat{\Psi}^e$are computed from the two Poisson equations, i.e. Eqs.(5.31c) and (5.31f)
3	values of $\hat{\Psi}^e$ at the 3 reference points A', B' and A are deduced, i.e. $\hat{\Psi}^e_{A'}$, $\hat{\Psi}^e_{B'}$ and $\hat{\Psi}^e_{A}$
4	βC_2^e is obtained from $\hat{\Psi}^e_{A'}$ and $\hat{\Psi}^e_{B'}$ by solving Eqs.(5.32a) and (5.32b),
5	βC_3^e is deduced from Eq.(5.32a),
6	$\beta C_1^e \hat{H}^e$ is computed from the Bernoulli equation for the envelope, i.e. Eq. (5.32d)
7	the point M′ where $\beta C_1^e \hat{H}^e$ is maximum is localized (it is generally not in the envelope),
8	then we set $\beta C_1^e = C_1^e \hat{H}^e_{\mathrm{M}'}$, i.e. Eq.(5.32c)
9	the enthalpy for the envelope $\hat{H}^e$ is computed from Eq. (5.32d)
10	the quantity $\beta C_1^e \hat{H}^e_A$ is deduced (see step 6)
11	the constant C_2^c is deduced from Eq.(5.32f)
12	the value of $C_1^c \hat{H}^c_A$ is deduced from Eq.(5.32e)
13	C_3^c is computed from Eq.(5.32g)
14	the point M where $C_1^c \hat{H}$ is maximum can be localized
15	then we set $C_1^c = C_1^c \hat{H}^c_{\mathrm{M}}$, i.e. Eq.(5.32h)
16	the enthalpy for the core $\hat{H}$ is computed from Eq.(5.32a)
17	the new enthalpies are determined, i.e. $\hat{H} \equiv \hat{H}(t+1)$ for the core, and $\hat{H}^e \equiv \hat{H}^e(t+1)$ for the envelope
18	a new value of the β-parameter is computed from Eq.(5.32i);
	see Sec. 5.2.3 for a discussion about the fixed point interation

Table 5.1: Main steps of the SCF-method for a bipolytropic star. The loop starts for a given value of β and two enthalpies $\hat{H}^c$ and $\hat{H}^e$.

5.2.2 Important remarks on the equation set

A few interesting properties come out of Eq.(5.32). First, we can eliminate $\hat{H}_2(\Gamma)$ from (5.32e) and (5.32i). We find, assuming $n_e > 0$

$$\frac{1+n_e}{1+n_1}\frac{C_1^c}{C_1^e}\beta^{\frac{1}{n_e}-1}\alpha(\Gamma^c)^{\frac{1}{n_e}+1} - \hat{H}^c(\Gamma_c)^{\frac{n_c}{n_e}-1} = 0, \tag{5.33}$$

which holds regardless of the rotation profiles. Since β is a scalar, the enthalpy of the core depends directly on the mass density jump, locally. We see that α varies along the interface according to $\hat{H}^c$. If α is uniform at Γ_c, then $\hat{H}^c$ (and subsequently $\hat{H}^e$) is a constant too. If the two polytropic indices happen to be equal, then $\alpha_2(\Gamma_c)$ =const. must hold, whatever the enthalpy of the core. This is for instance the case if the two layers have a different chemical composition, while their equilibrium is driven by the same physical mechanisms leading to $n_c = n_e$.

Another interesting point concerns the relationship between the two enthalpies at Γ_c. Actually, if we eliminate α between (5.32e) and (5.32i), then we find

$$\frac{1+n_e}{1+n_c}C_1^c\hat{H}^c(\Gamma_c)^{1+n_1} - \beta^2 C_1^e \hat{H}^e(\Gamma_c)^{1+n_e} = 0. \tag{5.34}$$

Unsurprisingly, there must be a fine tuning between the $\hat{H}^c$ and $\hat{H}^e$ all along Γ. We have $\hat{H}^c(\Gamma_c) \propto \hat{H}^e(\Gamma_c)$ when $n_c = n_e$. As we will see, this equation will be used to determine the location of the interface (see below).

Third, there is a tight link between the mass density jump at Γ_c and the rotation profiles as soon as a rotational discontinuity is present. Actually, suppose that the core

and the envelope share the same dimensionless centrifugal potential $\hat{\Phi}$, but the rotation rate differs on both sides of the interface, i.e. $\Phi(\Gamma_c^+) \neq \Phi(\Gamma_c^-)$. If we multiply (5.31d) by β and compare the obtained expression to (5.31a), we find

$$C_1^c \hat{H}^c(\Gamma_c)\left[1-\bar{\alpha}(\Gamma_c)\right] + C_2^c \hat{\Phi}(\Gamma_c)\left(1-\frac{1}{\omega_{ec}}\right) + \beta C_3^e - C_3^c = 0, \tag{5.35}$$

where we have used (5.27) to eliminate the gravitational potential, and (5.31e) to eliminate $\hat{H}^e$. It follows that $\hat{H}^c(1-\bar{\alpha})$ must be a constant all along Γ_c not only in the static case, but also in the presence of rotation provided $\omega_{ec} = 1$, that is, there is no rotational discontinuity (the rotation profile can change, but continuously). In contrast, the presence of any rotational discontinuity ($\omega_{ec} \neq 1$) implies that the quantity $\hat{H}^c(1-\bar{\alpha})$ must vary and this depends on $\hat{\Phi}(\Gamma_c)$. As a consequence of (5.33), if the rotation profile is imposed, the mass-density jump α cannot be uniform on this case, and the enthalpies also vary on Γ_c. This is physically acceptable. An abrupt change in the fluid velocity creates a depression that can be cancelled or compensated by an appropriate rise of concentration in the gas. If this fluid velocity is not uniform along the interface, then the increase in mass density may not be uniform either. We can give (5.34) an opposite sense. If the equilibrium of the system requires a constant mass density jump at the interface, then the rotation profile can not be fully arbitrary (this is not a common convention in the theory of figures).

5.2.3 `DROP` code, control parameter and fixed point

In our SCF code, our control parameter is defined by $\frac{OA}{OA'}$. By moving the point A along the Z-axis, we control the equilibrium the code is going to converge to. As we have seen in Sect.5.1.4, several equilibria exist for a single axis ratios. In particular, the β parameter is an output quantity. Note for Kadam et al. (2016) that this parameter is an input parameter.

In the case where two equilibria are possible, the initial value of β is critical. Let us consider the case of Sec.5.1.4 with $\alpha = 4$. We know what is the $\nu = f(q)$ function thus what we should obtain with the SCF method. By using the equation set Eq.(5.32), we can express the value of β at a given step $n+1$ as a function of its previous value at the step n which yields :

$$\beta_{n+1} = f(\beta) = \frac{1}{\alpha}\left(\frac{1}{1+\bar{\alpha}\frac{\Delta\tilde{\Psi}_{AM}+\beta C_2^e \Delta\tilde{\Phi}_{AM}}{\Delta\tilde{\Psi}_{A'A}+\beta C_2^e \Delta\tilde{\Phi}_{A'A}}}\right)^{n_c} = \frac{1}{\alpha}\left(\frac{1}{1+\bar{\alpha}h(\beta)}\right)^{n_c} \tag{5.36}$$

Searching for a solution for the Eq.(5.36) is actually searching for the fixed point of the function $f(\beta)$. We can see in Fig.5.4 the there are three fixed points P1, P2 and P3. P1 and P3 are attractive fixed points : β converges towards one of those two points depending on its initial value. P2 is a repulsive fixed point : β will converges towards this point. It is striking that, depending on the point we end on, the equilibrium found by the SCF is different. Our aim is to select this point.

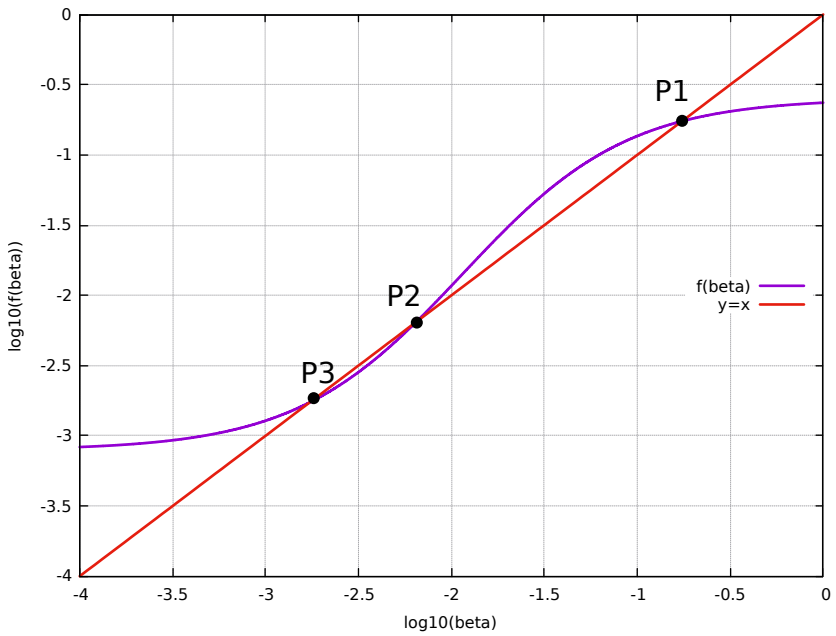

Figure 5.4: Graphical representation of $\beta_{n+1} = f(\beta_n)$ and three fixed points : P1 leading to low solutions, P2 leading to high solutions and P3 leading to non-physical solutions in the typical case where $n_c = 5$, $n_e = 1$ and $\alpha = 4$.

Physically, when β tends towards $P1$, the configuration consists in a core being a bit denser than the envelope : this equilibrium is at low ν in the (q, ν)-diagram. This is the "low solution". When β tends towards $P2$, the configuration consists in a core being moderately denser than the envelope : this equilibrium occurs for moderate ν in the (q, ν)-diagram. This is the "high solution". When β tends towards $P3$, the configuration consists in a core being overwhelmingly denser than the envelope : this equilibrium is at $\nu \sim 1$ in the (q, ν)-diagram. This family of equilibriums is resolution dependent and is not physically relevant.

Low solution

It is quite easy to converge to P1 by setting an initial value between 0.1 and 1. If we set a lower value, the SCF converges to P3.

High solution

To be able to converge towards P2, we need to transform this repulsive point into an attractive one. We need to make up a function that allows such a modification and behaviour. A first option is to create the function $f_1(\beta) = 2\beta - f(\beta)$. It is plotted in Fig.5.5. This function, although quite simple to obtain, does not work in any time. In fact, depending on $f(\beta)$, we can sometimes be stuck, oscillating around P2. To overcome this unwanted feature, we need to properly reverse the $f(\beta)$ function and make up a second function that we call $g(\beta)$. We have to create the function obtained through a reflection symmetry of $f(\beta)$ by the $y = x$ axis. This function is the inverse function of

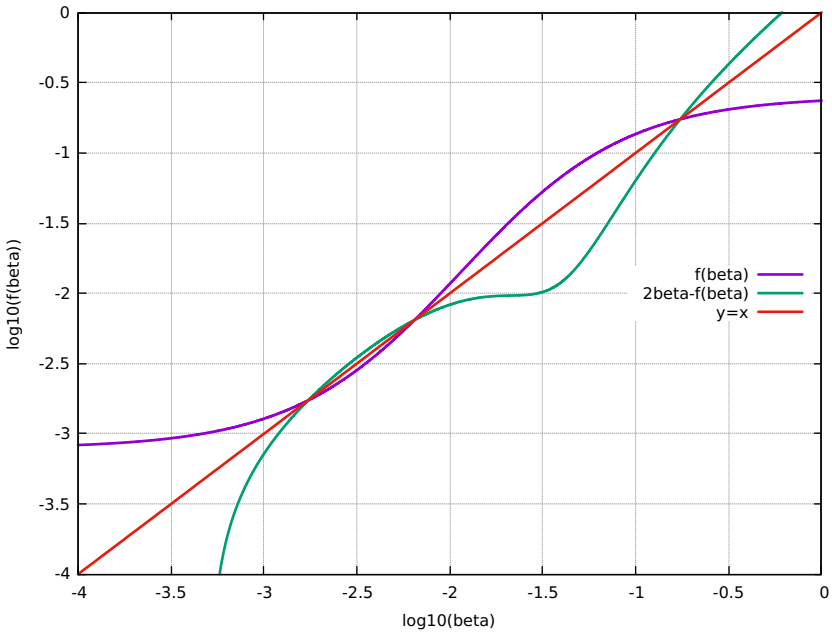

Figure 5.5: Graphical representation of $f_1(\beta) = \beta_{n+1} = 2\beta_n - f(\beta_n)$

$f(\beta)$ which satisfy $f \circ g(\beta) = \beta$. We inverse Eq.(5.36) and we have :

$$g(\beta) = \frac{\frac{1}{\tilde{\alpha}}\left(\frac{1}{(\alpha\beta)^{\frac{1}{n_c}}} - 1\right)\left(\Delta\tilde{\Psi}^c_{A'A} - \frac{\Delta\tilde{\Phi}_{A'A}}{\Delta\tilde{\Phi}_{A'B'}}\Delta\tilde{\Psi}^c_{A'B'}\right) - \left(\Delta\tilde{\Psi}_{AM} - \frac{\Delta\tilde{\Phi}_{AM}}{\Delta\tilde{\Phi}^c_{A'B'}}\Delta\tilde{\Psi}^c_{A'B'}\right)}{\left(\Delta\tilde{\Psi}^e_{AM} - \frac{\Delta\tilde{\Phi}_{AM}}{\Delta\tilde{\Phi}_{A'B'}}\Delta\tilde{\Psi}^e_{A'B'}\right) - \frac{1}{\tilde{\alpha}}\left(\frac{1}{(\alpha\beta)^{\frac{1}{n_c}}} - 1\right)\left(\Delta\tilde{\Psi}^e_{A'A} - \frac{\Delta\tilde{\Phi}_{A'A}}{\Delta\tilde{\Phi}_{A'B'}}\Delta\tilde{\Psi}^e_{A'B'}\right)}. \quad (5.37)$$

This function is plotted in Fig.5.6.

We have checked the efficiency of the fixed point method and we have reproduced the results of the analytical case presented earlier (see Fig.5.9). We have also worked on the optimization of the fixed point. It is presented in Sect.B.

5.3 Tests and validation of the modified DROP code

To verify that our code produces correct simulations and data, two tests have been performed. The first one consists in a simulation of a "false" bipolytrope where $n_c = n_e$ and $\alpha = 1$ which is compared to a single polytrope. We can select any value for $n < 5$ and we take $n = 1.5$. The second one is an attempt to reproduce results presented in Kadam et al. (2016).

5.3.1 The "false" bipolytrope

The "false" bipolytrope is a made up of a core and envelope with the same polytropic index $n_c = n_e = 1.5$ and without jump density at the interface, i.e. $\alpha = 1$. The axis ratio of the envelope is set to 1 so there is no rotation. The density of the polytrope with $n = 1.5$ and the false bipolytrope are plotted in Fig.5.7. The SCF convergence of both are

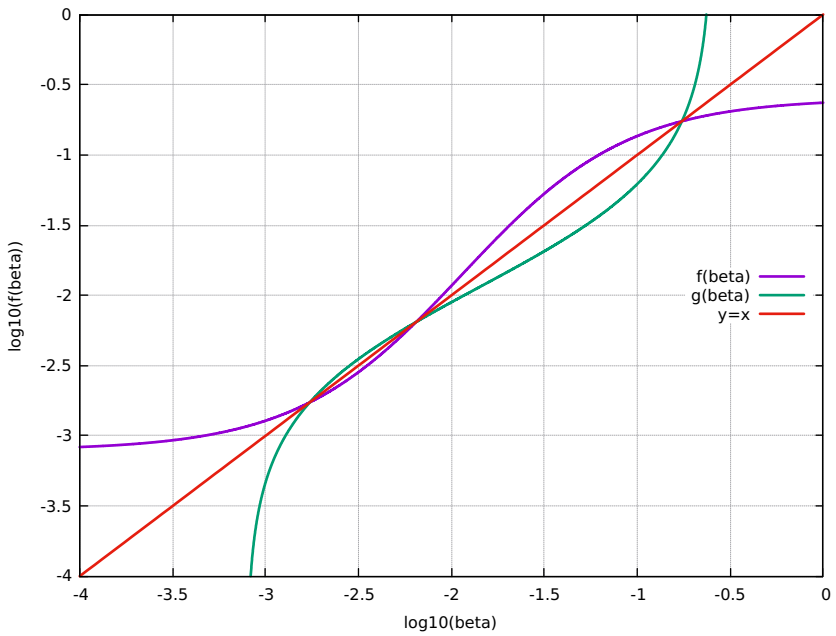

Figure 5.6: représentation graphique de $\beta_{n+1} = g(\beta_n)$

plotted in Fig.5.8. We can see that in both cases, the map densities are almost perfectly identical and that the density is perfectly continious at the core-envelope interface for the bipolytrope. Another similarity is the convergence speed : in both cases, it takes 32 iterations to converge. Output quantities are given in Tab.5.2 and we can see that the typical error is about a few $\sim 10^{-4}$. Other tests has been done successfully for any q ranging from 0 to 1. This first check proves that our algorithm for bipolytropes computes correctly and accuratly equilibrium and does not introduce any strong error on output quantities for any position of the core-envelope interface.

5.3.2 Comparison to Kadam et al. (2016)

the second test concerns the well known results about the SC-like-limit for $n_c = 5$ and $n_e = 1$. We manage to reproduce and improve the results from Kadam et al. (2016) with various axis ratios of the star. We proceed in a different fashion than in this paper : our control parameter is the axis ratio whereas theirs is the density contrast but we still obtain the same results which are plotted in Fig.5.9. We struggle to find accurate equilibrium when $q \to 0$ and $\nu \geq 0$ because the core is small and occupies only a few nodes of the computational grid but its relative mass is not negligible. Error on the boundary of the core produces error on the β which leads to a poor accuracy on the relative mass of the core. This problem can be overcome by using an adaptative mesh.

5.4 Degeneracy in the mass-radius relationship

A prime interest for the study of exoplanetary systems is the chemical composition and the internal structure. To infer such quantities, we basically need two physical properties

	polytrope	Hachisu	false bipolytrope ($\mathcal{L}=2$)		
	($l=\mathcal{L}=1$)	(1986)	core ($l=1$)	envelope ($l=2$)	total
N	129	>128			129
ℓ	7				7
n_l	+1.5000E+00	+1.5000E+00	+1.5000E+00	+1.5000E+00	
$\hat{z}(A_l)$	+1.0000E+00	+1.0000E+00	+6.6667E-01	+1.0000E+00	
q_l	+1.0000E+00	+1.0000E+00	+6.6667E-01	+3.3333E-01	
$\alpha_l(\mathrm{A}_l)$				+1.0000E+00	
ω_l				+1.0000E+00	
SCF-iterations	29				29
$\hat{H}_l(\mathrm{A}_l)$	+0.0000E+00		+3.3798E-01	+1.0000E+00	
$\beta_l^\dagger$			+1.0000E+00	+1.9649E-01	
Q_l		+1.0000E+00	+6.6666E-01	+3.3334E-01	
nodes Γ_l	251		167	251	
$\hat{V}_l$	+4.1883E+00	+4.17E+00	+1.2407E+00	+2.9482E+00	+4.1890E+00
$\hat{M}_l$	+6.9919E-01	+6.99E-01	+5.3071E-01	+8.5843E-01	+6.9938E-01
C_{1l}	+9.4134E-01		+9.4136E-01	+1.6192E+00	
C_{2l}	+3.3196E-06		-1.2064E-04	-6.1399E-04	
C_{3l}	-6.9920E-01		-6.9934E-01	-3.5592E+00	
ν_l	+1.0000E+00		+7.5883E-01	+2.4117E-01	
J_l	+2.6064E-04	+0.00E+00	+8.3701E-04	+3.7415E-03	+1.5722E-03
$\hat{T}_l$	+2.3744E-07	+0.00E+00	-4.5967E-06	-1.0457E-04	-8.6340E-06
$\hat{W}_l$	-4.1904E-01	-4.19E-01	-3.4269E-01	-1.9815E+00	-4.1919E-01
$\hat{U}_l$	+4.1906E-01	-4.19E-01	+3.7708E-01	+1.0891E+00	+4.1913E-01
VP	+1.5278E-05				-7.8934E-05
VT	+3.6460E-05	< +1.E-03			-1.8830E-04

Table 5.2: Input (top) and output (bottom) quantities for the false non-rotating bipolytrope in the conditions of Fig. 5.7, but for $\ell = 7$. The core-envelope interface is located at $q = \frac{2}{3}$. There is no jump condition (i.e. $\alpha = 1$). The results obtained in the same conditions for the polytrope are given in the second column.

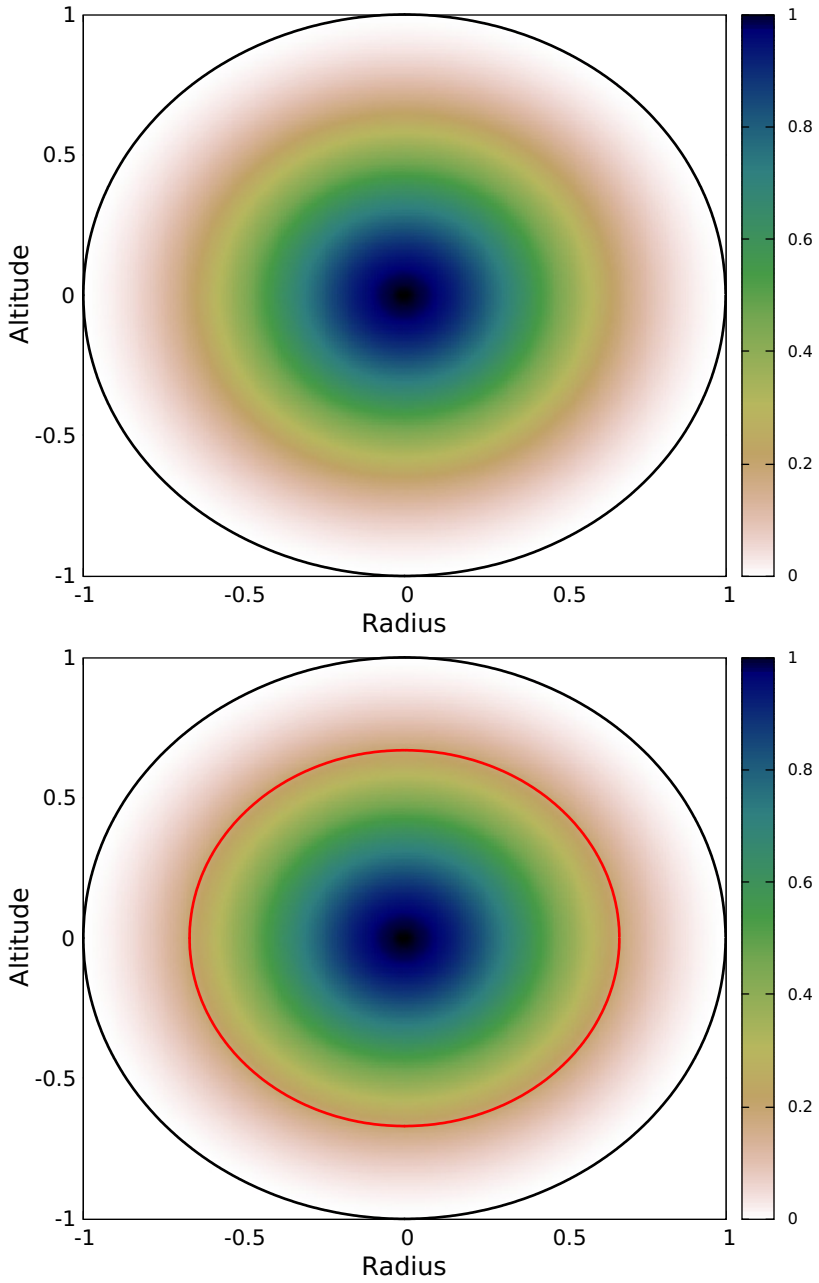

Figure 5.7: (top) : Density map of a non-rotating single-layered polytrope with $n = 1.5$ *(bottom) : Density map of a non-rotating bipolytrope with* $n_c = n_e = 1.5$, $\alpha = 1$ *and* $q = 0.66$. *The black line is the fluid boundary and the red line is the core-envelope interface.*

: the radius and the mass of the planet. We then derived other properties using models. One strong assumption is that one set of mass-radius is linked only to a a few chemical compositions, internal structures and other properties whereas in fact there are a high number, if not infinite number, of internal structures that lead to the same mass-radius set.

For instance, we only know so little about Jupiter's interior that there is no certainty on its internal structure. Regarding the hypothesis we do (i.e. the equation-of-state,

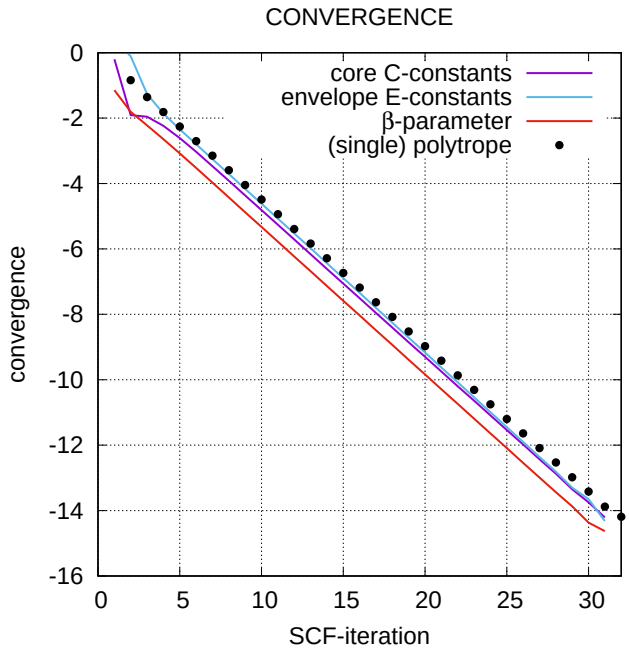

Figure 5.8: Convergence of the SCF constants in the case of a single polytrope and a bipolytrope.

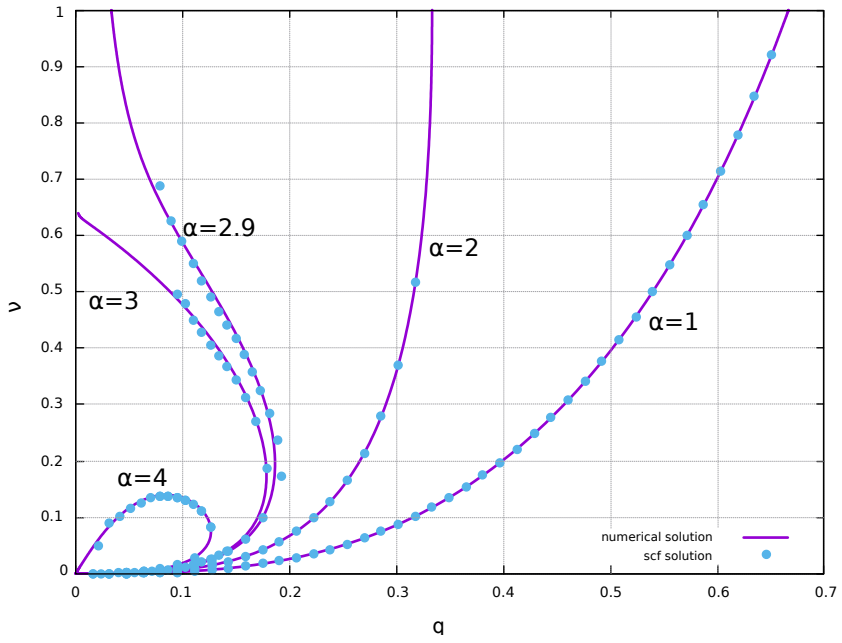

Figure 5.9: Plot of the relative mass of the core ν as a function of the relative radius of the core q for a non-rotating bipolytrope where $n_c = 5$, $n_e = 1$ and various value of density jump α. Straight lines are reference solutions. Dots are solutions found with the DROP-code.

.

the heavy element distribution, the separation between layers), the internal structure of Jupiter is highly changed (Miguel et al., 2016; Vazan et al., 2016; Smoluchowski, 1967). It is even more difficult to contraint internal structure of hot Jupiters since we have even less information on those (Komacek and Youdin, 2017). Another planet from our solar

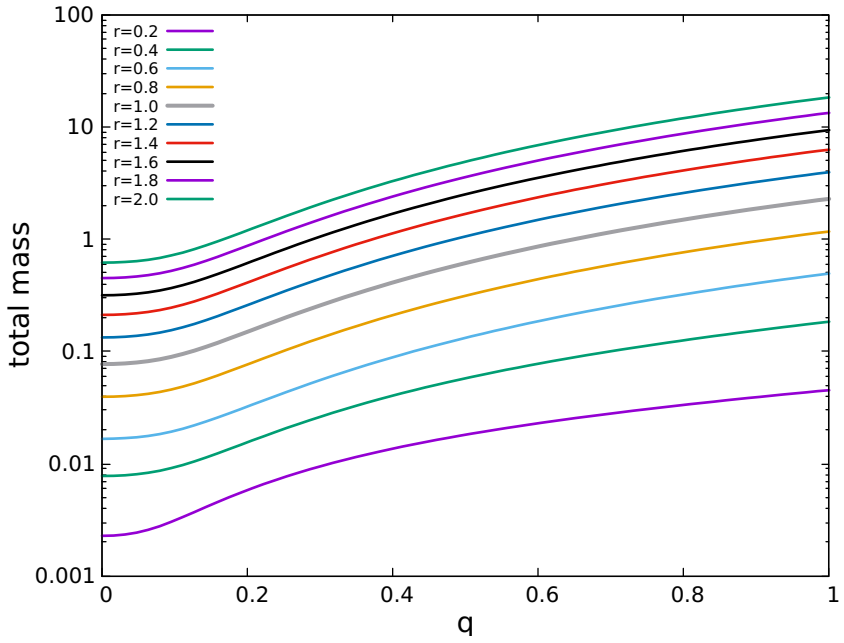

Figure 5.10: Total mass of the bipolytrope as a function of the relative radius of the core q for a non-rotating bipolytrope with $n_c = 0.5$, $n_e = 3$, $\alpha = 1$ and $e_e = 1$ for various value of the external radius r_s

system that is quite shy about giving information on its internal structure is Saturn.

With our bipolytropic model, we reproduced such degeneracy in the mass-radius-internal structure relationship by using various core radius q, external radius r_s, axis ratio of the envelope e_e, density jump α, polytropic index of the core n_c and polytropic index of the envelope n_e.

5.4.1 Effect of the external radius r_s

We produced several sequences by varying $q \in [0, 1]$ for some value of the external radius $r_s = 0.1, 0.4, 0.6, 0.8, 1.0, 1.2, 1.4, 1.6, 1.8, 2.0$. For those sequences, we set the density jump α to 1, the polytropic index of the core n_c to 0.5 and polytropic index of the envelope n_e to 3. Those sequences are shown in Fig.5.10. We can see that for a given value of r_s, the total mass of the star increases when q increases because the density in the envelope is steeper than in the core and as a result, the bigger the core is, the more matter there is.

It is striking that the same total mass can be obtain by different internal configuration and star size. For instance, a star with a total mass of 0.1 could be :

- a body with a $q = 0.1$ and a $r_s = 1$
- or a body with a $q = 0.3$ and a $r_s = 0.8$
- or body with a $q = 0.8$ and a $r_s = 0.6$

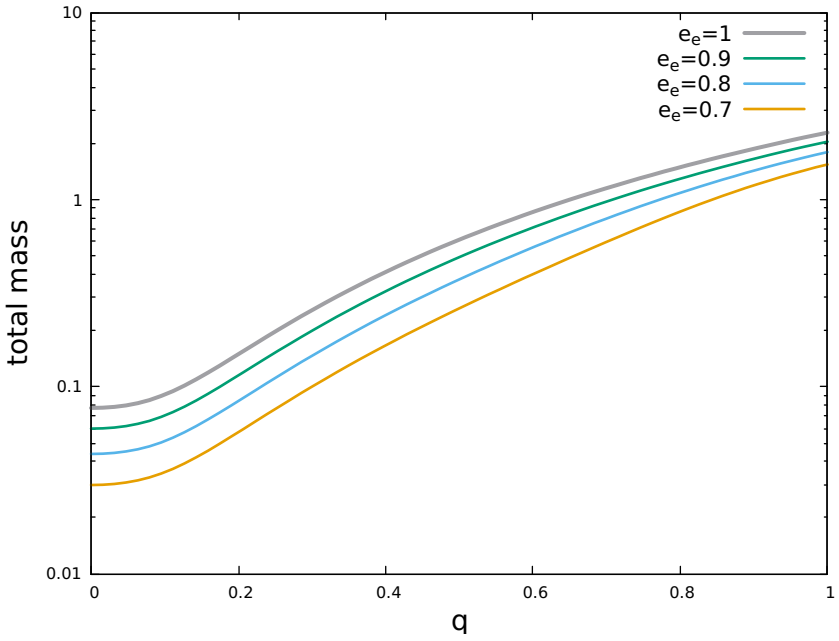

Figure 5.11: Total mass of the bipolytrope as a function of the relative radius of the core q for a rotating bipolytrope where $n_c = 0.5$,$n_e = 3$, $\alpha = 1$ and $r_s = 1$ for various value of the axis ratio e_e

5.4.2 Effect of the axis ratio of the envelope e_e

We can study the effect of the rotation on the total mass of a body by varying the axis ratio e. The lower the axis ratio, the faster the body spins. Sequences are made for $e_e = 1.0, 0.9, 0.8, 0.7$, an external radius r_s of 1, a density jump α of 1, a polytropic index of the core n_c of 0.5 and a polytropic index of the envelope n_e of 3. Results are shown in Fig.5.4.2. We can see that the slower the rotation, the higher the total mass. For a given external radius r_s, the more the body is flattened, the less volume it occupies and thus the lower the total mass is.

As for the previous section, we can see that several axis ratio e_e can lead to the same total mass. Lets take again a star with a total mass of 0.1, that can be achieved by taking :

- a body with a $q = 0.1$ and a $e_e = 1$
- or a body with a $q = 0.2$ and a $e_e = 0.9$
- or body with a $q = 0.25$ and a $e_e = 0.8$
- or body with a $q = 0.35$ and a $e_e = 0.7$

5.4.3 Effect of the density jump α

Another degeneracy in the mass-relationship radius can be brought by the density jump α between the core and the envelope. Sequences are made for various values of α =

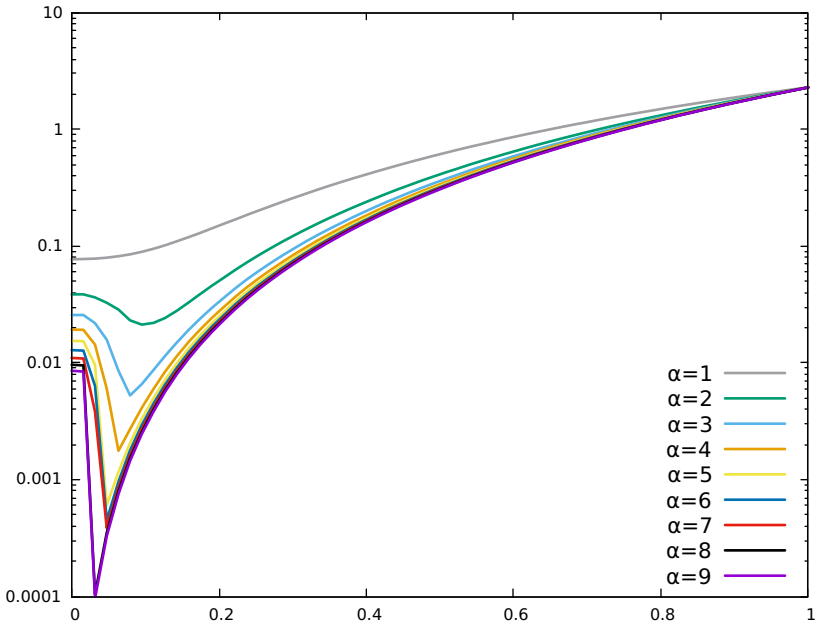

Figure 5.12: Plot of the total mass of the bipolytrope as a function of the relative radius of the core q for a rotating bipolytrope where $n_c = 0.5$,$n_e = 3$, $e_e = 1$ and r_s for various value of density jump α

$1, 2, 3, 4, 5, 6, 7, 8, 9$, an external radius r_s of 1, a polytropic index of the core n_c of 0.5 and a polytropic index of the envelope n_e of 3 and an axis ratio e_e of 1. Results are shown in Fig.5.12 We can see that the higher the density jump is, the lower the total mass is.

Once again, the same total mass can be achieved through different values of α. However, depending on the value of q, the difference brought by the change in α is not the same. If we take the case of the Earth with a massive and large core with a thin and low mass atmosphere, i.e. $q \sim 1$, the effect of a change in α is negligeable. A mass of 0.1 can be obtain with :

- a body with a $q = 0.1$ and a $\alpha = 1$
- or a body with a $q = 0.35$ and a $\alpha = 2$
- or body with a $q = 0.4$ and a $\alpha = 8$

5.4.4 Effect of the polytropic index of the core n_c and the envelope n_e

The equation-of-state of both layer also has a significant effect on the total mass of a body. Starting of with the EOS of the core, which means different n_c, sequences are generated for $n_c = 0., 0.5, 1., 1.5, 2., 2.5, 3., 3.5, 4., 4.5$, an external radius r_s of 1, a density jump α of 1, an axis ratio e_e of 1 and a polytropic index of the envelope n_e of 3.0 Results are shown on the *top* panel of Fig.5.13.

Finally, we study the effect of the EOS of the envelope. We generate sequences for $n_e = 0., 0.5, 1., 1.5, 2., 2.5, 3., 3.5, 4., 4.5$, an external radius r_s of 1, a density jump α of 1,

an axis ratio e_e of 1 and a polytropic index of the core n_c of 0.5. Results are shown on the *bottom* panel of Fig.5.13

We see that a mass of 0.1 can be obtain with :

- a body with a $q = 0.1$ and a $n_c = 0$
- or a body with a $q = 0.2$ and a $n_c = 1.5$
- or body with a $q = 0.35$ and a $n_c = 2.5$

or with :

- a body with a $q = 0.12$ and a $n_c = 3$
- or a body with a $q = 0.2$ and a $n_c = 4.0$
- or body with a $q = 0.25$ and a $n_c = 5.0$

5.4.5 Discussion

We cannot easily probe the internal structure of planets, almost all planets but Earth. As a consequence, their internal structure are highly uncertain and are mostly based on models. And as we saw, a small change in the problem can produce huge differences in the result. A numerous number of sets of paramaters like the EOS of each layer, the density jump between layers, the radius of the planet and its rotation rate can lead to the same mass. As a consequence, the sole knowledge of the mass-radius relationsip of a planet is not enough to know anything about it. We need to have more information than only those two properties. In the case of Jupiter and Saturn, we have access to a key measure which are the mass, central density, rotation rate and gravitational moments $J_{2n,n\geq 1}$ of the planets (Guillot, 1999; Guillot et al., 2004; Kong et al., 2016; Mankovich and Fortney, 2020; Buccino et al., 2020). The gravitational moments arise from the multipole expansion of the potential and are directly linked to the distribution of matter and not only to the mass of the planet. By having access to these moments and other properties such as the mass, the volume, the average density, the core density, the rotation velocity, we can start to constraint models of internal structure and dissociate configurations of same mass and same radius (see Sect.5.8).

5.5 Rotational discontinuity, $\omega_{ec} \neq 1$

The rotational discontinuity at the core/envelope interface is governed by the ω_{ec}-parameter. By setting $\omega_{ec} \neq 1$ in the equation set, the discontinuity is switched on. Two different situations are interesting to discuss : i) $n_e = n_c$ and ii) $n_e \neq n_c$. According to the previous discussion (see Sect. 5.2.2), a constant mass-density jump is expected in the first case, but not in the second one. Figure 5.14 shows the shape of the core and the shape of the envelope obtained for $\omega_{ec} = 2$ when the two layers have the same polytopic index. The mass-density jump is $\alpha = 4$ all along Γ_c. The equilibrium quantities computed for $\ell = 7$ are listed in Tab. A.2 (see Tab. A.1 for $\omega_{ec} = 1$). As expected, the oblateness of a core

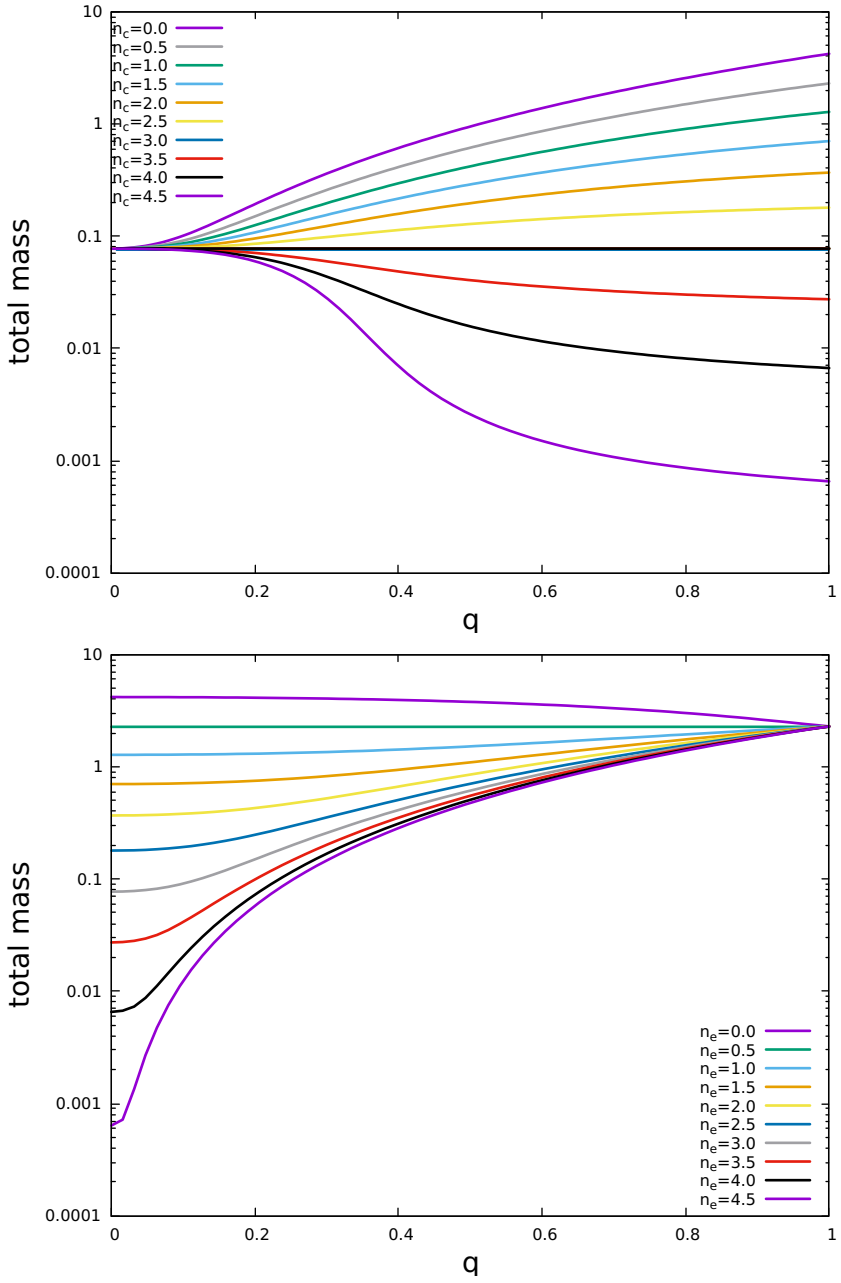

Figure 5.13: top panel : Total mass of the bipolytrope as a function of the relative radius of the core q for a rotating bipolytrope where $n_e = 3$, $\alpha = 1$, $e_e = 1$ and $r_s = 1$ for various value of the polytropic index of the core n_c.
bottom panel : Total mass of the bipolytrope as a function of the relative radius of the core q for a rotating bipolytrope where $n_c = 0.5$, $\alpha = 1$, $e_e = 1$ and $r_s = 1$ for various value of the polytropic index of the envelope n_e.

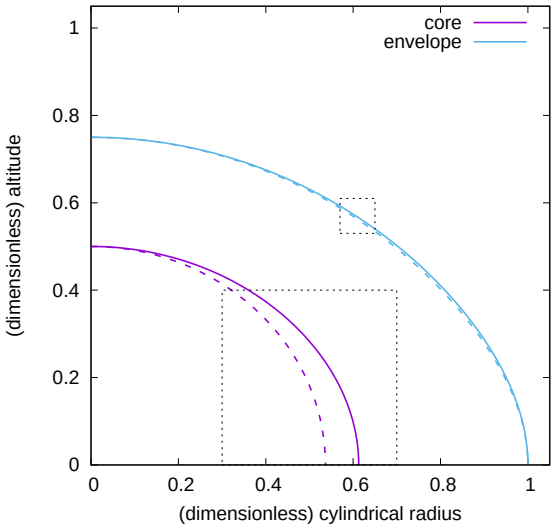

Figure 5.14: Effect of a rotational discontinuity at Γ_c on the core and on the envelope for the rotating bipolytrope with axis ratio $e_e = 0.75$, $q_Z = \frac{2}{3}$, mass-density jump $\alpha_2(\Gamma_1) = 4$. The polytropic index is the same for both layers, namely $n_c = n_e = 1.5$. Both layers are rigidly rotating : $\omega_{ec} = 1$ corresponds to the same rotation rate (dashed lines), and $\omega_{ec} = 2$ is for a core spinning ~ 1.41 times faster than the envelope (plain lines). See also Fig. 5.15 for a zoom.

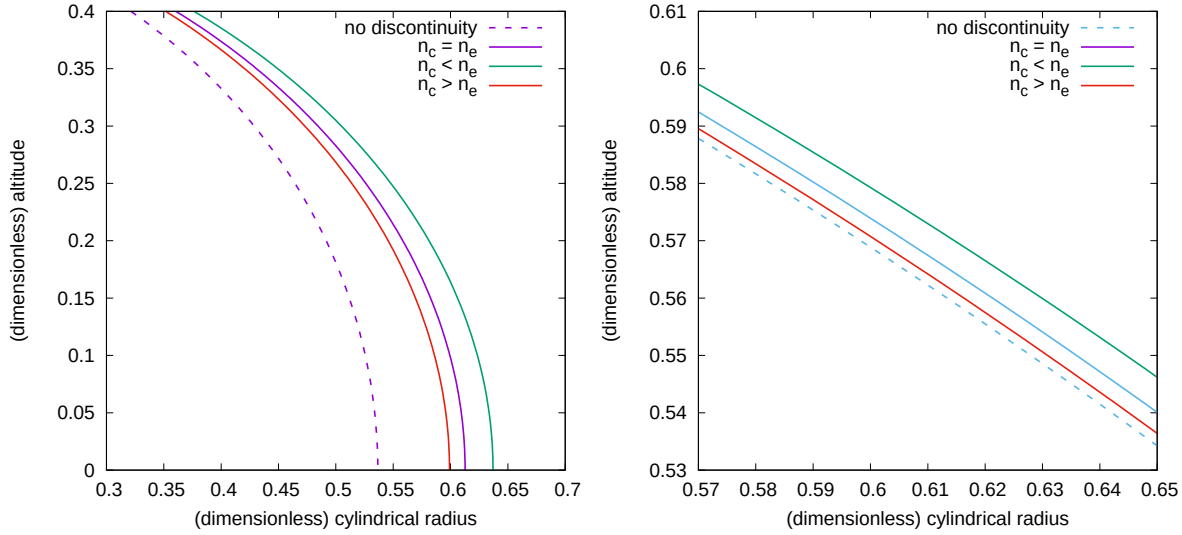

Figure 5.15: Effect of a rotational discontinuity $\omega_{ec} = 2$ on the interfaces Γ_c (top panel) and Γ_e (bottom panel) for the rotating biplytrope with axis ratio $e_e = 0.75$, $q_Z = \frac{2}{3}$ and mass-density jump $\alpha(\mathrm{A}') = 4$ for three different pairs (n_c, n_e) of polytropic indices : $(1.5, 1.5)$ (purple), $(1, 2)$ (green) and $(2, 1)$ (red). The case without rotational discontinuity (i.e. full rigid rotation with $\omega_{ec} = 1$), is given for comparison (dashed lines); see also Fig. 5.14.

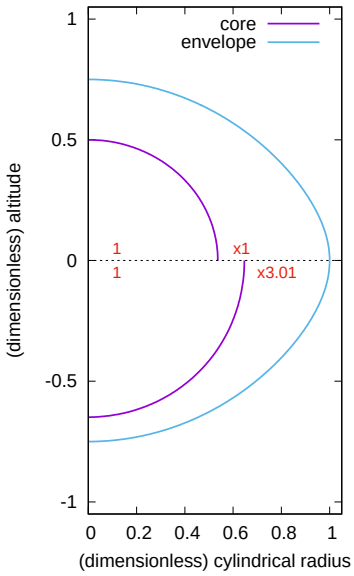

Figure 5.17: Configuration for two different bipolytropic configurations sharing the same size, surface velocity and total mass (and degeneracy parameter Ξ). Input parameters are from Tabs. A.1 (top) and A.5 (bottom). Each layer is in rigid rotation. Labels (red) corresponds to the rotation rate of the envelope relative to the core, i.e. $\frac{1}{\sqrt{\omega_{ec}}}$. The shape of the envelope is almost unchanged, in contrast with to the core.

that spins faster than the envelope increases (we find $e_c \sim 0.816$). The density contrast slightly increases, the core is more massive, in contrast with the envelope which is less massive. As a consequence, the total mass is increased with respect to the case without rotational discontinuity. We see that the total volume is slightly increased. The shape of the envelope is still sub-elliptical (see above).

The results obtained in the same conditions as above but for the new sets of polytropic indices $(n_c, n_e) = (1, 2)$ and $(n_c, n_e) = (2, 1)$ are listed in Tabs. A.3 and A.4 respectively. The differences between the configuration are important, while the changes in the shapes for the core and for the envelope are much less pronounced. Figure 5.15 displays the core/envelope interface zoomed about the point B_2 at the equator, and the fluid boundary zoomed at about 45° off the equatorial axis. We see that the volume (and the axis ratio) of the core is smaller when $n_c > n_e$. Because the β-parameter increases (by a factor ~ 3 typically with respect to the case with $n_c = n_e$), the mass of the configuration increases by a factor ~ 1.8, and the core rotates faster since the coefficient c_2^c increases by a factor ~ 1.7. Figure 5.16 displays $\alpha(\Gamma_c)$. We see that the mass density jump is not uniform along Γ_c, as predicted (see Sec. 5.2.2). Its value is set to 4 just on the polar axis, and decreases monotonically down to about 3.6 at the equatorial plane. The reverse situation is observed when $n_c < n_e$.

5.5.1 An example of degenerate configurations. Degeneracy parameter

An interesting question concerns the existence of degenerate states, i.e. configurations having different internal structure but sharing a few global quantities. This can be sus-

pected as soon as the number of free parameters is "sufficient". From an observational point of view, the quantities of prime importance are the equatorial radius, eventually the axis ratio (i.e. the polar radius), and the rotation velocity V, which is traditionnaly inferred from Doppler shifts. In the physical space, we have :

$$\begin{cases} R_{\rm eq.} = \hat{R}(\mathrm{B}_2) \times L \\ R_{\rm pol.} = e_e \hat{R}(\mathrm{B}_2) \times L \\ V_{\rm eq}^2(\mathrm{B}_2) = C_2^e \times G\rho_0^c L^2, \end{cases} \tag{5.38}$$

where $V_{\rm eq} = V(\mathrm{B}_2)$. So, two different configurations that share the same values for $R_{\rm eq}$, $R_{\rm pol}$ and $V_{\rm eq}(\mathrm{B}_2)$ are undistinguable for an observer measuring the size, shape and the equatorial velocity. In the present problem, it is easy to find such 2-layer configurations since we have 6 input parameters. An even more stricking situation arises if we also consider the mass $M_{\rm tot.} = \hat{M}_{\rm tot.} \times \rho_{10} L^3$ of the system. It turns out that two bipolytropic configurations having the same value for :

$$\frac{C_2^e \beta}{\hat{M}_{\rm tot.}} \equiv \Xi, \tag{5.39}$$

are totally undistinguishable from each other not only in size and velocity, but would also in mass, in spite of different internal structures (and different central densities ρ_0^c). Finding sets of parameters realizing such a degeneracy is less trivial. An example is shown in Fig. 5.17 where we have plotted the interfaces obtained for the parameter set listed in Tab. A.5. For this new configuration, the EOS for the core is close to incompressibility, and the EOS for the envelope could correspond to a radiation pressure dominated zone. The degeneracy parameter is $\Xi \approx 0.6419$, which is the same value as for the configuration obtained for the input parametres of Tab. A.1. The two solutions differ by values for ω_{ec}, q_Z, α and n_c. The internal structures are, however, very different, with, for instance, a factor ~ 5.16 between central densities. The mass density jump is larger, while the envelope, which rotates about 3 times faster, has almost the same shape. Note that the core is, again, very close to spherical.

5.6 Effect of the rotation on the SC-like-limit

Maeder (1971) first studied the effect of the rotation on the SC-limit through first order pertubation in the case of an isothermal core, $n_c = \infty$, and a radiative envelope, $n_e = 3$. He found that, depending on the rotation law, the SC-limit could decrease or increase. In the case of a solid rotation, the SC-limit undergoes a 3% reduction. Kadam et al. (2016) studied the impact of rotation on the SC-like-limit when $n_c = 5$, $n_e = 1$ and $\alpha = 4$ with the SCF method in the case of solid rotation and found the same trend but adressed an issue regarding the magnitude of the SC-like-limit reduction. In fact, the reduction due to rotation is far more important than firstly demonstrated by Maeder (1971) by typically an order of magnitude. For high rotation rate, the reduction is about $\sim 25\%$.

Due to the rotation, the point reflection is not longer valid and there is no reason for the core radius fraction along the R-axis q_R to be the same as along Z-axis q_Z. These two core radius fraction are defined as :

$$q_R = \frac{OB}{OB'} \tag{5.40}$$

$$q_Z = \frac{OA}{OA'} \tag{5.41}$$

5.6.1 Solid rotation

We generated $q_R - \nu$ and $q_Z - \nu$ diagrams for various axis ratio of the spheroid ranging from $e_e = 1$ (no rotation) to $e_e = 0.6$. The results are shown in Fig.5.18. Since there is two possible values of q_R and q_Z for a given value of ν and two possible values of ν for a given value of q_R or q_Z, it can be handy to plot properties of the bipolytrope as a function of a monotonous parameter. One parameter fulfilling this condition is the β parameter. We also show q_R and ν as function of the β parameter in Fig.5.19 along with some snapshots of equilibrium for $e_e = 0.6$ in Fig.5.20.

We can see that the SC-like-limit decreases when the rotation increases which means that a two-layer rotating star has a smaller lifespan than a non-rotating one because its core is not able to expand as much as it can when not rotating. It is expected to precipitate the evolution of a main sequence star into a red giant.

One should note that far from the critical rotation (i.e. axis ratio ≥ 0.70), the $q_R - \nu$ curve for a given axis ratio can be given by an homothetie from the $q - \nu$ curve without rotation following the equation :

$$q_{Re} = q_1 \cdot e_e^{\frac{2}{3}} \tag{5.42}$$

$$\nu_e = \nu_1 \cdot e_e^{\frac{2}{3}} \tag{5.43}$$

For an axis ratio of 0.6, the numerical results start to diverge from this empirical law because we are close to a critical rotation. We see it with the beak property in Fig.5.20 (*bottom left*). This behavior is the same as in the one-layered compressible case, see Sect.3.3). As a consequence, the mass of the envelope is vanishing and, therefore, the contribution of the mass core to the total mass of the star is greater resulting in a ν value higher than expected. This behaviour was not reported by Kadam et al. (2016). One eventuality is that the difference in the treatment of the discontinuity at the interface is responsible for that deviation.

We can see that the q_R as a tendency to be smaller with rotation whereas q_Z is greater with rotation. Another feature of interest is that the core gets more spherical as β decreases (see Fig.5.20 *bottom right*). It means that the less massive the envelope, the lower pressure on the core. Overall, the core is not drastically under the influence of the envelope's rotation.

5.6.2 The v-constant rotation law

Following Maeder (1971) results on differentially rotating bipolytrope, we have computed the equilibrium with the same configuration as in 5.6.1 but changing the solid rotation law to a v-constant law. Results are shown in Fig.5.21 along with snapshots of equilibrium for $e = 0.6$ in Fig5.22.

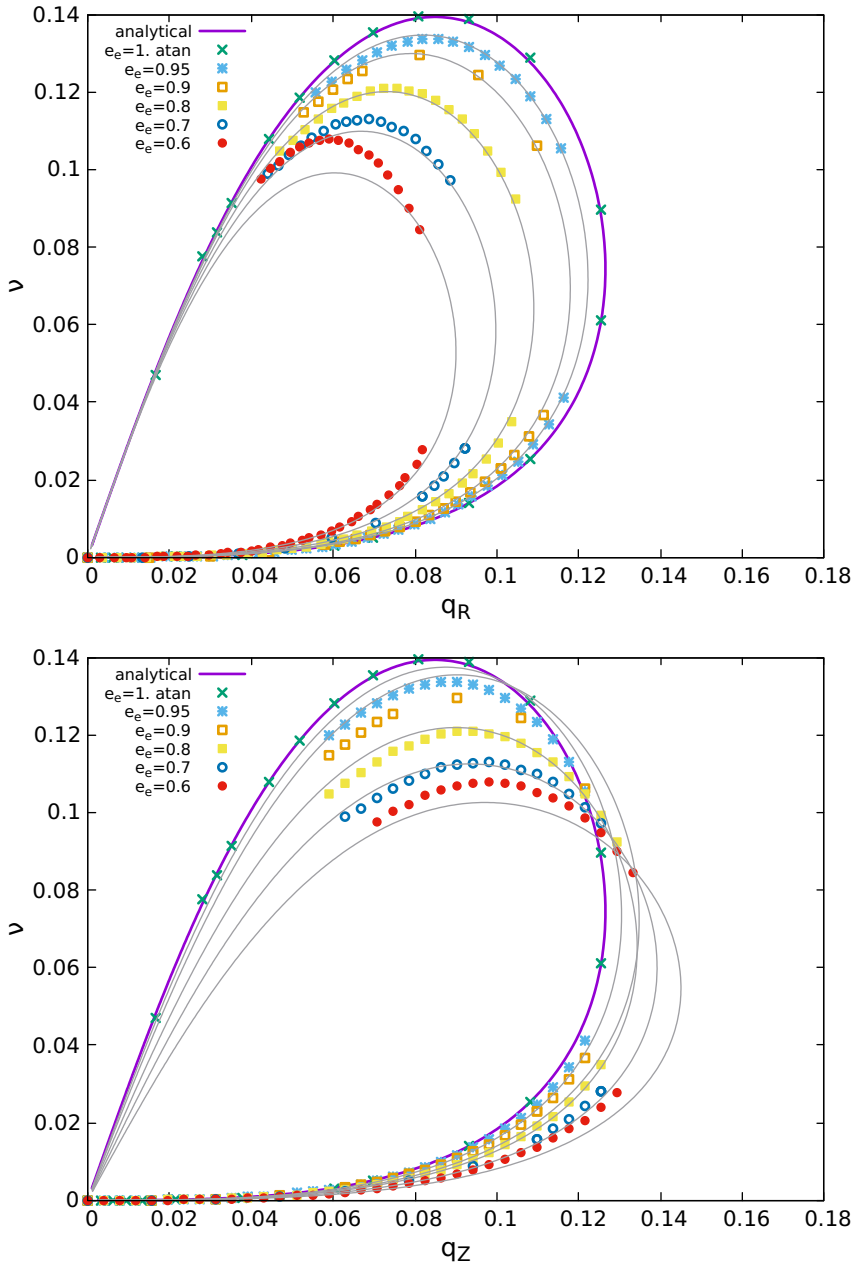

Figure 5.18: Plot of the relative mass of the core ν as a function of : (top) the relative radius of the core along the R-axis q_R and (bottom) the relative radius of the core along the Z-axis q_Z for a solidly rotating bipolytrope where $n_c = 5$,$n_e = 1$ and $\alpha = 4$. The purple straight line is the analytical solution. The green crosses denotes solution without rotation with an arctan *meshing. The grey straight lines are projected solutions for a given axis ratio by homothetie from the analytical solution. Dots are solutions found with the DROP-code.*

The effects of a v-constant rotation law is quite similar to the solid rotation cases for low rotation rates : q_R decreases, q_Z increases and ν decreases. For low rotation rates, there is no big difference in the shape of the core and the enveloppe, hence no big difference in the results. However, for moderate to high rotation rate (i.e. $e \leq 0.80$), differences

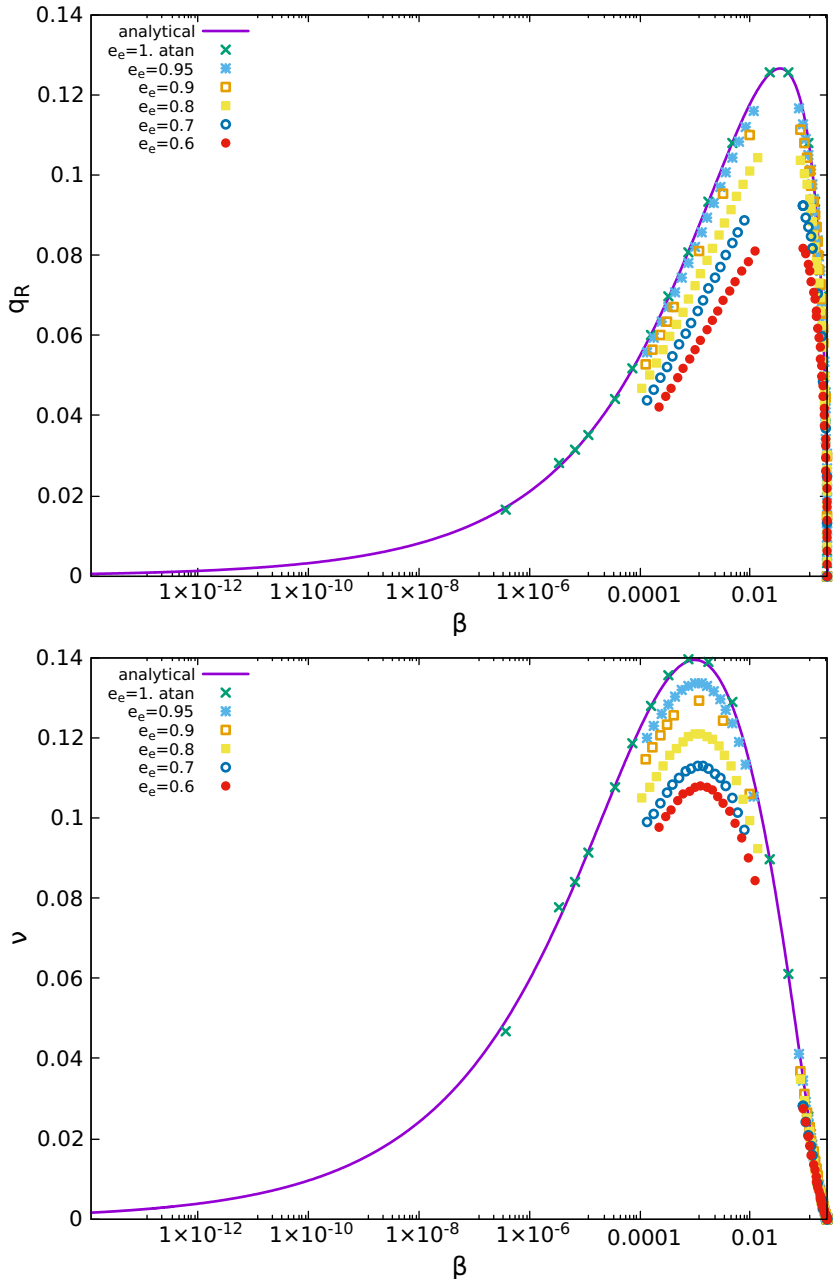

Figure 5.19: (top) : Relative core radius along the R-axis q_R as a function of the β parameter. (bottom) : Relative mass of the core ν as a function of the β parameter for a solidly rotating bipolytrope where $n_c = 5$,$n_e = 1$ and $\alpha = 4$ and varius axis ratio of the envelope e_e. The purple straight line is the analytical solution. The green crosses denotes solution without rotation with an arctan *meshing. Dots are solutions found with the DROP-code.*

start to appear. For starters, for small q_Z, the associated q_R rapidly grows altering the shape of the $q_R - \nu$ diagram. As shown in Fig.5.22 (*top left*), the smallest core possible (smallest q_Z, one node on the Z-axis), at a resolution of l=8, is already quite large resulting in a higher ν than for the solid rotation. With an infinite resolution, we would observe a continuous evolution of all the quantities mentionned above. An interesting feature of

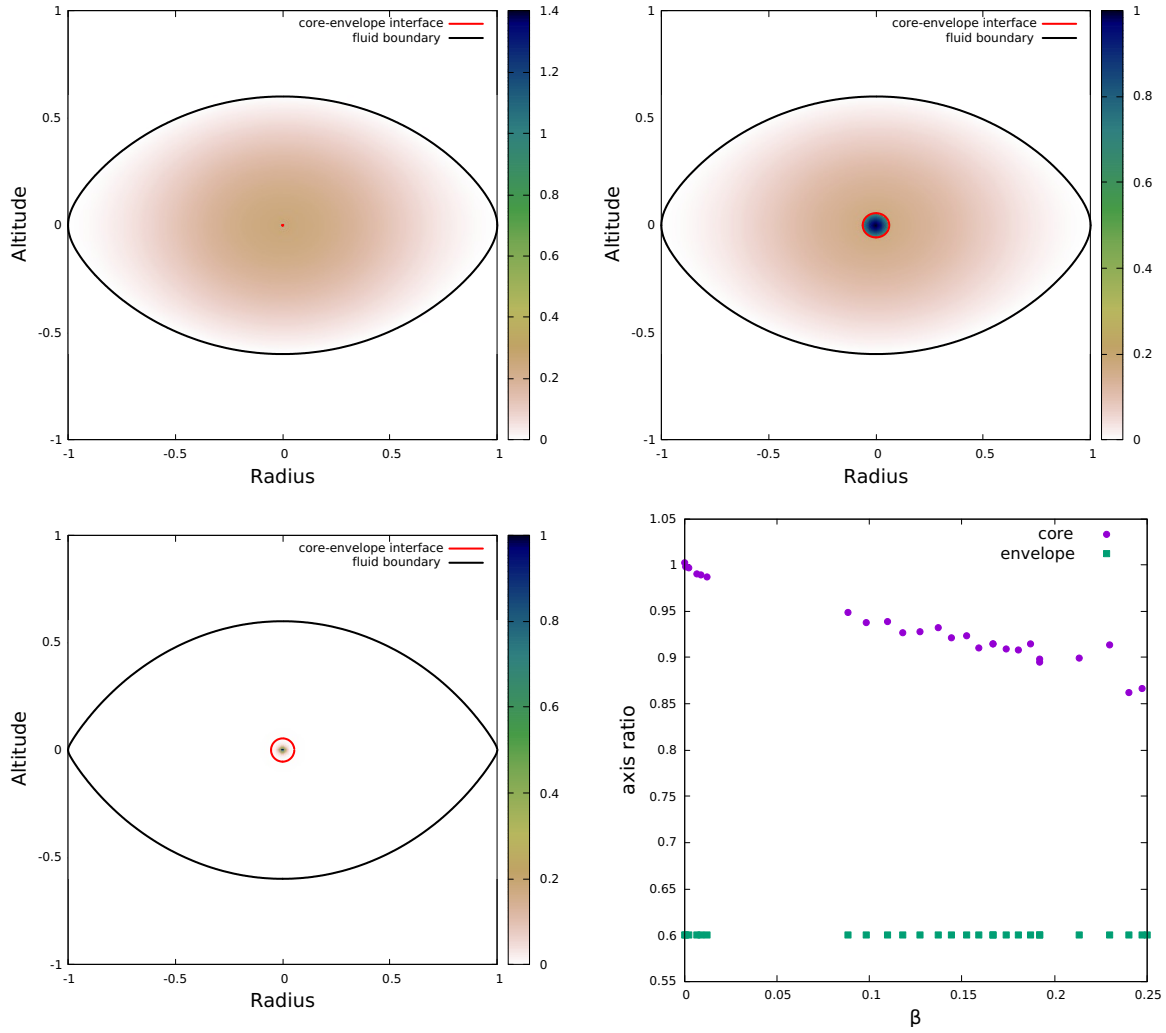

Figure 5.20: Density profile and axis ratios of the core and envelope of a solidly rotating bipolytrope with $n_c = 5$,$n_e = 1$,$\alpha = 4$ and $e_e = 0.6$.
(top left) : density for the smallest core possible at the given resolution (here l=8). (top right) : density for a core where $q_Z = 0.08$ and $\beta = 0.190$, low solution in the $q - \nu$ diagram. (bottom left) : density for a core where $q_Z = 0.08$ and $\beta = 4.34e - 4$, high solution in the $q - \nu$ diagram. (bottom right) : axis ratios of the core and the envelope as a function of β.

this small core configuration is that the core is close to be a torus. One could imagine a scenario where, when a protostar forms, its core is not a spheroid but, with all the rotation rate and angular momentum acquired, is instead a torus. It could a possible way of forming multiple star system since as we know, tori can be unstable and shatters.

We observe the same trend as for the solid rotation : the core gets rounder when β drops. However, for an axis ratio equals to 0.6, we do not observe a critical rotation with a v-constant law. As for single polytrope, a change in the rotation law produces also changes in the behavior of equilibrium : the critical rotation might appear at lower axis ratio with a v-constant rotation. We are in the process of investigating equilibrium with axis ratios equal to 0.5 and lower.

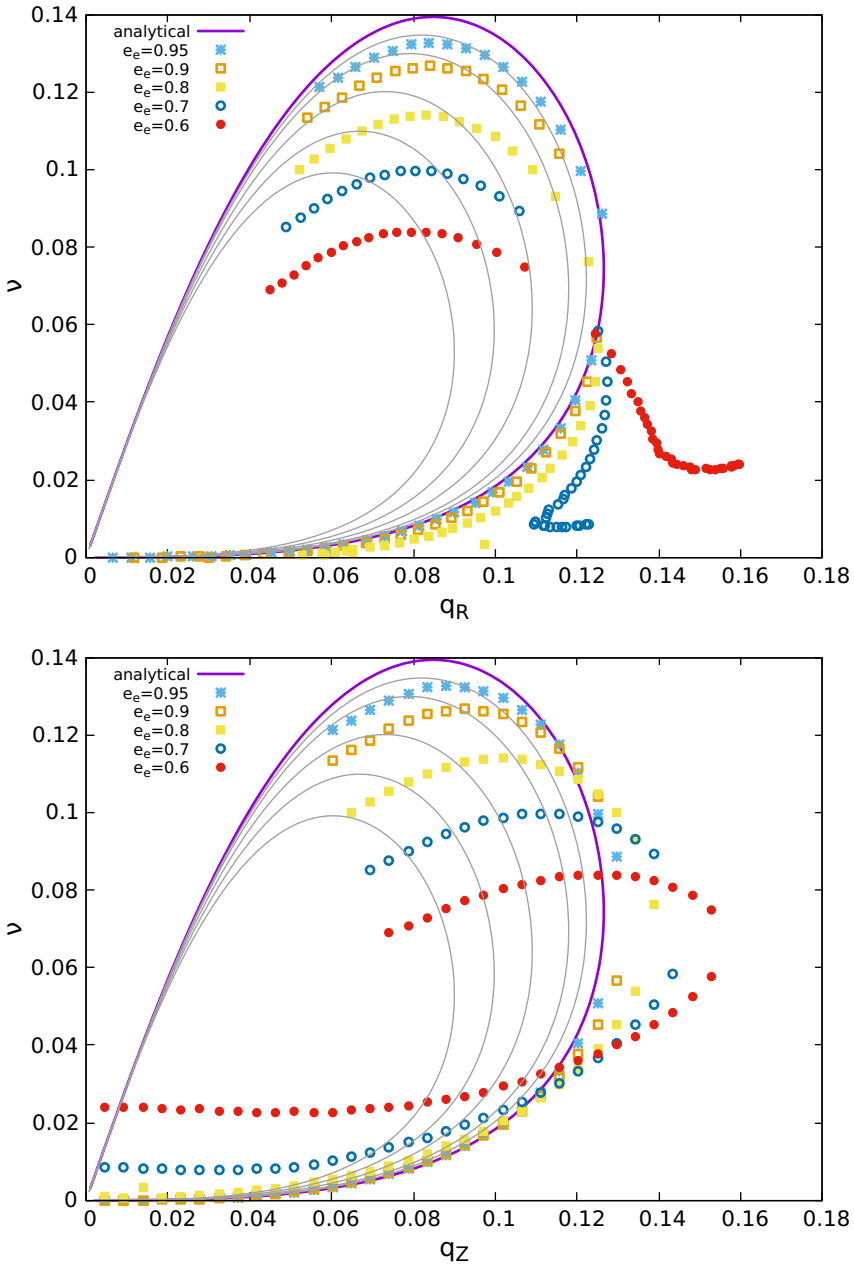

Figure 5.21: Relative mass of the core ν as a function of : (top) the relative radius of the core along the R-axis q_R and (bottom) the relative radius of the core along the Z-axis q_Z for a differentially rotating bipolytrope with a $v-$ constant rotation law where $n_c = 5$,$n_e = 1$ and $\alpha = 4$. The purple straight line is the analytical solution.The grey straight lines are projected solutions for a given axis ratio by homothetie from the analytical solution. Dots are solutions found with the DROP-code.

5.6.3 The j-constant rotation law

We also have considered the effect of a j- constant rotation law on a SC-like-limit. Equilibria were again computed in the same configuration as in 5.6.1. The results are shown in Fig.5.23 and are still under investigation for moderate to low axis ratio.

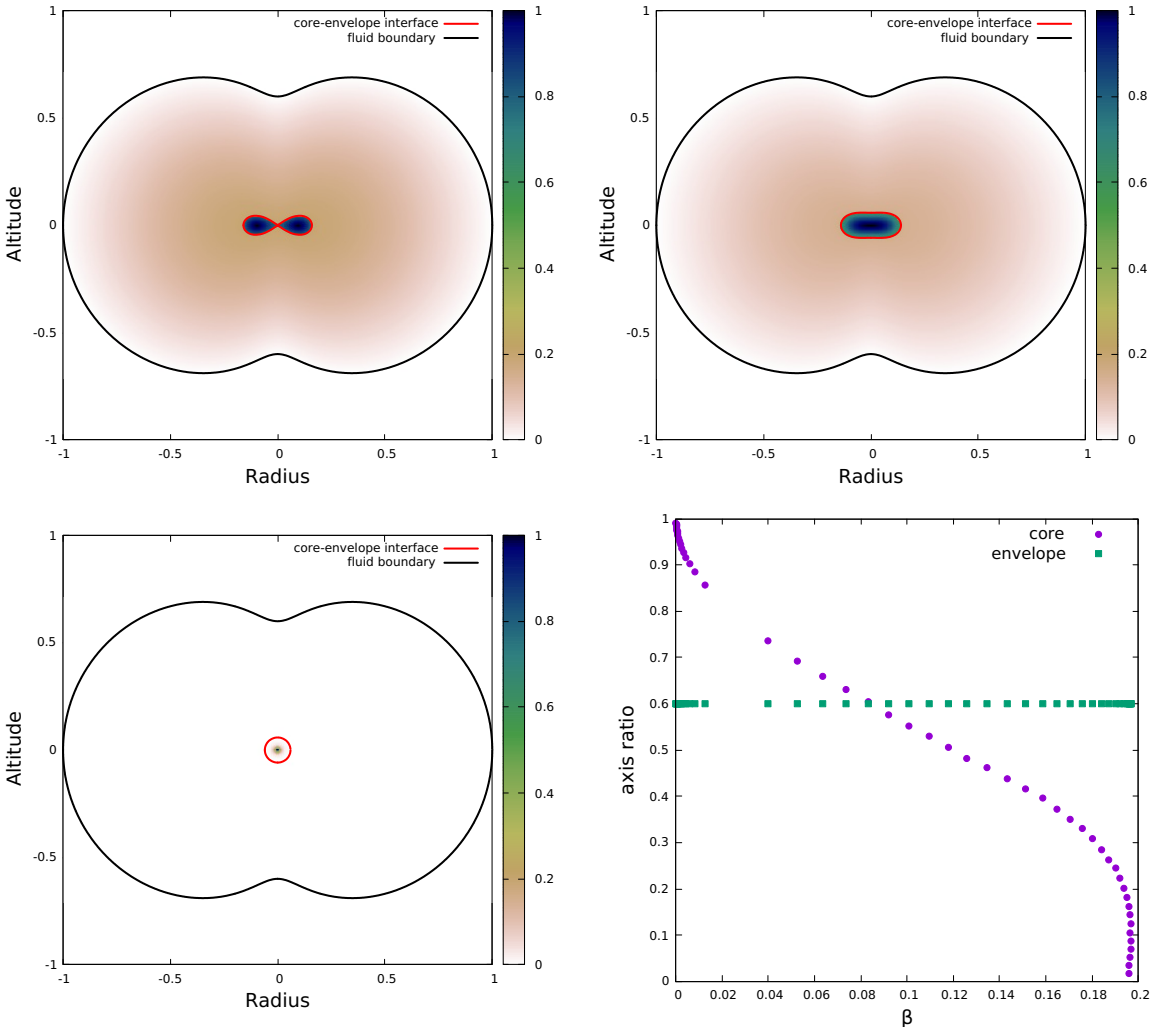

Figure 5.22: Density profile and axis ratios of the core and envelope of a differently rotating bipolytrope following a v-constant rotation law with $n_c = 5$,$n_e = 1$,$\alpha = 4$ and $e_e = 0.6$. (top left) : density for the smallest core possible at the given resolution (here l=8). (top right) : density for a core where $q_Z = 0.08$ and $\beta = 0.174$, low solution in the $q - \nu$ diagram. (bottom left) : density for a core where $q_Z = 0.08$ and $\beta = 1.68e - 4$, high solution in the $q - \nu$ diagram. (bottom right) : axis ratios of the core and the envelope as a function of β.

The previously observed features of differential rotations are intensified in this case : even at low rotation rate, we observe a rapid increase in the q_R for small q_Z.

5.7 Effect of binarity on the Schönberg-Chandrasekhar limit

It is interesting to investigate the effect of a massive companion on the internal structure of a layered stars and in particular the modification brought to the SC-like-limit. Indeed, young star are often surrounded by a massive disk and its presence can impact the internal

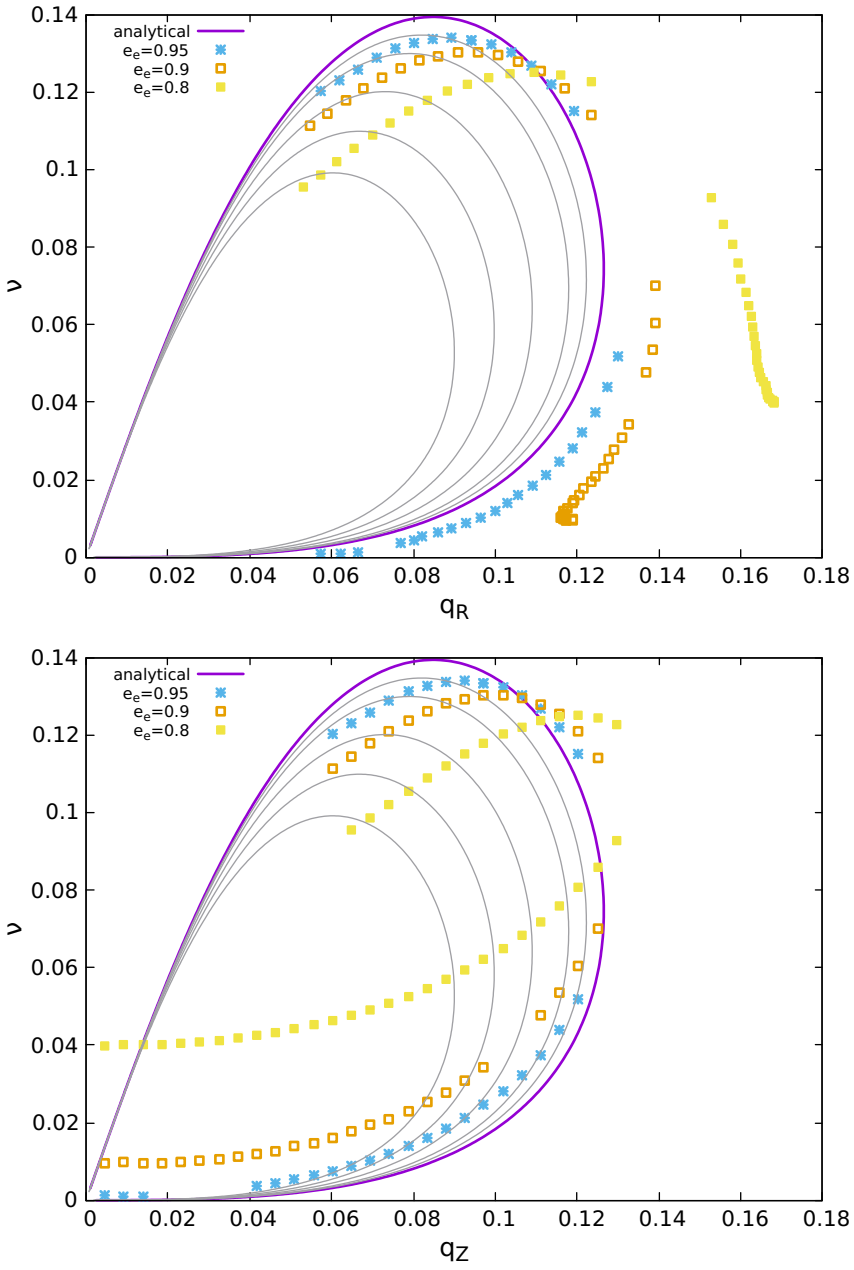

Figure 5.23: Relative mass of the core ν as a function of : (top) the relative radius of the core along the R-axis q_R and (bottom) the relative radius of the core along the Z-axis q_Z for a differentially rotating bipolytrope with a $j-$constant rotation law where $n_c = 5$,$n_e = 1$ and $\alpha = 4$. The purple straight line is the analytical solution.The grey straight lines are projected solutions for a given axis ratio by homothetie from the analytical solution. Dots are solutions found with the DROP-code.

structure of the star. In order to do so, we set up several multibody configurations starting with an elementary situation consisting of a bipolytrope surrounded by a massive infinitely thin loop and then moving on with a massive torus. We choose the well known bipolytrope case where $n_c = 5$, $n_e = 1$, $\alpha = 4$ and the axis ratio of the ellipsoid is $e = 0.8$.

5.7.1 Effect of a thin massive loop on the Schönberg-Chandrasekhar limit

To investigate the change upon the SC-like-limit by the presence of an external body, we start with a basic and simple situation where we add a thin loop around the central two-layered spheroid. We use our SCF code on a bipolytrope and we add the external gravitational potential of a loop as we do for the centrifugal potential.

Equation set with a surrouding massive loop

The gravitational potential of a loop is (Durand, 1953) :

$$\Psi_{loop} = -2G\lambda\sqrt{\frac{a}{R}}kK(k) \tag{5.44}$$

where λ is the linear density of the loop, a is the radius of the loop, K is the complete elliptic integral of the first kind and its modul k is defined by $k^2 = \frac{4aR}{(a+R)^2+z^2}$. By introducing the mass of the loop $M_{loop} = 2\pi\lambda a$, we can rewrite the gravitational potential given in Eq.(5.44) as :

$$\Psi_{loop} = -\frac{GM_{loop}}{\pi a}\sqrt{\frac{a}{R}}kK(k) \tag{5.45}$$

The total dimensionned gravitational potential of the system is now given by

$$\begin{aligned} \Psi_{tot} &= \Psi + \Psi_{loop} \\ \Psi_{tot} &= G\rho_0 L^2\left(\hat{\Psi} + \tfrac{\Psi_{loop}}{G\rho_0 L^2}\right) \end{aligned} \tag{5.46}$$

The quantity $\frac{\Psi_{loop}}{G\rho_0 L^2}$ can be rewritten in the form of :

$$\begin{aligned} \hat{\Psi}_{loop} &= \tfrac{M_{loop}}{\pi\rho_0 L^3\hat{a}}\sqrt{\tfrac{\hat{a}}{\hat{R}}}\hat{k}K(\hat{k}) \\ &= \tfrac{M_{loop}\cdot M_e}{M_e\pi\rho_0 L^3\hat{a}}\sqrt{\tfrac{\hat{a}}{\hat{R}}}\hat{k}K(\hat{k}) \\ &= \tfrac{\mu\hat{M}_e}{\hat{a}}\sqrt{\tfrac{\hat{a}}{\hat{R}}}\hat{k}K(\hat{k}) \end{aligned} \tag{5.47}$$

where μ is the mass ratio between the central spheroid (bipolytrope) and the loop and $\hat{M}_e = \frac{M_e}{\rho_0 L^3}$ is the dimensionless mass of the spheroid.

The fixed point function giving the β from the lower part of the $q-\nu$ diagram has to be updated with this new gravitational potential

$$\beta_{t+1} = f(\beta_t) = \frac{1}{\alpha}\left(\frac{1}{1+\bar{\alpha}\frac{\Delta\hat{\Psi}^c{}_{AM}+\beta_t\Delta\hat{\Psi}^e{}_{AM}+\Delta\hat{\Psi}^{loop}{}_{AM}+\beta_t C_2'\Delta\hat{\Phi}_{AM}}{\Delta\hat{\Psi}^c{}_{A'A}+\beta_t\Delta\hat{\Psi}^e{}_{A'A}+\Delta\hat{\Psi}^{loop}{}_{A'A}+\beta_t C_2'\Delta\hat{\Phi}_{A'A}}}\right)^{n_c} \tag{5.48}$$

The same update has to be done if we wish to compute the upper part of the $q-\nu$ diagram :

$$g(\beta_{t+1}) = \frac{\frac{1}{\bar{\alpha}}\left(\frac{1}{(\alpha\beta_t)^{\frac{1}{n_c}}}-1\right)\left(\Delta\hat{\Psi}^c_{A'A}+\Delta\hat{\Psi}^{loop}_{A'A}-\frac{\Delta\hat{\Phi}_{A'A}}{\Delta\hat{\Phi}_{A'B'}}\Delta\hat{\Psi}^c_{A'B'}\right)-\left(\Delta\hat{\Psi}^c{}_{AM}+\Delta\hat{\Psi}^{loop}_{AM}-\frac{\Delta\hat{\Phi}_{AM}}{\Delta\hat{\Phi}^c_{A'B'}}\Delta\hat{\Psi}^c_{A'B'}\right)}{\left(\Delta\hat{\Psi}^e_{AM}-\frac{\Delta\hat{\Phi}_{AM}}{\Delta\hat{\Phi}_{A'B'}}\Delta\hat{\Psi}^e_{A'B'}\right)-\frac{1}{\bar{\alpha}}\left(\frac{1}{(\alpha\beta_t)^{\frac{1}{n_c}}}-1\right)\left(\Delta\hat{\Psi}^e_{A'A}-\frac{\Delta\hat{\Phi}_{A'A}}{\Delta\hat{\Phi}_{A'B'}}\Delta\hat{\Psi}^e_{A'B'}\right)} \tag{5.49}$$

Results

In our simulation, we set the radius of the loop $\hat{a} = 5$ and we choose an spheroid-to-loop mass ratio μ. Note that we could do the opposite by setting the μ and varying the radius $\hat{a}$, those two different approach yield the same result since if $\hat{a}$ decreases or μ increases, the relative strength of the gravitational potential grows.

The presence of a massive loop around the spheroid modifies the aspect of the $q - \nu$ diagram. The more massive the loop, the more disrupted the $q - \nu$ diagram. Results are shown in Fig.5.24. We can see that the presence of the loop allows the core to expand a bit further more in radius, increasing q_{limit}, and to have a higher mass, increasing ν_{limit}. In other terms, the presence of massive companion increases the SC-like-limit and has the opposite effect of rotation which decreases the SC-like-limit. We can see that the loop has more effect on the SC-like-limit when the fractional mass of the core is low, i.e. lower part of the graph. However, when the loop is too massive, i.e. $\mu \geq 10$, this lower part starts to disapear because no equilibrium is found for $q \sim q_{limit}$.

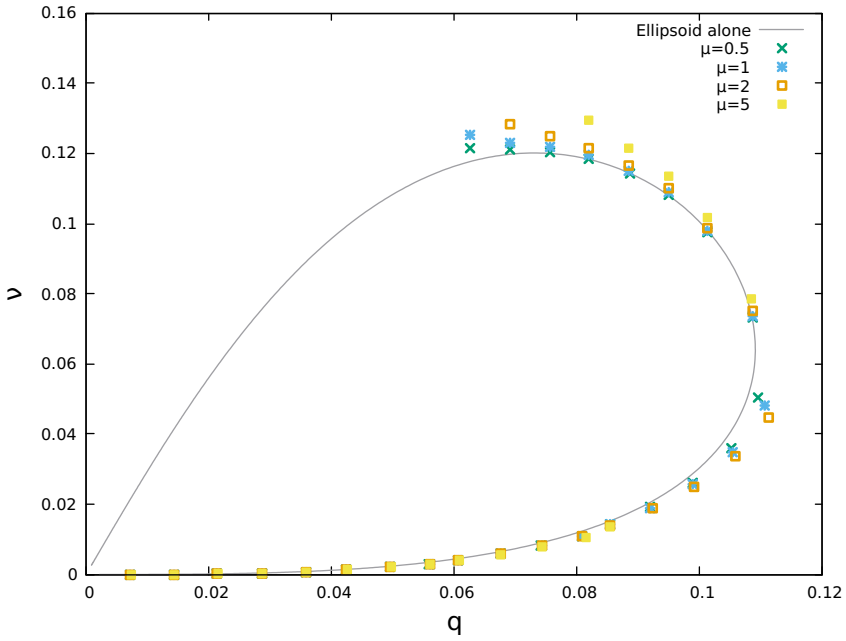

Figure 5.24: Plot of the relative mass of the core ν as a function of the relative radius of the core q for a rotating bipolytrope where $n_c = 5$,$n_e = 1$,$\alpha = 4$ and $e = 0.8$ in the presence of a massive thin loop at $r = 5$. The grey straight line is the projected solution for $e = 0.8$. Dots are solutions found with the DROP-code.

5.7.2 Effect of a companion on the SC-like-limit

We have seen that a loop has a significant effect on the bipolytrope. We have then considered a non-ponctual object around the bipolytrope using the *multibody version* of the SCF code. We center the torus on $\hat{R} = 5$ to limit a sensitivity to the Z coordinate. With a torus, we cannot choose the torus-to-spheroid ratio because both masses are output parameters so this ratio is known after convergence. We can still manage to influence this

ratio by controlling the size of the torus. Results are plotted in Fig.5.25 for a torus having half the mass of the central star and having twenty-five times the mass of the central star.

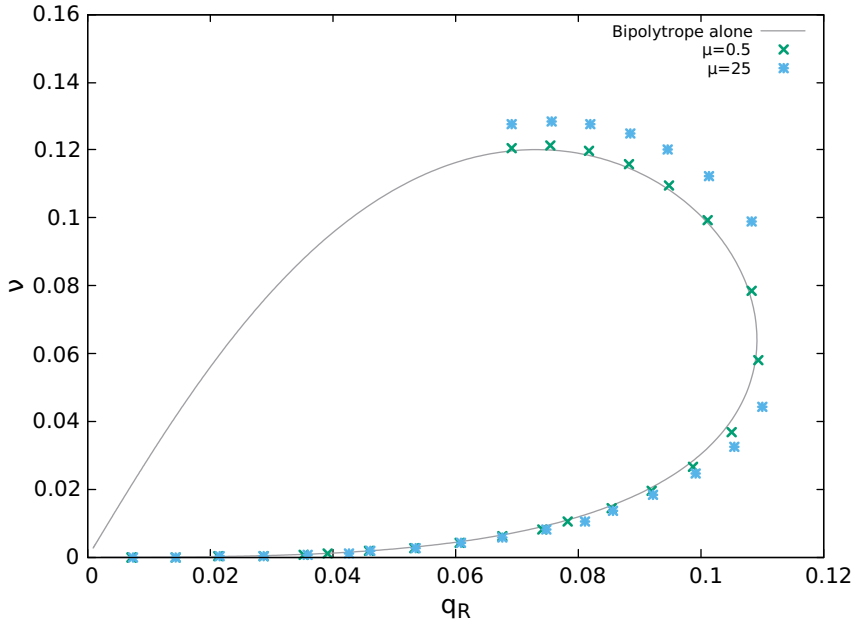

Figure 5.25: Relative mass of the core ν as a function of the relative radius of the core q for a rotating bipolytrope where $n_c = 5$,$n_e = 1$,$\alpha = 4$ and $e = 0.8$ perturbed by a massive torus centered at $\hat{r} = 5$. The grey straight line is the projected solution for $e = 0.8$. Dots are solutions found with the DROP-code.

The lower part of the graph is quite similar as it was with the presence of a ring : the external body allows the core to have a higher q_{limit} as the mass of the torus increases. On the upper part of the graph, the effects are much more pronounced due to the high mass ratio : the SC-like-limit is increased by $\sim 10\%$ with a supermassive torus and by a few % when it is a low mass torus.. The effects of a massive loop and a massive torus are similar : they increases the q_{limit} and the ν_{limit}. A huge difference between the effect of the loop and the effect of the ring is that the lower part never vanishes and equilibrium are always found even when $q \sim q_{limit}$.

5.7.3 Discussion

The Schönberg-Chandrasekhar limit is directly linked to the evolution of a star and its path in the HR diagram. As long as the core mass is below the SC-limit, the star remains on the main sequence and does not evolve into a red giant. The presence of a massive circumstellar disk in protoplanetary system could impact the evolution of the star in drastic manner by slowing it down. Because of the increased relative radius and relative mass of the core, it takes longer for the star to reach the SC-limit thus increasing the time spent by the star on the main sequence.

Close binary systems such as a star-star system or a star-hot jupiter configuration could be impacted by this modification of the $q - \nu$ relationship.

input parameters	
axis ratio	0.9351
q_Z	0.1587
n_c	0.3260
n_e	0.8850
α	3.073
ω_{ec}	1.000314

Table 5.3: Input parameters of the bipolytrope reproducing observed properties of Jupiter

5.8 Jupiter as a bipolytrope

We manage to reproduce the observed properties of Jupiter (mass, equatorial radius, mean density, gravitational moments and rotation period) with a bipolytrope. The input parameters are shown in Tab.5.3 and the map density is shown in Fig.5.26. These results are only preliminary and a wide survey of parameters will be needed. A small rotational discontinuity between the core and the envelope is required to obtain a nominal solution. Since $\omega_{ec} > 1$, the core spins faster than the envelope. The output quantities are shown in Tab.5.4

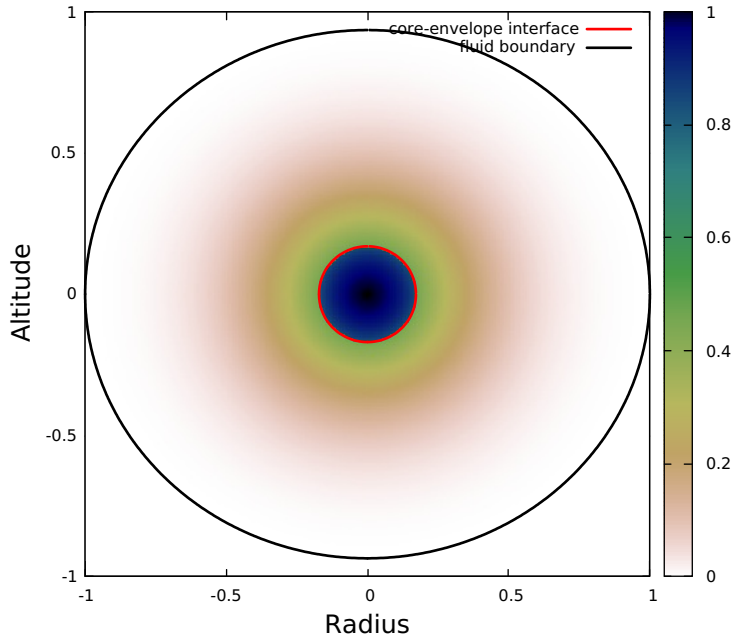

Figure 5.26: Map density of a bipolytrope reproducing the output quantities of Jupiter

	This work	Observed properties Helled (2019)
Equatorial radius (km)	71 492	71 492
Mass (10^{24} kg)	1 898	1 898
Mean density (g/cm^3)	1.3292	1.3262
J2	+14 696	14 696
J4	-587.29	-586.61
J6	+34.813	34.24
Rotation period (core)	09h 55m 29.57s	9h 55m 29.56s
Rotation period (envelope)	09h 55m 35.18s	

Table 5.4: Output properties of the bipolytrope reproducing observed properties of Jupiter. The reference observed data are shown on the right column.

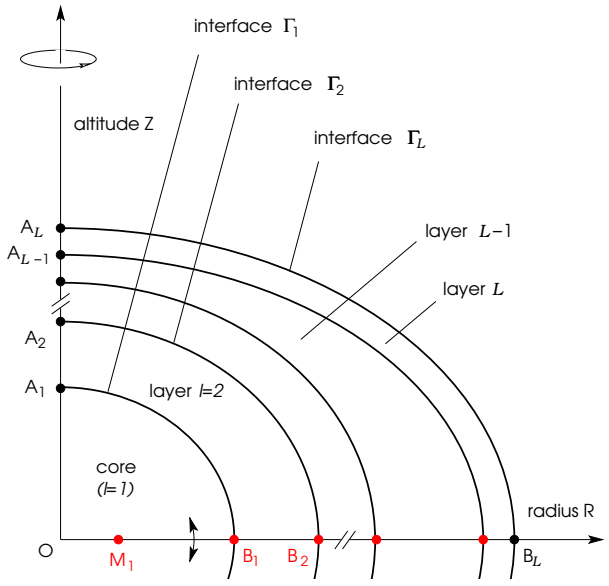

Figure 5.27: Configuration for the rotating, multilayer star/planet made of $\mathcal{L}$ layers (the deepest one, the core, has layer number 1). At each interface Γ_l, both a mass density jump and a rotational discontinuity are allowed. The rotation rate at the bottom of the outermost layer envelope is set through the reference points $A_\mathcal{L}$ and $B_\mathcal{L}$. The polar extension of the layers is set through the reference points A_1, A_2, ..., $A_{\mathcal{L}-1}$ on the polar axis.

5.9 General case : a $\mathcal{L}$-layer body

5.9.1 The full equation set

We now consider a system made of $\mathcal{L}$ gaseous layers, with $\mathcal{L} \geq 2$. Each layer is defined by a number l, a polytropic index for the EOS $n_l \geq 0$, the enthalpy $\hat{H}_l$, the mass density ρ_l (with magnitude ρ_{l0}), a rotation profile Ω_l (with magnitude Ω_{l0}) and associated centrifugal potential $\hat{\Phi}_l$, etc. By convention, $l = 1$ is the deepest domain, still called the "core", and the outermost layer has the index $l = \mathcal{L}$. The interface between two adjacent layers $l \in [2, \mathcal{L}]$ and $l' = l - 1$ is denoted $\Gamma_{l'}$, and the interface with the free space is $\Gamma_{\mathcal{L}}$. We also account for a possible mass density jump α_l and a rotational discontinuity ω_l at each interior interface, namely

$$\alpha_l = \left.\frac{\rho_{l'}}{\rho_l}\right|_{\Gamma_{l'}} > 0, \tag{5.50}$$

and

$$\sqrt{\omega_l} = \frac{\Omega_{l'0}}{\Omega_{l0}} > 0, \tag{5.51}$$

meaning that the layer l rotates faster than the one located just below when $\omega_l < 1$. We also define

$$\beta_l = \frac{\rho_{l0}}{\rho_{10}} > 0, \tag{5.52}$$

which is also valid for $l = 1$. As the consequence, in the reference frame of the core, the total gravitational potential writes

$$\hat{\Psi}_{1,\mathrm{tot}} = \hat{\Psi}_1 + \sum_{l=2}^{\mathcal{L}} \beta_l \hat{\Psi}_l. \tag{5.53}$$

The equilibrium of each layer $l \in [2, \mathcal{L}]$ is described by a set of equations similar to (5.23). More precisely, we have

$$\begin{cases} C_{1l}\hat{H}_l + \hat{\Psi}_{l,\mathrm{tot}} + C_{2l}\hat{\Phi}_l = C_{3l}, \\ \hat{\rho}_l = (\hat{H}_l)^{n_l} \quad \hat{H}_l(\Gamma_{l'}) \geq \hat{H}_l \geq \hat{H}_l(\Gamma_l), \\ \Delta\hat{\Psi}_{l,\mathrm{tot}} = 4\pi \frac{1}{\beta_l} \left(\hat{\rho}_1 + \beta_2\hat{\rho}_2 + \dots \right. \\ \qquad\qquad \left. + \beta_l\hat{\rho}_l + \dots + \beta_{\mathcal{L}}\hat{\rho}_{\mathcal{L}}\right), \end{cases} \tag{5.54}$$

where C_{3l} is the invariant,

$$\begin{cases} C_{1l} \equiv \frac{K_l(n_l+1)\rho_{l0}^{\gamma_l - 2}}{GL^2}, \\ C_{2l} \equiv \frac{\Omega_0^2}{G\rho_{l0}}, \end{cases} \tag{5.55}$$

For $l = 1$ (the core), (5.54) holds but $\hat{H}_1 \geq \hat{H}_1(\Gamma_1)$, while for the outermost layer $l = \mathcal{L}$, we have $\hat{H}_{\mathcal{L}} = 0$ in the absence of ambient pressure. For two adjacent layers l' and l, we have from (5.55b)

$$\beta_l C_{2l}\Omega_{l'0}^2 = \beta_{l'} C_{2l'}\Omega_{l0}^2, \tag{5.56}$$

which, given (5.51) and (5.52), also reads

$$\omega_l \beta_l C_{2l} = \beta_{l'} C_{2l'}. \tag{5.57}$$

There are also $\mathcal{L}-1$ additionnal equations for the pressure balance at each interior interface, namely

$$\bar{\alpha}_l \beta_{l'} C_{1l'} \hat{H}_{l'}(\Gamma_{l'}) - \beta_l C_{1l} \hat{H}_l(\Gamma_{l'}) = 0, \tag{5.58}$$

where

$$\bar{\alpha}_l = \alpha_l \frac{1+n_l}{1+n_{l'}}, \tag{5.59}$$

and yet another $\mathcal{L}-1$ equations corresponding to mass density jumps, or

$$\alpha_l \beta_l \hat{H}_l^{n_l}(\Gamma_{l'}) = \beta_{l'} \hat{H}_{l'}^{n_{l'}}(\Gamma_{l'}). \tag{5.60}$$

The full equation set for the $\mathcal{L}$-layer star/planet is therefore

$$\begin{cases}
C_{11}\hat{H}_1 + \hat{\Psi}_{1,\mathrm{tot}} + C_{21}\hat{\Phi}_1 = C_{31}, \\
\hat{\rho} = \hat{H}_1^{n_1}, \quad \hat{H}_1 \geq \hat{H}_1(\Gamma_1), \\
\Delta\hat{\Psi}_{1,\mathrm{tot}} = 4\pi\left(\hat{\rho}_1 + \beta_2\hat{\rho}_2 + \ldots \right. \qquad \text{(layer 1)} \\
\qquad\qquad \left. + \beta_l\hat{\rho}_l + \cdots + \beta_{\mathcal{L}}\hat{\rho}_{\mathcal{L}}\right) \\
\\
\bar{\alpha}_2 C_{11}\hat{H}_1(\Gamma_1) - \beta_2 C_{12}\hat{H}_2(\Gamma_1) = 0, \\
\quad \text{(pressure balance)} \\
\alpha_2\beta_2\hat{H}_2^{n_e}(\Gamma_1) = \hat{H}_1^{n_1}(\Gamma_1) \qquad (\rho-\text{jump}), \\
\omega_2\beta_2 C_{22} = C_{21} \quad \text{(scaling)}, \\
\ldots \\
C_{1l}\hat{H}_l + \hat{\Psi}_{l,\mathrm{tot}} + C_{2l}\hat{\Phi}_l = C_{3l}, \\
\hat{\rho}_l = \hat{H}_l^{n_l}, \quad \hat{H}_l(\Gamma_{l'}) \geq \hat{H}_l \geq \hat{H}_l(\Gamma_l), \\
\Delta\hat{\Psi}_{l,\mathrm{tot}} = 4\pi\frac{1}{\beta_l}\left(\hat{\rho}_1 + \beta_2\hat{\rho}_2 + \ldots \right. \qquad \text{(layer } l\text{)} \\
\qquad\qquad \left. + \beta_l\hat{\rho}_l + \cdots + \beta_{\mathcal{L}}\hat{\rho}_{\mathcal{L}}\right), \\
\\
\bar{\alpha}_l\beta_{l'}C_{1l'}\hat{H}_{l'}(\Gamma_{l'}) - \beta_l C_{1l}\hat{H}_l(\Gamma_{l'}) = 0, \\
\quad \text{(pressure balance)} \\
\alpha_l\beta_l\hat{H}_l^{n_l}(\Gamma_{l'}) = \beta_{l'}\hat{H}_{l'}^{n_{l'}}(\Gamma_{l'}) \qquad (\rho-\text{jump}), \\
\omega_l\beta_l C_{2l} = \beta_{l'}C_{2l'} \quad \text{(scaling)}, \\
\ldots \\
C_{1\mathcal{L}}\hat{H}_{\mathcal{L}} + \hat{\Psi}_{\mathcal{L},\mathrm{tot}} + C_{2\mathcal{L}}\hat{\Phi}_{\mathcal{L}} = C_{3\mathcal{L}}, \\
\hat{\rho}_{\mathcal{L}} = \hat{H}_{\mathcal{L}}^{n_{\mathcal{L}}}, \quad \hat{H}_{\mathcal{L}}(\Gamma_{\mathcal{L}-1}) \geq \hat{H}_{\mathcal{L}} \geq 0, \\
\Delta\hat{\Psi}_{\mathcal{L},\mathrm{tot}} = 4\pi\frac{1}{\beta_{\mathcal{L}}}\left(\hat{\rho}_l + \beta_2\hat{\rho}_2 + \ldots \right. \qquad \text{(layer } \mathcal{L}\text{)} \\
\qquad\qquad \left. + +\beta_l\hat{\rho}_l + \cdots + \beta_{\mathcal{L}}\hat{\rho}_{\mathcal{L}}\right).
\end{cases} \tag{5.61}$$

Note that all Poisson equations are formally equivalent. The total number of equations amounts to $5\mathcal{L}-2$. There are $\mathcal{L}$ enthalpies to determines and $4\mathcal{L}-1$ unknown constants (3 constants C_1, C_2 and C_3 for each layer and one constant β for each inerior interface). There are $3\mathcal{L}-2$ input parameters (one polytropic index per layer, one mass density jump and one rotational discontinuity per interface) and $\mathcal{L}+1$ reference points to define.

5.9.2 The Virial test

At equilibrium, the Virial equation accounts for all layers, and so we have

$$W_{\rm tot} + 2T_{\rm tot} + U_{\rm tot} = 0. \tag{5.62}$$

The gravitational term can be written in the form

$$\begin{aligned}
\frac{W_{\rm tot}}{G\rho_0^2 L^5} &= \frac{1}{2}\int \hat{\rho}\underbrace{\left(\hat{\Psi}_1 + \cdots + \beta_l\hat{\Psi}_l + \cdots + \beta_{\mathcal{L}}\hat{\Psi}_{\mathcal{L}}\right)}_{\hat{W}_{1,\rm tot}} d\tilde{V}_1 \\
&\quad + \ldots \\
&\quad + \beta_l^2 \times \frac{1}{2}\int \hat{\rho}_l \underbrace{\left(\frac{\hat{\Psi}_1}{\beta_l} + \cdots + \hat{\Psi}_l + \cdots + \frac{\beta_{\mathcal{L}}}{\beta_l}\hat{\Psi}_{\mathcal{L}}\right)}_{\hat{W}_{2,\rm tot}} d\hat{V}_l \\
&\quad + \ldots \\
&\quad + \beta_{\mathcal{L}}^2 \times \frac{1}{2}\int \hat{\rho}_{\mathcal{L}} \underbrace{\left(\frac{\hat{\Psi}_1}{\beta_{\mathcal{L}}} + \cdots + \frac{\beta_l}{\beta_{\mathcal{L}}}\hat{\Psi}_l + \cdots + \hat{\Psi}_{\mathcal{L}}\right)}_{\hat{W}_{\mathcal{L},\rm tot}} d\hat{V}_{\mathcal{L}}, \\
&= \hat{W}_{1,\rm tot} + \cdots + \beta_l^2\hat{W}_{l,\rm tot} + \cdots + \beta_{\mathcal{L}}^2\hat{W}_{\mathcal{L},\rm tot},
\end{aligned} \tag{5.63}$$

where $d\hat{V}_l = 2\pi\hat{a}d\hat{a}d\hat{z}$ is the elementary volume. The kinetic and pressure terms are respectively

$$\begin{aligned}
\frac{T_{\rm tot}}{G\rho_0^2 L^5} &= \frac{1}{2}\int \hat{\rho}C_{21}\hat{\Omega}_1^2\hat{a}^2 d\tilde{V}_1 + \ldots \\
&\quad + \beta_l^2 \times \frac{1}{2}\int \hat{\rho}_l C_{2l}\hat{\Omega}_l^2\hat{a}^2 d\hat{V}_l + \ldots \\
&\quad + \beta_{\mathcal{L}}^2 \times \frac{1}{2}\int \hat{\rho}_{\mathcal{L}} C_{2\mathcal{L}}\hat{\Omega}_{\mathcal{L}}^2\hat{a}^2 d\hat{V}_{\mathcal{L}}, \\
&= C_{21}\hat{T}_1 + \cdots + \beta_l^2 C_{2l}\hat{T}_l + \cdots + \beta_{\mathcal{L}}^2 C_{2\mathcal{L}}\hat{T}_{\mathcal{L}}
\end{aligned} \tag{5.64}$$

and

$$\begin{aligned}\frac{U_{\rm tot}}{G\rho_0^2L^5} &= \frac{3C_{11}}{1+n_1}\int \hat{\rho}\hat{H}_1 d\tilde{V}_1 + \dots \\ &+ \beta_l^2 \times \frac{3C_{1l}}{1+n_l}\int \hat{\rho}_l\hat{H}_l d\hat{V}_l + \dots \\ &+ \beta_{\mathcal{L}}^2 \times \frac{3C_{1\mathcal{L}}}{1+n_{\mathcal{L}}}\int \hat{\rho}_l\hat{H}_{\mathcal{L}} d\hat{V}_{\mathcal{L}} \\ &= \hat{U}_1 + \dots + \beta_l^2\hat{U}_l + \dots + \beta_{\mathcal{L}}^2\hat{U}_{\mathcal{L}}. \end{aligned} \tag{5.65}$$

In dimensionless form, (5.62) becomes

$$\begin{aligned}\underbrace{\hat{W}_1 + 2\hat{T}_1 + \hat{U}_1}_{\rm VP_1} + \dots + \beta_l^2 \underbrace{\left(\hat{W}_l + 2\hat{T}_l + \hat{U}_l\right)}_{\rm VP_l} + \dots \\ + \beta_{\mathcal{L}}^2 \underbrace{\left(\hat{W}_{\mathcal{L}} + 2\hat{T}_{\mathcal{L}} + \hat{U}_{\mathcal{L}}\right)}_{\rm VP_{\mathcal{L}}} = 0. \end{aligned} \tag{5.66}$$

As for the bipolytrope, individual values for VP_l have no great significance, only the weighted sum yields a measure of the quality of the solution. By dividing this equation by the gravitatinal term, we find

$$\mathrm{VT} = \frac{\sum_{l=1}^{\mathcal{L}} \mathrm{VP_l}}{|\sum_{l=1}^{\mathcal{L}} \beta_l^2 \hat{W}_l|}. \tag{5.67}$$

5.9.3 Major remarks

Again, some interesting properties follow from (5.61). As for the bipolytope case, each leayer is strongly influenced by the remaining, $\mathcal{L}-1$ ones. Even in the case $\mathcal{L}=3$, it seems cumbersome to investigate the role of the polytropic inidices, mass density jumps and rotational discontinuities on the global structure. In fact, we can easily derive the analog of (5.33), (5.34) and (5.35) by considering two adjacent layers with numbers $l \in [2, \mathcal{L}-1]$ and $l' = l-1$. For any point at $\Gamma_{l'}$, we get

$$\begin{cases} \frac{1+n_l}{1+n_{l'}}\frac{C_{1l'}}{C_{1l}}\beta_l^{\frac{1}{n_l}-1}\beta_{l'}^{1-\frac{1}{n_l}}\alpha_l(\Gamma_{l'})^{1+\frac{1}{n_l}} \\ \quad -\hat{H}_{l'}(\Gamma_{l'})^{\frac{n_{l'}}{n_l}-1} = 0, \\ \\ \frac{1+n_l}{1+n_{l'}}\beta_{l'}^2 C_{1l'}\hat{H}_{l'}(\Gamma_{l'})^{1+n_{l'}} \\ \quad -\beta_l^2 C_{1l}\hat{H}_l(\Gamma_{l'})^{1+n_l} = 0, \\ \\ \beta_{l'}C_{1l'}\hat{H}_{l'}(\Gamma_{l'})\left[1-\bar{\alpha}_l(\Gamma_{l'})\right] \\ \quad +\beta_{l'}C_{2l'}\left[\hat{\Phi}_{l'}(\Gamma_{l'}) - \frac{1}{\omega_l}\hat{\Phi}_l(\Gamma_{l'})\right] \\ \quad +\beta_l C_{3l} - \beta_{l'}C_{3l'} = 0, \end{cases} \tag{5.68}$$

where $n_l > 0$ is assumed. Helped with the discussion in Sect. 5.2.2, we come to the conclusions that, for two adjacent layers

- if the polytropic indices are equal, then the mass density jump is uniform along the common interface,
- if the mass density jump varies along the common interface, then the enthalpy is not uniform either
- there is no rotational discontinuity without mass density jump, unless $\omega_l \hat{\Phi}_{l'} - \hat{\Phi}_l = 0$ at the common interface,
- a non-uniform mass density jump along the common interface is compatible with a rotational discontinuity.

5.9.4 The procedure in details

The solutions can be efficiently captured through the SCF-method. The principle is the same as for the bipolytrope. We proceed from the outermost layer to the deepest one. At the two references points $\mathrm{A}_{\mathcal{L}}$ and $\mathrm{B}_{\mathcal{L}}$ located respetively at the pole and at the equator of $\Gamma_{\mathcal{L}}$ (see Fig. 5.27), the enthalpy is zero, and we use the normalisation condition at $\mathrm{A}_{\mathcal{L}-1}$ of $\Gamma_{\mathcal{L}-1}$, i.e. $\hat{H}_{\mathcal{L}}(\mathrm{A}_{\mathcal{L}-1}) = 1$. From these 3 values, the three quantities $\beta_{\mathcal{L}} C_{1\mathcal{L}}$, $\beta_{\mathcal{L}} C_{2\mathcal{L}}$ and $\beta_{\mathcal{L}} C_{3\mathcal{L}}$ for the layer $\mathcal{L}$ are fully determined with reference points. We then go the next layer. From the scaling relationship (5.57) and the equation for pressure balance (5.58), we first deduce $\beta_{\mathcal{L}-1} C_{2\mathcal{L}-1}$ and $\beta_{\mathcal{L}-1} C_{3\mathcal{L}-1}$. The normalisation of $\hat{H}_{\mathcal{L}-1}$ at $\mathrm{A}_{\mathcal{L}-2}$, i.e. $\hat{H}_{\mathcal{L}-1}(\mathrm{A}_{\mathcal{L}-2}) = 1$, yields the third quantity $\beta_{\mathcal{L}-1} C_{1\mathcal{L}-1}$. This is repeated down to layer 2. For the core, we proceed in the same way to get C_{21} and C_{31}. The normalisation of enthalpy of the core is obtained by searching the point M_1 where $\hat{H}_1$ is maximum, which yields C_{11} (M_1 does not necessarily stands on the polar axis). Given all these values, all the enthalpies $\hat{H}_1$, $\hat{H}_2$, …, $\hat{H}_{\mathcal{L}}$ can be determined in space, namely :

$$\begin{aligned} \hat{H}_l(\vec{r}) &= \frac{1}{C_{1l}} \left\{ C_{3l} - \left[\hat{\Psi}_{l,\mathrm{tot}}(\vec{r}) + C_{2l} \hat{\Phi}_l(\vec{r}) \right] \right\}, \\ &= \frac{1}{\beta_l C_{1l}} \left\{ \beta_l C_{3l} - \left[\hat{\Psi}_{1,\mathrm{tot}}(\vec{r}) + \beta_l C_{2l} \hat{\Phi}_l(\vec{r}) \right] \right\}. \end{aligned} \tag{5.69}$$

Then comes the update of the β-parameters, which is performed from the mass-density jump conditions.

The details of the procedure are summarized in Tab. 5.5. At the beginning, the enthalpies for the core, and layers above and the contrast parameters, respectively $\hat{H}_1(0)$, $\hat{H}_l(0)$ and $\beta_l(0)$ are guessed. Theses quantities, together with the $3\mathcal{L}$ constants and the $\mathcal{L}$ interfaces evolve during the cycle. It is stopped after t_{conv} iterations, when all quantities are stabilized.

Note that, when taking $\mathcal{L} = 2$, we find again the equations for a two-layer system previously shown (at the condition of replacing the subscript 1 by c and the subscript 2 by e).

5.9.5 A false tripolytrope

The first example is a false tripolytrope which consists in 3 non-rotating layers with the same polytropic index, without any mass density jump at the interfaces. We use the same

	substep	operation
preliminaries	interfaces, layers and Poisson equation	
		β_l and $\hat{H}_l(t)$ assumed to be known (starting guess, or from previous step $(t-1)$, for $l = 1, 2, \ldots, \mathcal{L}$, $(\beta_1 = 1)$
	1^*	the interfaces Γ_l are determined for $l = 1, \ldots, \mathcal{L}-1$
	1	the mass density $\hat{\rho}_l$ is computed for each layer $l = 1, 2, \ldots, \mathcal{L}$ from $\hat{H}_l$
	2^*	the potential $\hat{\Psi}_l$ is computed from the Poisson equation, see (5.61) for $l = 1, 2, \ldots, \mathcal{L}$
	2	the potential $\hat{\Psi}_{1,\mathrm{tot}}$ is computed for the actual set of β_l-parameters; $\beta_l \hat{\Psi}_{l,\mathrm{tot}} = \hat{\Psi}_{1,\mathrm{tot}}$
top layer	1	values for $\beta_{\mathcal{L}} C_{2\mathcal{L}}$ and $\beta_{\mathcal{L}} C_{3\mathcal{L}}$ are obtained from $\hat{\Psi}_{\mathcal{L}}(\mathrm{A}_{\mathcal{L}})$ and $\hat{\Psi}_{\mathcal{L}}(\mathrm{B}_{\mathcal{L}})$,
$l = \mathcal{L}$	2	$\beta_l C_{1\mathcal{L}}$ is obtained from the normalisation condition, i.e. $\hat{H}_l(\mathrm{A}_{\mathcal{L}-1}) = 1$
	3	$\beta_l C_{1\mathcal{L}} \hat{H}_{\mathcal{L}}$ is computed from the Bernoulli equation for the top layer, see (5.69)
	4	the new enthalpy $\hat{H}_{\mathcal{L}}(t+1) \leftarrow \hat{H}_{\mathcal{L}}$ is deduced from substeps 2 and 3, $\hat{H}_{\mathcal{L}}(\mathrm{A}_{\mathcal{L}-1})$ must be unity (normalisation condition)
	...	
intermediate layer	1	$\beta_l C_{2l}$ is deduced from (5.57)
$\mathcal{L} - l + 1$	2	$\beta_l C_{3l}$ is computed from (5.54a) and (5.58)
$l = 2, \ldots, \mathcal{L}-1$	3	$\beta_l C_{1l} \hat{H}_l$ is computed from the Bernoulli equation, see (5.69)
	4	$\beta_l C_{1l}$ is deduced from the normalisation condition at A_{l-1}
	5	the new enthalpy $\hat{H}_l(t+1) \leftarrow \hat{H}_l$ is deduced from substeps 3 and 4, $\hat{H}_l(\mathrm{A}_{l-1})$ must be unity (normalisation condition)
	...	
deepest layer	1	$\beta_1 C_{21}$ is deduced from (5.57)
(core) $l = 1$	2	$\beta_1 C_{31}$ is computed from (5.54a) and (5.58)
	3	$\beta_l C_{11} \hat{H}_1$ is computed from the Bernoulli equation, see (5.69)
	4	$\beta_l C_{1l}$ is deduced from the normalisation condition, i.e. $\exists\ \mathrm{M}_1$ such that $\beta_l C_{1l} \hat{H}_1$ is a maximum
	5	the new enthalpy $\hat{H}_1(t+1) \leftarrow \hat{H}_1$ is deduced from substeps 3 and 4, $\hat{H}_1(\mathrm{M}_1)$ must be unity (normalisation condition)
	final stage, release of new β_l coefficients from the jump conditions	
final stage	(release of new density contrast, mass-density jump and tests of convergence)	
		if convergence is not achieved, then $t \leftarrow t+1$ and go for another iteration, step 0

Table 5.5: Main steps of one iteration of the SCF-cycle for a $\mathcal{L}$-layer system. The algorithm proceeds from the outermost layer to the deepest one. The three reference points A_l for $l = [1, \mathcal{L}]$, and $B_{\mathcal{L}}$ are fixed. * optional*

input parameters as in Tab. 5.2. The core, the envelope and the "atmosphere" (layer $l = 3$) have the same extension, i.e. $q_1 = q_2 = \frac{1}{3}$. The structure at equilibrium is shown in Fig. 5.28. The results are listed in Tab. 5.6. There is an excellent agreement between this three-layer polytrope and the single polytrope. As for the bipolytrope, the impact of q_1 and q_2 is weak on the overall properties.

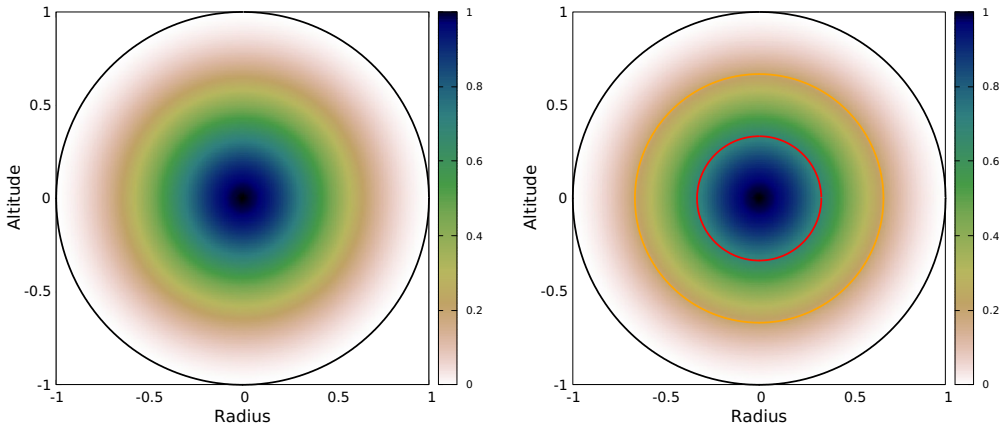

Figure 5.28: (left) : Density map of a non-rotating single-layered polytrope with $n = 1.5$ *(right) : Density map of a non-rotating tripolytrope with* $n_1 = n_2 = n_3 = 1.5$, $\alpha_2 = \alpha_3 = 1$ *and* $q = 0.66$. *The black line is the fluid boundary, the orange line is the envelope-atmosphere interface and the red line is the core-envelope interface.*

5.9.6 Discussion

This new algorithm allows us to generate $\mathcal{L}$-layer polytropes with a density jump and rotational discontinuity at possible at each interface. Some global trends are observed :

- The equilibrium is very sensitive to the magnitude of the density jumps and the rotational discontinuities. All layers are not affected with the same amplitude.
- The higher the density jump, the lower the total mass.
- When the core rotates faster than the envelope, its oblateness increases.
- There is a relative decoupling between the shape of the core and the shape of the envelope, i.e. the rotation of the envelope is not directly linked to the rotation of the core.
- Density jumps and rotation discontinuities are relatively connected since a rotational discontinuity induces a density jump. On the contrary, a density jump is possible without a rotational discontinuity.
- The density jump is constant on the interface between two layers if their polytropic indices are the same.

	polytrope ($l = \mathcal{L} = 1$)	Hachisu (1986)	false tripolytrope ($\mathcal{L} = 2$) core ($l = 1$)	env. ($l = 2$)	atm. ($l = 3$)	total
N	129	>128				129
ℓ	7					7
n_l	+1.5000E+00	+1.5000E+00	+1.5000E+00	+1.5000E+00	+1.5000E+00	
$\hat{z}(A_l)$	+1.0000E+00	+1.0000E+00	+3.3333E-01	+6.6667E-01	+1.0000E+00	
q_l	+1.0000E+00	+1.0000E+00	+3.3333E-01	+3.3333E-01	+3.3333E-01	
$\alpha_l(\mathrm{A}_l)$				+1.0000E+00	+1.0000E+00	
ω_l				+1.0000E+00	+1.0000E+00	
SCF-iterations	29					31
$\hat{H}_l(\mathrm{A}_l)$	+0.0000E+00		+7.7815E-01	+4.3432E-01	+0.0000E+00	
$\beta_l^\dagger$		+1.0000E+00	+6.8643E-01	+1.9647E-01		
Q_l		+3.3333E-01	+3.3333E-01	+0.0000E+00		
nodes Γ_l		251	84	168	251	
$\hat{V}_l$	+4.1883E+00	+4.17E+00	+1.5495E-01	+1.0861E+00	+2.9479E+00	+4.1889E+00
$\hat{M}_l$	+6.9919E-01	+6.99E-01	+1.2440E-01	+5.9220E-01	+8.5830E-01	+6.9953E-01
C_{1l}	+3.3196E-06		+9.4134E-01	+9.4133E-01	+1.0671E+00	+1.6192E+00
C_{2l}	-1.4787E-04		-2.1542E-04	-7.5264E-04		
C_{3l}	-6.9920E-01		-6.9948E-01	-1.0190E+00	-3.5602E+00	
ν_l	+1.0000E+00		+1.7783E-01	+5.8111E-01	+2.4106E-01	
J_l	+2.6064E-04	+0.00E+00	+6.4185E-05	+1.2569E-03	+4.1416E-03	+1.7406E-03
$\hat{T}_l$	+2.3744E-07	+0.00E+00	-3.9025E-07	-1.1133E-05	-1.2817E-04	-1.0583E-05
$\hat{W}_l$	-4.1904E-01	-4.19E-01	-9.4361E-02	-5.2741E-01	-1.9816E+00	-4.1936E-01
$\hat{U}_l$	+4.1906E-01	-4.19E-01	+1.2205E-01	+5.4161E-01	+1.0889E+00	+4.1928E-01
VP	+1.5278E-05					-1.0400E-04
VT	+3.6460E-05					-2.4800E-04

Table 5.6: Input (top) and output (bottom) quantities for the false non-rotating tripolytrope in the conditions of Fig. 5.28 with $\ell = 7$. The core-envelope interface is located at $qcor = q_2 = \frac{1}{3}$ and the envelope-atmosphere is located at $q = \frac{2}{3}$. There is no jump condition (i.e. $\alpha_2 = \alpha_3$). The results obtained in the same conditions for the polytrope are given in the second column.

- Two multilayer configurations having the same degeneracy parameter Ξ have the same observables : size, oblateness, surface velocity and total mass.

A complete exploration of the parameter space would be interesting in order to infer more precise trends. Even if it is rather doable for a two-layer system (6 input parameters), the difficulty grows rapidly with the number of layers since a $\mathcal{L}$-layer system requires $4\mathcal{L}-2$ input parameters.

Chapter 6

A brief application to the GG tau system

Contents

Exact solutions to the Poisson equation have been widely investigated for spheroidal systems (Milne, 1923; Chandrasekhar, 1969, 1933a; Chandrasekhar and Lebovitz, 1962; Kovetz, 1968) but there is far less light on toroidal systems. The Gauss theorem is a powerful tool to determine potential of spherical systems but it cannot be easily applied in other geometries. Nonetheless there is a need for analytical developments for such systems in order to have new fast and accurate method to calculate potential and forces (Wong, 1973, 1974; Cohl and Tohline, 1999; Kondratyev, 2018; Majic, 2018; Huré et al., 2019, 2020). As it is known, there is a wide diversity of systems hosting disks, tori and rings .

6.1 Early work from Wong (1973) on the potential theory of rings

In the context of nuclear physics, Wong (1973) has performed a Laplace expansion in toroidal coordinates of the Coulomb potential generated by a solid torus, i.e. he developped the potential in toroidal harmonics. Here we reproduce the first term of his development. As opposed to usual treatment, his work does not rely on any small parameter and is valid for any size of the torus.

As pictured in Fig.6.1, in toroidal coordinates, a surface of constant η describes a toroidal shell, a surface of constant θ describes a spherical bowl and a surface with a constant ϕ describes a plane. Moreover, we define the surface of the torus by $\eta = \eta_0$ as :

$$\eta_0 = \cosh^{-1}\left(\frac{R}{d}\right). \tag{6.1}$$

In the framework of gravitation, the potential is given by the Newton's integral :

$$\Psi(\vec{r}\,') = -G\iiint \frac{\rho(\vec{r})d^3r}{\mid \vec{r}-\vec{r}\,'\mid} \tag{6.2}$$

and reads in toroidal coordinates, if we assume incompressibility :

$$\Psi(\eta^{'},\theta^{'},\phi^{'}) = -G\rho_0 a^3 \iiint \frac{1}{\mid \vec{r}-\vec{r}\,'\mid}\theta(\eta-\eta_0)\frac{\sinh\eta}{(\cosh\eta-\cos\theta)^3}d\eta\ d\theta\ d\phi \tag{6.3}$$

where a is the radius of the focal ring. According to Wong (1973), the Green's function can be expanded as :

$$\frac{1}{\mid \vec{r}(\eta,\theta,\phi)-\vec{r}\,'(\eta,\theta,\phi)\mid} = \frac{1}{\pi a}\left[(\cosh\eta-\cos\theta)(\cosh\eta^{'}-\cos\theta^{'})\right]^{1/2} \tag{6.4}$$

$$\times\cos[m(\phi-\phi^{'})]\cos[n(\theta-\theta^{'})]\sum_{m,n}(-1)^m\epsilon_m\epsilon_n\frac{\Gamma(n-m+\frac{1}{2})}{\Gamma(n+m+\frac{1}{2})}\begin{cases}P^m_{n-1/2}(\cosh\eta)\ Q^m_{n-1/2}(\cosh\eta^{'}) & \eta^{'}>\eta\\ P^m_{n-1/2}(\cosh\eta^{'})\ Q^m_{n-1/2}(\cosh\eta) & \eta^{'}<\eta\end{cases} \tag{6.5}$$

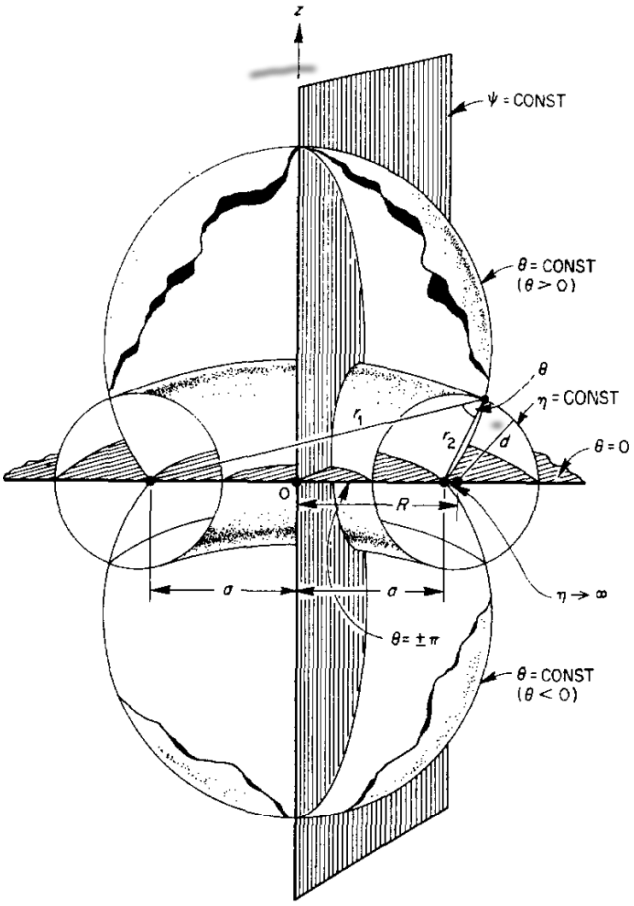

Figure 6.1: Toroidal coordinates (η, θ, ψ) for a torus with circular section defined by its major radius R and minor radius d. From Wong (1973).

where ϵ_m is the Neuman factor defined as : $\epsilon_1 = 1$ and $\epsilon_{m\geq 2} = 2$. $P^m_{n-1/2}$ and $Q^m_{n-1/2}$ are the Legendre functions of the first and second kind of order $n - 1/2$ and degree m.

After integrating over ϕ (the case for axysimmetry), the exterior potential reads :

$$\Psi(\eta^{'}, \theta^{'}) = -GM\frac{2\sqrt{2}}{3\pi^2 a}\frac{\sinh^3\eta_0}{\cosh\eta_0}(\cosh\eta^{'} - \cos\theta^{'})^{1/2}\sum_{n=0}^{\infty}\epsilon_n\cos(n\theta^{'})A_n\cosh(\eta^{'}) \tag{6.6}$$

where

$$A_n(\cosh(\eta^{'}) = P_{n-1/2}(\cosh\eta^{'})C_n(\cosh\eta_0) \tag{6.7}$$

and

$$C_n(\cosh\eta_0) = (n+\tfrac{1}{2})Q_{n+1/2}(\cosh\eta_0)Q^2_{n-1/2}(\cosh\eta_0) - (n-\tfrac{3}{2})Q_{n-1/2}(\cosh\eta_0)Q^2_{n+1/2}(\cosh\eta_0) \tag{6.8}$$

The lowest order is obtained by keeping only the leading term, i.e. by truncating the series when $n \geq 1$. Wong has also produced a formula for the interior solution. More details can be found in Wong (1973).

6.2 New analytical developments for the exterior potential

6.2.1 Introduction

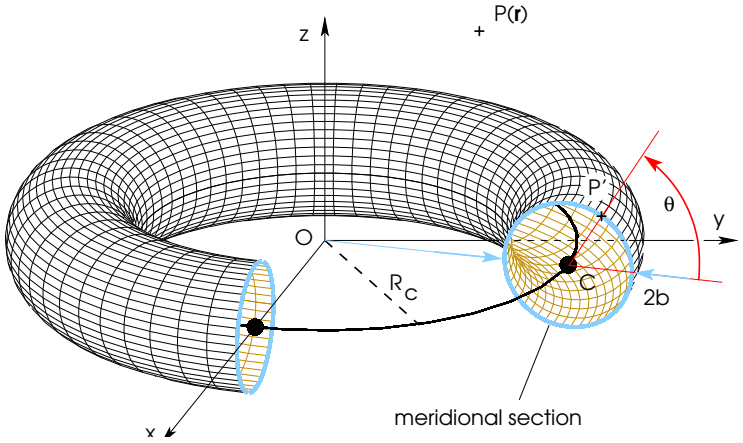

Figure 6.2: The infinitely thin, toroidal shell (main centre O and main radius R_C) with a circular meridional section (centre C and core radius b).

We use a different approach in Huré et al. (2020). Instead of performing a multipole expansion of the Newton's integral toroidal coordinate, we choose to expend the formula giving the potential of a thin toroidal shell using a bivariate Taylor expansion before integrating it over the section to have an expression for the solid torus.

The toroidal shell (see Fig.6.2) is centered on C, has a major radius R_C, a minor radius b and a circular meridional section. We define the shell parameter e as :

$$e \equiv \frac{b}{R_C} \tag{6.9}$$

and $e \in [0,1]$. We use cylindrical coordinates.

Given that the Green function of the Poisson equation is (Kellog, 1929; Durand, 1953) :

$$\mathcal{G}(R,Z;a,z) = -2\sqrt{\frac{a}{R}}k\mathbf{K}(k), \tag{6.10}$$

the gravitational potential generated by the thin toroidal shell at any point in space $P(\vec{r})$ is :

$$\Psi(\vec{r}) = -2G\int_0^{2\pi}\Sigma(\ell)\sqrt{\frac{a}{R}}k\mathbf{K}(k)d\ell, \tag{6.11}$$

where $d\ell = bd\theta$ and :

$$\mathbf{K}(k) = \int_0^{\frac{\pi}{2}}\frac{d\phi}{\sqrt{1-k^2\sin^2\phi}}, \tag{6.12}$$

is the complete elliptic integral of the first kind and

$$k = \frac{2\sqrt{aR}}{\Delta} \in [0,1], \tag{6.13}$$

is its modulus, and

$$\Delta^2 = (R+a)^2 + \zeta^2, \tag{6.14}$$

where $\zeta = Z - z$, and (a,z) are the cylindrical coordinates of any point P' belonging to the shell and Σ is the local surface density. Since our toroidal shell has a circular section, we have :

$$a = R_C + b\cos\theta \text{ and } z = b\sin\theta. \tag{6.15}$$

6.2.2 Exterior potential of a thin toroidal shell at the lowest order

The bivariate Taylor expansion over any function f depending on two independent variables x and y at the location (x_0,y_0) is given by :

$$f(x,y) = f(x_0,y_0) + \sum_{n=1}^{\infty}\frac{1}{n!}\left\{\left[(x-x_0)\frac{\partial}{\partial x'} + (y-y_0)\frac{\partial}{\partial y'}\right]^n f(x',y')\right\}_{\substack{x'=x_0\\y'=y_0}}. \tag{6.16}$$

For our problem, we perform this expansion for $x \equiv a$ and $y \equiv z$ and at $x_0 \equiv R_C$ and $y_0 \equiv 0$ over the specific term $\frac{\mathbf{K}(k)}{\Delta}$ in Eq.(6.11). We have then :

$$\begin{aligned}\left(\frac{\mathbf{K}(k)}{\Delta}\right) = &\left(\frac{\mathbf{K}(k)}{\Delta}\right)\Big|_{\substack{a=R_C\\z=0}} + (a-R_C)\left.\frac{\partial\left(\frac{\mathbf{K}(k)}{\Delta}\right)}{\partial a}\right|_{\substack{a=R_C\\z=0}}\\ &+ z\left.\frac{\partial\left(\frac{\mathbf{K}(k)}{\Delta}\right)}{\partial z}\right|_{\substack{a=R_C\\z=0}} + \frac{1}{2}(a-R_C)^2\left.\frac{\partial^2\left(\frac{\mathbf{K}(k)}{\Delta}\right)}{\partial a^2}\right|_{\substack{a=R_C\\z=0}}\\ &+ (a-R_C)z\left.\frac{\partial^2\left(\frac{\mathbf{K}(k)}{\Delta}\right)}{\partial a\partial z}\right|_{\substack{a=R_C\\z=0}} + \frac{1}{2}z^2\left.\frac{\partial^2\left(\frac{\mathbf{K}(k)}{\Delta}\right)}{\partial a\partial z}\right|_{\substack{a=R_C\\z=0}}\\ &+ \dots.\end{aligned} \tag{6.17}$$

Eq.(6.11) becomes, at the zeroth order :

$$\Psi(\vec{r}) \approx -4G\Sigma_0\kappa_0 b \times 2\pi R_C S_{0,0} \equiv \Psi_0(\vec{r}), \tag{6.18}$$

where Σ_0 is the typical magnitude of the surface density and :

$$\kappa_0 = \frac{\mathbf{K}(k_0)}{\Delta_0}, \tag{6.19}$$

$$k_0^2 = \frac{4R_C R}{\Delta_0^2}, \tag{6.20}$$

$$\Delta_0^2 = (R + R_C)^2 + Z^2, \tag{6.21}$$

and

$$S_{0,0} = \frac{1}{2\pi\Sigma_0 R_C}\int_0^{2\pi} \Sigma(\theta) a d\theta \tag{6.22}$$

called the "surface factor" in the following. If we consider *homogeneous* shells, we set Σ =const.= Σ_0 and so $S_{0,0} = 1$. We thus see that *the potential of a solid shell is equivalent to the one of a thin loop*. But note that this expression is general and can be used for any θ-dependent surface density.

6.2.3 Exterior potential of a solid torus at the lowest order

We can integrate the formula (6.11) over b to have an expression for the solid torus. We have to change Σ for ρdb where ρ is the mass density. Eq.(6.11) therefore becomes :

$$\Psi(\vec{r}) = -4G\int_0^b \int_0^{2\pi} \rho(b', \theta) a \frac{K(k)}{\Delta} a b' d\theta db'. \tag{6.23}$$

By replacing $\left(\frac{\mathbf{K}(k)}{\Delta}\right)$ with the Taylor expansion in Eq.(6.17) and letting ρ_0 be the magnitude of the density, we have :

$$\Psi_0(\vec{r}) = -4G\kappa_0 \times \pi R_C b^2 \rho_0 V_{0,0}, \tag{6.24}$$

where $V_{0,0}$ is the "volume factor" defined in general by

$$V_{0,0} = \frac{1}{\pi\rho_0 R_C b^2}\int_0^b b' db' \int_0^{2\pi} \rho(b', \theta) a d\theta, \tag{6.25}$$

where $b' = e' R_C \leq b$.

When considering a solid torus, we have $V_{0,0} = 1$ and we see that *the potential of a solid torus is equivalent to the one of a thin loop*. As in the the thin shell, it is some kind of approximate "Gauss theorem". And once again, we can prescribe any variable mass density in the section of the torus. For instance, we can choose a density that is invariant with respect to θ but is stratified in term of radius b'. One possibility for such a density is a paraboloid :

$$\rho(b') = \rho_0 \left[1 - \left(\frac{b'}{b}\right)^{2\alpha}\right] \tag{6.26}$$

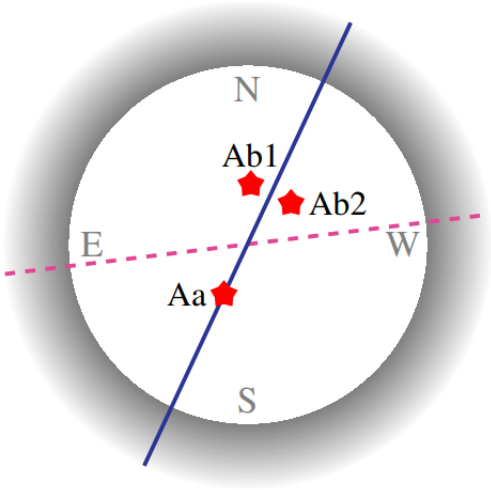

Figure 6.3: Diagram of the triple system in the center of GG Tauri from Brauer et al. (2019)

which gives a volume factor at the zeroth order :

$$V_{0,0} = \frac{\alpha}{1+\alpha} \tag{6.27}$$

Note that when $\alpha \to \infty$, $V_{0,0} \to 1$ and we meet the homogenous case.

A comparison between Wong (1973) and our work was made by Joel E. Tohline and demonstrated that when our parameter e tends towards 0, our first order expression is identical to the first order of Wong's development.

6.3 The ring in the GG Tauri system

GG Tauri is a complex 5-star system made of two stellar components, one at the center of the system and another one orbiting far away. For a few decades, the central component was thought to be a binary but Di Folco et al. (2014) showed that it was in fact a triple system made of a binary and a single star as depicted in Fig.6.3. The other orbiting component is a binary. Between those two components, there is a dense and compact ring shown in Fig.6.4. This ring is rather massive and accounts for 6% to 10% of the total mass of the system and its inner edge is around 180 au and its outer edge is at 260 au (Guilloteau et al., 1999).

The actual challenge regarding this object is to understand the presence of such a massive and yet compact ring in this kind of protoplanetary system. Beust and Dutrey (2005) and Beust and Dutrey (2006) made a first numerical simulation to model the ring using a N-body approach. In this model, the authors use massless test particles that do not interact and therefore the self-gravity is not taken into account. However, it gives some precious insights regarding the evolution and the internal structure of the ring. They showed that the orbiting time is far smaller than the evolution time (see Fig.6.5). Considering a keplerian rotation, the orbiting time t_{orbit} is of the order of a few hundred years whereas the time t_{evol} to witness a significant evolution is of the order of the million years. From this observation, we can say that the ring follows a steady evolution and that studying it in the framework of the equilibrium figure is feasible.

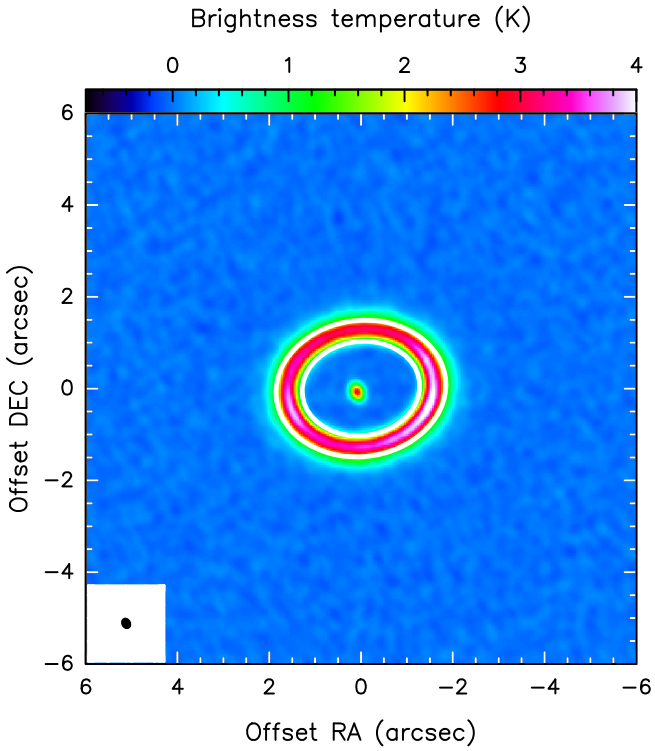

Figure 6.4: Observational data from the GG Tauri ring showing the brightness temperature. The central dot is the triple system. From Phuong et al. (2020)

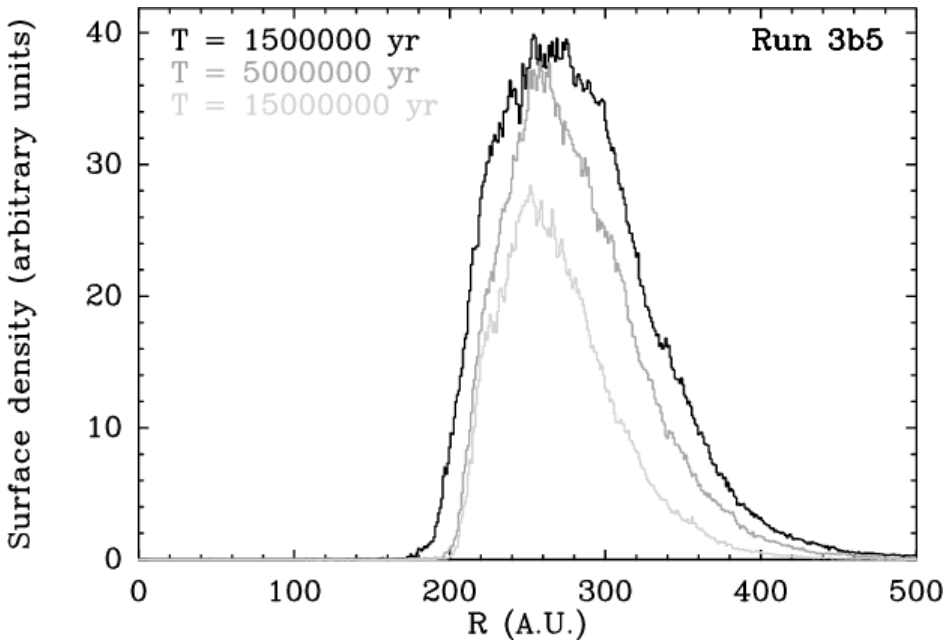

Figure 6.5: Surface density as a function of the radius for a n-body simulation with massless particles. From Beust and Dutrey (2006)

6.3.1 Hypothesis

To treat this physical ring with our model, we need to make a few hypothesis. Some have already been presented in Sect.2.1.1 such as the hydrostatic equilibrium, the isolated system and the polytropic EOS. For this matter, we add :

- Steady evolution hence treated as an equilibrium
- Axisymmetrical fluid as seen in Fig.6.4
- No accretion, no internal circulation, no magnetic field and no viscosity
- prescribed centrifugal potential, here a power-law :

$$\Phi(R) \sim R^{-s} \tag{6.28}$$

The Keplerian rotation is achieved for $s = 1$.

6.3.2 Equation set

The equation set of this problem is similar to the one used for rotating polytrope Eq.(3.11) except that we need to account for the central mass of the triple system. In order to do so, we add an external gravitational potential in the form of a point mass :

$$\Psi_{pm} = -\frac{GM}{R} \tag{6.29}$$

The total dimensionned gravitational potential of the system is now given by

$$\begin{aligned} \Psi_{tot} &= \Psi_{pm} + \Psi_{ring} && (6.30)\\ &= G\rho_0 L^2 \left(\frac{\Psi_{pm}}{G\rho_0 L^2} + \frac{\Psi_{ring}}{G\rho_0 L^2} \right) && (6.31)\\ &= G\rho_0 L^2 \left(\frac{\Psi_{pm}}{G\rho_0 L^2} + \hat{\Psi}_{ring} \right) && (6.32)\\ & && (6.33) \end{aligned}$$

The quantity $\frac{\Psi_{pm}}{G\rho_0 L^2}$ can be rewritten in the form of :

$$\begin{aligned} \frac{\Psi_{pm}}{G\rho_0 L^2} &= \frac{M_{pm}}{\rho_0 L^2 R} \\ &= \frac{M_{pm} M_{ring}}{M_{ring} \rho_0 L^3 \hat{R}} \\ &= \frac{\mu M_{ring}}{\hat{R}} \\ &= \frac{\hat{A}}{\hat{R}} \end{aligned} \tag{6.34}$$

where μ is the mass ratio between the central mass and the loop and $\hat{M}_{ring} = \frac{M_{ring}}{\rho_0 L^3}$ is the dimensionless mass of the ring.

6.3.3 Solver

We use the DROP code to find equilibrium states in those given conditions. We need to set 4 parameters in order to produce a solution which are :

Axis ratio e	0.692 (Guilloteau et al., 1999)
Mass ratio μ	$0.06 \sim 0.1$ (Guilloteau et al., 1999)
Polytropic index n	essentially unknown
Centrifugal exponent s	essentially unknown

Both the axis ratio and the mass ratio are fairly well known thanks to observations (Guilloteau et al., 1999). On the contrary, the rotation law inside the ring and the distribution of matter in it are full of uncertainties.

6.3.4 Internal structure

We first have computed some axisymmetrical internal structure. An example of meridional section for $n = 1.5$ and $s = 1$ is shown in Fig.6.6 on the top panel. On the bottom panel of Fig.6.6 is shown two meridional sections obtained in Beust and Dutrey (2006) with the N-body code without taking into account the self-gravity of the ring. We can see that, with the self-gravity, the ring is far less widen and spreads far much less in terms of radius and altitude. The self-gravity has for effect to bound the matter more tightly. We see that the ring has not a circular section but there is a clear stratification from the center of the ring to the surface.

6.3.5 Effect of the centrifugal exponent s

We can study the effect of the rotation law on the internal structure of the ring. We computed several equilibria with various centrifugal exponent. One equilibrium in sub-keplerian rotation with $s = 0.85$, one equilibrium in keplerian rotation with $s = 1$ and two equilibria in super-keplerian rotation with $s = 2$ and $s = 2.5$. The higher the centrifugal exponent, the higher the gradient of the centrifugal potential and therefore the higher the force produced by rotation. Meridional sections in the physical space are shown in Fig.6.7. We can see that as the rotation gradient increases, the meridional section of the ring inflates.

6.3.6 Effect of the polytropic index n

We also have computed equilibrium for various index. Fig.6.8 shows the surface density for $n = 1$, $n = 2$ and $n = 5$. Surface densities are obtained by integrating the mass density of the ring along the altitude axis. We choose to present surface density because we can compare it directly to observations. We can see that density profiles are different. As the polytropic index increases, the profile is more peaked and presents larger density wings. As a consequence, the maximum surface density is higher for higher n. The maximum of the density is also slighly shifted to the left as n increases.

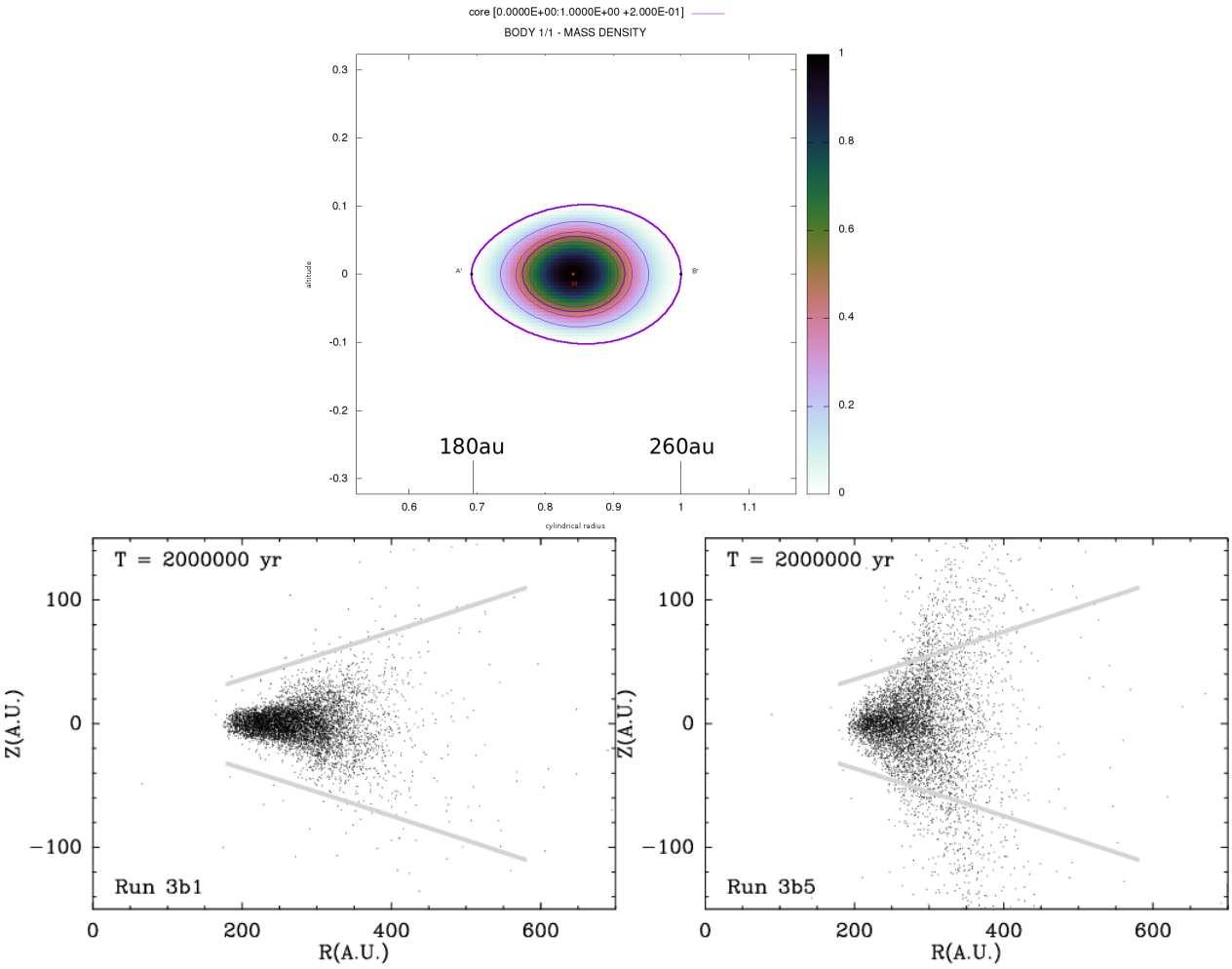

Figure 6.6: (top panel) 3D internal structure obtain with the **DROP***-code of a ring in keplerian rotation, i.e. $s = 1$, of polytropic index $n = 1.5$ and with a mass ratio $\mu = 15.23$. (bottom panel) Meridional section of a n-body simulation taken from Beust and Dutrey (2006).*

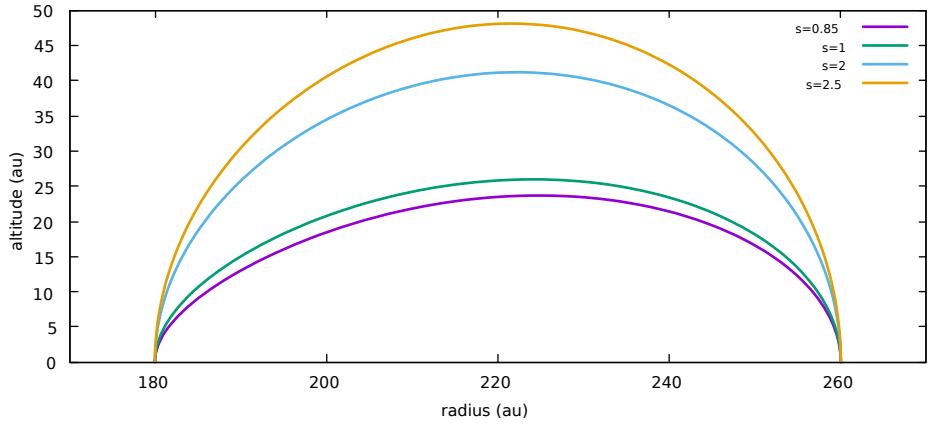

Figure 6.7: Meridional sections of the ring generated with the **DROP***-code for several values of the centrifugal exponent s. The polytropic index is $n = 1.5$ and the mass ratio is $\mu = 15.23$*

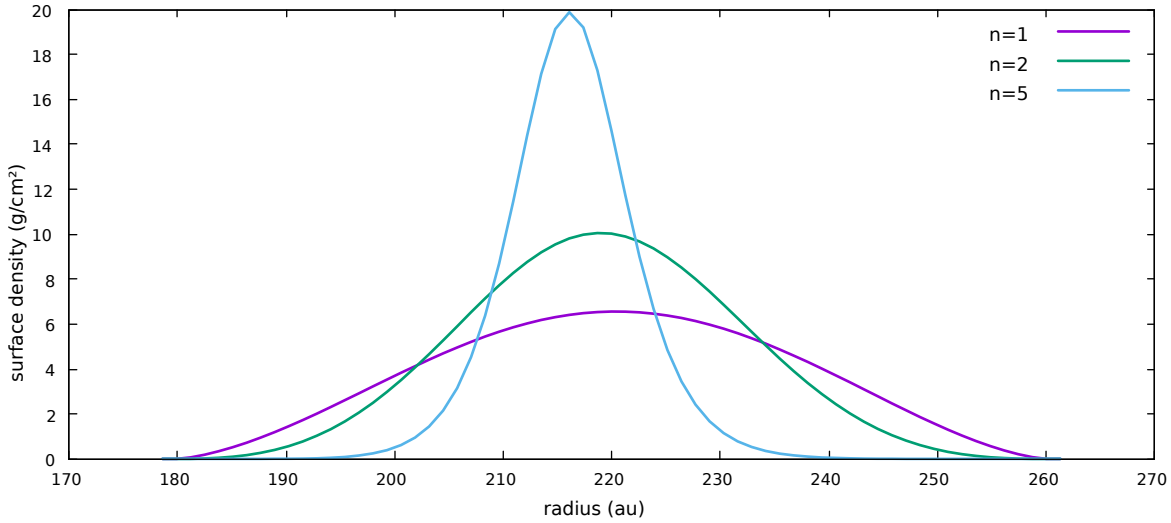

Figure 6.8: Surface densities of the ring generated with the DROP-code for several values of the polytropic index n. The centrifugal exponent is $s = 1$ and the mass ratio is $\mu = 15.23$

6.3.7 Constraints on the internal structure of the ring

In order to sort all these computations and determine which one fits the best the GG Tau system, we need observational parameters to constraint our model. We know that the effect in the change of the EOS of the ring produces far more noticeable modifications than the change in the rotation law. As a consequence, it seems more relevant to reproduce the observed density surface than the meridional section. Moreover, the density surface is more easily obtained than other geometrical properties (Dutrey et al., 1997; Tang et al., 2016; Phuong et al., 2018, 2020; Phuong et al., 2020) For instance, a way to constrain properties would be to fit the FWHM of the density of the ring (see Fig.6.9). It is directly linked to the polytropic index. This work is still under progress.

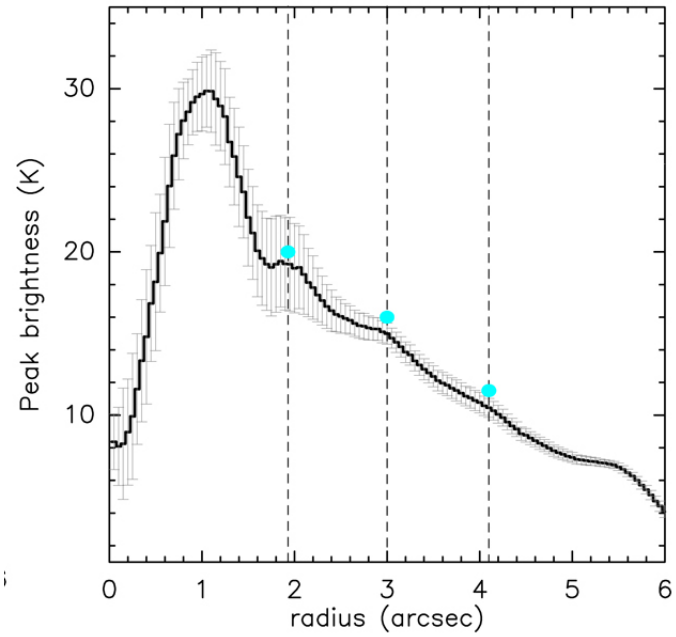

Figure 6.9: Radial dependance of the peak brightness temperature of CO(2-1) in the plane of the disk. From Phuong et al. (2020).

Chapter 7

Conclusion and perspectives

In this thesis, we have studied self-gravitating, multidomain systems which can consist in multibody fluids or multi-layer systems. We have seen that such systems can be handled from the Bernoulli equation whose solutions is captured with the SCF method. In the case of a multi-layer configuration (where pressure balance at the interface sets a severe constraint), the key role of the mass-density jump coupled with the rotational discontinuity has been demonstrated. This is interesting for stellar and planetary systems. Many open questions have been addressed in the manuscript.

7.1 Improvements of the DROP code

The two major points of improvments made in the DROP code is the treatment of multibody and multi-layer systems with any kind of differental rotation profile. We have reported the results assuming a rigid rotation, a v-constant and j-constant rotation. In the case of the GG Tau system (see below), a quasi-keplerian rotation has been tested. The code is capable of generating many kinds of configurations, with a number of bodies and layers theoretically as large as desired. The only limitation is obviously the computation power at our disposal (the time for convergence of the SCF iterations may become prohibitively long). While not discussed here, we can also produce multidomain systems (see Fig.7.1).

There is still work to be done with the code. We have only worked with axisymmetrical configurations, and the extension to 3D equilibria seem necessary to characterized interactions of close binaries like double stars or a hot Jupiters orbiting close to parent star. In its current state, the code computes the equilibrium under three forces : the gravitational force, the centrifugal force and pressure forces. More physical processes could be implemented in order to carry out more complex equilibria. For instance, this could be irradiation from an external source, or the magnetic field (internal or external). Stars are the seat of highly strong magnetic fields and it would be interesting to understand its effect on the star and its surroundings. At last, the implementation of a generalised adaptative mesh for any rotation is required to have better accuracy on, for instance, the core mass fraction - core radius fraction of multi-layer systems.

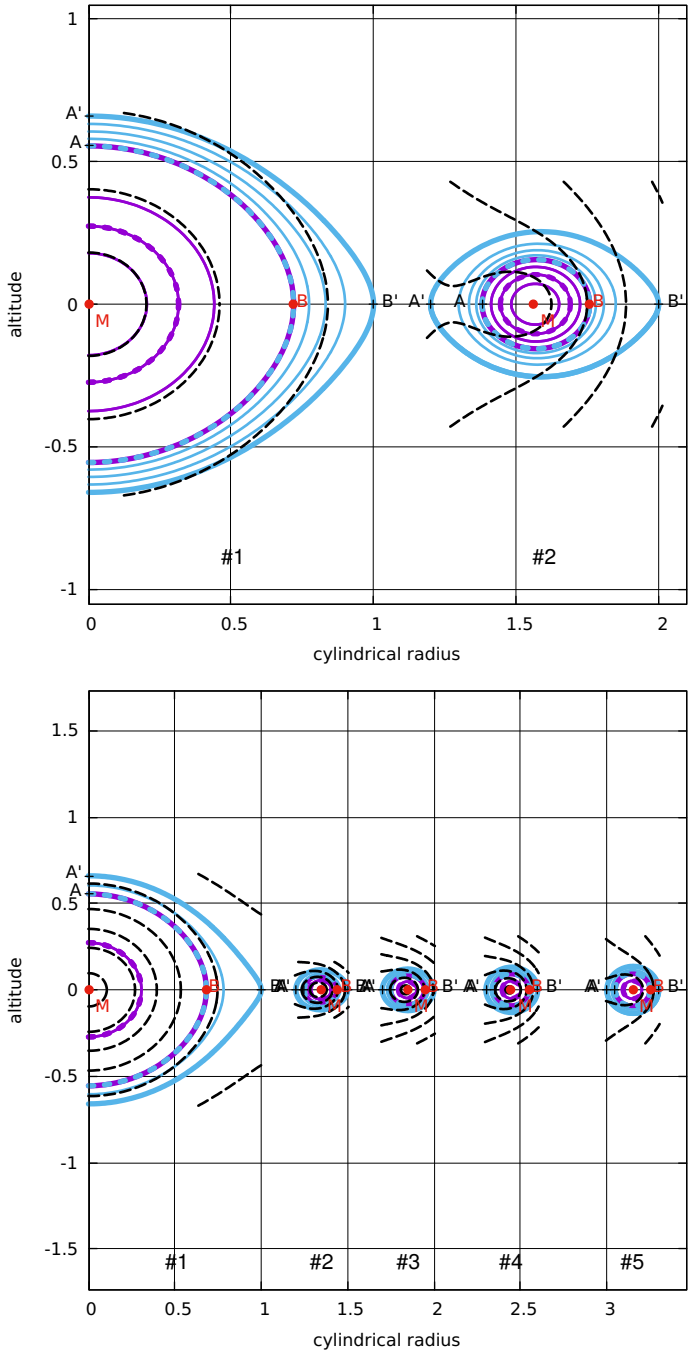

Figure 7.1: Examples of multidomain configurations computed with the `DROP` *code.*

7.2 Multibody configurations

We have investigated the 2-body equilibrium composed of a central spheroid and a surrounding ring in details. We have shown that, in both the incompressible and compressible assumption, the solutions are gathered on a well defined are in the reference diagram $\omega^2 - j^2$. We have also shown that the higher the density contrast between the ring and the spheroid, the higher rotation the system can sustain. Bifurcations along the ascending

part of the Maclaurin are made of a dominant spheroid and a tiny massless loop. We pointed out that a compressible spheroid or ring can exceed its critical rotation with the gravitational support of its companion. We have highlighted the connections between the end-point of the ε_2 sequence, the end-point of the ε_3 sequence, the Maclaurin sequence and the One-Ring sequence.

Other space parameter surveys can be done with a ring-ring system or with more than 2 objects. In the compressible assumption, we have suggested that such configurations could help in understanding the properties and structure of transient circumstellar ring in Be-stars, ringed accretion and ring segregation in young protoplanetary disk. There is also more physics to be done with a less idealistic EOS. It could have application in various field of physics such as the physics of fast rotators like Be-Stars (Meilland et al., 2006), the physics of planetary disks (Wisdom and Tremaine, 1988) and the genesis of the Moon via a possible Synestia (Lock et al., 2018).

7.3 The Schönberg-Chandrasekhar limit

It was known that the SC-limit or SC-like-limit is modified under the effect of rotation (Maeder, 1971; Kadam et al., 2016) but some features were missed. For starters, the variation of the SC-limit in (Maeder, 1971) was greatly underestimated. We show that, in solid rotation, the SC-like-limit can be reduced as much as 20%. We also report the existence of a critical rotation that was not seen in (Kadam et al., 2016). One possibility to explain such a difference between these two works is the treatment of the discontinuity. Finally, we point out that the core get rounder as the β-parameter decreases. Regarding differential rotation, there is apparently no great litterature and much remains to be done. We have shown that differential rotation decreases the SC-like-limit but in a far more drastic manner. For a v-constant rotation, the SC-like-limit is decreased by 40%. One strong difference from the solid rotation case is that no critical rotation is found for the same axis ratio.

We have demonstrated the impact of a rotation jump at the interface of the core-envelope in a 2-layer system and its effect on the SC-like-limit is under investigation. A study on the effect of the presence of a photosphere on the SC-like-limit has to be done. Would the SC-like-limit change drastically using a 3-layer polytrope, or would remain overall the same ? The complete study of differential rotation for j-constant is still under progress.

7.4 Internal structures and degeneracies

We have shown that different internal structures can lead to the same mass-radius and mass-radius-surface velocity relationship by tweaking the input parameters : the geometrical properties, the EOS of the layers, the density and rotation jumps. We have also demonstrated that there is no similarity between the shape of the deepest layer and the shape of the outermost one. Therefore, there is an uncertainty on the stratification of the body. This is especially challenging regerading the undertanding of the internal structure of planets and exoplanets.

We have developed diagnostic tools able to model and characterize internal structure of observed bodies that are known to be stratified. Current applications are in progress on Jupiter and Saturn to constraint their internal structure by reproducing their observables : the mass, the central density, the rotation rate and the gravitational moment. We have tried to fit the gravitational moments for Jupier with our code, in the 2-layer case with the data taken from Helled (2019).

7.5 Applications to the GG Tau and HL Tau systems

According to Guilloteau et al. (1999), the GG Tau ring relative to the central triplet is large enough to expect an impact of self-gravity on the internal structre of the ring and its own spin, namely a deviation on the assumed keplerian law. Super-keplerian motion is expected. We have started an study of the GG Tau ring based on the `DROP` code. The parameters that can be constrained with repect to available observational data are mainly the EOS and the rotation profile. Self-gravity has a clear impact on the meridional section, whatever the polytropic index: the ring is probably less extended than previously thought (Beust and Dutrey, 2005, 2006). The best fit seems a torus with polytropic index ≤ 1. We have also considered a rotation law close to Keplerian. More work is needed to determine more precisely the best profile. Another interesting aspect is the possible seperation of gas and dust in the ring. It is likely that dust is more gathered around the midplane than the gas. Our two-layer model could then be used in this context. It would be interesting to couple such an analysis with hydrodynamical, time-dependent simulations.

Another system that should be worth to investigate is the HL Tau system, which shows an exceptional multi-ring structure, with well-defined gaps. While the presence of forming planets in the gaps is highly suspected, we can not rule out that the systems is a self-gravitating systems in which axially symetrical instabilities have lead to detached ring. This second hypothesis can be tested with our model.

Appendices

Appendix A

Tables for the bipolytropes

bipolytrope $\mathcal{L}=2$	core $(l=1)$	envelope $(l=2)$	total
N			129
n_l	+1.5000E+00	+1.5000E+00	
$z(A_l)$	+5.0000E-01	+7.5000E-01	
q_l	+6.6667E-01	+3.3333E-01	
$\alpha_l(\mathrm{A}_l)$		+4.0000E+00	
ω_l		+1.0000E+00	
SCF-iterations			41
$\hat{H}_l(\mathrm{A}_l)$	+7.0193E-02	+1.0000E+00	
$\beta_l^\dagger$	+1.0000E+00	+4.6493E-03	
nodes Γ_l	151	251	
$\hat{V}_l$	+6.0218E-01	+2.3359E+00	+2.9381E+00
$\hat{M}_l$	+1.2796E-01	+4.8909E-01	+1.3024E-01
C_{1l}	+2.9748E-01	+1.7965E+01	
C_{2l}	+8.3597E-02	+1.7981E+01	
C_{3l}	-2.3498E-01	-3.7067E+01	
J_l	+2.5264E-03	+4.2020E-02	+2.7218E-03
$\hat{T}_l$	+3.6523E-04	+1.3066E+00	+3.9348E-04
$\hat{W}_l$	-2.4972E-02	-1.1065E+01	-2.5212E-02
$\hat{U}_l$	+2.4289E-02	+6.3688E+00	+2.4427E-02
VP			+2.1788E-06
VT			+8.6419E-05

Table A.1: Input (top) and output (bottom) quantities for the rigidly rotating bipolytrope with a mass density jump $\alpha_2 = 4$ and $e_2 = 0.75$ as the axis ratio (see Fig. 5.17). See Tab.5.2 for the meaning of the variables.

bipolytrope $\mathcal{L}=2$	core $(l=1)$	envelope $(l=2)$	total
N			129
n_l	+1.5000E+00	+1.5000E+00	
$z(A_l)$	+5.0000E-01	+7.5000E-01	
q_l	+6.6667E-01	+3.3333E-01	
$\alpha_l(\mathrm{A}_l)$		+4.0000E+00	
ω_l		+2.0000E+00	
SCF-iterations			46
$\hat{H}_l(\mathrm{A}_l)$	+7.3827E-02	+1.0000E+00	
$\beta_l^\dagger$	+1.0000E+00	+5.0149E-03	
nodes Γ_l	161	251	
$\hat{V}_l$	+7.7608E-01	+2.1953E+00	+2.9714E+00
$\hat{M}_l$	+1.5341E-01	+3.9258E-01	+1.5538E-01
C_{1l}	+3.2191E-01	+1.8956E+01	
C_{2l}	+1.8853E-01	+1.8797E+01	
C_{3l}	-2.7469E-01	-4.0557E+01	
J_l	+5.5445E-03	+5.4590E-02	+5.8183E-03
$\hat{T}_l$	+1.2037E-03	+1.1816E+00	+1.2334E-03
$\hat{W}_l$	-3.3411E-02	-9.3243E+00	-3.3645E-02
$\hat{U}_l$	+3.1063E-02	+4.6898E+00	+3.1181E-02
VP			+2.3341E-06
VT			+6.9375E-05

Table A.2: Input (top) and output (bottom) quantities for the rotating bipolytrope with axis ratio $e_2 = 0.75$, mass density jump $\alpha_2 = 4$ and rotational discontinuity $\omega_2 = 2$ (see Fig. 5.14). See Tab. 5.2 for the meaning of the variables.

bipolytrope $\mathcal{L}=2$	core $(l=1)$	envelope $(l=2)$	total
N			129
n_l	+1.0000E+00	+2.0000E+00	
$z(A_l)$	+5.0000E-01	+7.5000E-01	
q_l	+6.6667E-01	+3.3333E-01	
$\alpha_l(\mathrm{A}_l)$		+4.0000E+00	
ω_l		+2.0000E+00	
SCF-iterations			46
$\hat{H}_l(\mathrm{A}_l)$	+6.4945E-02	+1.0000E+00	
$\beta_l^\dagger$	+1.0000E+00	+1.6236E-02	
nodes Γ_l	164	251	
$\hat{V}_l$	+8.4114E-01	+2.1654E+00	+3.0065E+00
$\hat{M}_l$	+2.8134E-01	+2.8188E-01	+2.8591E-01
C_{1l}	+4.2501E-01	+1.0200E+01	
C_{2l}	+3.2386E-01	+9.9732E+00	
C_{3l}	-5.0766E-01	-2.2767E+01	
J_l	+1.7641E-02	+4.9628E-02	+1.8446E-02
$\hat{T}_l$	+5.0195E-03	+4.3486E-01	+5.1342E-03
$\hat{W}_l$	-9.8506E-02	-3.8160E+00	-9.9512E-02
$\hat{U}_l$	+8.8811E-02	+1.6494E+00	+8.9246E-02
VP			+2.3311E-06
VT			+2.3425E-05

Table A.3: Input (top) and output (bottom) quantities for the rotating bipolytrope with axis ratio $e_2 = 0.75$*, mass density jump* $\alpha_2 = 4$ *and rotational discontinuity* $\omega_2 = 2$ *when* $n_1 < n_e$ *(see Figs. 5.14 and 5.15). See Tab. 5.2 for the meaning of the variables.*

bipolytrope $\mathcal{L}=2$	core $(l=1)$	envelope $(l=2)$	total
N			129
n_l	+2.0000E+00	+1.0000E+00	
$z(A_l)$	+5.0000E-01	+7.5000E-01	
q_l	+6.6667E-01	+3.3333E-01	
$\alpha_l(\mathrm{A}_l)$		+4.0000E+00	
ω_l		+2.0000E+00	
SCF-iterations			47
$\hat{H}_l(\mathrm{A}_l)$	+8.5709E-02	+1.0000E+00	
$\beta_l^\dagger$	+1.0000E+00	+1.8365E-03	
nodes Γ_l	159	251	
$\hat{V}_l$	+7.4083E-01	+2.2098E+00	+2.9506E+00
$\hat{M}_l$	+8.7209E-02	+5.9537E-01	+8.8302E-02
C_{1l}	+2.4351E-01	+3.0305E+01	
C_{2l}	+1.1095E-01	+3.0207E+01	
C_{3l}	-1.5115E-01	-6.3360E+01	
J_l	+1.8902E-03	+6.8595E-02	+2.0162E-03
$\hat{T}_l$	+3.1481E-04	+3.1103E+00	+3.2530E-04
$\hat{W}_l$	-1.2248E-02	-2.1469E+01	-1.2320E-02
$\hat{U}_l$	+1.1629E-02	+1.2490E+01	+1.1671E-02
VP			+1.4776E-06
VT			+1.1993E-04

Table A.4: Input (top) and output (bottom) quantities for the rotating bipolytrope with axis ratio $e_2 = 0.75$, mass density jump $\alpha_2 = 4$ and rotational discontinuity $\omega_2 = 2$ when $n_1 > n_e$ (see Figs. 5.14 and 5.15). See Tab. 5.2 for the meaning of the variables.

bipolytrope $\mathcal{L}=2$	core $(l=1)$	envelope $(l=2)$	total
N			129
n_l	+5.0000E-01	+3.0000E+00	
$z(A_l)$	+6.4881E-01	+7.5000E-01	
q_l	+8.6508E-01	+1.3492E-01	
$\alpha_l(\mathrm{A}_l)$		+7.0000E+00	
ω_l		+1.1032E-01	
SCF-iterations			35
$\hat{H}_l(\mathrm{A}_l)$	+1.0087E-02	+1.0000E+00	
$\beta_l^\dagger$	+1.0000E+00	+1.4348E-02	
nodes Γ_l	190	251	
$\hat{V}_l$	+1.1429E+00	+1.7940E+00	+2.9369E+00
$\hat{M}_l$	+6.5706E-01	+1.0494E+00	+6.7211E-01
C_{1l}	+7.2364E-01	+9.4965E+00	
C_{2l}	+4.7589E-02	+3.0066E+01	
C_{3l}	-1.0184E+00	-6.1991E+01	
J_l	+2.0445E-02	+9.3217E-02	+2.1782E-02
$\hat{T}_l$	+2.2300E-03	+6.4236E+00	+3.5524E-03
$\hat{W}_l$	-4.4404E-01	-3.5518E+01	-4.5136E-01
$\hat{U}_l$	+4.4238E-01	+9.3063E+00	+4.4430E-01
VP			+4.5970E-05
VT			+1.0185E-04

Table A.5: Input (top) and output (bottom) quantities for the configuration sharing the same degeneracy parameter as for the one corresponding to Tab A.1. See Tab. 5.2 for the meaning of the variables.

Appendix B

Optimization of the fixed point

We can improve the convergence speed of the fixed point iteration by modifying the function $h(\beta, \lambda) = \lambda f(\beta) + (1 + \lambda)\beta$ avec $\lambda \in \mathbb{R}$. To maximize the convergence, we need that $\frac{\partial h}{\partial \beta} = 0$. Using this relation, we can find a value of λ optimizing the convergence :

$$\lambda_{opt} = \frac{1}{1 - \frac{\partial f}{\partial \beta}} \tag{B.1}$$

B.1 low solution

In the case of the low solution solution, f(β) is defined as :

$$f(\beta) = \frac{1}{\alpha}\left(\frac{1}{1 + \bar{\alpha}\frac{\Delta\tilde{\Psi}_{AM} + \beta C_2' \Delta\tilde{\Phi}_{AM}}{\Delta\tilde{\Psi}_{A'A} + \beta C_2' \Delta\tilde{\Phi}_{A'A}}}\right)^{n_c} = \frac{1}{\alpha}\left(\frac{1}{1 + \bar{\alpha}k(\beta)}\right)^{n_c} \tag{B.2}$$

with

$$k(\beta) = \frac{\Delta\tilde{\Psi}_{AM} + \beta C_2' \Delta\tilde{\Phi}_{AM}}{\Delta\tilde{\Psi}_{A'A} + \beta C_2' \Delta\tilde{\Phi}_{A'A}} \tag{B.3}$$

However,

$$\frac{\partial f}{\partial \beta} = \frac{1}{\alpha}\frac{\partial}{\partial \beta}\left(\frac{1}{1 + \bar{\alpha}k(\beta)}\right)^{n_c} = -\frac{\bar{\alpha} n_c}{\alpha}\frac{\partial k}{\partial \beta}\left(\frac{1}{1 + \bar{\alpha}k(\beta)}\right)^{n_c+1} \tag{B.4}$$

We only need to have the derivative of k with respect to β. Let us define $k = \frac{u}{v}$ or :

$$\begin{gathered} u(\beta) = \Delta\tilde{\Psi}_{AM} + \beta C_2' \Delta\tilde{\Phi}_{AM} \\ \text{and} \\ v(\beta) = \Delta\tilde{\Psi}_{A'A} + \beta C_2' \Delta\tilde{\Phi}_{A'A} \end{gathered} \tag{B.5}$$

We also have : $\Delta\tilde{\Psi}_{XY} = \tilde{\Psi}^c_{XY} - \beta\tilde{\Psi}^e_{XY}$ and $\beta C_2' = -\frac{\Delta\tilde{\Psi}_{A'B'}}{\Delta\tilde{\Phi}_{A'B'}}$.
It yields :

$$\begin{gathered} u' = \frac{\partial u}{\partial \beta} = \Delta\tilde{\Psi}^e_{AM} - \Delta\tilde{\Psi}^e_{A'B'}\frac{\Delta\tilde{\Phi}_{AM}}{\Delta\tilde{\Phi}_{A'B'}} \\ \text{and} \\ v' = \frac{\partial v}{\partial \beta} = \Delta\tilde{\Psi}^e_{A'A} - \Delta\tilde{\Psi}^e_{A'B'}\frac{\Delta\tilde{\Phi}_{A'A}}{\Delta\tilde{\Phi}_{A'B'}} \end{gathered} \tag{B.6}$$

The expression of k' is therefore given by :

$$\frac{\partial k}{\partial \beta} = \frac{u'v - uv'}{v^2} \tag{B.7}$$

$$\frac{\partial k}{\partial \beta} = \frac{\left(\Delta\tilde{\Psi}^e_{AM} - \Delta\tilde{\Psi}^e_{A'B'}\frac{\Delta\tilde{\Phi}_{AM}}{\Delta\tilde{\Phi}_{A'B'}}\right)\left(\Delta\tilde{\Psi}_{A'A} + \beta C_2'\Delta\tilde{\Phi}_{A'A}\right) - \left(\Delta\tilde{\Psi}_{AM} + \beta C_2'\Delta\tilde{\Phi}_{AM}\right)\left(\Delta\tilde{\Psi}^e_{A'A} - \Delta\tilde{\Psi}^e_{A'B'}\frac{\Delta\tilde{\Phi}_{A}}{\Delta\tilde{\Phi}_{A'}}\right.}{\left(\Delta\tilde{\Psi}_{A'A} + \beta C_2'\Delta\tilde{\Phi}_{A'A}\right)^2} \tag{B.8}$$

We have now the complete formula giving λ_{opt} by using Eqs.(B.1), (B.4) and (B.8) :

$$\lambda_{opt_f} = \frac{1}{1 + \frac{\bar{\alpha}n_c}{\alpha}\frac{\partial k}{\partial \beta}\left(\frac{1}{1+\bar{\alpha}k(\beta)}\right)^{n_c+1}} \tag{B.9}$$

The fixed point iteration is now on $h(\beta, \lambda_{opt_f}) = \lambda_{opt_f} f(\beta) + (1 - \lambda_{opt_f})\beta$. An example is given in Fig.B.1. We see that the optimized convergence is ~ 3 times faster.

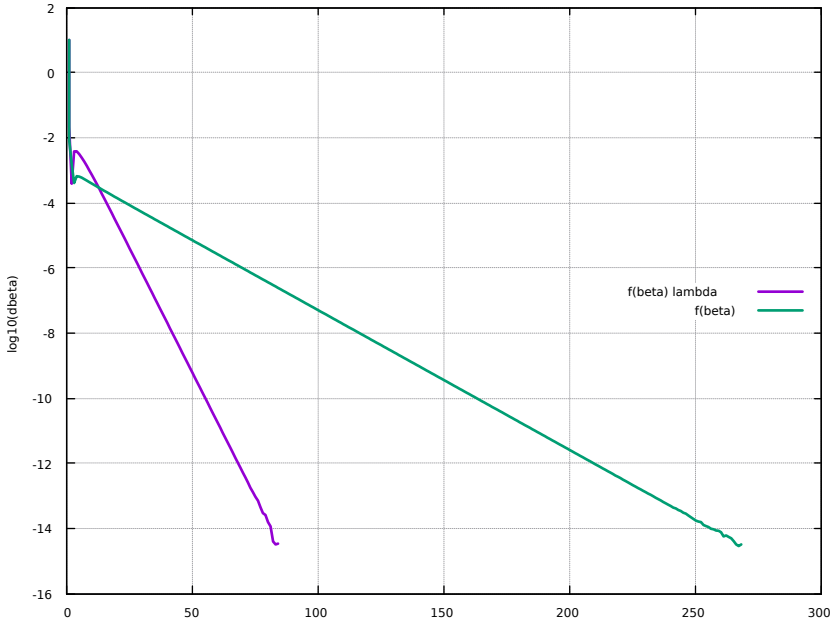

Figure B.1: Convergence of $f(\beta)$ in green and $h_f(\beta)$ in purple

B.2 High solution

B.2.1 $f_1(\beta) = 2\beta - f(\beta)$

The function to optimize is not $f(\beta)$ anymore but $2\beta - f(\beta)$. The only thing changing from Sect.B.1 is the derivative which is now : $\frac{\partial f_1}{\partial \beta} = 2 - f'(\beta)$. We find that :

$$\lambda_{opt_{f_1}} = \frac{1}{1 - 2 - \frac{\bar{\alpha}n_c}{\alpha}\frac{\partial k}{\partial \beta}\left(\frac{1}{1+\bar{\alpha}k(\beta)}\right)^{n_c+1}} \tag{B.10}$$

And the optimized function is :

$$h_{f1}(\beta,\lambda) = \lambda_{opt_{f_1}} f_1(\beta) + (1-\lambda_{opt_{f_1}})\beta = \lambda_{opt_{f_1}}(2\beta - f(\beta)) + (1-\lambda_{opt_{f_1}})\beta \tag{B.11}$$

An example is given in Fig.B.2.

B.2.2 $g(\beta)$

The function to optimize is g(β) :

$$g(\beta) = \frac{\frac{1}{\tilde{\alpha}}\left(\frac{1}{(\alpha\beta)^{\frac{1}{n_c}}} - 1\right)\left(\Delta\tilde{\Psi}^c_{A'A} - \frac{\Delta\tilde{\Phi}_{A'A}}{\Delta\tilde{\Phi}_{A'B'}}\Delta\tilde{\Psi}^c_{A'B'}\right) - \left(\Delta\tilde{\Psi}_{AM} - \frac{\Delta\tilde{\Phi}_{AM}}{\Delta\tilde{\Phi}^c_{A'B'}}\Delta\tilde{\Psi}^c_{A'B'}\right)}{\left(\Delta\tilde{\Psi}^e_{AM} - \frac{\Delta\tilde{\Phi}_{AM}}{\Delta\tilde{\Phi}_{A'B'}}\Delta\tilde{\Psi}^e_{A'B'}\right) - \frac{1}{\tilde{\alpha}}\left(\frac{1}{(\alpha\beta)^{\frac{1}{n_c}}} - 1\right)\left(\Delta\tilde{\Psi}^e_{A'A} - \frac{\Delta\tilde{\Phi}_{A'A}}{\Delta\tilde{\Phi}_{A'B'}}\Delta\tilde{\Psi}^e_{A'B'}\right)} \tag{B.12}$$

Let us set :

$$g(\beta) = \frac{A - (\alpha\beta)^{\frac{1}{n_c}}(A+B)}{(\alpha\beta)^{\frac{1}{n_c}}(C+D) - D} = \frac{u}{v}, \tag{B.13}$$

where :

$$\begin{aligned} A &= \left(\Delta\tilde{\Psi}^c_{A'A} - \frac{\Delta\tilde{\Phi}_{A'A}}{\Delta\tilde{\Phi}_{A'B'}}\Delta\tilde{\Psi}^c_{A'B'}\right), \\ B &= \left(\Delta\tilde{\Psi}_{AM} - \frac{\Delta\tilde{\Phi}_{AM}}{\Delta\tilde{\Phi}^c_{A'B'}}\Delta\tilde{\Psi}^c_{A'B'}\right), \\ C &= \left(\Delta\tilde{\Psi}^e_{AM} - \frac{\Delta\tilde{\Phi}_{AM}}{\Delta\tilde{\Phi}_{A'B'}}\Delta\tilde{\Psi}^e_{A'B'}\right), \\ D &= \left(\Delta\tilde{\Psi}^e_{A'A} - \frac{\Delta\tilde{\Phi}_{A'A}}{\Delta\tilde{\Phi}_{A'B'}}\Delta\tilde{\Psi}^e_{A'B'}\right). \end{aligned} \tag{B.14}$$

We then have :

$$\frac{\partial g}{\partial\beta} = \frac{u'v - uv'}{v^2}, \tag{B.15}$$

with :

$$\begin{aligned} u(\beta) &= A - (\alpha\beta)^{\frac{1}{n_c}}(A+B) \\ v(\beta) &= (\alpha\beta)^{\frac{1}{n_c}}(C+D) - D \end{aligned} \tag{B.16}$$

and :

$$\begin{aligned} u' &= -(A+B)\frac{(\alpha\beta)^{\frac{1}{n_c}}}{\beta n_c} \\ v' &= (C+D\frac{(\alpha\beta)^{\frac{1}{n_c}}}{\beta n_c} \end{aligned} \tag{B.17}$$

The expression of λ_{opt_g} is :

$$\lambda_{opt_g} = \frac{1}{1-\frac{\partial g}{\partial\beta}} = \frac{1}{1 - \frac{\left(\left(-(A+B)\frac{(\alpha\beta)^{\frac{1}{n_c}}}{\beta n_c}\right)\left((\alpha\beta)^{\frac{1}{n_c}}(C+D)-D\right) - \left(A-(\alpha\beta)^{\frac{1}{n_c}}(A+B)\right)\left((C+D)\frac{(\alpha\beta)^{\frac{1}{n_c}}}{\beta n_c}\right)\right)}{\left((\alpha\beta)^{\frac{1}{n_c}}(C+D)-D\right)^2}} \tag{B.18}$$

And the expression of the optimized function is finally : $h_g = \lambda_{opt_g} g(\beta) + (1+\lambda_{opt_g})g(\beta)$

An example of is given in Fig.B.2. We see that the convergence of the g function is a bit faster than the f_1 function. However, the optimized fixed point algorithm for f_1 and g are almost equivalent, although less smooth than their non-optimized counterpart.

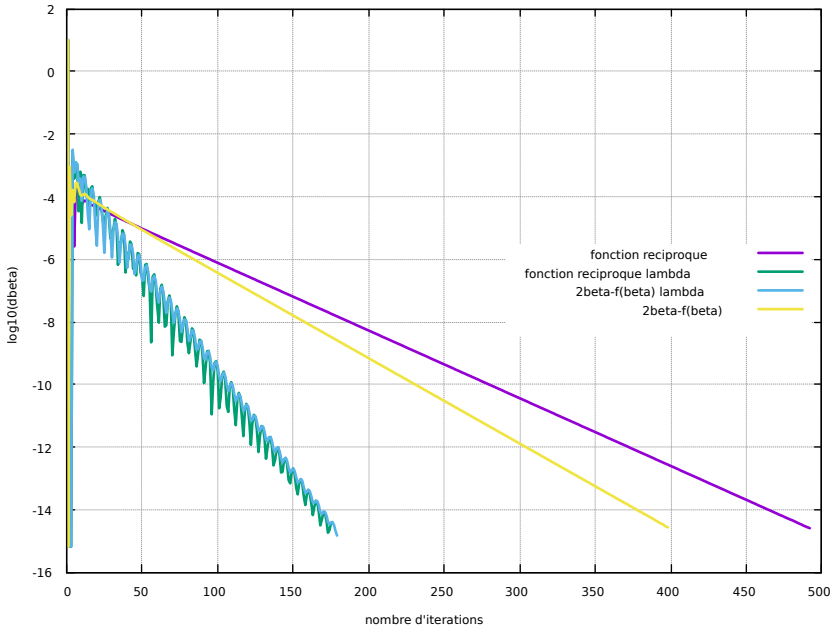

Figure B.2: Convergence of : $f_1(\beta)$ in yellow, $h_{f_1}(\beta)$ in light blue, $g(\beta)$ in purple and h_g in green.

Appendix C

Accepted papers

MNRAS **000**, 1–?? (???) Preprint 19 July 2019 Compiled using MNRAS LATEX style file v3.0

Rigidly rotating, incompressible spheroid-ring systems: new bifurcations, critical rotations and degenerate states

B. Basillais[1,2⋆], and J.-M. Huré[1,2]
[1] *Univ. Bordeaux, LAB, UMR 5804, F-33615, Pessac, France*
[2] *CNRS, LAB, UMR 5804, F-33615, Pessac, France*

Received ??? / Accepted ???

ABSTRACT

The equilibrium of incompressible spheroid-ring systems in rigid rotation is investigated by numerical means for a unity density contrast. A great diversity of binary configurations is obtained, with no limit neither in the mass ratio, nor in the orbital separation. We found only detached binaries, meaning that the end-point of the ϵ_2-sequence is the single binary state in strict contact, easily prone to mass-exchange. The solutions show a remarkable confinement in the rotation frequency-angular momentum diagram, with a total absence of equilibrium for $\Omega^2/\pi G\rho \gtrsim 0.21$. A short band of degeneracy is present next to the one-ring sequence. We unveil a continuum of bifurcations all along the ascending side of the Maclaurin sequence for eccentricities of the ellipsoid less than ≈ 0.612 and which involves a gradually expanding, initially massless loop.

Key words: gravitation — methods: numerical — stars: interiors — (stars:) binaries: general — stars: rotation

1 INTRODUCTION

Despite its academic character, the theory of figures gives essential information on self-gravitating fluids like the mass, size, shape, rotation rate and energy content, which can be confronted with observations (Horedt 2004). A broad range of applications is concerned, e.g. normal and compact stars, binaries, interstellar cores, planets (and initially the Earth), and galaxies (see e.g. Chandrasekhar 1969). There is a large variety of allowed configurations depending on the equation of state, prescribed rotation profile, internal circulations and environmental effects like external gravity, magnetic fields or ambient pressure (see e.g. Hachisu 1986a; Fujisawa & Eriguchi 2014; Huré et al. 2018). The possibility of discovering new states, even in the incompressible and axisymmetrical limits, is an exciting source of motivation and also very challenging from a technical point of view (Hachisu & Eriguchi 1984; Hachisu et al. 1986b; Nishida et al. 1992; Woodward et al. 1992).

In a pioneering paper, Eriguchi & Hachisu (1983) have studied the conditions for "core-ring" and especially "ring-ring" equilibria and their position in the classical ω^2-j^2 diagram. In particular, they showed that there is a maximum rotation rate for core-ring states in rigid rotation. More recently, Ansorg et al. (2003) have characterized the bifurcations along the descending part of the Maclaurin sequence (MLS) with an unprecedented accuracy from spectral decomposition of the fluid boundary (see also Hachisu et al. 1986a). They computed new series of figures, denoted $\epsilon_{k\geq 2}$, which display a strong flattening and a marked wavy shape. When k is an even number, $\frac{k}{2}$ pinchings are present on both sides of the equatorial plane. At the end-point of the corresponding sequence, the spheroid is on the verge of splitting into a central core surrounded by $m-1=\frac{k}{2}$ ring(s). A similar phenomenon exists when k is an odd number (a single ring may lead to multiple, concentric ringlets). We have continued this investigation for $k=2$ (i.e., the "spheroid-ring" case) to determine which states can really exist beyond the sequence ending. This kind of configuration is important for the physics of accretion disks and tori around normal and compact stars (Masuda et al. 1998; Abramowicz et al. 1998), mass-transfer, rotation and angular momentum exchange between the two components. For this purpose, we have used a new version of the `DROP` code (Huré & Hersant 2017) which enables to take into account $m>1$ detached bodies in mutual interaction. The wide exploration of the parameter space permits to answer several major pending questions. In particular, no contact binary other than the one reported in Ansorg et al. (2003) was detected. The equilibrium states clearly fill the bottom part of the ω^2-j^2 diagram (the rotation frequency must not exceed a certain threshold), while they slightly overtake the one-ring sequence (ORS) (e.g. Hachisu 1986a). In some cases, two different states are characterized by the

⋆ E-mail:baptiste.boutin-basillais@u-bordeaux.fr

same rotation rate and angular momentum. Besides, we find a collection of new routes linking the MLS and the ORS for ellipsoids with an initial eccentricity lower than ≈ 0.612. These results, once expanded to compressible systems, might have interesting implications in various domains, e.g. the physics of fast rotators and transient rings around Be-stars (Meilland et al. 2006), accretion around compact stars (Trova et al. 2018), the torus in active galactic nuclei (Mason 2015), massive disks and rings orbiting proto-stars (Kratter & Matzner 2006; Takahashi & Inutsuka 2016), planetary rings (Wisdom & Tremaine 1988), and the formation of the Earth-Moon system (Lock & Stewart 2017).

2 THEORETICAL BACKGROUND

A figure of equilibrium basically obeys a first integral for the fluid motion and thermodynamical content $H - \Psi - \Phi$ =const., which combines the enthalpy $H = \int dP/\rho$ of the fluid, the gravitational potential Ψ and the centrifugal potential Φ (Horedt 2004). As for any self-gravitating fluid, Ψ and ρ are linked through the Poisson equation $\Delta\Psi = 4\pi G\rho$. In the incompressible limit of interest here, the potential can be expressed as a one-dimensional integral over the fluid boundary (Wong 1974; Ansorg et al. 2003), which introduces a substantial simplification. An equation of state (EOS) $P(\rho)$ as well as a rotation profile (through Φ) are to be prescribed in addition. Part of the technical difficulty in solving this coupled equations comes from the fact that neither the fluid boundary nor the mass density are not known in advance. A traditionnal way to capture the solutions is the Self-Consistent-Field (SCF) method, which iterates on the enthalpy field from an initial seed until convergence (Ostriker & Mark 1968; Hachisu 1986a). Note that this method is also used in Eriguchi & Hachisu (1983), while Ansorg et al. (2003) can directly solve, without any iteration, a linear system where the unknowns are the coefficients describing the fluid boundary. The case of multi-body configurations, i.e. systems consisting in several detached bodies in mutual interactions, introduces new difficulties. There are more degrees of freedom (Hachisu 1986b). For m bodies, we have typically $2m-1$ parameters, which are for instance m axis ratios and $m-1$ orbital separations. More options are possible, since each body can also have its own EOS and rotation profile (Hachisu et al. 1986a).

The results reported here are based upon the `DROP`-code whose capabibities are described in Huré & Hersant (2017). A new version allowing to compute the equilibrium of concentric m-bodies in mutual interaction is fully operational. We focus on the case with $m = 2$ where a ring (body number 2, or the secondary) surrounds a central body (body number 1, or the primary). The system is depicted in Fig. 1. The problem is scale free. We work in dimensionless cylindrical coordinates $(\hat{R}, \hat{Z})$. The spheroid and the ring are both homogeneous (zero polytropic index) and they share the same rigid rotation law (i.e. $\hat{\Phi} = -\frac{1}{2}\hat{R}^2$). An important assumption concerns the mass density contrast which scales the density of each body with respect to its neighbour (or to a reference body), namely

$$\eta = \rho_2/\rho_1. \qquad (1)$$

This quantity is set to unity in the following, as in

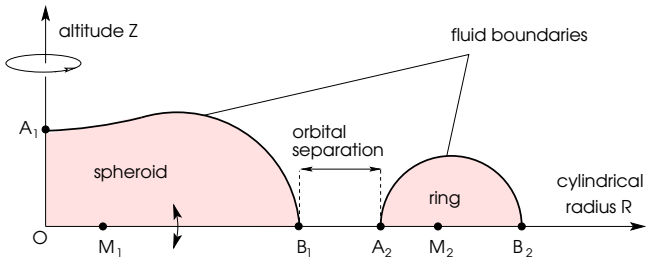

Figure 1. Configuration for a spheroid-ring system. The relative separation is $s = \mathrm{B_1A_2/OB_1}$ and the axis ratios are $e_i = \mathrm{OA}_i/\mathrm{OB}_i$ $(i = 1, 2)$. Points M refer to the maximum enthalpy.

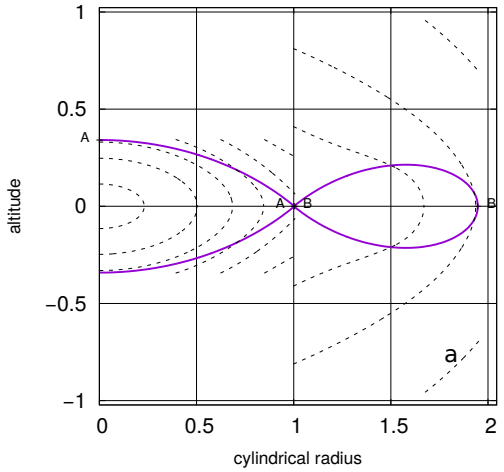

Figure 2. Equilibrium state at the end-point of the ϵ_2-sequence to be compared with (Ansorg et al. 2003). Colors stand for the fluid boundary where the enthalpy vanishes (*bold pink*), and a few isopotential lines are given (*dashed black*); see also Fig. 1 and Tab. 1.

Eriguchi & Hachisu (1983). In practicality, each body has its own computational grid, which is nominal in terms of accuracy and stability of the SCF method. The two Poisson equations are discretized at second-order and solved by using the multigrid method (Briggs et al. 2000). Neumann Boundary Conditions (BCs) are implemented at $\hat{Z} = 0$ for the ring, and additionnally at $\hat{R} = 0$ for the central body, and Dirichlet BCs elsewhere. All volume integrals (BCs and output quantities) take into account the fluid boundaries, which are detected through a 8-point directionnal Freeman chain code from the enthalpy maps. This is essential to get clean solutions, especially for "hard" EOS where $\partial \ln P/\partial \ln \rho < 1$.

If the mass density contrast is fixed and the rotation law is the same for both components, then there are only 3 parameters for $m = 2$. The most natural triplet is composed of the two axis ratios $e_i = \mathrm{OA}_i/\mathrm{OB}_i$ and the relative orbital separation $\mathrm{B_2A_1/OB_1} \equiv s$ (see Fig. 1). With such a choice, however, the mass density contrast between the two bodies is not under control. We can easily impose a specific value if η is part of the input set. We then take $(\eta = 1, e_2, s)$ as parameters, which means that the axis ratio of the central body e_1 becomes an output quantity. As observed, this does not alter the convergence properties of the SCF method. The code has been extensively checked for $m = 1$, and more

recently for m up to 7 (Boutin-Basillais & Huré 2018). The computations have been performed with $N = 129$ grid nodes per direction, which corresponds to $\ell = 7$ levels of multigrid. Numerical schemes being second-order accurate in the grid spacing, errors (including the Virial parameter) are of the order of $1/N^2 \sim 10^{-4}$ typically (the results are given with four significant digits at most).

3 SURVEY OF THE PARAMETER SPACE

We have first detected the end-point of the ϵ_2 sequence computed in Ansorg et al. (2003). The equilibrium is shown in Fig. 2 and the output data are gathered in Tab. 1 (rows 1 and 2). We see that our results are in excellent agreement, given the adopted resolution. Next, we have generated a large number of equilibria by varying the axis ratio e_2 of the ring and the separation s (while holding $\eta = 1$). In contrast with single-body equilibria, *any pair of parameters does not necessarily lead to a solution*. The number of successful runs is of the order of 33000. All computed solutions are such that $e_1 \gtrsim 0.33$ and $e_2 \gtrsim 0.51$. There is no limit in the mass ratio $M_1/M_2 \in [0, \infty[$. Besides, the orbital separation s ranges from 0 to ∞. A few examples of converged structures are given in Fig. 3. Associated data are listed in Tab. 1 (rows 3 to 9). Unsurprisingly, binarity induces deviations in shape with respect to single body figures. The central body shows a slight contraction between the pole and the equator, while the ring is substantially flatter. The volume of each fluid is therefore reduced compared to the single body case. All bodies have a convex shape. We find only *detached binaries* (see Sect. 5). This means that the only system in contact system is the end-point of the ϵ_2-sequence (Ansorg et al. 2003).

Figure 4 shows the results plotted in the ω^2-j^2 diagram, where ω and j are respectively the dimensionless rotation rate Ω and the dimensionless angular momentum J defined by

$$\begin{cases} \omega^2 = \frac{\Omega^2}{4\pi G\rho}, \\ j^2 = \frac{J^2}{4\pi G M^{10/3}\rho^{-1/3}}, \end{cases} \tag{2}$$

where $M = M_1 + M_2$ is the total mass. Note that there is no ambiguity in the definition of ρ since the mass density contrast is unity. We have superimposed the MLS, the ORS and the Jacobi sequence for convenience. We clearly see that all solutions are concentrated between the ascending part of the MLS and a *first limit curve* (hereafter, the "high-ω limit"), which meets the MLS at the critical point C $(0.00171, 0.05306)$ where the axis ratio of the primary is $e_1 \approx 0.791$ and the orbital separation is $s \approx 0.691$. There is *no solution for* $\omega \gtrsim \omega_l(j)$. An analog is known for binary stars (Hachisu & Eriguchi 1984). In the left part of it, this limit curve is close to linear, with

$$\omega_l^2 \approx 0.0536 + 0.09 j^2. \tag{3}$$

The right-part of it is slightly bended and meets the end-point of the ϵ_2-branch where $e_1 \approx 0.341$. This is due to the critical rotation (see Fig. 3c). The configurations located close to the MLS consist in a prominent central body and a small ring (Fig. 3b). The orbital separations are moderate to large, but non-zero (see below). For points located well in between the MLS and the ORS (Fig. 3d), the two bodies are comparable in size and mass. The solutions overtake the ORS, and reach a *second limit curve* (hereafter, the "high-j limit"), which asymptotically merges with the ORS for large values of j, and attains the end-point of the ϵ_2-sequence where $j^2 \sim 0.03$. There is probably a slight abuse of convention here in naming this limit since it does not correspond to a unique, impassable value of j (this remark holds for the high-ω limit). We simply mean that, for a given value of ω, there is a maximal allowed value for j (with no equilibrium beyond). These maximal values tend to ∞ when $\omega \to 0$. Another interesting point is the presence of *a zone of degeneracy* located between the ORS and the high j-limit (Fig. 3f and g), where two different configurations correspond to a single pair (j^2, ω^2). A point located close to the ORS can correspond to two very different configurations. Either the spheroid has a small size and relative mass, the ring dominates and the orbital separation s is large (Fig. 3e and g). Then the ring resembles very much the single ring. Or the spheroid and the ring have comparable mass and size. In this case, the ring (in particular, its axis ratio) is very different from the single ring equilibrium (Fig. 3f). In this region where the rings are among the largest in size, the convergence of the SCF method is tricky (the number of SCF iterations rises, and the Virial parameter deteriorates).

4 EQUILIBRIUM SEQUENCES

4.1 Sequences with a variable orbital separation (growth of the primary)

The top panel of Fig. 5 shows four sequences bifurcating from the ORS and corresponding to a decreasing orbital separation s, while the axis ratio of the secondary e_2 is held fixed. Since s is infinite onto the ORS, leaving this branch means the birth and growth of a central spheroid and the decrease of the diameter of the ring. We see that, whatever the axis ratio of the initial ring on the ORS, one *can never reach* the MLS, but the high-ω limit where $j \gtrsim 0.00171$. When e_2 is significantly lower than unity, one reaches the high-ω limit more directly. When $e_2 \to 1$, the sequence is first quasi-horizontal, and then goes vertically along the MLS to finally attain the high ω-limit. Asymptotically, for $e_2 \to 1$, one leaves the ORS at infinity and one reaches the critical point C where $s \approx 0.691$ (see below). As s diminishes, we observe that e_1 is decreasing as well, which means that the central body flattens as the ring comes closer. The total mass M decreases along the sequence (j decreases) whereas the mass ratio M_1/M_2 increases.

4.2 Sequences with a variable axis ratio for the ring (growth of the equatorial ring)

The middle panel of Fig. 5 shows three new sequences branching off from the MLS, which are obtained for a given value of the orbital separation. Leaving the MLS implies the creation and subsequent growth of an equatorial, fictitious ring with an axis ratio $e_2 = 1$ (i.e. a massless loop), positionned at an inital separation s. The lowest permitted value happens to be ≈ 0.691. This occurs at the critical point C. Therefore, any bifurcation from the MLS means that s stands in the range $[0.691, \infty[$, while $e_1 \gtrsim 0.791$. By

input parameters							
e_2	s	M	M_1/M_2	j^2	ω^2	e_1	comment/ref.
0.5162*	0.0000		0.4105	0.02972	0.05433	0.3413	Ansorg et al. (2003)
0.5162*	0.0051	8.8511	0.4095	0.02973	0.05419	0.3413	configuration a, Fig. 2
0.9900	1.1204	3.6708	1026.8	0.00088	0.03107	0.8807	configuration b, Fig. 3
0.6380	0.3516	4.7567	1.0632	0.02056	0.05470	0.6092	configuration c, Fig. 3
0.9000	1.9118	5.3008	2.7043	0.01148	0.01318	0.9304	configuration d, Fig. 3
0.6000	5.0000	5.3798	0.0042	0.03109	0.03055	0.5548	configuration e, Fig. 3
0.7100	1.2021	11.558	0.3472	0.03257	0.02883	0.7240	configuration f, Fig. 3
0.6200	3.0844	143.49	0.0174	0.03260	0.02881	0.5926	configuration g, Fig. 3
0.9990	0.6910	3.2874	3×10^5	0.00170	0.05306	0.7906	critical point C, 4

Table 1. Values obtained for the equilibria shown in Figs. 2 and 3 (see text for the numerical setup); *end-point of the ϵ_2-sequence. Columns 1 and 2 are input parameters. See also Fig. 4.

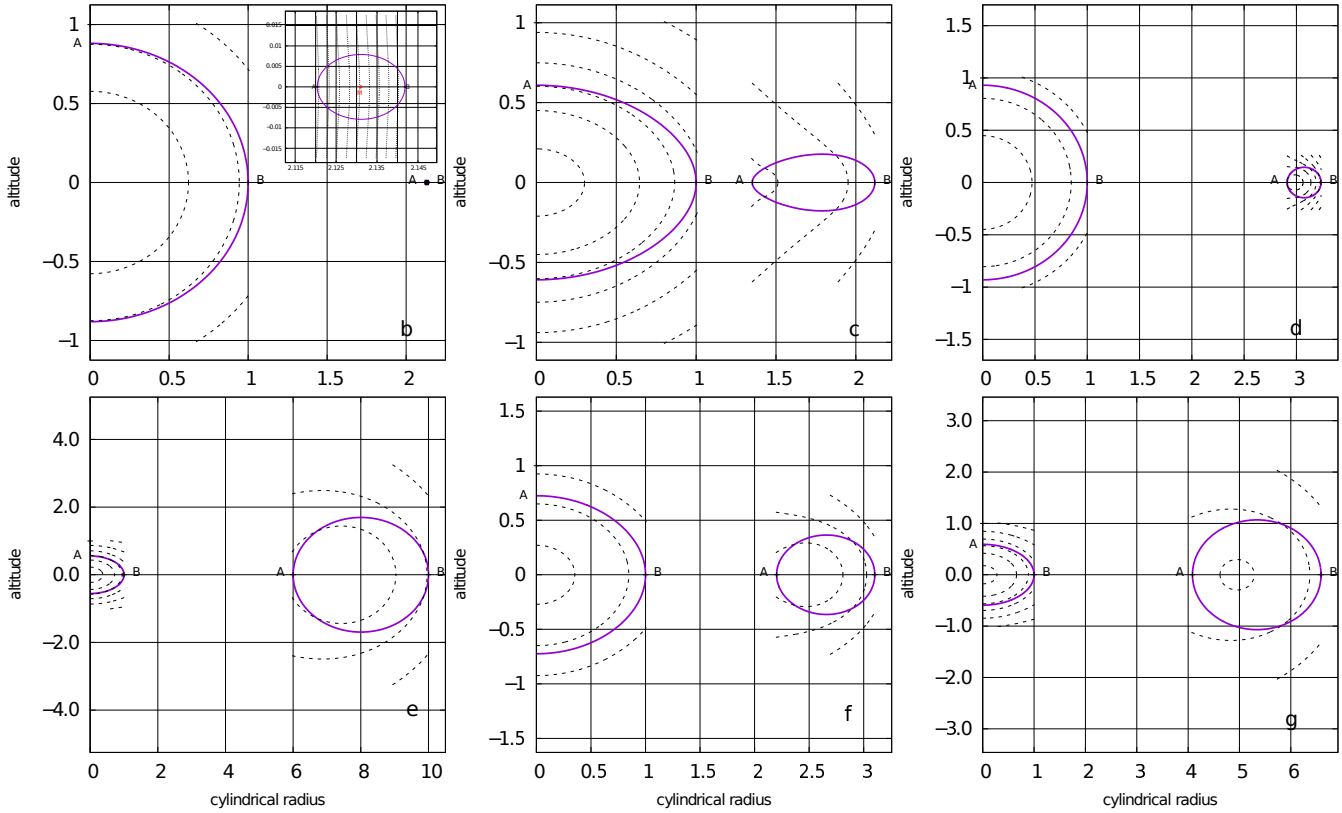

Figure 3. Same legend as for Fig. 2 but for 6 equilibria among the many runs performed (see Tab. 1 for associated key quantities) For panel b, the details of ring structure are given in the inset.

gradually enlarging the ring, one gets closer to the ORS. We observe that the central spheroid flattens, i.e. e_1 decreases. The mass ratio M_1/M_2 is plotted versus e_2 in Fig. 6 for these sequences. When the axis ratio of the ring is close to unity, the relative mass tends to zero and the overall equilibrium is guided by the central body (i.e. near the MLS). As soon as e_2 starts to decrease, the initial massless ring grows in size and in mass, and, it finally dominates the equilbrium when $e_2 \to 0.55$ (i.e. near the ORS). The total mass M increases along the sequence (j increases) whereas the mass ratio M_1/M_2 decreases.

4.3 Sequence with fixed ring's center

It is interesting to consider a series of solutions obtained by holding the main radius of the ring $R_c = \mathrm{OA}_2 + \frac{1}{2}\mathrm{A}_2\mathrm{B}_2$ fixed relative to the size of the primary. The bottom panel of Fig. 5 shows the results obtained for five values of R_c/OB_1. As above, we start from the MLS by enlarging an initial massless loop (a fictitious ring with zero diameter) at a relative separation $s = R_c/\mathrm{OB}_1 - 1$. Again, bifurcations from the MLS are possible as long as we stay below the critical point C. As the ring grows, the axis ratio of the primary e_1 decreases as one goes towards the ORS. For the largest values of R_c/OB_1, the sequences have a large amplitude, cross the diagram rather horizontally ($\omega \sim$ const.), then overtake the

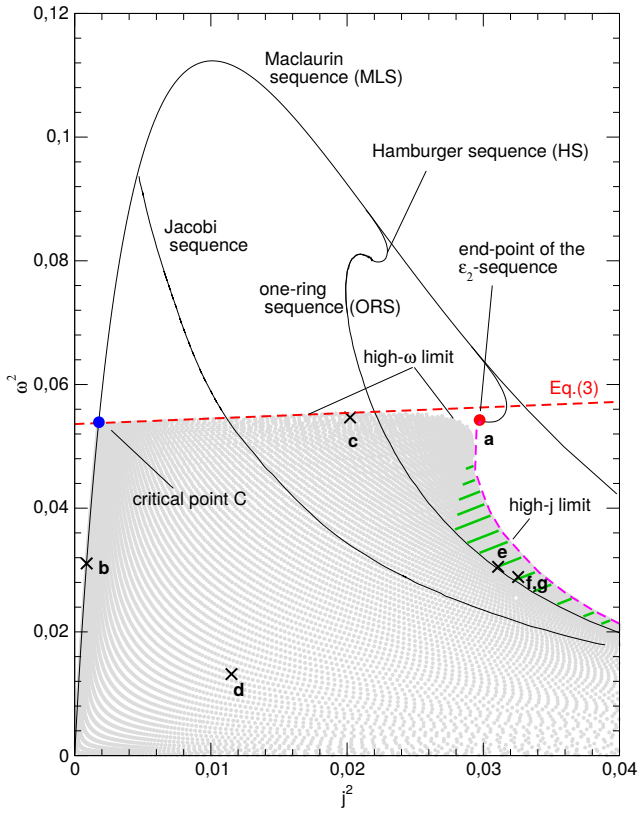

Figure 4. The spheroid-ring solutions (*gray dots*) populate the ω^2-j^2 diagram in between the MLS, the high-ω limit and the high-j limit (see text for explanations). The MLS, ORS, Jacobi-sequence, Hamburger-sequence and ϵ_2 sequence are also shown (*plain lines*). Points labelled a to f (*cross*) correspond to equilibria shown in Fig. 3; see also Tab. 1. There is a band of degeneracy rightward to the ORS (*green dashed zone*).

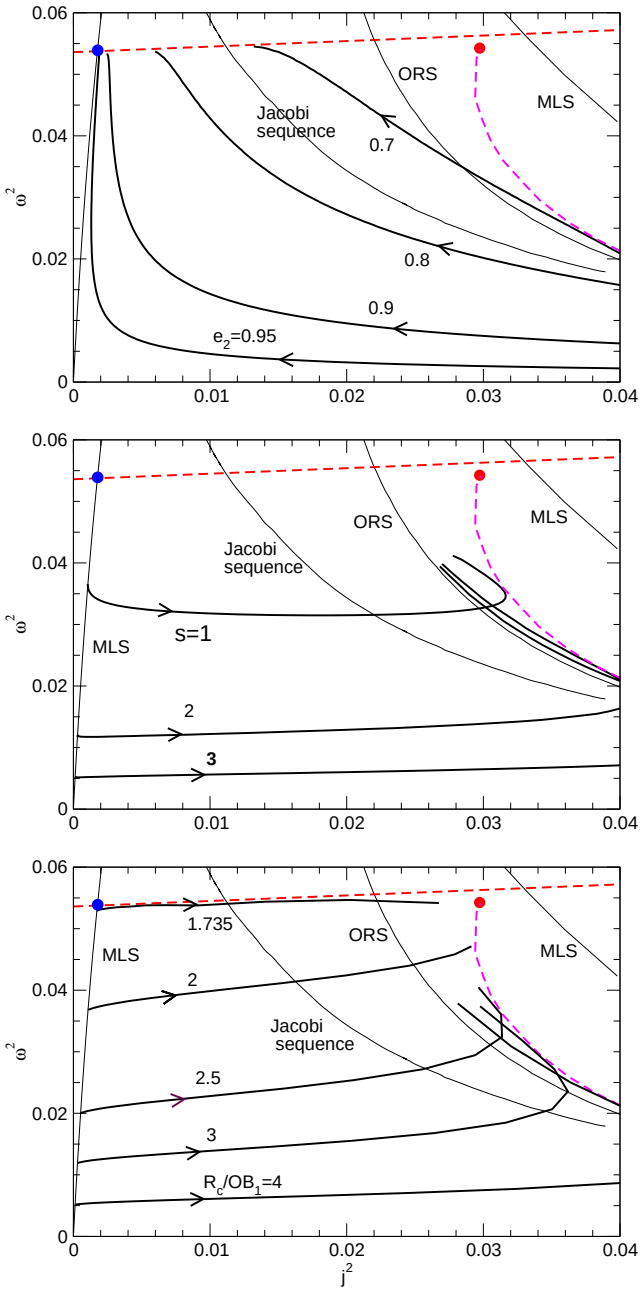

Figure 5. Sequences obtained for constant values of e_2 when leaving the ORS (*ton panel*), for constant orbital separation s (*middle panel*) and constant position of the ring center relative to the spheroid (*bottom panel*) when bifurcating from the ORS; see also Fig. 4. Curves are labelled with the actual values of the fixed parameter.

ORS sequence, and go inside the band of degeneracy. These sequences end when e_2 reaches the nominal value of ≈ 0.55. The case with $R_c/\mathrm{OB}_1 = 1.735$ is remarkable as it almost coincides with the high-ω limit. The run of M and M_1/M_2 is the same as for the case with $s = \text{const}$.

4.4 Sequences with a constant mass ratio M_1/M_2

As in Eriguchi & Hachisu (1983), we have built sequences for which the mass ratio M_1/M_2 is held constant. This corresponds to systems undergoing mass exchange between the two components, or even mass-loss or accretion from the ambient medium. We can easily extract from the data cube a subset of solutions corresponding to a given output quantity $x \pm \Delta x$, where the bandwith Δx depends on the density of the data cube (the parameter survey has not an infinite numerical resolution in s and e_2). Sequences obtained for $M_1/M_2 \in \{0.01, 0.5, 1, 2, 10, 100\}$ with an error on M_1/M_2 of about $\approx 10^{-4}$ typically are shown in Fig. 7 (top panel). When $M_1/M_2 \to 0$, the sequence is located near the ORS. This is expected since the equilibrium is mostly dominated by the ring. On the contrary, when $M_1/M_2 \to \infty$, the sequence is close to the MLS, and it terminates on the high-ω limit. This is in agreement with Eriguchi & Hachisu (1983). In all cases, we observe that the axis ratios e_1 and e_2 and the separation s are gradually decreasing while ω increases.

4.5 Sequences with a constant total mass

Sequences associated with a constant total mass $M = M_1 + M_2$ are also of particular interest, since a spheroid-ring system may evolve over some period with a given amount of matter, without any contact with the environment. Se-

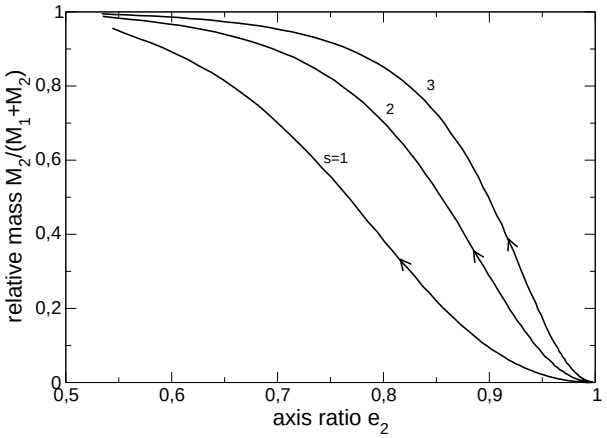

Figure 6. Relative mass of the ring versus its axis ratio for the 3 sequences obtained with a constant s (see Fig. 5, middle panel).

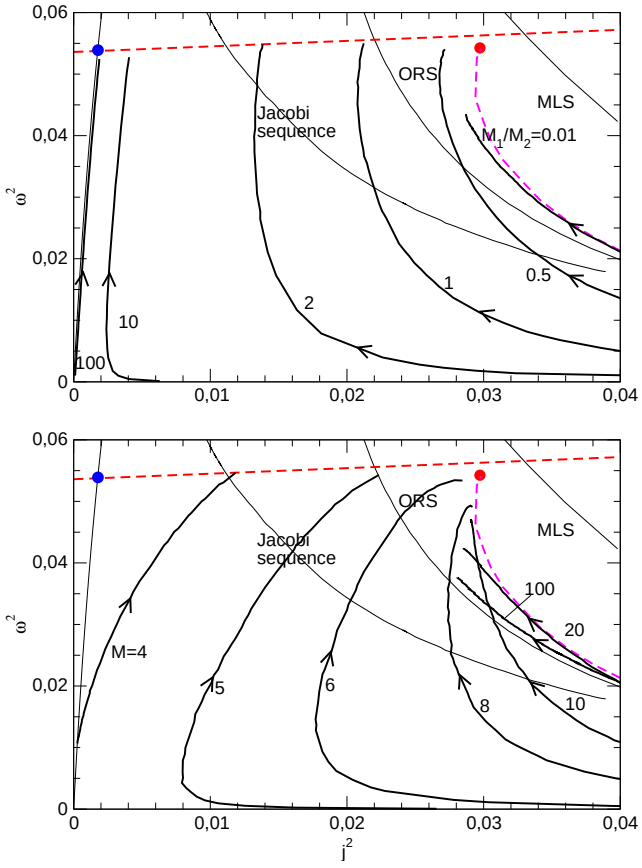

Figure 7. Sequences obtained for constant values of the mass ratio M_1/M_2 *(top panel)*, and for constant values of the total mass M *(bottom panel)*. For a given total mass, some sequences seem to converge towards the end-point of the ϵ_2-sequence.

quences obtained for $M = \{4, 5, 6, 8, 10.20, 100\}$ (still with a precision of the order of 10^{-4} in relative) are displayed in Fig. 7 (bottom panel). The sequences start next to the ORS where M_1 and M_2 are comparable and, as they approach the high-ω limit, M_1 decreases while M_2 increases. Along this sequence, values of e_1, e_2 and s are again decreasing while ω increases.

5 CONCLUSION AND PERSPECTIVES

We have studied the figures of equilibrium for spheroid-ring systems, assuming rigid rotation and incompressibility, by surveying the parameter space (e_2, s) for a unity density contrast. This work is complementary to the papers by Eriguchi & Hachisu (1983) and Ansorg et al. (2003). While, for single-body equilibria, there is a solution for any axis ratio, this is no more true for a spheroid-ring system. As shown, a limited set of input parameters leads to a solution, and the rotation rate must be rather low. There is no contact binary except the end-point of the ϵ_2-equilibrium. Many states of critical rotation populate the equilibrium diagram in the vicinity of this singular point, for which the SCF method struggles with converging. In this zone indeed, the configurations are highly sensitive to the input parameters. A very small change in the rotation rate or/and the angular momentum implies a drastic modification of the orbital separation and/or axis ratio, and vice versa. This sensitivity, already pointed out in Eriguchi & Hachisu (1983), might be of great importance regarding the stability and the evolution of the binary. The end-point of the ϵ_2-equilibrium seems an ideal state for any potential exchange of matter between the two components. A perturbation in the mass and dynamical content might drive the system to a very different configuration, unless some kind of selfregulation sets in. It would be interesting to investigate this question in more detail (e.g. Woodward et al. 1992; Abramowicz et al. 1998; Montero et al. 2010).

Eriguchi & Hachisu (1985) have shown that the MLS bifurcates towards the ORS through an intermediate body that is concave in shape. Direct routes from the MLS to the ORS are in fact possible in the ascending part of the MLS at much lower rotation rates, provided the axis ratio of the central spheroid is greater than ≈ 0.791. At the new bifurcation points, a massless fictitious ring takes root at a relative orbital separation $s \gtrsim 0.691$, and grows up when leaving the MLS towards the ORS, while the spheroid depreciates. This clearly indicates that tiny self-gravitating rings can orbit at some distance around massive quasi-spherical bodies, planets (Wisdom & Tremaine 1988) and stars (Meilland et al. 2006). This meets the fundamental question of the stability of all solutions in the data cube, which would be interesting to analyze, for instance through time-dependent simulations.

We can envisage a similar approach for each $\epsilon_{k>2}$ sequence unveiled by Ansorg et al. (2003), with multiple detached rings possibly present. In particular, the end-point of the ϵ_3 sequence should lead to another kind of detached binary, i.e. a ring-ring configuration (Eriguchi & Hachisu 1983). Despite such a system is probably highly unstable, it would be interesting to see if such systems display similar features (limited domain of solutions, degenerate states, bifurcations).

Finally, two severe assumptions would be worth reconsidering. The first one concerns the mass density constrast which has been set to unity. There is no reason to believe that gravitationally interacting fluids evolve with the same mass density. How the configurations computed here and the associated sequences be modified if the condition $\eta = 1$ is relaxed? Besides, we have considered only incompressible fluids, which is another strong hypothesis. It would be interesting to examine the case of "softer" EOSs. How are the

results changed for a non-zero polytropic index? The impact of the rotation law can also be investigated.

ACKNOWLEDGEMENTS

We thank the referee, Prof. Y. Eriguchi, for fruitful comments on this paper. Part of this work has been presented at the 689. WE-Heraeus-Seminar "Accretion in strong gravity" in Bad Honnef, Germany.

REFERENCES

Abramowicz M. A., Karas V., Lanza A., 1998, A&A, 331, 1143
Ansorg M., Kleinwächter A., Meinel R., 2003, MNRAS, 339, 515
Boutin-Basillais B., Huré J.-M., 2018, in SF2A-2018: Proceedings of the Annual meeting of the French Society of Astronomy and Astrophysics Multi-body figures of equilibrium in axial symmetry. pp 111–112
Briggs W. L., Henson V. E., McCormick S. F., 2000, A multigrid tutorial (2nd ed.). Society for Industrial and Applied Mathematics, Philadelphia, PA, USA
Chandrasekhar S., 1969, Ellipsoidal figures of equilibrium. Yale Univ. Press
Eriguchi Y., Hachisu I., 1983, Progress of Theoretical Physics, 69, 1131
Eriguchi Y., Hachisu I., 1985, A&A, 148, 289
Fujisawa K., Eriguchi Y., 2014, MNRAS, 438, L61
Hachisu I., 1986a, ApJS, 61, 479
Hachisu I., 1986b, ApJS, 62, 461
Hachisu I., Eriguchi Y., 1984, Ap&SS, 99, 71
Hachisu I., Eriguchi Y., Nomoto K., 1986a, ApJ, 308, 161
Hachisu I., Eriguchi Y., Nomoto K., 1986b, ApJ, 311, 214
Horedt G. P., ed. 2004, Polytropes - Applications in Astrophysics and Related Fields Vol. 306 of Astrophysics and Space Science Library
Huré J.-M., Hersant F., 2017, MNRAS, 464, 4761
Huré J.-M., Hersant F., Nasello G., 2018, MNRAS, 475, 63
Kratter K. M., Matzner C. D., 2006, MNRAS, 373, 1563
Lock S. J., Stewart S. T., 2017, Journal of Geophysical Research (Planets), 122, 950
Mason R. E., 2015, Planet. Space Sci., 116, 97
Masuda N., Nishida S., Eriguchi Y., 1998, MNRAS, 297, 1139
Meilland A., Stee P., Zorec J., Kanaan S., 2006, A&A, 455, 953
Montero P. J., Font J. A., Shibata M., 2010, Physical Review Letters, 104, 191101
Nishida S., Eriguchi Y., Lanza A., 1992, ApJ, 401, 618
Ostriker J. P., Mark J. W.-K., 1968, ApJ, 151, 1075
Takahashi S. Z., Inutsuka S.-i., 2016, AJ, 152, 184
Trova A., Schroven K., Hackmann E., Karas V., Kovář J., Slaný P., 2018, Phys. Rev. D, 97, 104019
Wisdom J., Tremaine S., 1988, AJ, 95, 925
Wong C.-Y., 1974, ApJ, 190, 675
Woodward J. W., Sankaran S., Tohline J. E., 1992, ApJ, 394, 248

MNRAS **000**, 1–?? (???) Preprint 19 May 2020 Compiled using MNRAS LATEX style file v3.0

The exterior gravitational potential of toroids

J.-M. Huré[1⋆], B. Basillais[1], V. Karas[2], A. Trova[3], and O. Semerák[4]
[1] *Laboratoire d'Astrophysique de Bordeaux, Univ. Bordeaux, CNRS, B18N, allée Geoffroy Saint-Hilaire, 33615 Pessac, France*
[2] *Astronomical Institute, Academy of Sciences, Boční II 1401, CZ-14100 Prague, Czech Republic*
[3] *University of Bremen, Center of Applied Space Technology and Microgravity (ZARM), 28359 Bremen, Germany*
[4] *Institute of Theoretical Physics, Faculty of Mathematics and Physics, Charles University, CZ-180 00 Prague, Czech Republic*

Received ??? / Accepted ???

ABSTRACT

We perform a bivariate Taylor expansion of the axisymmetric Green function in order to determine the exterior potential of a static thin toroidal shell having a circular section, as given by the Laplace equation. This expansion, performed at the centre of the section, consists in an infinite series in the powers of the minor-to-major radius ratio e of the shell. It is appropriate for a solid, homogeneous torus, as well as for inhomogeneous bodies (the case of a core stratification is considered). We show that the leading term is identical to the potential of a loop having the same main radius and the same mass — this "similarity" is shown to hold in the $\mathcal{O}(e^2)$ order. The series converges very well, especially close to the surface of the toroid where the average relative precision is $\sim 10^{-3}$ for $e = 0.1$ at order zero, and as low as a few 10^{-6} at second order. The Laplace equation is satisfied *exactly* in every order, so no extra density is induced by truncation. The gravitational acceleration, important in dynamical studies, is reproduced with the same accuracy. The technique also applies to the magnetic potential and field generated by azimuthal currents as met in terrestrial and astrophysical plasmas.

Key words: Gravitation — Methods: analytical — Methods: numerical

1 INTRODUCTION

The derivation of reliable and compact expressions for the gravitational potential of massive toroids is a long-standing problem of dynamical astronomy, from planetary to galactic scales. This is essential not only to examine the motion of test-particles and fluids orbiting around, in the classical framework as well as in general relativity (Nieto 2005; Šubr & Karas 2005; Semerák & Suková 2010; Tresaco et al. 2011; Iorio 2012), but also to understand the conditions for the formation, evolution and stability of toroids themselves (Dyson 1893; Hachisu 1986; Chandrasekhar 1987; Tohline & Hachisu 1990; Woodward et al. 1992; Storzer 1993; Christodoulou 1993; Hashimoto et al. 1993; Eriguchi & Mueller 1993; Nishida & Eriguchi 1994; Pickett et al. 1997; Horedt 2004; Lehmann et al. 2019). While it is relatively easy to deduce the mass density corresponding to a given potential (e.g. Binney & Tremaine 1987), the inverse procedure is very complicated by analytical means, and it is almost impossible to go beyond the classical series representations and to get closed forms (Clement 1974; Cohl et al. 2001; Petroff & Horatschek 2008). Fully numerical approaches may be preferred for their apparent simplicity, but the computing times are generally large, often prohibitive at high spatial resolution, especially for very inhomogeneous configurations and/or very extended systems like discs. The numerical accuracy of discretization schemes is mainly limited when treating thin sources (having less than three spatial dimensions) whose field typically suffers a certain irregularity at their position.

In axial symmetry, the Green function $\mathcal{G}(\vec{r}|\vec{r}')$ of the Poisson equation involves the complete elliptic integral of the first kind $\mathbf{K}$ whose argument (or modulus) gathers all the pertinent variables (Kellogg 1929; Durand 1953; Fukushima 2016). The presence of a special function is a real obstacle when it is to be convolved with any non-trivial mass density $\rho(\vec{r}')$. One can overcome this difficulty by expanding $\mathbf{K}$ over the modulus, but the "dual" nature of the series – different for large and for short separations – means piecewise approximations whose connection requires technical efforts. This is done for instance in Bannikova et al. (2011) who match together the internal and the external potentials of the solid (i.e. homogeneous) torus from a minimization procedure.

This article brings a new contribution to this general and challenging problem. It is inspired by Huré et al. (2019) who derived a reliable approximation for the *interior* po-

⋆ E-mail:jean-marc.hure@u-bordeaux.fr

tential of a toroidal shell of circular cross-section, based on a bivariate expansion performed at the pole (or focal ring) of the toroidal coordinates. At this singular point, all the partial derivatives of the Green function are exceptionally analytical. Unfortunately, the "pole" method does not apply outside the shell cavity because the line segment linking the focal ring to any exterior point crosses the shell where the Green function is basically singular. We generate accurate approximations for the *exterior* solution of the toroidal shell by expanding the axisymmetric Green function as a Taylor series *before integrating over the source*. As for the classical multipole expansion, the shell potential writes as an infinite series (e.g. Majic 2020), but our approach differs in that the origin of coordinates does not play a special role: the expansion is performed at the centre of the toroid section. Such an approach has been reported very recently by Kondratyev (2018) in the case of the solid torus. The author writes the external potential in the form $\sum_n \phi_n e^{2n}$ (e is the minor-to-major radius ratio, i.e. the torus parameter). He then uses the second-order expression to set constraints on the masses of thin, virialized rings orbiting an asteroid.

In this article, we go beyond the hypothesis made in Bannikova et al. (2011) and in Kondratyev (2018) by considering inhomogenous systems too. In particular, we show that, when the toroid is radially stratified from the centre to the surface, only moments of the density need to be calculated. The method has an unexpected efficiency, not only at large distances, but also quite close to the surface of the toroid. The leading term has a correct behaviour at infinity as well as on the Z-axis, and it obeys the Laplace equation. As a matter of fact, these desirable properties are shared by *all* terms of the expansion. There is thus no spurious noise or extra density induced in space, whatever the truncation order. We treat orders 0 to 2 explicitly (a driver F90-program is appended). The resulting shell potential can be recast in the form of a "modified monopole" or in the form of an "equivalent loop", which concept has been discussed in Stahler (1983), while proofs are found in Bannikova et al. (2011) and Kondratyev (2018). We show that the exterior potential of the solid torus, which is of more astrophysical relevance than the shell, is easily deduced, with all the properties observed for the shell maintained. The method also applies to the determination of the vector potential and magnetic field of electromagnetism for toroids carrying a purely azimuthal current (Trova et al. 2018).

The paper is organized as follows. In Sect. 2, the expression for the potential of a toroidal shell is given in its integral form. The axisymmetric Green function is expanded, in a bivariate manner, in Sect. 3. The leading term is calculated and compared with the potential of a monopole (i.e. a point mass) and of a circular loop. Its precision is checked against an "exact" numerical reference in Sect. 4. The 1st-order and 2nd-order approximations are treated then similarly in Sect. 5. In Sect. 6 we show how the exterior and interior solutions match together at the shell surface. The procedure leading to the nth-order term is detailed in Sect. 7. The case of a solid torus is treated in Sect. 8, while the case of core-stratified toroids is the aim of Sect. 9. The formula for the gravitational acceleration is derived in Sect. 10. In particular, we show that the vertical component that rules

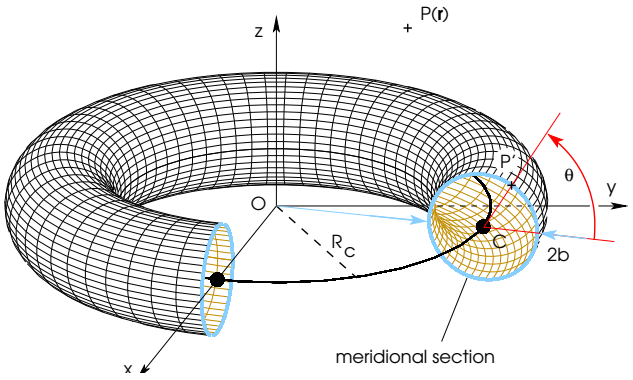

Figure 1. The infinitely thin, toroidal shell (main centre O and main radius R_c) with a circular meridional section (centre C and core radius b).

hydrostatic equilibrium differs by a factor of about 2 from Paczyński's estimate valid for thin discs (Paczynski 1978). This result is suited to examining the stability of rings (e.g. Wisdom & Tremaine 1988). From the radial component, we deduce the circular velocity of test particles orbiting in the equatorial plane. This formula can be helpful in explaining the deviations to the Kepler's law in massive systems (e.g. Guilloteau et al. 1999). Section 11 is devoted to the magnetic potential due to toroidal currents (the leading term is derived). Two general comments are found in Sect. 12. Conclusions and perspectives are found in the last section.

2 POTENTIAL OF THE TOROIDAL SHELL

We consider the simplest possible toroidal shell, as depicted in Fig. 1. The major radius is R_c and the meridional section is circular, with centre C and minor radius

$$b \equiv eR_c \leq R_c, \tag{1}$$

where $e \in [0,1]$ denotes the shell parameter. We work in cylindrical coordinates (R,Z), using the symmetry axis of the shell as the Z-axis, and xOy as the plane of symmetry. For this specific problem, the Green function of the Poisson equation (e.g. Kellogg 1929; Durand 1953) is

$$\mathcal{G}(R,Z;a,z) = -2\sqrt{\frac{a}{R}}k\mathbf{K}(k), \tag{2}$$

where

$$\mathbf{K}(k) = \int_0^{\frac{\pi}{2}} \frac{d\vartheta}{\sqrt{1-k^2\sin^2\vartheta}} \tag{3}$$

is the complete elliptic integral of the first kind,

$$k = \frac{2\sqrt{aR}}{\Delta} \in [0,1] \tag{4}$$

is its modulus, and

$$\Delta^2 = (R+a)^2 + \zeta^2, \tag{5}$$

where $\zeta = Z - z$, and (a,z) are the cylindrical coordinates of any point P' belonging to the shell. Basically, (2) corresponds to the potential created by an infinitesimally thin circular ring with unit mass per unit length, radius a and

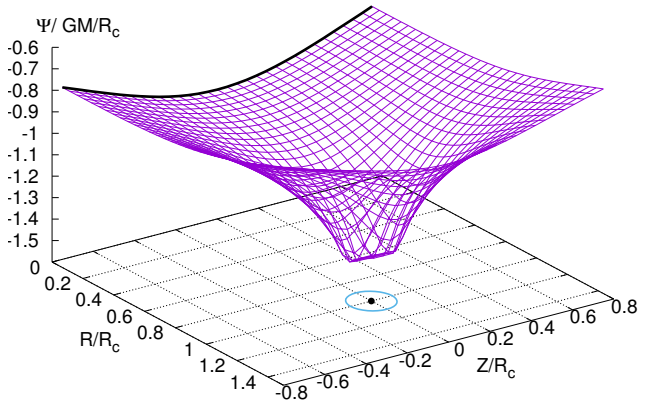

Figure 2. The gravitational potential of the toroidal shell in units of GM/R_c (homogeneous case) obtained by direct numerical computation of the integral in (6). The axis are in units of the main radius R_c. The normalized core radius (or shell parameter) is $e \equiv b/R_c = 0.1$. Also shown are the values on the Z-axis from the formula by Sácha & Semerák (2005) (*thick black line*), the projected shell section (*blue line*) and its centre C (*black dot*); see also Fig. 1.

altitude z. This function is known to be logarithmically singular at the location of the ring (where $k \to 1$). The gravitational potential generated, at any point P($\vec{r}$) of space, by such the axisymmetric shell is then given by the integral

$$\Psi(\vec{r}) = -2G \int_0^{2\pi} \Sigma(\ell) \sqrt{\frac{a}{R}} k\mathbf{K}(k) d\ell, \tag{6}$$

where Σ is the local surface density, and $d\ell$ is the infinitesimal length along the shell section. In the case of a shell with a circular section of radius R_c, a and z are simply given by

$$a = R_c + b\cos\theta, \qquad z = b\sin\theta, \tag{7}$$

where $\theta \in [0, 2\pi]$ is the angular position of any point P' on the shell with respect to the equatorial plane (see Fig. 1). The infinitesimal length then takes its simplest form, namely $d\ell = b d\theta$. Other options are possible, but the subsequent calculations are much more complicated (see Sect. 12).

The surface density Σ may be variable in local latitude θ. However, even if it is independent of θ, (6) cannot in general be integrated into a compact form, except on the Z-axis (Šácha & Semerák 2005). An example of a direct numerical estimate of Ψ is given in Fig. 2 for $e = 0.1$. We use the trapezoidal rule as the quadrature scheme. We will use such a numerical potential, denoted $\Psi_{\rm ref}$ in the following, as a "reference" against which we will compare our approximations. As shown in Huré et al. (2019), the potential inside the shell cavity is a quasi-linear function of the cylindrical radius R, and it is weakly sensitive to the Z-coordinate, especially when $e \ll 1$. We see that the potential outside the cavity has a more complex structure. It resembles the potential of a loop, as already pointed out (e.g. Wong 1973; Bannikova et al. 2011; Kondratyev 2018).

3 EXPANSION OF THE GREEN FUNCTION. ZERO-ORDER FORMULA

As quoted in the introduction, the elliptic integral $\mathbf{K}$ may be expanded over k at $k \to 0$, which means far away from the source or close to the Z-axis, and over $k' = \sqrt{1-k^2}$ at $k \to 1$, e.g. close to or even inside the source (see e.g. Abramowitz & Stegun 1964; Gradshteyn & Ryzhik 2007). However, such two series have to be matched somewhere (Bannikova et al. 2011). In the present paper, we propose a more synthetic approach which consists in expanding the axisymmetric Green function over a and z, before integration over θ in (6). We expect to preserve the asymptotic behaviour of the potential at large distances. Let us remind that, for any "regular enough" function f of two independent variables x and y, the bivariate Taylor expansion at (x_0, y_0) writes

$$f(x,y) = f(x_0,y_0) + \sum_{n=1}^{\infty} \frac{1}{n!} \left\{ \left[(x-x_0)\frac{\partial}{\partial x'} + (y-y_0)\frac{\partial}{\partial y'} \right]^n f(x',y') \right\}_{\substack{x'=x_0 \\ y'=y_0}}. \tag{8}$$

The expansion is performed in $x \equiv a$ and $y \equiv z$, at the centre C of the shell, i.e. at $x_0 \equiv R_c$ and $y_0 \equiv 0$ (see Sect. 12 for the expansion at the focal ring). We see from (7) that this is valid for $e < 1$, which in astrophysical toroids (typically orbiting a massive central body) is safely satisfied.

In fact, it is not necessary to expand the whole Green function. In particular, the term $\sqrt{a}$ is not problematic and it can be left aside. There are several options. For instance, if we expand $k\mathbf{K}(k)$ or $\mathbf{K}(k)$, the subsequent integration over θ will generate a new series of elliptic integrals (again, see Sect. 12). That is not a problem per se, but it complicates the calculations when the solid torus is considered. Seeing that the complication can be avoided when extracting the other factor $\sqrt{a}$ contained in the modulus (4), we finally choose to expand

$$\frac{\mathbf{K}(k)}{\Delta} \equiv \kappa \tag{9}$$

as

$$\begin{aligned} \kappa = {} & \kappa|_{\substack{a=R_c \\ z=0}} + (a-R_c) \left.\frac{\partial\kappa}{\partial a}\right|_{\substack{a=R_c \\ z=0}} \\ & + z \left.\frac{\partial\kappa}{\partial z}\right|_{\substack{a=R_c \\ z=0}} + \frac{1}{2}(a-R_c)^2 \left.\frac{\partial^2\kappa}{\partial a^2}\right|_{\substack{a=R_c \\ z=0}} \\ & + (a-R_c) z \left.\frac{\partial^2\kappa}{\partial a \partial z}\right|_{\substack{a=R_c \\ z=0}} + \frac{1}{2} z^2 \left.\frac{\partial^2\kappa}{\partial a \partial z}\right|_{\substack{a=R_c \\ z=0}} \\ & + \dots . \end{aligned} \tag{10}$$

Note that κ is nothing but the axisymmetric Green function, i.e. $\oint |\vec{r} - \vec{r}'|^{-1} d\phi$. Since it is a function of a, z, R and Z, the infinite series is a polynomial (of "infinite" degree) in a and z, whose coefficients are functions of R and Z. This series naturally exhibits powers of the shell parameter e which come from the partial derivatives and from the terms $a - R_c$ and z as well; see (7). With (10), (6) becomes, at the lowest (zeroth) order,

$$\Psi(\vec{r}) \approx -4G\Sigma_0\kappa_0 b \times 2\pi R_c S_{0,0} \equiv \Psi_0(\vec{r}), \tag{11}$$

where

$${k_0}^2 = \frac{4R_cR}{\Delta_0^2}, \tag{12}$$

$n+m$	n	m	$J_{n,m}$	$S_{n,m}$	$V_{n,m}$
0	0	0	$\frac{1}{\pi}B(\frac{1}{2},\frac{1}{2})=1$	1	1
1	1	0	0	$\frac{1}{2}e^2$	$\frac{1}{4}e^2$
	0	1	0		
2	2	0	$\frac{1}{\pi}B(\frac{3}{2},\frac{1}{2})=\frac{1}{2}$	$\frac{1}{2}e^2$	$\frac{1}{4}e^2$
	1	1	0		
	0	2	$\frac{1}{\pi}B(\frac{1}{2},\frac{3}{2})=\frac{1}{2}$	$\frac{1}{2}e^2$	$\frac{1}{4}e^2$
3	3	0	0		
	2	1	0		
	1	2	0		

Table 1. Expressions for $J_{n,m}$ required when expanding the Green function up to second order. Also given are the surface factor $S_{n,m}$ and the volume factor $V_{n,m}$.

$$\Delta_0^2 = (R+R_c)^2 + Z^2, \tag{13}$$

$$\kappa_0 = \frac{\mathbf{K}(k_0)}{\Delta_0}, \tag{14}$$

and

$$S_{0,0} = \frac{1}{2\pi\Sigma_0 R_c}\int_0^{2\pi}\Sigma(\theta)ad\theta \tag{15}$$

called the "surface factor" in the following. In this paper, we will consider *homogeneous* shells, so we set Σ =const.= Σ_0. Anticipating higher orders, let us define the whole series of definite integrals

$$J_{n,m} = \frac{1}{2\pi}\int_0^{2\pi}\cos^n\theta\sin^m\theta d\theta, \tag{16}$$

where n and m are positive integers. They can all be written in terms of the complete Beta function $B(\frac{n+1}{2},\frac{m+1}{2})$; see the Appendix A. We give $J_{n,m}$ for the first few values of n and m in Tab. 1. We note in particular that $J_{n,m}=0$ when either m, or n or $m+n$ is odd. We have $S_{0,0}=J_{0,0}+eJ_{1,0}=1$ and so the zero-order approximation for the potential of the shell is approximately given by

$$\Psi_0(\vec{r}) = -8\pi G\Sigma_0 b R_c\kappa_0. \tag{17}$$

3.1 Comparison with the potential of a point mass

It is easy to compare (17) to the potential of some simple sources, like the potential of a monopole (or point mass at the origin), which is of major interest in dynamical studies. Introducing the mass of the homogeneous shell $M_{\rm shell} = 4\pi^2\Sigma_0 bR_c$, (17) writes

$$\Psi_0(\vec{r}) = -\frac{GM_{\rm shell}}{r}\times g_{0,0}, \tag{18}$$

where $r=\sqrt{R^2+Z^2}$ is the spherical radius, and

$$g_{0,0} = \frac{r}{\Delta_0}\frac{2}{\pi}\mathbf{K}(k_0). \tag{19}$$

We see that (17) differs from the monopole potential only by the quantity $g_{0,0}$ which is a function of the position in space only. In the physical space, it also depends on R_c,

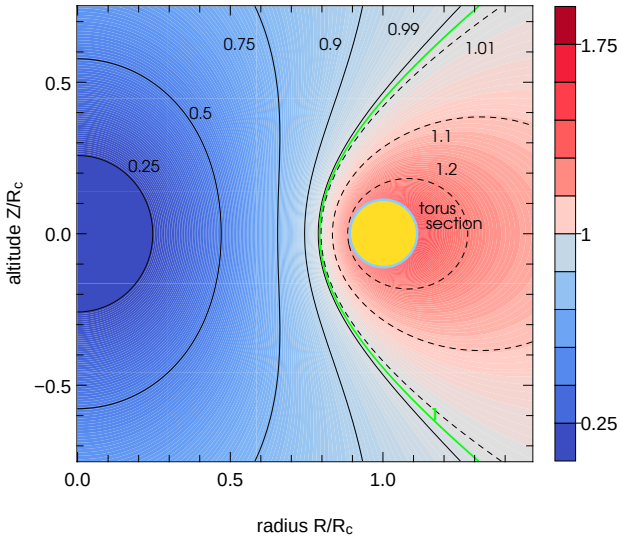

Figure 3. The factor $g_{0,0}$ given by (19) and representing the deviation between the potential of a monopole and the zero-order potential of the toroidal shell. The conditions are the same as for Fig. 2. The shell section is indicated (*thick black line*). A few contour lines are given : $g_{0,0}<1$ (*blue domain*), $g_{0,0}=1$ (*green line*), and $g_{0,0}>1$ (*red domain*).

but not of e, i.e. $g_{0,0}\equiv g_{0,0}(\vec{r};R_c)$. The meridional-plane contours of $g_{0,0}$ are shown in Fig. 3 in the neighborhood of the shell. The contours are closed, except the $g_{0,0}=1$ one. The region where $g_{0,0}>1$ surrounds the shell section, while $g_{0,0}<1$ concerns the central region near the Z-axis. This kind of map is helpful for dynamical studies since it indicates very well the families of bounded and unbounded trajectories of test particles moving with a constant angular momentum (on equatorial or inclined toroidal orbits and on purely meridional orbits).

3.2 Comparison with the potential of a circular loop

Let us also compare the zero-order shell potential (17) and that of a circular loop of radius R_c and mass $M_{\rm loop}=2\pi\lambda R_c$, which writes

$$\begin{aligned}\Psi^{\rm loop}(\vec{r}) &= -2G\lambda\sqrt{\frac{a}{R}}k_0\mathbf{K}(k_0) \\ &= -\frac{GM_{\rm loop}}{r}\underbrace{\frac{r}{\Delta_0}\frac{2}{\pi}\mathbf{K}(k_0)}_{g_{0,0}}.\end{aligned} \tag{20}$$

We see that, at the zeroth order, $\Psi_0=\Psi^{\rm loop}$ at any point P in space, and for any value of e, provided $M_{\rm shell}=M_{\rm loop}$. According to Kondratyev (2018) (see also below), there is no term in the expansion led by e and, more generally, by odd powers of e (this is not guaranteed as soon as Σ varies with θ). This implies that $\Psi^{\rm shell}=\Psi^{\rm loop}+\mathcal{O}(e^2)$. We can thus conclude that (similarity theorem 1):

a homogeneous toroidal shell of main radius R_c and circular section generates, at the first order in the e-parameter, the same exterior potential as a circular loop

of same radius R_c and same mass.

This result has a few important consequences. First, the approximation thus behaves correctly at infinity and on the Z-axis as well ($\lim_{k\to 0}\mathbf{K}(k_0)=\frac{\pi}{2}$ and $k_0/\sqrt{R}$ is finite at the Z-axis). Second, the gravitational acceleration inherits these properties, i.e. the similarity theorem also applies to $\vec{g}=-\nabla\Psi$ (see below). Third, the formula (17) does not generate any residual mass distribution in space. This is easily verifiable by calculating the Laplacian of κ_0 (see the Appendix B for the demonstration), i.e.

$$\nabla^2\Psi_0 = 4\pi G\rho^{\rm res} = 0. \tag{21}$$

This property is also intrinsic to the interior solutions reported in Huré et al. (2019).

4 NUMERICAL TESTS. DOMAIN OF VALIDITY

Let us now compare the expression (17) to the numerical reference (see Sect. 2). We quantify the relative difference by

$$\epsilon = \log\left|\frac{\Psi-\Psi_{\rm ref}}{\Psi_{\rm ref}}\right|. \tag{22}$$

Figure 4 shows ϵ in the upper half-plane $Z>0$ for $e=0.1$. If we limit the statistics to the domain exterior to the shell, the average precision is of the order of 10^{-3} in the vicinity of the shell, and it is much lower in the far field. The deviation with respect to the reference never exceeds 1%. The error is maximal near the surface of the shell, which is not a surprise. On the other hand, the best approximation is achieved in a narrow domain going from the top of the shell to infinity along the line $Z\sim 0.7R$.

Our expansion is performed at the center C of the shell section. The expanded function thus has to be smooth enough between C and any point P located at the shell surface. This, however, is not the case for $\mathbf{K}(k)/\Delta$ which is singular for any point P(R,Z) belonging to the line segment [CP']. Therefore, the formula (10) and subsequently *the zero-order approximation is only valid outside the cavity*, namely for

$$(R-R_c)^2+Z^2-b^2>0. \tag{23}$$

The comparison has been checked for different values of the shell parameter e. The results are plotted in Fig. 5 where values of ϵ have been averaged over values contained inside a squared box $[1-2e,1+2e]\times[0,4e]$ (in dimensionless units) encompassing the shell section (see Fig. 4); interior values are excluded. We see that the smaller the shell parameter, the better the approximation. The precision of the zero-order approximation remains better than 1% for shell parameter as large as about 0.3, which is remarkable.

5 EXPANSION UP TO 2ND ORDER

Though already very good, the zero-order approximation can be improved by considering further terms in the expansion. For order one, we have to calculate

$$\int_0^{2\pi}\left[(a-R_c)\left.\frac{\partial\kappa}{\partial a}\right|_{\substack{a=R_c\\z=0}}+z\left.\frac{\partial\kappa}{\partial z}\right|_{\substack{a=R_c\\z=0}}\right]abd\theta, \tag{24}$$

where a and z are still given by (7). Because the derivatives are evaluated at $a=R_c$ and $z=0$, they are not concerned by the integration over θ and can be carried out of the operator. There are two new surface factors to calculate, namely (we do not include Σ in these definitions, since we assume it is

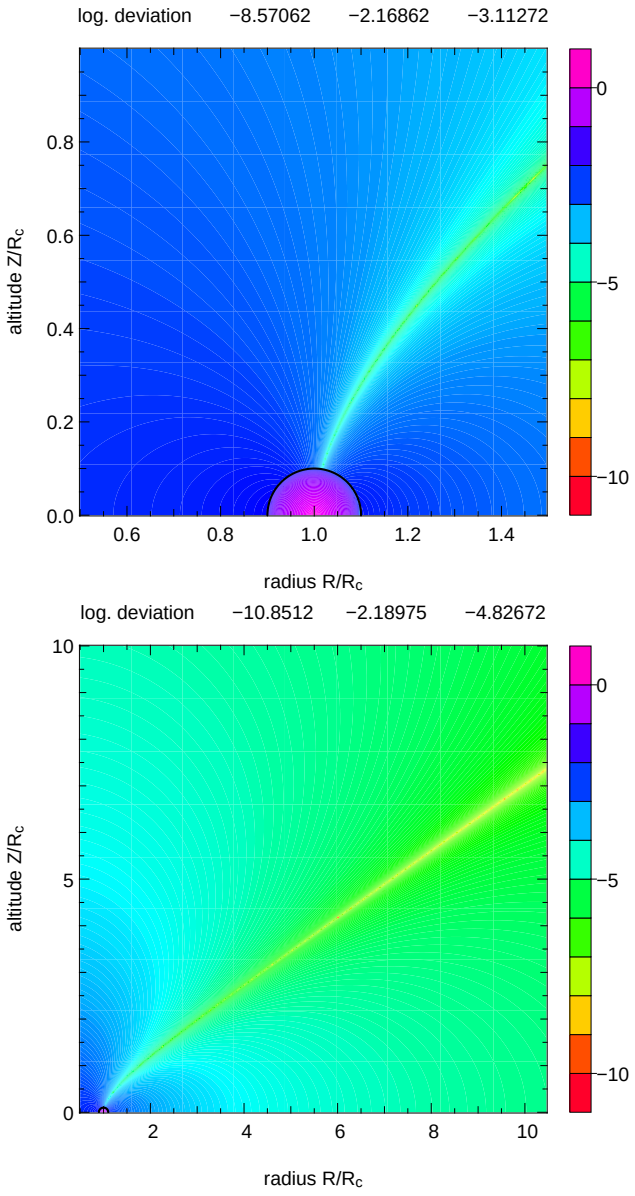

Figure 4. The log. of the relative deviation defined by (22) between Ψ computed by direct integration, i.e. $\Psi_{\rm ref}$, and the zero-order approximation given by (17), in the vicinity of the shell (*top*) and at longer range (*bottom*). The parameter of the shell (*thick black circle*) is $e=0.1$; see Fig. 2 for the associated potential. The numbers given at the top, from left to right, refer to the minimal, maximal and mean values for ϵ, respectively, reached within the actual computational box (and exterior to the shell).

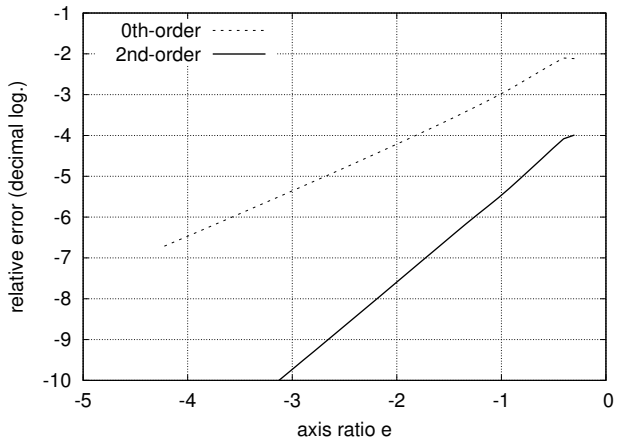

Figure 5. Average of the log. of the relative deviation defined by (22) versus the shell parameter for the 0th-order (*dotted line*) and the 2nd-order approximation (*solid line*). The sample gather values contained inside the computational box $4e \times 4e$ around the shell section (and exterior to it).

constant)

$$S_{1,0} = \frac{1}{2\pi R_c^2} \int_0^{2\pi} (a - R_c) a d\theta, \tag{25}$$

and

$$S_{0,1} = \frac{1}{2\pi R_c^2} \int_0^{2\pi} z a d\theta, \tag{26}$$

but this latter term vanishes (since $J_{0,1}$ and $J_{1,1}$ are zero). In the first order, the potential writes $\Psi \approx \Psi_0 + \Psi_1$, where Ψ_0 is given by (17) and

$$\Psi_1 = -8\pi G \Sigma_0 b R_c^2 \left.\frac{\partial \kappa}{\partial a}\right|_{R_c,0} \times S_{1,0}, \tag{27}$$

where $S_{1,0} = e(J_{1,0} + eJ_{2,0})$. Note that the derivative $\frac{\partial \kappa}{\partial a}$ is analytical (see the Appendix C). Since $J_{1,0} = 0$, the first-order correction depends on e^2. As $2\pi J_{2,0} = 2B(\frac{3}{2}, \frac{1}{2}) = \pi$, we have

$$S_{1,0} = \frac{1}{2} e^2. \tag{28}$$

It is pertinent to account for the next term in the Taylor expansion which also contains a contribution varying as e^2. This term is

$$\frac{1}{2} \int_0^{2\pi} \left[(a - R_c)^2 \left.\frac{\partial^2 \kappa}{\partial a^2}\right|_{R_c}_0 + 2(a - R_c) z \left.\frac{\partial^2 \kappa}{\partial a \partial z}\right|_{R_c}_0 + z^2 \left.\frac{\partial^2 \kappa}{\partial z^2}\right|_{R_c}_0 \right] a b d\theta, \tag{29}$$

and so the 2nd-order approximation is given by $\Psi \approx \Psi_0 + \Psi_1 + \Psi_2$, with

$$\Psi_2 = -8\pi G \Sigma_0 b R_c^3 \times \frac{1}{2} \left[\left.\frac{\partial^2 \kappa}{\partial a^2}\right|_{R_c}_0 S_{2,0} + 2 \left.\frac{\partial^2 \kappa}{\partial a \partial z}\right|_{R_c}_0 S_{1,1} + \left.\frac{\partial^2 \kappa}{\partial z^2}\right|_{R_c}_0 S_{0,2} \right], \tag{30}$$

where the derivatives are given in the Appendix C. The new surface factors are (again, Σ is removed from these definitions)

$$S_{2,0} = \frac{1}{2\pi R_c^3} \int_0^{2\pi} (a - R_c)^2 a d\theta, \tag{31}$$

$$S_{1,1} = \frac{1}{2\pi R_c^3} \int_0^{2\pi} (a - R_c) z a d\theta, \tag{32}$$

and

$$S_{0,2} = \frac{1}{2\pi R_c^3} \int_0^{2\pi} z^2 a d\theta. \tag{33}$$

We see that $S_{1,1} = 0$, again because of the odd power of z. The non-zero terms are $S_{2,0} = e^2(J_{2,0} + eJ_{3,0})$ and $S_{0,2} = e^2(J_{0,2} + eJ_{1,2})$, where $J_{3,0} = J_{1,2} = 0$, $2\pi J_{2,0} = 2B(\frac{3}{2}, \frac{1}{2}) = \pi$. $S_{2,0} = S_{0,2} = \frac{1}{2}e^2$. We thus see that it is necessary to include *both* orders 1 and 2 simultaneously in order to obtain a consistent e^2-approximation. This new approximation can be put in the form of a modified monopole, like we did for the zeroth-order expression. There is one specific correction factor $g_{n,m} \equiv g_{n,m}(\vec{r}; R_c, e)$ for each non-zero surface factor $S_{n,m}$. We find

$$\Psi_1 = -\frac{GM_{\rm shell}}{r} g_{1,0}, \tag{34}$$

where

$$g_{1,0} = r \frac{2}{\pi} \left.\frac{\partial \kappa}{\partial a}\right|_{\substack{a=R_c \\ z=0}} R_c S_{1,0}, \tag{35}$$

and

$$\Psi_2 = -\frac{GM_{\rm shell}}{r} \frac{1}{2} (g_{2,0} + g_{0,2}), \tag{36}$$

where

$$g_{2,0} = r \frac{2}{\pi} \left.\frac{\partial^2 \kappa}{\partial a^2}\right|_{\substack{a=R_c \\ z=0}} R_c^2 S_{2,0}, \tag{37}$$

and

$$g_{0,2} = r \frac{2}{\pi} \left.\frac{\partial^2 \kappa}{\partial z^2}\right|_{\substack{a=R_c \\ z=0}} R_c^2 S_{0,2}. \tag{38}$$

Because of the circular section, $S_{2,0} = S_{0,2}$ which implies that the partial sum $\Psi_1 + \Psi_2$ can be rewritten in a very compact form. We actually find

$$g_{1,0} + \frac{1}{2}(g_{2,0} + g_{0,2}) = r \frac{2}{\pi} \times \frac{e^2}{8k'^2 \Delta_0^3} \times \left\{ \left[\Delta_0^2 - 2R_c(R_c + R)\right] \mathbf{E}(k) - k'^2 \Delta_0^2 \mathbf{K}(k) \right\}, \tag{39}$$

which is to be multiplyed by $-GM_{\rm shell}/r$.

Figure 6 compares the second-order approximation obtained from (17), (27) and (30) with the reference values (see Sect. 2), as computed under the same conditions as in Fig. 4. We notice that the e^2-approximation reproduces the potential with almost 6-digits precision in the close vicinity of the shell. At larger distances, the expansion is extremely efficient (in the present example, the potential is known with more than 10 digits for $r/R_c \gtrsim 5$ typically). The variation of the averaged precision as a function of the shell parameter e is plotted in Fig. 5, in the same conditions as for the zeroth-order approximation.

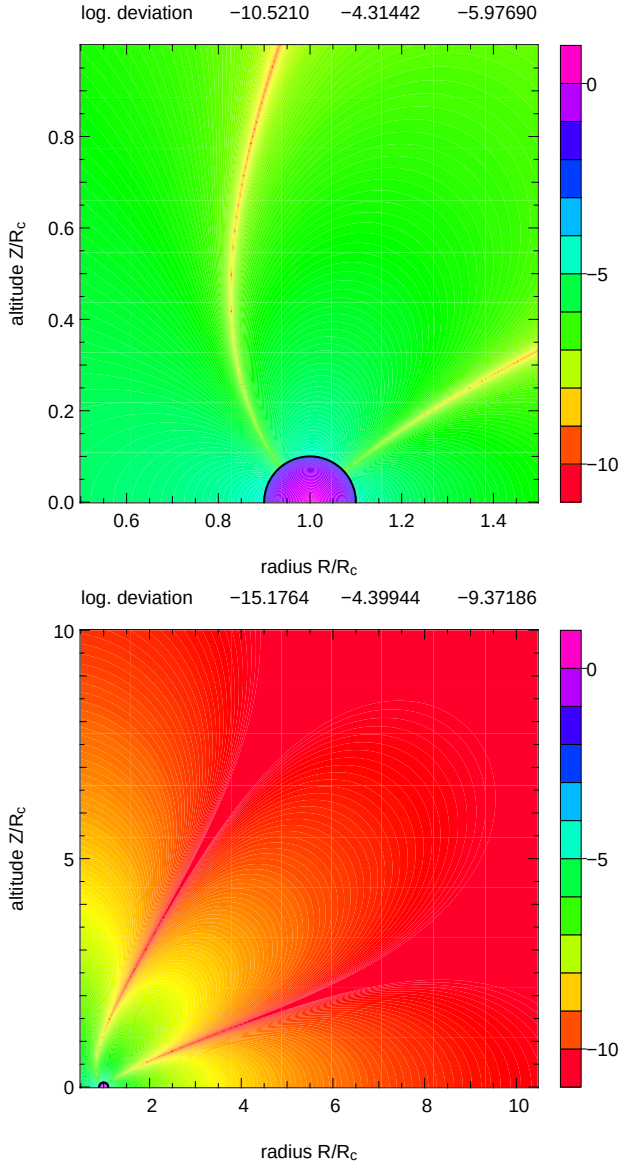

Figure 6. The same legend and the same conditions as for Fig. 4, but for the 2nd-order approximation (i.e. e^2-approximation).

6 VALUES AT THE SURFACE. MATCH WITH THE INTERIOR SOLUTION

At the surface of the shell, we have $R = R_c + b\cos\theta$ and $Z = b\sin\theta$, or equivalently $(R - R_c)^2 + Z^2 - b^2 = 0$ with $R \in [R_c - b, R_c + b]$. If we introduce these expressions in (12), the modulus k_0 simplifies into

$$ {k_0}^2 = \frac{4RR_c}{4RR_c + b^2}. \tag{40} $$

Using these values in (17), (27) and (30), we get the potential at the shell surface, which can be compared to the values obtained from the interior solution reported in Huré et al. (2019); see their equations (35), (36) and (39). The results are displayed in Fig. 7, again for $e = 0.1$. We see that the matching is very good at the second order (with at least 4 correct digits). At the zeroth order, the interior solution reduces to a constant potential throughout the toroidal cavity, which is quite crude while the exterior solution already depends on the radius R.

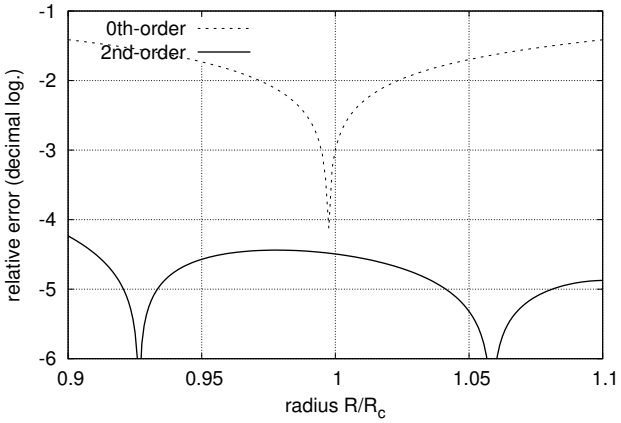

Figure 7. Logarithm of the difference between the interior solution (Huré et al. 2019) and the exterior solution for the 0th-order (*dotted line*) and 2nd-order approximations (*plain line*). The shell parameter is $e = 0.1$.

7 GENERALIZATION TO NTH-ORDER EXPANSION

It is possible to include further terms in the Taylor series. Since the expansion writes formally

$$ \kappa = \kappa_0 + \sum_{n=1}^{\infty} \frac{1}{n!} \sum_{m=0}^{n} \binom{n}{m} (a - R_c)^{n-m} z^m \left. \frac{\partial^n \kappa}{\partial a^{n-m} \partial z^m} \right|_{\substack{a=R_c \\ z=0}}, \tag{41} $$

where $\binom{n}{m}$ denotes the binomial coefficient, the potential can be exactly reconstructed by multiplying (41) by a, followed by the integration over the latitude angle θ. If the infinite series is truncated at order N, the potential is of the form

$$ \Psi \approx \Psi_0 + \sum_{n=1}^{N} \Psi_n, \tag{42} $$

where the nth-order contribution Ψ_n is made of $n+1$ terms, namely

$$ \Psi_n = -4G\Sigma_0 \times \frac{1}{n!} \sum_{m=0}^{n} \binom{n}{m} \left. \frac{\partial^n \kappa}{\partial a^{n-m} \partial z^m} \right|_{\substack{a=R_c \\ z=0}} \times 2\pi b R_c^{n+1} S_{n-m,m}, \tag{43} $$

where we have set (still in the homogeneous case)

$$ S_{n,m} = \frac{1}{2\pi R_c^{n+m+1}} \int_0^{2\pi} (a - R_c)^n z^m a \, d\theta = e^{n+m} (J_{n,m} + e J_{n+1,m}). \tag{44} $$

Note that $\Psi_{n+1} \ll \Psi_n$ when $e \ll 1$, and the equality in (42) is obtained in the limit $N \to \infty$. In the form of the modified monopole representation, the n-order correction is

$$ \Psi_n = -\frac{GM_{\rm shell}}{r} \sum_{m=0}^{n} g_{n,m}, \tag{45} $$

$n+m$	n	m	$V_{n,m}$ homogeneous	(59)
0	0	0	1	$\frac{\alpha}{\alpha+1}$
1	1	0	$\frac{1}{4}e^2$	$\frac{\alpha}{4(\alpha+2)}e^2$
	0	1		
2	2	0	$\frac{1}{4}e^2$	$\frac{\alpha}{4(\alpha+2)}e^2$
	1	1	0	0
	0	2	$\frac{1}{4}e^2$	$\frac{\alpha}{4(\alpha+2)}e^2$

Table 2. Expressions for the volume factor $V_{n,m}$ in the case of core-stratified toroids according to (58) and (59).

where

$$g_{n,m} = \frac{2}{\pi} r \times \frac{1}{n!}\binom{n}{m} \left.\frac{\partial^n \kappa}{\partial a^{n-m}\partial z^m}\right|_{\substack{a=R_c\\z=0}} R_c^n S_{n-m,m}. \quad (46)$$

Since the two operators $\nabla^2_{R,Z}$ and $\partial^n/\partial a^{n-m}\partial z^m$ act on different spaces, we have

$$\nabla^2_{R,Z}\left(\frac{\partial^n \kappa}{\partial a^{n-m}\partial z^m}\right) = \frac{\partial^n}{\partial a^{n-m}\partial z^m}\left(\nabla^2_{R,Z}\kappa\right) = 0 \quad (47)$$

for any pair (n,m). This is expected because κ is a harmonic function (see Sec. 4). We thus conclude that $\nabla^2_{R,Z}\Psi_n = 0$, for any n, which means that each term of the expansion separately obeys the Laplace equation. Therefore, expanding the Green function over a and z induces no residual source mass in space, whatever the order of the truncation.

8 THE SOLID TORUS

The above solution for the shell can be employed to obtain the potential of a solid toroid. This is achieved by integrating (6) over b, while the surface density Σ is changed for ρdb, ρ being the mass density. The result is

$$\Psi(\vec{r}) = -4G\int_0^b\int_0^{2\pi} \rho(b',\theta) a\kappa b' d\theta db', \quad (48)$$

where κ can be replaced by its Taylor expansion, namely (10). In the leading term, i.e. using just (17), we have

$$\Psi_0(\vec{r}) = -\,4G\kappa_0 \times \pi R_c b^2 \rho_0 V_{0,0}, \quad (49)$$

where ρ_0 is some typical mass density, and $V_{0,0}$ is the "volume factor" defined in general by

$$V_{0,0} = \frac{1}{\pi\rho_0 R_c b^2}\int_0^b b'db'\int_0^{2\pi}\rho(b',\theta)ad\theta, \quad (50)$$

where $b' = e'R_c \le b$. As quoted, the mass density ρ may vary with both θ and b' (see below). In the *homogenous case*, we have ρ =const.= ρ_0, and so (50) becomes

$$V_{0,0} = \frac{2}{\rho_0 e^2}\int_0^e \rho(e')e'S_{0,0}(e')de' = \frac{2}{e^2}\int_0^e e'S_{0,0}(e')de', \quad (51)$$

where the dependence of the surface factor with the shell parameter e has been explicited. Introducing the total mass of the homogeneous torus $M_{\rm solid} = 2\pi^2\rho_0 b^2 R_c$, the zero-order formula can be written in the form

$$\Psi_0(\vec{r}) = -\frac{GM_{\rm solid}}{r} g_{0,0}, \quad (52)$$

where we have set

$$g_{0,0} = \frac{r}{\Delta_0}\frac{2}{\pi}\mathbf{K}(k_0)V_{0,0}. \quad (53)$$

Again, the difference from the point-mass potential is represented by the term $g_{0,0}$, while the deviation with respect to the potential of a massive loop (of radius $a = R_c$) is given by the volume factor $V_{0,0}$. For the zero-order approximation, we have $V_{0,0} = 1$, and so $\Psi^{\rm solid} = \Psi^{\rm loop} + \mathcal{O}(e^2)$. We can thus conclude (similarity theorem 2):

a solid torus of main radius R_c and circular section generates, at the first order in the e-parameter, the same exterior potential as a circular loop of radius R_c and same mass.

The derivation of the e^2-term requires $V_{1,0}$, $V_{2,0}$ and $V_{0,2}$, which are listed in Tab. 2. These quantities happen to be equal (due to the circular section). As a consequence, the partial sum $\Psi_1 + \Psi_2$ resembles[1] the formula derived in Kondratyev (2018). We finally find

$$\Psi_1 + \Psi_2 = e^2\left(-\frac{G\pi\rho_0 R_c b^2}{4k'^2\Delta_0^3} \times \left\{\left[\Delta_0^2 - 2R_c(R_c+R)\right]\mathbf{E}(k) - k'^2\Delta_0^2\mathbf{K}(k)\right\}\right). \quad (54)$$

We have compared (49) to a reference obtained by direct numerical integration of (48). As we have observed, the error map is the same as for the shell, which is expected since the only difference between the shell and the torus stands in the volume factor which is analytical. This remark holds for the e^2-approximation.

More terms in the expansion of κ can be accounted for. The n-order contribution is

$$\Psi_n = -4G\frac{1}{n!}\sum_{m=0}^{n}\binom{n}{m}\left.\frac{\partial^n\kappa}{\partial a^{n-m}\partial z^m}\right|_{\substack{a=R_c\\z=0}} \times 2\pi R_c^{n+1}\rho_0\int_0^b S_{n-m,m}(b')b'db', \quad (55)$$

where $S_{n-m,m}$ depends on b' as indicated. If we set the volume factor $V_{n,m}$ to

$$V_{n,m} = \frac{1}{2\pi R_c^{n+m+1}}\frac{2}{b^2}\int_0^b b'db'\int_0^{2\pi}(a-R_c)^n z^m a d\theta. = \frac{2}{e^2}\int_0^e S_{n,m}(e')e'de', \quad (56)$$

then Ψ_n has the same form as (45) where $S_{n-m,m}$ is just to be replaced by $V_{n-m,m}$ and $M_{\rm shell}$ by $M_{\rm solid}$. It can be checked that Ψ_n is harmonic.

[1] We notice two differences between (54) and the formula (14) by Kondratyev (2018): the factor R_0^3 should be $R_0 r_0^2 \equiv R_c b^2$ (since the ϕ_2 term is multiplied by e^2), and the factor 16 at the denominator should be 4.

9 INHOMOGENOUS SYSTEMS

As a matter of fact, (41) works for inhomogenous systems. Actually, the expansion depends on a and z only through powers of $\cos\theta$ and $\sin\theta$. If $\Sigma(\theta)$ is prescribed, the knowledge of any term Ψ_n just requires the calculation of the surface factors according to

$$S_{n,m} = \frac{1}{2\pi\Sigma_0 R_c^{n+m+1}} \int_0^{2\pi} \Sigma(\theta)(a-R_c)^n z^m a d\theta \qquad (57)$$
$$= \frac{e^{m+n}}{2\pi\Sigma_0} \int_0^{2\pi} \Sigma(\theta)\cos^n\theta \sin^m\theta(1+e\cos\theta)d\theta.$$

We see that the $S_{n,m}$'s are combinations of moments of the surface density profile, which are analytical for a wide family of $\Sigma(\theta)$-profiles. In a similary way for the solid torus, if ρ depends both on θ and on $b' \leq b$, then the volume factors are calculated following

$$V_{n,m} = \frac{1}{2\pi\rho_0 R_c^{n+m+1}} \frac{2}{b^2}$$
$$\times \int_0^b b' db' \int_0^{2\pi} \rho(b',\theta)(a-R_c)^n z^m a d\theta, \qquad (58)$$
$$= \frac{e^{m+n}}{\pi\rho_0}$$
$$\times \int_0^1 x'^{n+m+1} dx' \int_0^{2\pi} \rho(x',\theta)\cos^n\theta\sin^m\theta(1+bx'\cos\theta)d\theta,$$

where we have set $b' = bx' \leq b$. We can go a little bit further in the analysis by considering the case where the two variables b' and θ are separable, i.e. $\rho(b',\theta) = f(b') \times g(\theta)$. This corresponds to toroids having a core stratification. For instance, if we assume the θ-invariance and (with $2\alpha > -1$)

$$\rho(b') = \rho_0 \left[1 - \left(\frac{b'}{b}\right)^{2\alpha}\right], \qquad (59)$$

then the volume factor required at order zero (i.e. $n = m = 0$) is

$$V_{0,0} = \int_0^1 2x'(1-x'^{2\alpha})dx'$$
$$= \frac{\alpha}{1+\alpha}. \qquad (60)$$

Note that $V_{0,0} \to 1$ as $\alpha \to \infty$. Since $M_{\rm solid} V_{0,0}$ is just the total mass M of the (inhomogeneous) core-stratified torus, we have $\Psi = \Psi^{\rm loop} + \mathcal{O}(e^2)$. We can conclude that (similarity theorem 3):

a core-stratified torus of main radius R_c and circular section generates, at the first order in the e-parameter, the same exterior potential as a circular loop of radius R_c and same mass.

Table 2 lists values of $V_{n,m}$ corresponding to (59).

10 GRAVITATIONAL ACCELERATION

For a massive loop, the non-zero components of acceleration $\vec{g} = -\vec{\nabla}\Psi$ are given by (Durand 1953; Huré 2005)

$$g_R = \frac{GM_{\rm loop}}{2\pi R_c R}\sqrt{\frac{R_c}{R}} \qquad (61)$$
$$\times k_0 \left[\mathbf{E}(k_0) - \mathbf{K}(k_0) + \frac{(R_c-R){k_0}^2\mathbf{E}(k_0)}{2R_c {k'_0}^2}\right],$$

and

$$g_Z = -\frac{GM_{\rm loop} Z}{4\pi R R_c\sqrt{RR_c}} \frac{{k_0}^3\mathbf{E}(k_0)}{{k'_0}^2}. \qquad (62)$$

According to the similarity theorems 1 to 3, the acceleration outside a shell, solid torus, or core-stratified toroid is the same as for a loop having the same mass M, and deviations are $\mathcal{O}(e^2)$. This result is very convenient for a study of the motion of orbiting test-particles. Several types of trajectories can be distinguished. Of particular interest are circular trajectories tied to the equatorial plane of the shell/torus and having $R \notin [R_c - b, R_c + b]$. The orbital velocity $v_\phi^2 = R\nabla_R\Psi$ is easily deduced from (61). We find

$$v_\phi^2(R) = \frac{GM}{R+R_c}\frac{1}{\pi}\left[\mathbf{K}(k_0) + \frac{R+R_c}{R-R_c}\mathbf{E}(k_0)\right], \qquad (63)$$

where $k_0 = \frac{2\sqrt{RR_c}}{R+R_c}$ follows from (12) where Z has been set to 0. Figure 8 displays (63) versus the radius. Note that $v_\phi^2(R) \leq 0$ for $R \in [0, R_c - b]$, which means that orbits are in principle forbidden in this region, unless a massive central object is present. The Keplerian profile associated to a point mass at the origin is shown in comparison. For $R \geq R_c + b$, the velocity is super-Keplerian. It is a decreasing function of the radius, the maximum value being reached at the outer radius $R_c + b$ of the toroid. To the detriment of precision, we can replace the elliptic integrals by more standard functions when $k_0 \to 1$, which corresponds to particles orbiting very close to the inner/outer radius of the toroid. Within this limit, $\mathbf{K}(k_0) \sim \ln\frac{4(R+R_c)}{|R-R_c|}$ and $\mathbf{E}(k_0) \sim 1$.

Another interesting quantity is the vertical component of acceleration at the surface of thin/small rings. It is a fundamental ingredient that governs the hydrostatic equilibrium of astrophysical discs (e.g. Shakura & Sunyaev 1973; Pringle 1981). By setting $\mathbf{E}(k_0) \approx 1$, which again corresponds to the vicinity of the toroid, we find

$$g_Z = -2\pi G\rho b \frac{\sin\theta}{\sqrt{1+e\cos\theta+\frac{e^2}{4}}}, \qquad (64)$$

where $\theta \in [0,\pi]$ above the equatorial plane. This quantity is plotted in Fig. 9 for $e = 0.1$ as the torus parameter. It varies between 0 at the inner/outer edges to about $-2\pi G\rho b$ at $\theta = \frac{\pi}{2}$. It is interesting to see that Paczynski's approximation (Paczynski 1978), classically written as $-4\pi G\rho Z$, overestimates the acceleration by a factor 2 in the middle of the toroid. This observation may e.g. be of importance in oscillation modes in planetary or other rings (Wisdom & Tremaine 1988; Lehmann et al. 2019). It also means that, in a geometrically thin discs where Paczynski's approximation is valid, half of the vertical acceleration comes from the local contribution of matter while the other half comes from the global or long-range distribution of matter (Trova et al. 2014).

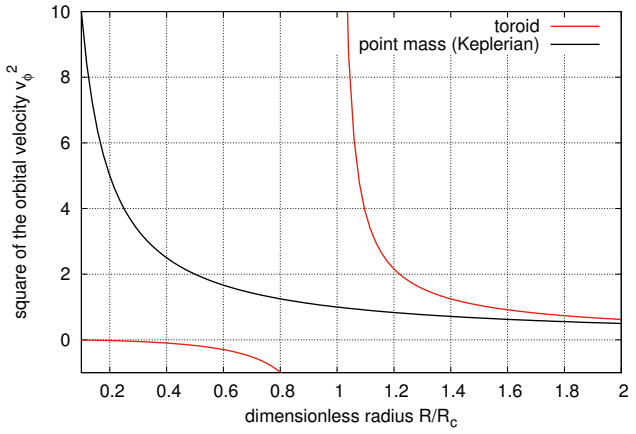

Figure 8. Square of the circular velocity in the equatorial plane of the toroid as given by (63), i.e. at order zero. The curve has to be truncated at the actual outer radius, which is $1+e$ in dimensionless units. Negative values take sense only when a massive central object is present. The Keplerian velocity due to a point mass with the same mass is shown in comparison.

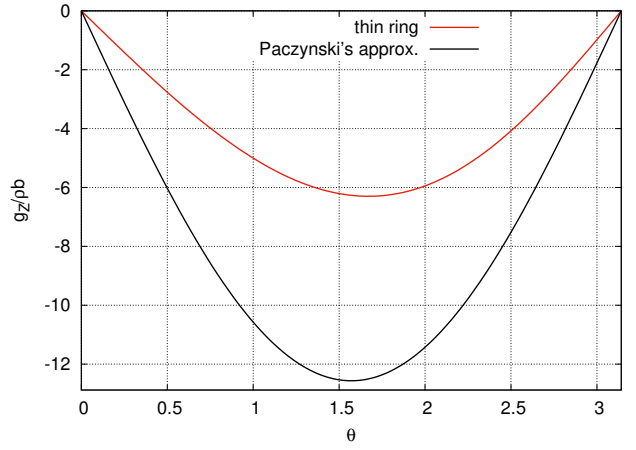

Figure 9. Vertical acceleration at the surface of the toroid in units of $G\rho b$. Paczynski's approximation valid for geometrically thin, extended systems is shown in comparison.

11 MAGNETIC POTENTIAL AND FIELD FOR PURELY AZIMUTHAL CURRENTS (IN SURFACE AND VOLUME)

The method presented in this paper can also be applied to the determination of the vector potential $\vec{A}$ of electromagnetism. Toroidal currents are met in both terrestrial and astrophysical plasmas (Dini et al. 2009; Trova et al. 2018). The magnetic potential $\vec{A} = A_\phi \vec{e}_\phi$ of a toroidal shell carrying a purely azimuthal electric current $\sigma\vec{e}_\phi$ is obtained by summing over the contribution of individual current loops (Jackson 1998; Cohl et al. 2001), namely

$$A_\phi(\vec{r}) = \frac{\mu_0}{2\pi}\int_0^{2\pi} \sigma(\theta)\sqrt{\frac{a}{R}}\frac{\left(2-k^2\right)\mathbf{K}(k) - 2\mathbf{E}(k)}{k} bd\theta\,, \tag{65}$$

where $I = b\oint\sigma(\theta)d\theta$ is the total current. Similarly as for the gravitational problem, we have to select some part of the Green function. A convenient choice appears to be

$$\frac{1}{\Delta}\left\{\frac{2}{k^2}\left[\mathbf{K}(k)-\mathbf{E}(k)\right]-\mathbf{K}(k)\right\} \equiv \kappa'. \tag{66}$$

By expanding κ' over a and z at the center C of the shell, i.e. at $a=R_c$ and $z=0$, and integrating over the latitude θ (see Sec. 3), we get the leading term

$$\begin{aligned} A_\phi(\vec{r}) &= \frac{\mu_0 b}{\pi}\times\kappa_0'\int_0^{2\pi}\sigma a d\theta \\ &= 2\mu_0\sigma b R_c\kappa_0' S_{0,0}, \end{aligned} \tag{67}$$

where κ_0' stands for κ' evaluated at C, σ =const. is assumed, and $S_{0,0}$ is given by (15). A θ-dependent surface density of current would lead to a different surface factor. Again, we notice that (67) formally differs from the expression for a current loop only by the term $S_{0,0}$, which is unity in the homogeneous case. We thus state (similarity theorem 4):

a toroidal shell of main radius R_c and circular section carrying a uniform surface current generates, at the first order in the e-parameter, the same exterior magnetic potential as a circular loop of radius R_c carrying the same current.

The theorem holds in the $\mathcal{O}(e^2)$ order. It applies likewise to the magnetic field $\vec{B} = \nabla\times\vec{A}$. The e^2-approximations for the poloidal components B_R and B_Z of the shell are then given by

$$B_R = \frac{\mu_0 I}{2\pi}\frac{Z}{R\Delta_0}\left[\frac{R^2+R_c^2+Z^2}{(R-R_c)^2+Z^2}\mathbf{E}(k_0)-\mathbf{K}(k_0)\right], \tag{68}$$

$$B_Z = \frac{\mu_0 I}{2\pi}\frac{1}{\Delta_0}\left[-\frac{R^2-R_c^2+Z^2}{(R-R_c)^2+Z^2}\mathbf{E}(k_0)+\mathbf{K}(k_0)\right]. \tag{69}$$

We can deduce the magnetic potential and field of a solid torus carrying a uniform current density $\vec{J} = J_\phi\vec{e}_\phi$, following the procedure given in Sec. 8. The e^2-approximation for the vector potential is obtained from (67) where $S_{0,0}$ is to be replaced by $V_{0,0}$ (which is also unity in the present case). So we can state that (similarity theorem 5):

a toroid of main radius R_c and circular section carrying a uniform volume current density generates, at the first order in the e-parameter,, the same exterior magnetic potential (and the field) as a circular loop of radius R_c carrying the same current.

The reader can verify that this theorem also works for a core-stratified current, as for the gravitationnal problem.

12 GENERAL COMMENTS

The paper resides on the expansion of $\mathbf{K}(k)/\Delta$. Other options are possible as quoted before. If we expand $k\mathbf{K}(k)$ instead of $\mathbf{K}(k)/\Delta$ in the Green function, one can show that $g_{0,0}$ is changed for

$$g_{0,0} = \frac{r}{\Delta_0}\frac{2}{\pi}\mathbf{K}(k_0)\times S_{0,0}, \tag{70}$$

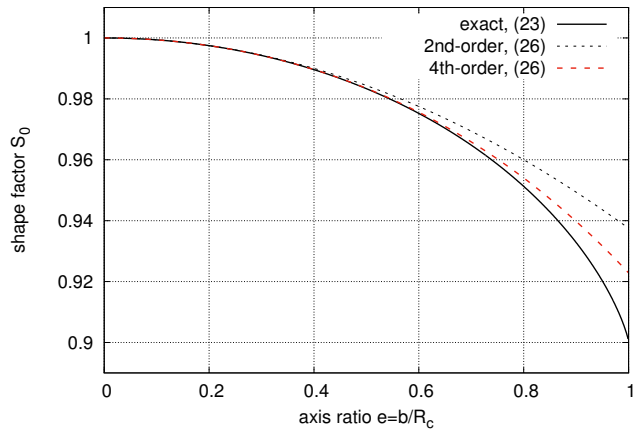

Figure 10. The quantity $S_{0,0}$ given by (71).

where

$$S_{0,0} = \frac{2}{\pi}\mathbf{E}(p)\sqrt{1+e}, \tag{71}$$

$$\mathbf{E}(k) = \int_0^{\pi/2} \sqrt{1-k^2\sin^2\vartheta}\, d\vartheta \tag{72}$$

is the complete elliptic integral of the second kind, and

$$p^2 = \frac{2e}{1+e} \in [0,1]. \tag{73}$$

With this approach, again, $S_{0,0}$ still does not depend on R and Z, but solely on e. It is plotted in Fig. 10. As we can see, its range of variation, namely $[\frac{2\sqrt{2}}{\pi}, 1]$, is very small. As a consequence, (19) and (70) are very close, and Fig. 3 is almost unchanged. Besides, we have

$$S_{0,0} = 1 - \frac{e^2}{16} - \frac{15e^4}{1024} + \dots \tag{74}$$

for $e \leq 1$. Since $S_{0,0} = 1$ for $e = 0$, we still have $\lim_{e\to 0} \Psi_0 = \Psi^{\rm loop}$. The similarity theorem 1 reads in this case:

a homogeneous toroidal shell of mass M, main radius R_c and circular section of radius $b = eR_c$ generates, at the second order in the e-parameter, the same exterior potential as a circular loop of radius R_c and mass $MS_{0,0}$, where $S_{0,0}$ is given by (71).

It can be shown after some algebra that the next three surface factors are respectively

$$S_{1,0} = \frac{2}{3\pi}\sqrt{1+e}\,[\mathbf{E}(p) - (1-e)\mathbf{K}(p)]\,, \tag{75}$$

$$S_{2,0} = \frac{8}{15\pi}\sqrt{1+e}\left[\left(\frac{9}{2}e^2 - 1\right)\mathbf{E}(p) + (1-e)\mathbf{K}(p)\right], \tag{76}$$

and

$$S_{0,2} = \frac{4}{15\pi}\sqrt{1+e}\,[(3e^2+1)\mathbf{E}(p) - (1-e)\mathbf{K}(p)]\,. \tag{77}$$

and the corresponding error map is, as verified, similar to Fig. 6.

Another important comment concerns the point where the expansion is performed. In Huré et al. (2019), the choice for the expansion at the focal ring $a = R_{\rm p}$ was strategical: this is the only point in space which makes the modulus k of the elliptic integral constant all along the circular section of the shell. The motivation for chosing the centre of the circular section here (instead of the focal ring) is similar: the calculation of the integral in (6) is facilitated, in particular through the expression for $d\ell = bd\theta$. If we use for instance the toroidal coordinates $(\eta,\zeta) \in [0,\infty[\times[-\pi,\pi[$, the integral over θ in (6) can be converted into an integral over ζ. We have in this case

$$a = R_{\rm p}\frac{\sinh\eta}{\cosh\eta - \cos\zeta}, \qquad z = R_{\rm p}\frac{\sin\zeta}{\cosh\eta - \cos\zeta}, \tag{78}$$

where $R_{\rm p}$ is the radius of the pole (or focal ring), and the line element is $d\ell = R_{\rm p}\frac{d\zeta}{\cosh\eta - \cos\zeta}$. As a consequence, the potential writes

$$\Psi(\vec{r}) = -4G{R_{\rm p}}^2\int_{-\pi}^{\pi}\frac{\mathbf{K}(k)}{\Delta}\sinh\eta\frac{\Sigma(\zeta)d\zeta}{(\cosh\eta - \cos\zeta)^2}, \tag{79}$$

where the modulus k and Δ depend on ζ. The expansion of κ in $x_0 = R_{\rm p}$ (and $y_0 = 0$ still; see Sects. 3 and 7) generates, for the homogeneous shell, integrals of the form

$${R_{\rm p}}^{n+m+2}\int\frac{(\cosh\eta - \cos\zeta - \sinh\eta)^n}{(\cosh\eta - \cos\zeta)^{n+m+2}}\sin^m\zeta d\zeta. \tag{80}$$

At order zero (i.e., for $n = m = 0$), we find

$$\Psi(\vec{r}) \approx -8G{R_{\rm p}}^2\Sigma_0\kappa_0 S_{0,0}, \tag{81}$$

where

$$\begin{aligned} S_{0,0} &= 2\sinh\eta_0\int_{-\pi}^{\pi}\frac{d\zeta}{(\cosh\eta_0 - \cos\zeta)^2}, \\ &= \frac{\cosh\eta_0}{\sinh^2\eta_0} = \frac{b{R_c}}{{R_{\rm p}}^2}, \end{aligned} \tag{82}$$

and so we recover (17). For higher terms, (80) have to be calculated analytically for all pairs (n,m), and this manifestly requires more effort than for the J_{nm}'s.

13 CONCLUSION AND PERSPECTIVES

The exterior potential of a static thin toroidal shell, as given by the Laplace equation, is obtained from a double Taylor expansion of the axisymmetric Green function. Each term is then integrated over the source, as in the multipole theory. Here, the expansion is performed at the centre of the circular section instead of the origin of coordinates. The series converges very well and provides a solution which satisfies the Laplace equation in every order, so no "ghost" sources are induced by truncation. In practice, the efficiency of the method is remarkable, with already 3 correct digits at order zero for toroids having an axis ratio of 0.1. At order 2, this precision is almost doubled (to 6 digits), which should be sufficient for most applications.

At order 2 in the shell parameter (minor-to-major radius ratio), a shellular, solid or core-stratified toroid generates an *exterior* potential (and field) similar to that of a thin circular loop having same main radius and same mass. We meet the results by Bannikova et al. (2011) and Kondratyev (2018). A few similarity theorems, which all resemble the Gauss theorem, have been proposed. The approximations

for the exterior potential reported here together with the interior solutions reported in Huré et al. (2019) yield a complete decription of the potential of a toroidal shell of circular section, at any point of space. It then becomes possible to deduce the interior solution for the solid torus, since both interior and exterior shell solutions are required in this operation. Next, the energy for the formation of a solid torus becomes accessible. It would be worth to generalize the method to any kind of source shape, not limited to circular section, through specific prescriptions for $a(\theta)$ and $z(\theta)$, or $z(a)$. This would open exciting perspectives, in particular for oblate structures such as geometrically thin discs.

ACKNOWLEDGMENTS

We are grateful to the referee, Dr M. Majic, for useful comments, and in particular for pointing out the article by Kondratyev (2018) we were not aware of at the time of submission.

V. Karas acknowledges Czech Science Foundation project No. 19-01137J. A. Trova acknowledges support from the Research Training Group 1620 "Models of Gravity" funded by the German Science Foundation DFG. O. Semerák is grateful for support from GACR-17/13525S grant of the Czech Science Foundation. We thank V. Tikhonchuk for references about terrestrial plasmas.

REFERENCES

Abramowitz M., Stegun I. A., 1964, Handbook of Mathematical Functions with Formulas, Graphs, and Mathematical Tables, ninth dover printing, tenth gpo printing edn. Dover, New York
Bannikova E. Y., Vakulik V. G., Shulga V. M., 2011, MNRAS, 411, 557
Binney J., Tremaine S., 1987, Galactic dynamics. Princeton, NJ, Princeton University Press, 1987, 747 p.
Chandrasekhar S., 1987, Ellipsoidal figures of equilibrium
Christodoulou D. M., 1993, ApJ, 412, 696
Clement M. J., 1974, ApJ, 194, 709
Cohl H. S., Rau A. R. P., Tohline J. E., Browne D. A., Cazes J. E., Barnes E. I., 2001, Phys. Rev. A, 64, 052509
Dini F., Baghdadi R., Amrollahi R., Khorasani S., 2009, arXiv e-prints, p. arXiv:0909.0660
Durand E., 1953, Electrostatique. Vol. I. Les distributions.. Ed. Masson
Dyson F. W., 1893, Royal Society of London Philosophical Transactions Series A, 184, 1041
Eriguchi Y., Mueller E., 1993, ApJ, 416, 666
Fukushima T., 2016, MNRAS, 463, 1500
Gradshteyn I. S., Ryzhik I. M., 2007, Table of Integrals, Series, and Products, Seventh Edition. Academic Press
Guilloteau S., Dutrey A., Simon M., 1999, A&A, 348, 570
Hachisu I., 1986, ApJS, 61, 479
Hashimoto M., Eriguchi Y., Arai K., Mueller E., 1993, A&A, 268, 131
Horedt G. P., ed. 2004, Polytropes - Applications in Astrophysics and Related Fields Vol. 306 of Astrophysics and Space Science Library
Huré J., Trova A., Karas V., Lesca C., 2019, MNRAS, 486, 5656
Huré J.-M., 2005, A&A, 434, 1
Iorio L., 2012, Earth Moon and Planets, 108, 189
Jackson J. D., 1998, Classical Electrodynamics, 3rd Edition
Kellogg O. D., 1929, Foundations of Potential Theory. New-York: Frederick Ungar Publishing Company
Kondratyev B. P., 2018, Technical Physics, 63, 311
Lehmann M., Schmidt J., Salo H., 2019, A&A, 623, A121
Majic M., 2020, Applied Numerical Mathematics, 148, 98
Nieto M. M., 2005, Phys. Rev. D, 72, 083004
Nishida S., Eriguchi Y., 1994, ApJ, 427, 429
Paczynski B., 1978, Acta Astron., 28, 91
Petroff D., Horatschek S., 2008, MNRAS, 389, 156
Pickett B. K., Durisen R. H., Link R., 1997, Icarus, 126, 243
Pringle J. E., 1981, ARA&A, 19, 137
Semerák O., Suková P., 2010, MNRAS, 404, 545
Shakura N. I., Sunyaev R. A., 1973, A&A, 24, 337
Stahler S. W., 1983, ApJ, 268, 155
Storzer H., 1993, A&A, 271, 25
Tohline J. E., Hachisu I., 1990, ApJ, 361, 394
Tresaco E., Elipe A., Riaguas A., 2011, Celestial Mechanics and Dynamical Astronomy, 111, 431
Trova A., Huré J.-M., Hersant F., 2014, A&A, 563, A132
Trova A., Schroven K., Hackmann E., Karas V., Kovář J., Slaný P., 2018, Phys. Rev. D, 97, 104019
Šácha J., Semerák O., 2005, Czechoslovak Journal of Physics, 55, 139
Šubr L., Karas V., 2005, in S. Hledík & Z. Stuchlík ed., RAGtime 6/7: Workshops on black holes and neutron stars A manifestation of the Kozai mechanism in the galactic nuclei. pp 281–293
Wisdom J., Tremaine S., 1988, AJ, 95, 925
Wong C. Y., 1973, Annals of Physics, 77, 279
Woodward J. W., Sankaran S., Tohline J. E., 1992, ApJ, 394, 248

APPENDIX A: INTEGRALS $J_{N,M}$

From Gradshteyn & Ryzhik (2007), we have

$$\int_0^{\pi/2} \cos^n\theta \sin^m\theta d\theta = \frac{1}{2}B\left(\frac{n+1}{2}, \frac{m+1}{2}\right), \tag{A1}$$

where $B(x,y) = \frac{\Gamma(x)\Gamma(y)}{\Gamma(x+y)}$ is the complete Beta function, and $\Gamma(x)$ is the Gamma function. From this expression, we can easily deduce $J_{n,m}$ (integral bounds 0 and 2π). We find

$$J_{n,m} = \frac{1}{2}B\left(\frac{n+1}{2}, \frac{m+1}{2}\right)\left[1+(-1)^n\right]\left[1+(-1)^{n+m}\right]. \tag{A2}$$

It follows that $J_{n,m} = 0$ when n is even or when $n+m$ is even (n and m have different parity). The expression for $J_{n,m}$ are given in Tab. 1 for $n = \{0,1,2,3,4\}$ and $m = \{0,1,2,3,4\}$.

APPENDIX B: RESIDUAL MASS DENSITY

The residual density is found from the Poisson equation, i.e.

$$\nabla^2\left[\frac{\mathbf{K}(k)}{\sqrt{(a+R)^2+Z^2}}\right] = \frac{k_0\mathbf{K}(k_0)}{4R^2} + \left[\frac{\partial^2 k}{\partial R^2} + \frac{\partial k^2}{\partial Z^2}\right]\frac{\mathbf{E}(k_0)}{{k'_0}^2} + \left[\left(\frac{\partial k}{\partial R}\right)^2 + \left(\frac{\partial k}{\partial Z}\right)^2\right]\frac{(1+{k_0}^2)\mathbf{E}(k_0) - {k'_0}^2\mathbf{K}(k_0)}{k{k'_0}^4}, \tag{B1}$$

where the partial derivatives of $\mathbf{K}(k)$ and $\mathbf{E}(k)$ with respect to the modulus k are found in mathematical textbooks (Gradshteyn & Ryzhik 2007). By expanding all the terms inside the curly brackets, this quantity is strictly zero provided $a - R \neq 0$ and $Z \neq 0$, which never occurs in free space.

APPENDIX C: PARTIAL DERIVATIVES

There are different ways to calculate the partial derivatives of κ with respect to a and z. We find convenient to rewrite $\mathbf{K}(k)$ as the definite integral over the azimuth, i.e. (3). The denominator is then expanded and rearranged so that the n-order derivative with respect to a and z writes

$$\begin{aligned}\frac{\partial^n\kappa}{\partial a^{n-m}\partial z^m} &= \frac{\partial^n}{\partial a^{n-m}\partial z^m}\int_0^{\frac{\pi}{2}}\frac{d\phi}{\sqrt{\Delta^2 - 4aR\sin^2\phi}} \\ &= \int_0^{\frac{\pi}{2}} d\phi \frac{\partial^n}{\partial a^{n-m}\partial z^m}\left\{[a+R\cos(2\phi)]^2 + [R\sin(2\phi)]^2 + \zeta^2\right\}^{-1/2}.\end{aligned} \tag{C1}$$

Denoting $D = [a+R\cos(2\phi)]^2 + [R\sin(2\phi)]^2 + \zeta^2$, we have

$$\frac{\partial D^{-1/2}}{\partial a} = -\left[a+R\cos(2\phi)\right]D^{-3/2} \tag{C2}$$

and

$$\frac{\partial^2 D^{-1/2}}{\partial a^2} = -D^{-3/2} + 3\left[a+R\cos(2\phi)\right]^2 D^{-5/2}. \tag{C3}$$

It follows that

$$\frac{\partial\kappa}{\partial a} = \int_0^{\frac{\pi}{2}}\frac{\partial D^{-1/2}}{\partial a}d\phi = -(a+R)\Delta^{-3}\frac{\mathbf{E}(k)}{k'^2} + 2R\Delta^{-3}\frac{\mathbf{E}(k) - k'^2\mathbf{K}(k)}{k^2k'^2} \tag{C4}$$

and

$$\begin{aligned}\frac{\partial^2\kappa}{\partial a^2} &= \int_0^{\frac{\pi}{2}}\frac{\partial^2 D^{-1/2}}{\partial a^2}d\phi \\ &= -\Delta^{-3}\frac{\mathbf{E}(k)}{k'^2} + 3\Delta^{-3}\frac{\mathbf{E}(k)}{k'^2} - 3\zeta^2\Delta^{-5}\frac{2(1+k'^2)\mathbf{E}(k) - k'^2\mathbf{K}(k)}{3k'^4} - 12R^2\Delta^{-5}\frac{(1+k'^2)\mathbf{E}(k) - 2k'^2\mathbf{K}(k)}{3k^4k'^2}, \\ &= 2\Delta^{-3}\frac{\mathbf{E}(k)}{k'^2} - \zeta^2\Delta^{-5}\frac{2(1+k'^2)\mathbf{E}(k) - k'^2\mathbf{K}(k)}{k'^4} - 4R^2\Delta^{-5}\frac{(1+k'^2)\mathbf{E}(k) - 2k'^2\mathbf{K}(k)}{k^4k'^2},\end{aligned} \tag{C5}$$

For the z-derivatives, we have

$$\frac{\partial D^{-1/2}}{\partial z} = \zeta D^{-3/2}, \qquad \frac{\partial^2 D^{-1/2}}{\partial z^2} = -D^{-3/2} + 3\zeta^2 D^{-5/2} \tag{C6}$$

and, consequently,

$$\frac{\partial \kappa}{\partial z} = \zeta \int_0^{\frac{\pi}{2}} \frac{\partial D^{-1/2}}{\partial z} d\phi = \zeta \Delta^{-3} \frac{\mathbf{E}(k)}{k'^2} \tag{C7}$$

and

$$\frac{\partial^2 \kappa}{\partial z^2} = \int_0^{\frac{\pi}{2}} \frac{\partial^2 D^{-1/2}}{\partial z^2} d\phi = -\Delta^{-3} \frac{\mathbf{E}(k)}{k'^2} + \zeta^2 \Delta^{-5} \frac{2(1+k'^2)\mathbf{E}(k) - k'^2 \mathbf{K}(k)}{k'^4}. \tag{C8}$$

APPENDIX D: F90 PROGRAM FOR THE EXTERIOR POTENTIAL

```
Program F90drivercode3
  ! "The exterior gravitational potential of toroids"
  ! Hure, Basillais, Karas, Trova & Semerak (2019), MNRAS
  ! gfortran F90drivercode3.f90; ./a.out
  ! not optimized
  Implicit None
  Integer,Parameter::AP=Kind(1.00D+00)
  Real(Kind=AP),Parameter::PI=ATAN(1._AP)*4
  Real(KIND=AP)::B,RC,MASS,E ! core radius, main radius and mass of the shell, and axis ratio
  Real(KIND=AP)::KMOD,KMOD2,KPRIM,KPRIM2 ! moduli
  Real(KIND=AP)::R,Z,PSI ! cylindrical coordinates and potential value where it is estimated
  Real(KIND=AP)::Z2,VAL,DELTA,DELTA2,DELTA3,DELTA4,DELTA5 ! misc
  Real(KIND=AP)::KMOD4,KPRIM4,S0,S10,S20,S02,D32,S2D32,D52,S2C2D52 ! misc
  Real(KIND=AP)::ELLIPTICK,ELLIPTICE ! complete elliptic integrals
  ! ? input parameters (properties of the shell)
  B=0.1_AP
  RC=1._AP
  E=B/RC
  MASS=B*RC*PI**2*4
  print*,"Mass of the shell",MASS
  ! ? values of R and Z where the potential is requested (must be outside the cavity!)
  R=RC*2
  Z=RC*2
  Z2=Z**2
  If ((R-RC)**2+Z2-B**2<0._AP) Then
     ! approximation not valid inside the shell
     PSI=0._AP
  Else
     DELTA2=(R+RC)**2+Z2
     KMOD2=RC*R*4/DELTA2
     DELTA=Sqrt(DELTA2)
     KPRIM2=((R-RC)**2+Z2)/DELTA2
     ! values of K(k) and E(k) to be set here !
     ! ELLIPTICE=
     ! ELLIPTICK=
     !misc.
     DELTA3=DELTA2*DELTA
     DELTA5=DELTA3*DELTA2
     KMOD4=KMOD2**2
     KPRIM4=KPRIM2**2
     ! surface factors
     S0=1._AP
     S10=E**2/2
     S20=E**2/2
     S02=S20
     ! coefficients
     D32=ELLIPTICE/KPRIM2
     S2D32=(ELLIPTICE-KPRIM2*ELLIPTICK)/KPRIM2/KMOD2
     D52=((1._AP+KPRIM2)*ELLIPTICE*2-KPRIM2*ELLIPTICK)/KPRIM4/3
     S2C2D52=((1._AP+KPRIM2)/KPRIM2*ELLIPTICE-ELLIPTICK*2)/KMOD4/3
     ! order 0
```

```
      VAL=ELLIPTICK/DELTA*S0
      ! order 1
      VAL=VAL+RC*(-(R+RC)*D32/DELTA3+S2D32/DELTA3*R*2)*S10
      ! order 2
      VAL=VAL+RC**2*((-D32/DELTA3+D32/DELTA3*3-D52*Z2/DELTA5*3-S2C2D52/DELTA5*R**2*12)*S20&
           &+(-D32/DELTA3+D52*Z2/DELTA5*3)*S02)/2
      PSI=-VAL*B*RC*PI*8
      Print *,"Potential value (2nd-order)",PSI,PSI/MASS*RC
  Endif
End Program F90drivercode3
```

Appendix D

Paper to be submitted

MNRAS **000**, 1–?? (???) Preprint 3 November 2020 Compiled using MNRAS LATEX style file v3.0

A computational method for rotating, multi-layer spheroids with internal jumps

Draft-paper — To be submitted soon — Do not circulate, please

B. Basillais[1,2]*, and J.-M. Huré[1,2]†
[1] *Univ. Bordeaux, LAB, UMR 5804, F-33615, Pessac, France*
[2] *CNRS, LAB, UMR 5804, F-33615, Pessac, France*

Received ??? / Accepted ???

ABSTRACT

We discuss the structure of differentially rotating, multilayer spheroids containing mass-density jumps and rotational discontinuities at the interfaces. The study is based upon a scale-free, numerical method. Polytropic equation-of-states and cylindrical rotation profiles are assumed. The Bernoulli equation and the Poisson equation for the gravitational potential are solved for each layer separately on a common computational grid. The 2-layer (core/envelope) case is first investigated in details. We find that the core and the envelope are not, in general, homothetical in shape (cores are more than spherical than the envelope). Besides, the occurence of a mass-density jump all along the interface is prone to a rotational discontinuity (unless the polytropic indices are the same). In particular, for given rotation laws, the mass density jump is not uniform along the interface. Tests, trends and examples (e.g. false bipolytrope, critical rotation, degenerate configurations) are given. Next, we consider the general case of systems made of $\mathcal{L} > 2$ layers. This includes the full equation set, the Virial equation, a comprehensive step-by-step procedure and two examples of tripolytropic systems. The properties observed in the 2-layer case hold for any pairs of adjacent layers. In spite of a different internal structure, two multilayer configurations can share the same mass, same axis ratio, same size and same surface velocity (which is measured through a degeneracy parameter). Applications concern the determination of the interior of planets, exoplanets, stars and compact objects.

Key words: Gravitation — stars: interiors — stars: rotation — Methods: analytical — Methods: numerical

1 INTRODUCTION

Understanding the internal structure of planets and stars is probably among the oldest problem of astrophysics and it is still a major and very active field of modern research. Depending on several factors (e.g. initial conditions, equation-of-state, mechanisms transporting energy and particles, environment), these objects expands a complex layered structure (cores, envelopes, mantles, convective zones, atmospheres, etc.) which remains hard to characterize. As a matter of fact, observations furnish either surface data (i.e. velocity fields) or global quantities (e.g. size, shape), this is the reason why the production of reliable diagnostic tools capable of modeling the deepest regions is crucial. Not only the composition and thermodynamical conditions, but also the internal dynamics (at least global motions) are uncertain. If much is known about the Sun and a few planets in the Solar System (e.g. Maeder 2009; Baraffe et al. 2014; Vinyoles et al. 2017; Helled & Guillot 2018; Christensen-Dalsgaard 2020), the properties of many systems remain poorly known and matter of debate (e.g. Snellen et al. 2014; Kong et al. 2014).

In a seminal paper, Schönberg & Chandrasekhar (1942) have shown that an isothermal, stellar core capable of supporting a radiative envelope can not exceed a certain limit in mass, according on the composition of the two layers (of the order of 10% for a hydrogen envelope and a helium core). The sharp change in the mass density at the "core/envelope" interface — as a consequence of pressure balance, any change in the mean molecular weight generates a mass density jump — is though to play a significant role on the evolution of low- and intermediate-mass stars, precisely on the transition from the normal to the giant phase (Beech 1986; Eggleton et al.

* E-mail:baptiste.boutin-basillais@u-bordeaux.fr
† E-mail:jean-marc.hure@u-bordeaux.fr

1998; Trimble & Aschwanden 1999; Stancliffe et al. 2009; Ball et al. 2012; Hekker & Christensen-Dalsgaard 2017). As demonstrated in Maeder (1971), the impact of rotation on this fractional limit is weak in the case of a global rigid rotation (see also Kadam et al. 2016), unless the core spins much faster than the envelope. Interfaces between layers are possible zones of changes in the dynamics, in the equation-of-state or/and in the transport mechanisms, which are presumably tighly coupled (Spiegel & Zahn 1992; Kiuchi et al. 2010; Broomhall et al. 2014). The problem of multi-layered systems is therefore of great interest, not only for normal and compact stars (Milne 1936a,b; Spiegel & Zahn 1992; Remus et al. 2012; Weppner et al. 2015; Jackson et al. 2005; MacGregor et al. 2007; Caimmi 2016; Brooks et al. 2017) but also for planets (Lunine et al. 1983; Horedt & Hubbard 1983a; Kubo-Oka & Nakazawa 1997; Léger et al. 2004; Adams et al. 2008; Kong et al. 2010; Tricarico 2014; Kong et al. 2016; Mousis et al. 2020), for interstellar cores and filaments (Curry & McKee 2000; Toci & Galli 2015; Gholipour 2018) and gas discs (Chiang & Goldreich 1997; D'Alessio et al. 1998; Huré 2000).

This article is a novel contribution to the problem of multilayer spheroids. It is based on the theory of rotating polytropes (e.g. Chandrasekhar 1969; Hachisu 1986; Horedt 2004). Our approach is fully numerical (even when the number of layers involved is low, the analytical treatment becomes rapidly cumbersome; see e.g. Caimmi 2016). Axial and equatorial symmetries are assumed. We take into account mass density jumps and rotational discontinuities at the layer interfaces, and we analyze their coupling (Kiuchi et al. 2010; Kadam et al. 2016). In real systems, transitions between regimes always occur over a zone of finite, non-zero thickness. Jumps and discontinuities considered here must be regarded as limit-cases. From a technical point of view, we use a single computational grid for all layers, but each layer is treated separately in terms of mass density scaling and gravitational potential. Actually, as observed for bipolytropes (e.g. Eggleton et al. 1998), the mass density in the system can differ by orders of magnitude from the deepest layer to the outermost one, and the introduction of a (envelope-to-core) constrast parameter appears very convenient. Besides, the presence of mass density jumps does not permit to solve the Poisson equation for the total potential at once (two different values cannot be assigned to a single grid node). Finally, as in Huré & Hersant (2017), we use a specific boundary detection method to determine all the interfaces. As a matter of fact, rotation makes the shape of systems non-conformal to any classical coordinate system (except in the incompressible case). The knowledge of boundaries is essential to get reliable values for the mass, for the gravitational potential, etc.

The organization of the paper is the following. We present the equation sets relevant for the 2-layer spheroid (i.e. the bipolytrope) in Sec. 2. The tight link between the mass density jump and a discontinuity in the rotation rate at the core/envelope interface is discussed. In Sect. 3, we comment on the numerical method, based on the Self-Consistent-Field (SCF) method. A comprehensive algorithm and the Virial equation, which serves as a test for the solutions, are given. Section 4 is devoted to tests and examples. For instance, the 2-layer white dwarf involving the v-constant rotation profile by Kiuchi et al. (2010) is reproduced with an excellent agreement. We show that some configurations can have the same shape (envelope size and axis ratio), same total mass and surface velocity, but a different internal structure. Accordingly, a degeneracy parameter is defined. We discuss the general case of a $\mathcal{L}$-layer system in Sec. 5. The corresponding set of equations, the Virial equation and a step-by-step procedure are explicitely given. We illustrate the method by two examples of a 3-layer spheroid. We conclude in Sect. 6. Tables are appended.

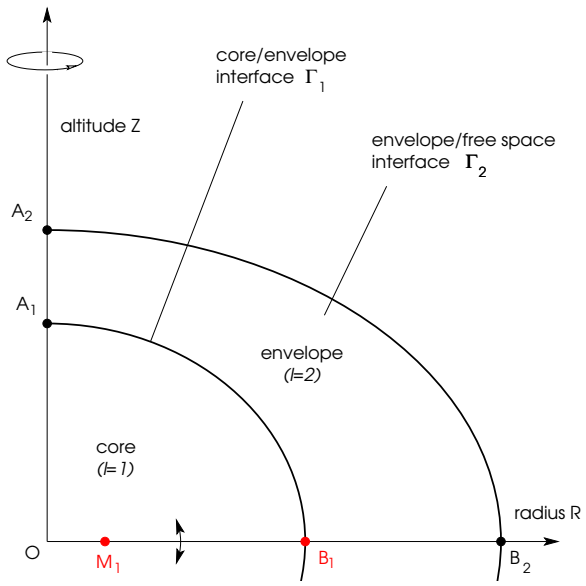

Figure 1. Scheme for the rotating bipolytrope made of a core and an envelope. Equatorial and cylindrical symmetries are assumed. At the core/envelope interface, both a mass density jump and a rotational discontinuity are allowed. The rotation rate of the envelope is set through the reference points A_2 and B_2. The extension of the core on the z-axis is set by A_1. At point M_1, the enthalpy of the core goes through a maximum. Both B_1 (the equatorial size of the core) and M_1 are output quantities (*red*).

2 THEORETICAL BACKGROUND

The equilibrium of a self-gravitating fluid in global rotation is basically determined from the Bernoulli equation linking the gravitational potential Ψ, the centrifugal potential Φ and the enthalpy $H = \int \frac{dP}{\rho}$, where P is the gas pressure and ρ is the mass density (Chandrasekhar 1969; Hachisu 1986). We assume a polytropic equation-of-state (EOS), i.e. $P = K\rho^\gamma$, where $n = \frac{1}{\gamma-1} \geq 0$ is the polytropic index and $K > 0$ is the gas constant, which enables a simple definition of the enthalpy, i.e. $\nabla H = (n+1)\nabla\frac{P}{\rho}$. It is widely used in the modeling of both terrestrial and astrophysical fluids. In dimensionless form[1], the relevant equation set is

[1] The notation is $x = x_0\hat{x}$ for any variable x with magnitude x_0.

(Huré & Hersant 2017)

$$\begin{cases} C_1\hat{H} + \hat{\Psi} + C_2\hat{\Phi} = C_3, \\ \hat{\rho} = \hat{H}^n, \quad \hat{H} \geq 0, \\ \Delta\hat{\Psi} = 4\pi\hat{\rho}, \end{cases} \tag{1}$$

where $\Psi = \hat{\Psi} \times G\rho_0 L^2$,

$$\begin{cases} C_1 \equiv \frac{K(n+1)\rho_0^{\gamma-2}}{GL^2}, \\ C_2 \equiv \frac{\Omega_0^2}{G\rho_0}, \end{cases} \tag{2}$$

and L, $\rho_0 L^3$ and $1/\Omega_0$ are the length scale, mass scale and orbital time scales of the system, respectively. In fact, (1a) is compatible for rotation profiles that depend on the cylindrical radius R only (e.g. Amendt et al. 1989), i.e. $\vec{\Omega}(\vec{r}) = \Omega(R)\vec{e}_z$. This includes the rigid rotation, the j-constant and the v-constant rotation laws (Hachisu 1986). Shellular rotation, more appropriate to stellar structure (Zahn 1992; Maeder 2009; Eggenberger 2013), is excluded (see, however, Fujisawa 2015). The associated centrifugal potential, defined by

$$\hat{\Phi}(R) = -\int \hat{\Omega}^2(\hat{R})\hat{R}d\hat{R}, \tag{3}$$

is therefore a function of R only. Finally, as quoted in (1b), the physically relevant solutions correspond to regions of positive enthalpy, i.e. $\hat{H} \geq 0$. Unless there is an external pressure (Viala et al. 1978; Huré et al. 2018), $\hat{H} = 0$ defines the fluid boundary. It is well known that for certain EOS such a boundary is located at infinity (Horedt 2004).

2.1 The two-layer system

The above equation set is valid for a single body with a single layer (and single EOS). When the system is made of several domains that are physically connected (like multi-layer configurations) or disconnected (i.e. multi-body configurations), the equation set is to be replicated and eventually enriched with additional constraints. The total gravitational potential makes the link between all domains ($\mathcal{L}$ in total), i.e. $\Psi_{\rm tot} = \Psi_1 + \Psi_2 + \cdots + \Psi_{\mathcal{L}}$. For multilayer systems of interest here, the pressure must be continuous at any interface interior to the fluid, oherwise transverse motions follow. This generates additional equations (one per layer). For a two-layer star or planet made of a "core" (layer number 1) surrounded by an "envelope" (layer number 2), (1) formally holds, provided some adjustments. There are two interfaces where the pressure balance must be satisfyied : the core/boundary interface and the envelope/free space boundary (denoted Γ_1 and Γ_2, respectively). These interfaces are lines in the meridional $(\hat{R}, \hat{Z})$-plane. The system is depicted in Fig. 1.

2.2 Pressure balance and mass density jump at the core/envelope interface

The requirement of pressure balance all along Γ_1 writes

$$K_1{\rho_1}^{\gamma_1} - K_2{\rho_2}^{\gamma_2}|_{\Gamma_1} = 0, \tag{4}$$

while we have $\rho_2(\Gamma_1) \neq \rho_1(\Gamma_1)$ in general, depending on the gas constants. Thin zones of high mass-density gradient are present in stars (Beech 1986; Eggleton et al. 1998) and in planets (Horedt & Hubbard 1983b; Kubo-Oka & Nakazawa 1997; Valencia et al. 2006; Kramm et al. 2011; Baraffe et al. 2014). This fully justifies the introduction of a mass density jump, as a limit-case. We thus set

$$\left.\frac{\rho_1}{\rho_2}\right|_{\Gamma_1} \equiv \alpha_2. \tag{5}$$

So, for a rocky planet surrounded by a water ocean, or for a main sequence star having a helium core and an hydrogen envelope, we have $\alpha_2 > 1$ at the interface. In contrast, for a cold envelope dominated by molecules surrounding a hotter core made of atoms, $\alpha_2 < 1$ is expected. Note that α_2 can vary along the interface (see below).

As mentionned, the pressure balance must also hold at the fluid surface Γ_2. If the system is isolated, then $\rho_2(\Gamma_2) = 0$ (the enthalpy vanishes).

2.3 Geometrical parameters and mass density scaling

We define the axis ratio of the envelope by

$$\frac{\mathrm{OA}_2}{\mathrm{OB}_2} \equiv e_2, \tag{6}$$

where points A_2 and B_2 both belong to Γ_2 and are located on the polar and equatorial axis respectively (this is therefore the axis ratio of the system as a whole). In a similar way, we have

$$\frac{\mathrm{OA}_1}{\mathrm{OB}_1} \equiv e_1, \tag{7}$$

for the core, where A_1 and B_1 belong to the core/envelope interface (see again Fig. 1). As rotation generally produces oblate configurations, e_1 and e_2 are expected to be lower than unity (see, hovewer, Fujisawa & Eriguchi 2014, 2015). The size of the core relative to the size of the system is, on the polar axis, given by

$$q_1 = \frac{\mathrm{OA}_1}{\mathrm{OA}_2} \in [0, 1], \tag{8}$$

and we have $q_2 = 1 - q_1$ for the envelope. So, $q_1 \to 0$ corresponds to a very small core, while $q_1 \to 1$ is for a very small envelope.

The masses contained in the core and in the envelope may differ by orders of magnitudes (Eggleton et al. 1998; Ball et al. 2012; Kadam et al. 2016). For this reason, we find appropriate that each layer has its own mass density scaling. We therefore define $\rho_1 = \rho_{10} \times \hat{\rho}_1$ for the core, and $\rho_2 = \rho_{20} \times \hat{\rho}_2$ for the envelope, and

$$\beta_2 = \frac{\rho_{20}}{\rho_{10}} \tag{9}$$

as the envelope-to-core mass density ratio (or contrast parameter). Then, in the "reference frame" of the core, the total gravitational potential writes

$$\hat{\Psi}_{1,\rm tot} = \hat{\Psi}_1 + \beta_2\hat{\Psi}_2. \tag{10}$$

where $\hat{\Psi}_l$ is the gravitational potential of layer $l \in [1, 2]$. As we have $\hat{\Psi}_{2,\rm tot} = \hat{\Psi}_1/\beta_2 + \hat{\Psi}_2$ in the reference frame of the envelope, we see that $\hat{\Psi}_{1,\rm tot} = \beta_2\hat{\Psi}_{2,\rm tot}$.

2.4 Rotational discontinuity

Since there is one Bernoulli equation per layer, there are 6 constants in total, namely C_{11}, C_{21}, C_{31}, C_{12}, C_{22} and C_{32}, and, in principle, two centrifugal potentials (Kiuchi et al. 2010). If the rotation profiles connect continuously at the interface (which is expected in real systems), then there is a single scaling parameter Ω_0 for both layers. On the contrary, in the case of a rotational discontinuity, there are two values to consider, although $\hat{\Omega}(R)$ can be the same function of the radius. We then define Ω_{10} for the core and Ω_{20} for the envelope. It follows from (2) that

$$\begin{cases} C_{21} = \frac{\Omega_{10}^2}{G\rho_{10}}, \\ C_{22} = \frac{\Omega_{20}^2}{G\rho_{20}}. \end{cases} \tag{11}$$

We measure the magnitude of the rotational discontinuity through the parameter ω_2 defined by

$$\sqrt{\omega_2} = \frac{\Omega_{10}}{\Omega_{20}} > 0. \tag{12}$$

So, $\omega_2 > 1$ corresponds to a core spinning faster than the envelope. This case has been considered for instance in Maeder (1971). As a consequence, the two constants C_{21} and C_{22} are linked by

$$\beta_2 \omega_2 C_{22} = C_{21}. \tag{13}$$

2.5 Equation set for bipolytropic stars/planets. Important remarks

Given (1), (4), (5), (12) and (13), the final equation set for bipolytropic stars/planet is

$$\begin{cases} C_{11}\hat{H}_1 + \hat{\Psi}_{1,\mathrm{tot}} + C_{21}\hat{\Phi}_1 = C_{31}, \\ \hat{\rho}_1 = \hat{H}_1^{n_1}, \quad \hat{H}_1 \geq \hat{H}_1(\Gamma_1), \\ \Delta\hat{\Psi}_{1,\mathrm{tot}} = 4\pi\left(\hat{\rho}_1 + \beta_2\hat{\rho}_2\right) \qquad \text{(layer 1)}, \\ \\ \bar{\alpha}_2 C_{11}\hat{H}_1(\Gamma_1) - \beta_2 C_{12}\hat{H}_2(\Gamma_1) = 0 \\ \qquad \text{(pressure balance)}, \\ \alpha_2\beta_2\hat{H}_2^{n_2}(\Gamma_1) = \hat{H}_1^{n_1}(\Gamma_1) \qquad (\rho-\text{jump}), \\ \omega_2\beta_2 C_{22} = C_{21} \qquad \text{(scaling)}, \\ \\ C_{12}\hat{H}_2 + \hat{\Psi}_{2,\mathrm{tot}} + C_{22}\hat{\Phi}_2 = C_{32}, \\ \hat{\rho}_2 = \hat{H}_2^{n_2}, \quad \hat{H}_2(\Gamma_1) \geq \hat{H}_2 \geq \hat{H}_2(\Gamma_2) = 0 \\ \Delta\hat{\Psi}_{2,\mathrm{tot}} = 4\pi\left(\frac{1}{\beta_2}\hat{\rho}_1 + \hat{\rho}_2\right) \qquad \text{(layer 2)}, \end{cases} \tag{14}$$

where

$$\bar{\alpha}_2 = \alpha_2 \frac{1+n_2}{1+n_1}. \tag{15}$$

Note that (14c) and (14i) are equivalent. This set is made of 8 equations. It is in principle sufficient to determine a solution, i.e. $\hat{H}_1$ and $\hat{H}_2$. This requires a few input data. Depending on the strategy for finding the solutions, various sets of input parameters can be considered (see below).

A few interesting properties come out of (14). First, if we eliminate α_2 between (14d) and (14e), then we find

$$\frac{1+n_2}{1+n_1} C_{11}\hat{H}_1(\Gamma_1)^{1+n_1} - \beta_2^2 C_{12}\hat{H}_2(\Gamma_1)^{1+n_2} = 0. \tag{16}$$

Unsurprisingly, there must be a fine tuning between the $\hat{H}_1$ and $\hat{H}_2$ all along Γ. Note that $\hat{H}_1(\Gamma_1) \propto \hat{H}_2(\Gamma_1)$ when $n_1 = n_2$. Second, we can eliminate $\hat{H}_2(\Gamma_1)$ from (14d) and (14e). We find, assuming $n_1 > 0$ and $n_2 > 0$

$$\frac{1+n_2}{1+n_1}\frac{C_{11}}{C_{12}}\beta_2^{\frac{1}{n_2}-1}\alpha_2(\Gamma_1)^{\frac{1}{n_2}+1} - \hat{H}_1(\Gamma_1)^{\frac{n_1}{n_2}-1} = 0, \tag{17}$$

which holds regardless of the rotation profiles. Since β_2 is a scalar, we see that α_2 varies along the interface according to $\hat{H}_1$. If α_2 is uniform at Γ_1 (this includes the no-jump case), then $\hat{H}_1$ (and subsequently $\hat{H}_2$) is constant too. If the two polytropic indices happen to be equal, then $\alpha_2(\Gamma_1)$ =const. must hold, whatever the enthalpy of the core. This is for instance the case if the two layers have a different chemical composition, while their equilibrium is driven by the same mechanisms leading to $n_1 = n_2$.

Third, there is a tight link between the mass density jump, the rotation profiles and the rotational discontinuity at Γ_1. Actually, suppose that the core and the envelope share the same dimensionless centrifugal potential $\hat{\Phi} = \hat{\Phi}_1 = \hat{\Phi}_2$, but the rotation rate differs on both sides of the interface, i.e. $\Phi(\Gamma_1^+) \neq \Phi(\Gamma_1^-)$. If we multiply (14g) by β_2 and compare the obtained expression to (14a), we find

$$C_{11}\hat{H}_1(\Gamma_1)\left[1-\bar{\alpha}_2(\Gamma_1)\right] + C_{21}\hat{\Phi}(\Gamma_1)\left(1-\frac{1}{\omega_2}\right) + \beta_2 C_{32} - C_{31} = 0, \tag{18}$$

where we have used (10) to eliminate the gravitational potential, and (14d) to eliminate $\hat{H}_2$. It follows that $\hat{H}_1(1-\bar{\alpha}_2)$ must be a constant all along Γ_1 not only in the static case, but also in the presence of rotation provided $\omega_2 = 1$, that is, there is no rotational discontinuity. In contrast, the presence of any rotational discontinuity ($\omega_2 \neq 1$) implies that the quantity $\hat{H}_1(1-\bar{\alpha}_2)$ must vary and this depends on $\hat{\Phi}$ at the interface. Besides, as a consequence of (17), if the rotation profile is imposed, the mass-density jump α_2 cannot be uniform on this case, and the enthalpies also vary on Γ_1. This is physically acceptable. An abrupt change in the fluid velocity creates a depression that can be cancelled or compensated by an appropriate rise in the density of the gas. If this fluid velocity is not uniform along the interface, then the increase in mass density may not be uniform either. We can give (16) another meaning : if the equilibrium of the system requires a constant mass density jump at the interface, then the rotation profile can not be fully arbitrary (this is not a common convention in the theory of figures). In fact, we can derived an expression more general than (18) in the case where $\hat{\Phi}_1 \neq \hat{\Phi}_2$ (see Sec. 5). The case $n_1 = n_2$ appears singular in the sense that uniform values for α_2 and for $\hat{H}_1$ at the interface imply $\hat{\Phi}_2(\Gamma_1) - \omega_2\hat{\Phi}_1(\Gamma_1)$ =const., i.e. proportionality between the rotation rates at the interface.

3 SOLUTIONS FROM THE SELF-CONSISTENT-FIELD (SCF) METHOD

We remind that, for the (one-layer) polytrope, solving the Poisson equation (1c) for $\hat{\Psi}$, or, equivalently, computing the integral

$$\hat{\Psi}(\vec{r}) = \iiint \frac{\hat{\rho}(\vec{r}')dV'}{|\vec{r}' - \vec{r}|}, \tag{19}$$

is the critical point of problem, since neither the shape nor the mass density profile of the system are known in advance.

Since $\hat{\rho}$ is a function of $\hat{H}$ through (1b), we see that (1a) and (19) can be combined into a single, non-linear integro-algebraic equation for $\hat{H} \geq 0$, namely

$$\hat{H} = \mathcal{I}[\hat{H}]. \tag{20}$$

where $\mathcal{I}$ contains the integral operator. In this way, the enthalpy $\hat{H}$ appears as some sort of "fixed point" in the space of functions (see, e.g. Odrzywołek 2003). This is the principle of the Self-Consistent-Field (SCF) method for finding numerically the solutions (Ostriker & Mark 1968; Hachisu 1986) : from one seed (or starting guess) for $\hat{H}$, the integro-algebraic equation is solved iteratively, together with the three constants C_1, C_2 and C_3. From the enthalpy known at step t, the enthalpy at step $t+1$ is estimated as

$$\hat{H}(t+1) \leftarrow \mathcal{I}\left[\hat{H}(t)\right], \tag{21}$$

and the process is repeated until the left-hand-side and the right-hand side coincide.

3.1 Reference points, self-normalized solutions and supplementary key-equations

As shown in Kiuchi et al. (2010), the SCF-method is feasible for the bipolytropic system. We see from (14g) that C_{22} and C_{32} can be computed as soon as $\hat{\Psi}_{2,\rm tot}$ and $\hat{\Phi}_2$ are known at 2 points at the surface (i.e. onto Γ_2) where the enthalpy $\hat{H}_2$ vanishes. A convenient choice is the pair of reference points $\rm A_2$ and $\rm B_2$ already introduced in Sec. 2.3 (see also Fig. 1). The third constant for the envelope C_{12} can be deduced provided the value of $\hat{H}_2$ is known or imposed at some internal point $\rm M_2$. As for the single-layer case (Hachisu 1986), we can impose a normalization of the solution, i.e. $\hat{H}_2(\rm M_2) = 1$. The additional set of equations to consider is

$$\begin{cases} \hat{\Psi}_{2,\rm tot}(\rm A_2) + C_{22}\hat{\Phi}(\rm A_2) = C_{32}, \\ \hat{\Psi}_{2,\rm tot}(\rm B_2) + C_{22}\hat{\Phi}(\rm B_2) = C_{32}, \\ C_{12}\hat{H}_2(\rm M_2) + \hat{\Psi}_{2,\rm tot}(\rm M_2) + C_{22}\hat{\Phi}(\rm M_2) = C_{32}, \\ \hat{H}_2(\rm M_2) = 1. \end{cases} \tag{22}$$

By solving this system for the 3 constants, the enthalpy for the envelope is fully determined from (14g), namely

$$\begin{aligned} \hat{H}_2(\vec{r}) &= \frac{1}{C_{12}}\left\{C_{32} - \left[\hat{\Psi}_{2,\rm tot}(\vec{r}) + C_{22}\hat{\Phi}(\vec{r})\right]\right\}, \\ &= \frac{1}{\beta_2 C_{12}}\left\{\beta_2 C_{32} - \left[\hat{\Psi}_{1,\rm tot}(\vec{r}) + \beta_2 C_{22}\hat{\Phi}(\vec{r})\right]\right\}. \end{aligned} \tag{23}$$

Note that this assumes a value for β_2 (required in the computation of the total potential), even temporary (see below). Can we proceed in a similar way to get the 3 constants for the core in order to deduce $\hat{H}_1$? Actually, the core can be regarded as a single polytrope undergoing an external pressure at Γ_1 due to the envelope. However, the link between $\hat{H}_2(\Gamma_1)$ and $\hat{H}_1(\Gamma_1)$ is not established at this level, because C_{11} is not known yet; see (14d). We must therefore consider another path. The point is that C_{21} is easily deduced from C_{22} from (14), and C_{31} is obtained by combining (14a) and (14d). The remaining constant C_{11} is obtained provided the enthalpy of the core is imposed somewhere. As for the envelope, we seek for normalized solutions, i.e. $\hat{H}_1(M_1) = 1$ at some point $\rm M_1$. We then have

$$\begin{cases} C_{21} = \omega_2\beta_2 C_{22}, \\ \frac{\beta_2}{\alpha_2}C_{12}\hat{H}_2(\Gamma_1) + \hat{\Psi}_{1,\rm tot}(\Gamma_1) + C_{21}\hat{\Phi}(\Gamma_1) = C_{31}, \\ C_{11}\hat{H}_1(\rm M_1) + \hat{\Psi}_{1,\rm tot}(\rm M_1) + C_{22}\hat{\Phi}(\rm M_1) = C_{31}, \\ \hat{H}_1(\rm M_1) = 1, \end{cases} \tag{24}$$

which yields the 3 constants for the core. Note that, in practical, only one point of the interface is to be selected in (24b), while this equation must be fulfilled everywhere on Γ_1. We use $\rm A_1$ as the third reference point (see Sec. 2.1 and Fig. 1). The point $\rm M_2$ appearing in (22c) is selected onto the core/envelope interface, and $\rm M_2 \equiv A_1$ appears the most convenient choice.

It follows from (14a) and (24) that the enthalpy for the core is fully determined, i.e.

$$\hat{H}_1(\vec{r}) = \frac{1}{C_{11}}\left\{C_{31} - \left[\hat{\Psi}_{1,\rm tot}(\vec{r}) + C_{21}\hat{\Phi}(\vec{r})\right]\right\}. \tag{25}$$

As a matter of fact, (14e) has not been taken into account yet. This equation is therefore used to determine the (yet unspecified) mass density contrast, namely

$$\left.\frac{1}{\alpha_2}\,\frac{\hat{H}_1^{n_1}}{\hat{H}_2^{n_2}}\right|_{\Gamma_1} = \beta_2. \tag{26}$$

Except if the problem is solved, this value has no reason to be i) the same as the one used to compute $\hat{\Psi}_{\rm tot}$ and appearing in (22) and (24), and ii) the same all along the interface. This series of operations is repeated until the solution is found.

3.2 The step-by-step procedure

The series of operation listed in Sec. 3.1 is repeated until convergence (see Tab. A1 for more details about the implementation). There are 6 input parameters in total : n_1, n_2, e_2, q_1, $\alpha_2(\rm A_1)$ and ω_2. By fixing e_2 and q_1, we impose the location of the points $\rm A_2$, $\rm B_2$ and $\rm A_1$. The point where the interface Γ_1 meets the equatorial axis, the point B_1 (see again Fig. 1), is not in advance. Other choices are possible (e.g. Kiuchi et al. 2010). The rotation profiles and subsequently the associated functions $\hat{\Phi}_1(\hat{R})$ and $\hat{\Phi}_2(\hat{R})$ are supposed to be prescribed. At the beginning of the SCF-iterations, the enthalpies for the core and for the envelope and the contrast parameter β_2 are guessed. We use two paraboloids that satisfy the normalization condition and the interface condition. The enthalpies, the six constants C_{1l}, C_{2l} and C_{3l} with $l \in [1,2]$ and the two interfaces Γ_1 and Γ_2 evolve during the SCF-iterations. The identification of the two layers (through the interfaces) is a critical point of the problem. As in Huré & Hersant (2017), we use a 8-point directional Freeman chain code. This technique can find the zeros of a bivariate function from one numerical cell to the next one, by avoiding a complete scan of the computational grid. As soon as Γ_1 and Γ_2 are known, the computation of all integrated quantities, to begin with the gravitational potentials $\hat{\Psi}_l$ at the grid edges (boundary values required to solve the Poisson equation for each layer) is possible, is straightforward. As announced in the introduction, the Poisson equation is solved separately for the core and for the envelope (because mass density jumps cannot be described by a single computational grid). We use multigrid, which involves ℓ levels of refinement, and $N = 2^\ell + 1$ grid nodes per direction for the

finest grid. The two layers, however, share the same grid, which makes straightforward the computation of the total potential through (10).

In principle, the convergence of the process is declared after a certain number of iterations (a few tens typically), when all quantities do not vary anymore. Since all quantities generally get stabilized at the same time, it is sufficient to observe the variation of only one quantity from step t to step $t+1$ in the cycle. As the criterion, we use

$$\delta C_{l\in[1,2]} = \sqrt{\sum_{i=1,3} \left[C_{il}(t+1) - C_{il}(t)\right]^2} \leq \epsilon, \tag{27}$$

where ϵ is typically a few times the computer precision. Some authors work with the Virial parameter VP (see Sec. 3.3). The main drawback is that VP is limited by the precision of the numerical schemes and by the actual resolution. This is about 10^{-4} for a hundred grid nodes per direction. Actually, as we have experienced, there are many situations where the cycle seems to converge, but does not converge and oscillates instead. Clearly, the machine precision can be reached, more or less rapidly depending on the polytropic index and proximity to critical configurations. . We have incorporated the above procedure into the `DROP`-code (Huré & Hersant 2017). The numerical setup is basically the same in the paper throughout. As we use centered finite-difference schemes that are second-order in the mesh spacing, the expected precision is therefore of the order of $1/h^2 = 1/N^2$, which is $\sim 10^{-3}$ for $\ell = 4$ (low resolution) and $\sim 10^{-5}$ for $\ell = 7$ (moderate resolution). The dimensionless equatorial radius $\hat{R}(\mathrm{B}_2)$ of the envelope is set to unity. The computing time is very short, a few seconds typically on a standard laptop for $\ell = 4$, which enables to perform a large number of runs.

3.3 The Virial test

After convergence, all output quantities (mass, angular momentum, etc.) can be determined. The Virial test is customary used to measure the coherence of the numerical solutions. Theoretically, the total gravitational energy W_t, the total internal energy U_t and total kinetic energy T_t for a self-gravitating system at equilibrium are linked by

$$W_{\rm tot} + 2T_{\rm tot} + U_{\rm tot} = 0. \tag{28}$$

For a bipolytrope, the gravitational term can be written in the form

$$\begin{aligned}\frac{W_{\rm tot}}{G\rho_0^2 L^5} &= \frac{1}{2}\int \hat{\rho}_1 \underbrace{(\hat{\Psi}_1 + \beta_2\hat{\Psi}_2)}_{\hat{\Psi}_{1,\rm tot}} d\tilde{V}_1 \\ &\quad + \beta_2^2 \times \frac{1}{2}\int \hat{\rho}_2 \underbrace{\left(\frac{\hat{\Psi}_1}{\beta_2} + \hat{\Psi}_2\right)}_{\hat{\Psi}_{2,\rm tot}} d\tilde{V}_2, \\ &= \hat{W}_1 + \beta_2^2 \hat{W}_2\end{aligned} \tag{29}$$

where $d\tilde{V}_1 = 2\pi\hat{a}d\hat{a}d\hat{z}$ is the elementary volume (the expression is the same for the envelope). The kinetic and pressure terms are respectively

$$\begin{aligned}\frac{T_{\rm tot}}{G\rho_0^2 L^5} &= \frac{1}{2}\int \hat{\rho}_1 C_{21}\hat{\Omega}_1^2\hat{a}^2 d\tilde{V}_1 \\ &\quad + \beta_2^2 \times \frac{1}{2}\int \hat{\rho}_2 C_{22}\hat{\Omega}_2^2\hat{a}^2 d\tilde{V}_2, \\ &= C_{21}\hat{T}_1 + \beta_2^2 C_{22}\hat{T}_2\end{aligned} \tag{30}$$

and

$$\begin{aligned}\frac{U_{\rm tot}}{G\rho_0^2 L^5} &= \frac{3C_{11}}{1+n_1}\int \hat{\rho}_1 \hat{H} d\tilde{V}_1 + \beta_2^2 \times \frac{3C_{12}}{1+n_2}\int \hat{\rho}_2 \hat{H}_2 d\tilde{V}_2, \\ &= \hat{U}_1 + \beta_2^2 \hat{U}_2\end{aligned} \tag{31}$$

In dimensionless form, (50) thus reads

$$\underbrace{\hat{W}_1 + 2\hat{T}_1 + \hat{U}_1}_{\rm VP_1} + \beta_2^2 \underbrace{\left(\hat{W}_2 + 2\hat{T}_2 + \hat{U}_2\right)}_{\rm VP_2} = 0, \tag{32}$$

where VP_1 and VP_2, individually, have no great significance. Because of numerical errors, $\mathrm{VP} = \mathrm{VP}_1 + \beta_2^2\mathrm{VP}_2$ is not stricly zero. For any solution, however, it must be a small value (compared to unity). It is customary to define the Virial parameter relative to the gravitational term, namely

$$\mathrm{VT} = \frac{\mathrm{VP}}{|\hat{W}_1 + \beta_2^2\hat{W}_2|}. \tag{33}$$

4 NUMERICAL TESTS, CAPABILITIES AND TRENDS

In this section, we illustrate the method by computing the structure of bipolytopic systems for various sets of parameters. The aim of this section is not a wide exploration of the parameter space, but a selection of a few configurations. As already outlined in Sec. 3.2, a given configuration is obtained by prescribing the rotation profiles in both layers and by fixing 6 parameters.

4.1 A false bipolytrope. Impact on the location of the core/envelope interface

The first example is a "false" bipolytrope which consists in a core and an envelope having the same polytropic index, no mass density jump at the interface and no rotation, i.e. $e_2 = 1$, $\alpha_2(\Gamma_1) = 1$, $\hat{\Omega} = 0$, and $\omega_2 = 1$. The potential $\hat{\Phi}(\hat{R})$ can thus be set to zero. We select $n_2 = n_1 = \frac{3}{2}$, which corresponds, for instance, to a static, fully convective system. This case has been considered for instance in Hachisu (1986). The equilibrium structure computed for $q_1 = \frac{2}{3}$ is shown in Fig. 2 at $\ell = 4$. The convergence is reached after 32 iterations. The interfaces Γ_1 and Γ_2 consist in 19 points and 29 points, respectively. The main output quantities obtained for $\ell = 7$ are given in Tab. B1. We notice the "perfect" continuity of the fields from the core to the envelope, and the excellent agreement between the corresponding (single) polytrope. Actually, the deviation in the mass, volume and gravitational energy of the configuration is of the order of a few 10^{-4}, which is also the value of the Virial parameter.

It is interesting to check the impact of the position of the core/envelope interface (i.e. point A_1, parameter q_1; see Fig. 1) on the results. This is shown in Fig. 3 where we have plotted the average of the absolute deviation between the

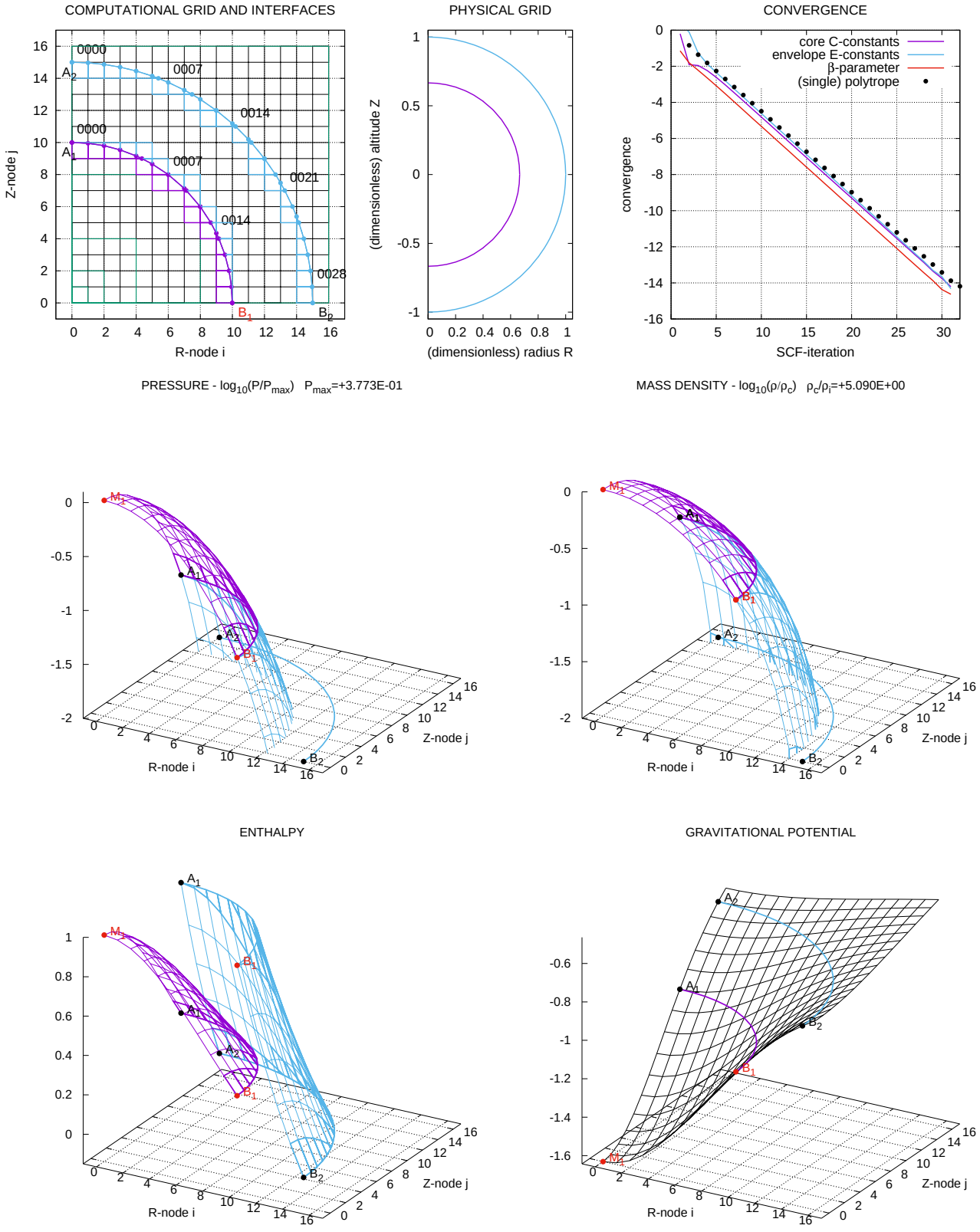

Figure 2. The false bipolytrope considered in Sect. 4.1, i.e. $n_1 = n_2 = 1.5$, $q = \frac{2}{3}$, static case, $\alpha_2 = 1$: the interfaces Γ_1 and Γ_2 in the numerical grid (*top left*) and in the physical space (*top middle*), the convergence of the constants (*top right*), the gas pressure (*middle left*), the mass density (*middle right*), the enthalpies (*bottom left*) and the gravitational potential (*bottom right*). The grid resolution corresponds to $\ell = 4$ levels of multigrid (i.e. 17×17 nodes per direction). Only the data for the core (*cyan*) and for the envelope (*purple*) are shown. From the contour detection method, Γ_1 and Γ_2 consist in 19 and 29 nodes, respectively. (*bold*). The triangular, tetrahedral and pentahedral numerical cells bordering the interfaces are enhanced (*bold*). Output quantities obtained for $\ell = 7$ are listed in Tab. B1.

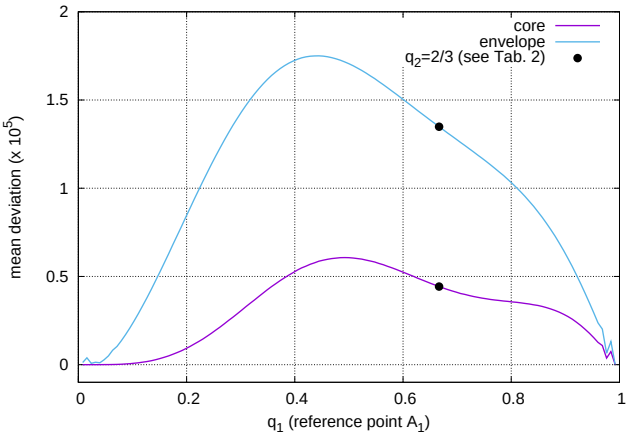

Figure 3. Comparison between the enthalpy of the single polytrope and enthalpy of the false bipolytrope as a function of the relative size q_1 of the core. Values are the mean absolute deviations computed in each layer. The numerical resolution corresponds to $\ell = 7$ (see Tab. B1).

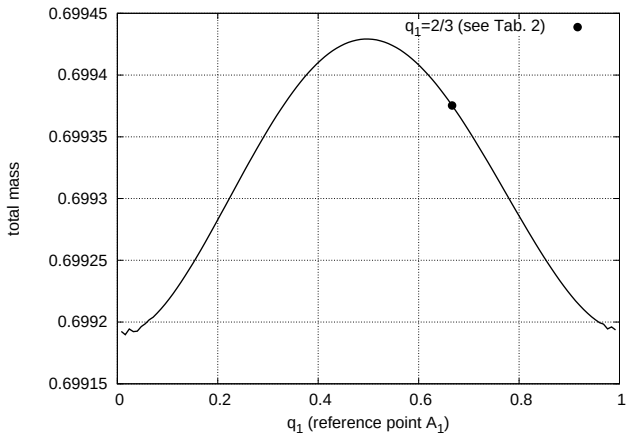

Figure 4. Mass of the false bipolytrope as a function of the relative size q_1 of the core, in the conditions of Fig. 3.

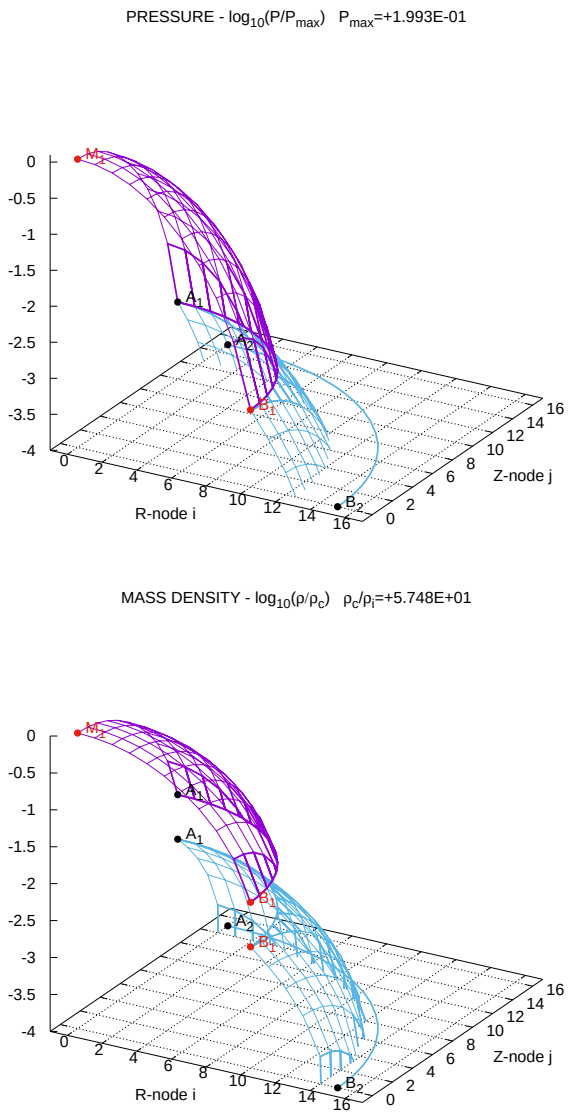

Figure 5. Same legend as for Fig. 2 (only the internal pressure and mass density are shown) but for $\alpha = 4$ at the core-envelope interface (see also Tab. B2).

enthalpy in each layer and the value obtained for the single polytrope as q_1 varies in the full range. We find that this deviation is less than $\sim 10^{-5}$. We find that the sensitivity to q_1 remains weak, although it is the largest when the interface stands roughly in the middle of the system. Figure 4 shows the variation of the total mass of the system versus q_1. We conclude that the method does not introduce any strong bias on the output quantities for any value of q_1. Very similar results have been obtained for other sets of polytropic indices, in particular for $n_1 = n_2 = 1$ which can be compared to the Schuster-Emden (analytical) solution.

4.2 Effect of the mass density jump

We consider the same bipolytrope as in Sect. 4.1, but we now introduce a mass densiy jump at the core/envelope interface, still in the absence of any rotation. Figure 5 shows the pressure and mass density inside the system obtained at low reslution for $\alpha = 4$. We remind that this case is of special interest for H-burning stars in which He constitutes the main ingredient at the center (although the polytropic indices considered here are not appropriate). The output quantities obtained for $\ell = 7$ are listed in Tab. B2. We see that the pressure is perfectly continuous when crossing Γ_1, as well as its gradient (we have $n_1 = n_2$ here). Since the mass density in the envelope is decreased with respect to the no-jump solution, the total mass of the systems is therefore decreased, by a factor ~ 2.5, and the gravitational energy is decreased by a factor 4.8. Note the very small value of the β_2-parameter that is responsible for these new values. As we have checked, the code is capable of considering $\alpha_2 \gg 1$. This is interesting for instance to investigate planets made of a rocky core surrounded by a thick ocean or atmosphere. We can also generate configurations where the mass density jump is smaller than unity, which leads to more

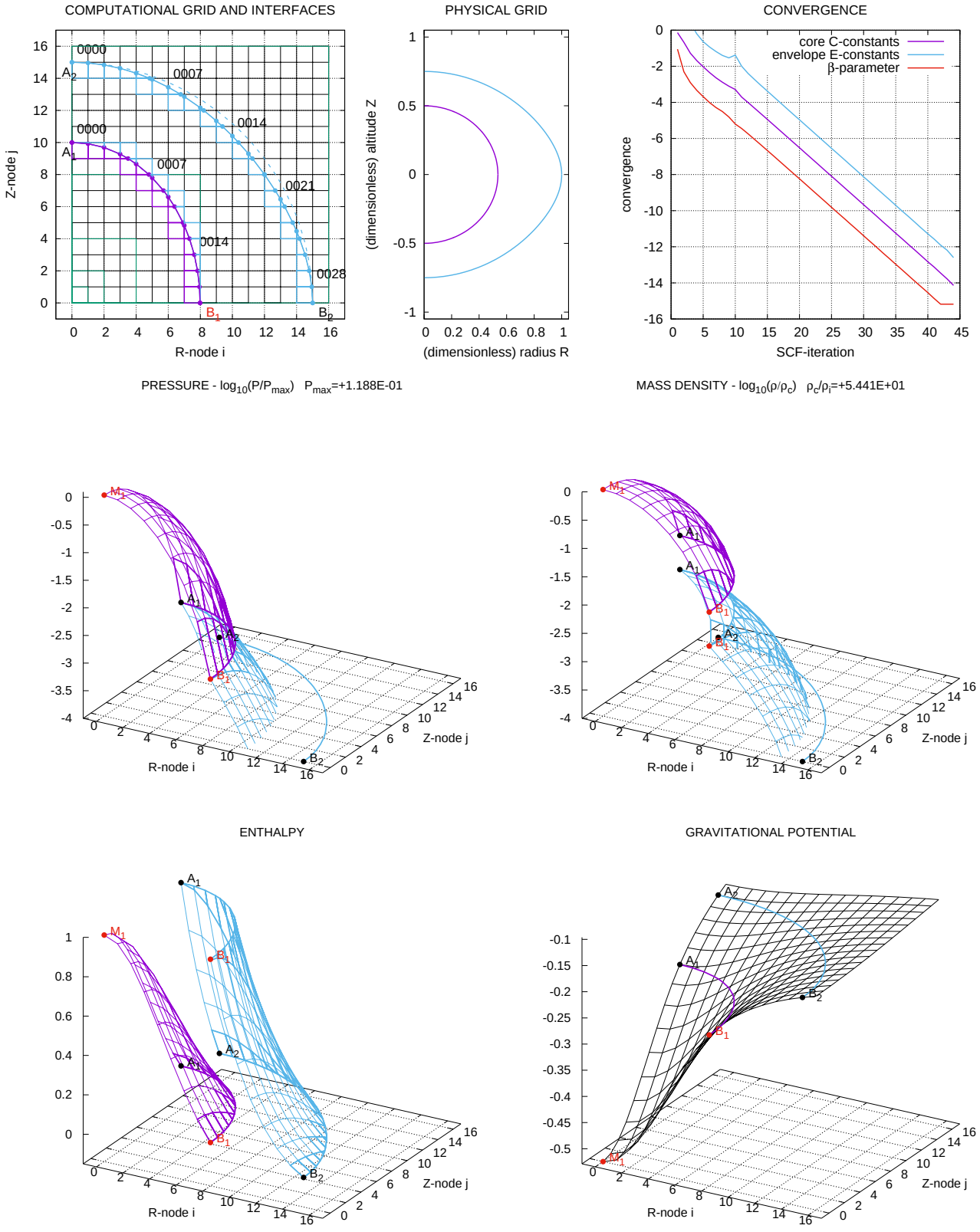

Figure 6. Same legend as for Fig. 2 but for $\alpha = 4$ at the core-envelope interface and rigid rotation for both layers (no rotational discontinuity). The axis ratio of the envelope is 0.75. See also Tab. B3.

massive systems (but to probably more mechanically unstable solutions). Clearly, for a given mass-density jump, the polytropic indices and the position of core-envelope interface play a critical role.

4.3 Example of a rotating bipolytrope with mass density jump

In the next example, we assume the same parameter as above, but the whole system is now in rigid rotation at the same rate for both layers, i.e. we have $\hat{\Omega} = 1$ and $\omega_2 = 1$. The centrifugal potential is $\hat{\Phi}(\hat{R}) = -\frac{1}{2}\hat{R}^2$. The magnitude of rotation is set by the axis ratio of the envelope e_2. Since we work with $\hat{R}(\mathrm{B}_2) = 1$, e_2 is nothing but $\hat{Z}(\mathrm{A}_2)$. As it is well known, only oblate solutions exist in the present context, but it may happen that there is no equilibrium for a given axis ratio if the rotation rate is too high. At the so-called critical rotation (or mass-shedding limit) actually, the pressure gradient just vanishes at the equator, leaving matter on the verge of separation. We select $e_2 = 0.75$; in the single polytrope case, the state of critical rotation occurs for $e^{\mathrm{crit.}} \approx 0.617$ (Hachisu 1986). The results obtained for $\ell = 4$ are displayed in Fig. 6. The equilibrium values obtained for $\ell = 7$ are listed in Tab. B3. The system has an oblate shape for both the envelope and the core. The axis ratio of the core is of the order of ≈ 0.932. This value is therefore much larger than for the envelope. In other words, the core is more spherical than the envelope. As a consequence, the envelope is more extended at the equator than at the pole. This effect is more or less pronounced depending on the polytropic indices, but it does not depends very much on the mass-density jump. We find that, if $n_1 > n_2$, then the sphericity of the core increases and the equatorial extension of the envelope increases. The effect remains, however, weak. In all cases, the shape of the envelope is slightly "sub-elliptical" in the sense that the Γ_2 happens to be interior to the ellipse formed by the reference points A_2 and B_2.

4.4 Case of a critical rotation

The difference in shape in between the core and the envelope is better amplified in the case of a critical rotation. From the solution presented in Sec. 4.3, we have gradually decreased the axis ratio e_2 from 0.75 until the critical rotation is reached. For $\ell = 7$, we find $e_2 \sim 0.6589$ as the final value. Table B4 gathered the output data for this configuration. The shapes at equilibrium are plotted in Fig. 7. We clearly see the "beak-shape" of the surface of the envelope at B_2, typical of a critical rotation. Interestingly enough, we find $e_1 \sim 0.927$ as the axis ratio of the core, which value is almost the same as out of critical rotation (see before). The global shape of the core is relatively unsensistive to the shape of the envelope, as long as q_1 is not too close to unity. When $q_1 \to 1$, the core dominates and tends to merge with the tiny envelope, and the critical rotation involves significantly lower values of e_2 (in the limit of $e^{\mathrm{crit.}}$).

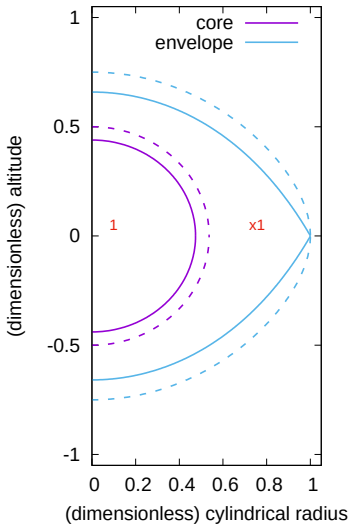

Figure 7. Interfaces Γ_1 and Γ_2 for the state of critical rotation for $n_1 = n_2 = 1.5$ and $\alpha = 4$ (*plain lines*). The configuration considered in Fig. 6 and in Sect. 4.3 is shown in comparison (*dashed lines*). The two layers rotate at the same rate.

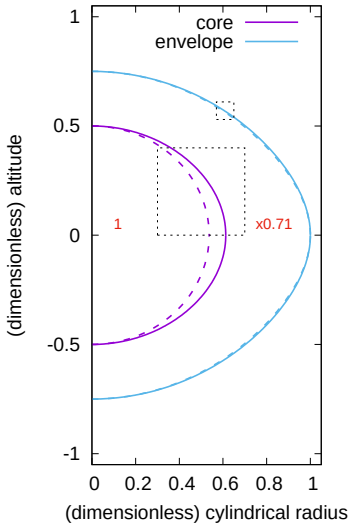

Figure 8. Effect of a rotational discontinuity at Γ_1 on the core and on the envelope for the rotating bipolytrope with axis ratio $e_2 = 0.75$, $q_2 = \frac{2}{3}$, mass-density jump $\alpha_2(\Gamma_1) = 4$. The polytropic index is the same for both layers, namely $n_1 = n_2 = 1.5$. Both layers are rigidly rotating : $\omega_2 = 1$ corresponds to the same rotation rate (*dashed lines*), and $\omega_2 = 2$ is for a core spinning ~ 1.41 times faster than the envelope (*plain lines*). See also Fig. 9 for a zoom.

4.5 Case with rigid rotation, mass-density jump and rotational discontinuity

The rotational discontinuity at the core/envelope interface is governed by the ω_2-parameter. By setting $\omega_2 \neq 1$ in the equation set, the discontinuity is switched on. Two different situations are interesting to discuss : i) $n_2 = n_1$ and ii) $n_2 \neq n_1$. According to the previous discussion (see Sect. 2.5), a

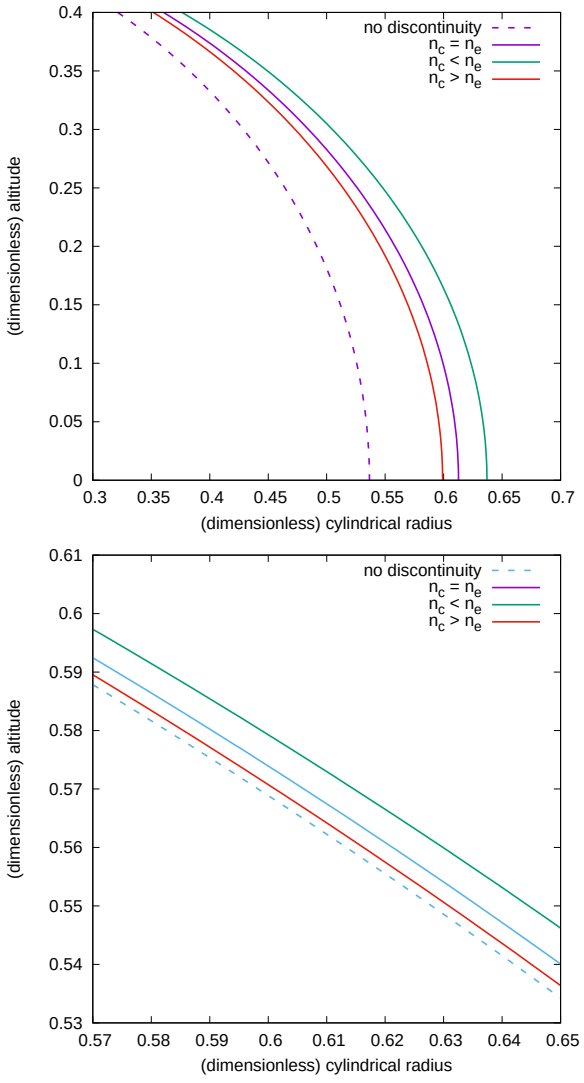

Figure 9. Effect of a rotational discontinuity $\omega_2 = 2$ on the interfaces Γ_1 (*top panel*) and Γ_2 (*bottom panel*) for the rotating biplytrope with axis ratio $e_2 = 0.75$, $q_2 = \frac{2}{3}$ and mass-density jump $\alpha_2(\mathrm{A}_1) = 4$ for three different pairs (n_1, n_2) of polytropic indices : $(1.5, 1.5)$ (*purple*), $(1, 2)$ (*green*) and $(2, 1)$ (*red*). The case without rotational discontinuity (i.e. full rigid rotation with $\omega_2 = 1$), is given for comparison (*dashed lines*); see also Fig. 8.

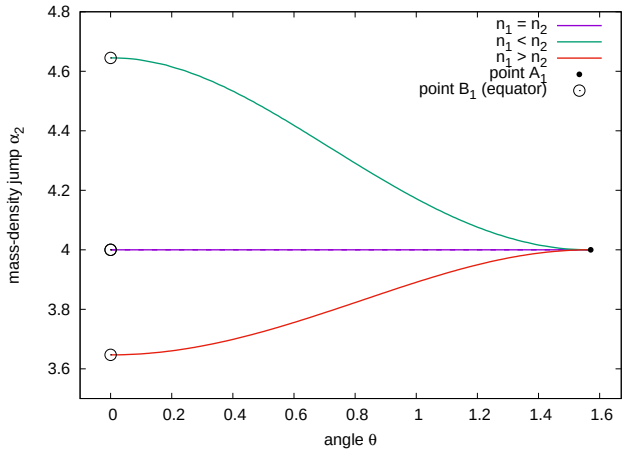

Figure 10. Effect of a rotational discontinuity $\omega_2 = 2$ on the mass-density jump along the interface for the rotating bipolytrope with axis ratio $e_2 = 0.75$ and $q_2 = \frac{2}{3}$ for three pairs of polytropic indices $(n_1, n_2) = \{(1, 1), (1, 2), (2, 1)\}$. The angle θ is the polar angle of the interface Γ_1 in the $(\hat{R}, \hat{Z})$-plane, i.e. $\tan\theta = \hat{Z}/\hat{R}|_{\Gamma_1}$.

constant mass-density jump is expected in the first case, but not in the second one. Figure 8 shows the shape of the core and the shape of the envelope obtained for $\omega_2 = 2$ when the two layers have the same polytopic index. The mass-density jump is $\alpha_2 = 4$ all along Γ_1. The equilibrium quantities computed for $\ell = 7$ are listed in Tab. B5 (see Tab. B3 for $\omega_2 = 1$). As expected, the oblateness of a core that spins faster than the envelope increases (we find $e_1 \sim 0.816$). The density contrast slightly increases, the core is more massive, in contrast with the envelope which is less massive. As a consequence, the total mass is increased with respect to the case without rotational discontinuity. We see that the total volume is slightly increased. The shape of the envelope is still sub-elliptical (see above).

The results obtained in the same conditions as above but for the new sets of polytropic indices $(n_1, n_2) = (1, 2)$ and $(n_1, n_2) = (2, 1)$ are listed in Tabs. B6 and B7 respectively. The differences between the configuration are important, while the changes in the shapes for the core and for the envelope are much less pronounced. Figure 9 displays the core/envelope interface zoomed about the point B_2 at the equator, and the fluid boundary zoomed at about 45° off the equatorial axis. We see that the volume (and the axis ratio) of the core is smaller when $n_1 > n_2$. Because the β_2-parameter increases (by a factor ~ 3 typically with respect to the case with $n_1 = n_2$), the mass of the configuration increases by a factor ~ 1.8, and the core rotates faster since the coefficient C_{21} increases by a factor ~ 1.7. Figure 10 displays $\alpha(\Gamma_1)$. We see that the mass density jump is not uniform along Γ_1, as predicted (see Sec. 2.5). Its value is set to 4 just on the polar axis, and decreases monotonically down to about 3.6 at the equatorial plane. The reverse situation is observed when $n_1 < n_2$.

4.6 A comparison with Kiuchi's paper

Kiuchi et al. (2010) have computed the structure of a rotating, 2-layer white dwarf, in the limit of a fully degenerate, ultrarelativistic gas. Figure 11 shows the solution obtained the following parameters $n_1 = n_2 = 3$, $e_2 = 0.6$, $q_1 = \frac{5}{6}$ and $\omega_2 = 0.7572$. We use a softened v-constant rotation law in core and the envelope (which, thus, rotates a little bit faster). By varying the mass density jump, the size of core varies, but for $\alpha_2(\mathrm{A}_1) \approx 1.6660$, we get $e_1 \approx 1$, which corresponds to the case reported in Kiuchi et al. (2010) (see their Tab. 3 and Fig. 6.). Output values are gathered in Tab. B8. Since the two polytropic indices are equal, the mass density jump is uniform all along the interface, which is confirmed on output. There is an excellent agreement between the two results (while the numerical resolution is about 3.5 lower here). in particular, for $L = 3057$ km and $\rho_{10} = 5.629 \times 10^9$ g/cm^3, the total mass is $M_{\mathrm{tot.}} \approx 1.6509$ M$_\odot$, which agrees within 0.2% with the author's estimates.

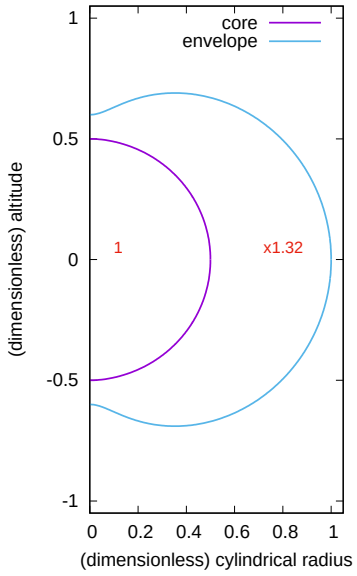

Figure 11. Configuration for a 2-layer white dwarf obtained for the same conditions as in Kiuchi et al. (2010). The resolution corresponds to $\ell = 7$. The rotational profile corresponds to softened v-constant law (the softening parameter is 0.1 in both layers). Labels (*red*) correspond to the rotation rate of the envelope relative to the core, i.e. $\frac{1}{\sqrt{\omega_2}}$.

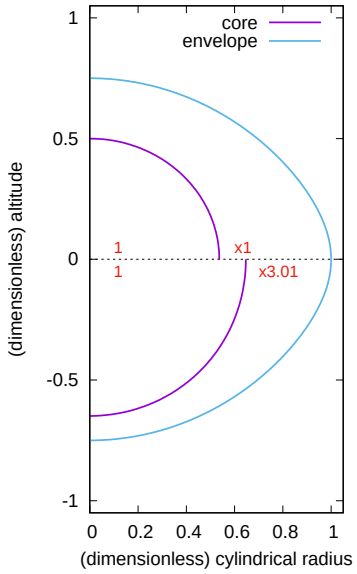

Figure 12. Configuration for two different bipolytropic configurations sharing the same size, surface velocity and total mass (and degeneracy parameter Ξ). Input parameters are from Tabs. B3 (*top*) and B9 (*bottom*). Each layer is in rigid rotation. Labels (*red*) corresponds to the rotation rate of the envelope relative to the core, i.e. $\frac{1}{\sqrt{\omega_2}}$. The shape of the envelope is almost unchanged, in contrast with to the core.

4.7 An example of degenerate configurations. Degeneracy parameter

An interesting question concerns the existence of degenerate states, i.e. configurations having different internal structure but sharing a few global quantities. This can be suspected as soon as the number of free parameters is "sufficient". From an observational point of view, the quantities of prime importance are the equatorial radius, eventually the axis ratio (i.e. the polar radius), and the rotation velocity V, which is traditionnaly inferred from Doppler shifts. In the physical space, we have

$$\begin{cases} R_{\rm eq.} = \hat{R}(\mathrm{B}_2) \times L \\ R_{\rm pol.} = e_2 \hat{R}(\mathrm{B}_2) \times L \\ V_{\rm eq}^2(\mathrm{B}_2) = C_{22} \times G\rho_{20} L^2, \end{cases} \tag{34}$$

where $V_{\rm eq} = V(\mathrm{B}_2)$. So, two different configurations that share the same values for $R_{\rm eq}$, $R_{\rm pol}$ and $V_{\rm eq}(\mathrm{B}_2)$ are undistinguable for an observer measuring the size, shape and the equatorial velocity. In the present problem, it is easy to find such 2-layer configurations since we have 6 input parameters. An even more stricking situation arises if we also consider the mass $M_{\rm tot.} = \hat{M}_{\rm tot.} \times \rho_{10} L^3$ of the system. It turns out that two bipolytropic configurations having the same value for

$$\frac{C_{22}\beta_2}{\hat{M}_{\rm tot.}} \equiv \Xi_2, \tag{35}$$

are totally undistinguishable from each other not only in size and velocity, but would also in mass, in spite of different internal structures (and different central densities ρ_{10}). Finding sets of parameters realizing such a degeneracy is less trivial. An example is shown in Fig. 12 where we have plotted the interfaces obtained for the parameter set listed in Tab. B9. For this new configuration, the EOS for the core is close to incompressibility, and the EOS for the envelope could correspond to a radiation pressure dominated zone. The degeneracy parameter is $\Xi \approx 0.6419$, which is the same value as for the configuration obtained for the input parametres of Tab. B3. The two solutions differ by values for ω_2, q_1, α_2 and n_1. The internal structures are, however, very different, with, for instance, a factor ~ 5.16 between central densities. The mass density jump is larger, while the envelope, which rotates about 3 times faster, has almost the same shape. Note that the core is, again, very cose to spherical.

5 GENERALIZATION: THE $\mathcal{L}$-LAYER STAR/PLANET. THEORY, PROCEDURE AND EXAMPLES.

5.1 Notations

We now consider a system made of $\mathcal{L}$ layers, with $\mathcal{L} \geq 2$. Each layer is defined by a number l, a polytropic index for the EOS $n_l \geq 0$, the enthalpy $\hat{H}_l$, the mass density ρ_l (with magnitude ρ_{l0}), a rotation profile Ω_l (with magnitude Ω_{l0}) and associated centrifugal potential $\hat{\Phi}_l$, etc. By convention, $l = 1$ is the deepest layer, still called the "core", and the outermost layer has the index $l = \mathcal{L}$. The interface between two adjacent layers $l \in [2, \mathcal{L}]$ and $l' = l - 1$ is denoted $\Gamma_{l'}$, and the interface with the free space is $\Gamma_{\mathcal{L}}$. The system is

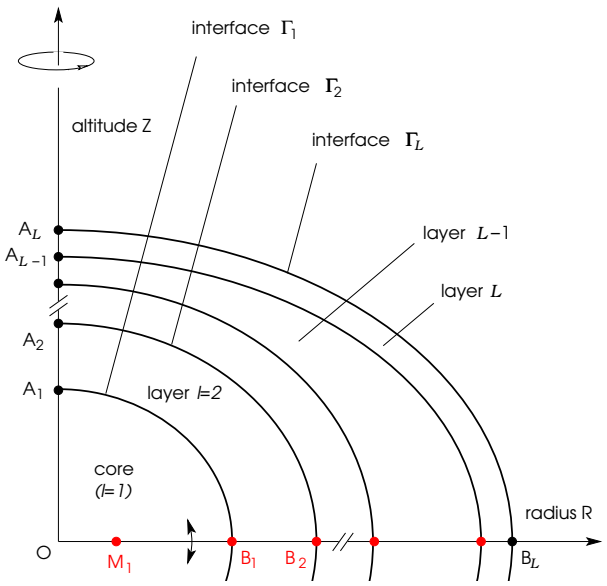

Figure 13. Configuration for the rotating, multilayer star/planet made of $\mathcal{L}$ layers (the deepest one, the core, has layer number 1). At each interface Γ_l, both a mass density jump and a rotational discontinuity are allowed. The rotation rate at the bottom of the outermost layer envelope is set through the reference points $\mathrm{A}_\mathcal{L}$ and $\mathrm{B}_\mathcal{L}$. The polar extension of the layers is set through the reference points A_1, A_2, ..., $\mathrm{A}_{\mathcal{L}-1}$ on the polar axis.

depicted in Fig. 13. As for the 2-layer case, we defined the axis ratio of layer l by

$$\frac{\mathrm{OA}_l}{\mathrm{OB}_l} \equiv e_l, \tag{36}$$

where points A_l and B_l both belong to Γ_l and are located on the polar and equatorial axis respectively. We still have (8) for the core. The polar extension of each layer relative to the full polar radius is defined by

$$q_l = \frac{\mathrm{A}_{l'}\mathrm{A}_l}{\mathrm{OA}_\mathcal{L}} \in [0,1], \tag{37}$$

and $q_1 = \frac{\mathrm{OA}_1}{\mathrm{OA}_\mathcal{L}}$ for the core. It follows that $q_1 + \sum_{l=2,\mathcal{L}} q_l = 1$.

5.2 The full equation set

The equilibrium of each layer $l \in [2,\mathcal{L}]$ is described by a set of equations similar to (1), namely

$$\begin{cases} C_{1l}\hat{H}_l + \hat{\Psi}_{l,\mathrm{tot}} + C_{2l}\hat{\Phi}_l = C_{3l}, \\ \hat{\rho}_l = (\hat{H}_l)^{n_l} \quad \hat{H}_l(\Gamma_{l'}) \geq \hat{H}_l \geq \hat{H}_l(\Gamma_l), \\ \Delta\hat{\Psi}_{l,\mathrm{tot}} = 4\pi\frac{1}{\beta_l}\left(\hat{\rho}_1 + \beta_2\hat{\rho}_2 + \ldots \right. \\ \qquad\qquad \left. + \beta_l\hat{\rho}_l + \cdots + \beta_\mathcal{L}\hat{\rho}_\mathcal{L}\right), \end{cases} \tag{38}$$

where C_{3l} is the invariant,

$$\begin{cases} C_{1l} \equiv \frac{K_l(n_l+1)\rho_{l0}^{\gamma_l-2}}{GL^2}, \\ C_{2l} \equiv \frac{\Omega_0^2}{G\rho_{l0}}, \end{cases} \tag{39}$$

For $l=1$ (the core), (38b) holds but $\hat{H}_1 \geq \hat{H}_1(\Gamma_1)$, while for the outermost layer $l=\mathcal{L}$, we have $\hat{H}_\mathcal{L} = 0$ in the absence of ambient pressure. We can account for a mass density jump α_l and a rotational discontinuity ω_l at each interior interface. The relevant parameters are

$$\alpha_l = \left.\frac{\rho_{l'}}{\rho_l}\right|_{\Gamma_{l'}} > 0, \tag{40}$$

and

$$\sqrt{\omega_l} = \frac{\Omega_{l'0}}{\Omega_{l0}} > 0. \tag{41}$$

So, the layer l rotates faster than the one located just "below", i.e. layer l', when $\omega_l < 1$. As for the 2-layer case, we define a contrast parameter for layer l

$$\beta_l = \frac{\rho_{l0}}{\rho_{10}} > 0, \tag{42}$$

where the reference value is the value in the core ρ_{10} (note that $\beta_1 = 1$). As the consequence, in the core frame, the total gravitational potential writes

$$\hat{\Psi}_{1,\mathrm{tot}} = \sum_{l=1}^{\mathcal{L}} \beta_l\hat{\Psi}_l, \tag{43}$$

where $\hat{\Psi}_l$ is the potential due to the layer l. For the two adjacent layers l and $l' = l-1$, we have from (39b)

$$\beta_l C_{2l}\Omega_{l'0}^2 = \beta_{l'}C_{2l'}\Omega_{l0}^2, \tag{44}$$

which, given (41) and (42), also reads

$$\omega_l\beta_l C_{2l} = \beta_{l'}C_{2l'}. \tag{45}$$

There are also $\mathcal{L}-1$ additionnal equations similar to (4) accounting for the pressure balance at each interior interface, namely

$$\bar{\alpha}_l\beta_{l'}C_{1l'}\hat{H}_{l'}(\Gamma_{l'}) - \beta_l C_{1l}\hat{H}_l(\Gamma_{l'}) = 0, \tag{46}$$

where

$$\bar{\alpha}_l = \alpha_l\frac{1+n_l}{1+n_{l'}}, \tag{47}$$

and yet another $\mathcal{L}-1$ equations corresponding to mass density jumps

$$\alpha_l\beta_l\hat{H}_l^{n_l}(\Gamma_{l'}) = \beta_{l'}\hat{H}_{l'}^{n_{l'}}(\Gamma_{l'}). \tag{48}$$

The full equation set for the $\mathcal{L}$-layer system is therefore

$$
\begin{cases}
C_{11}\hat{H}_1 + \hat{\Psi}_{1,\mathrm{tot}} + C_{21}\hat{\Phi}_1 = C_{31}, \\
\hat{\rho}_1 = \hat{H}_1^{n_1}, \quad \hat{H}_1 \geq \hat{H}_1(\Gamma_1), \\
\Delta\hat{\Psi}_{1,\mathrm{tot}} = 4\pi\left(\hat{\rho}_1 + \beta_2\hat{\rho}_2 + \ldots \right. \qquad \text{(layer 1)} \\
\qquad\qquad \left. + \beta_l\hat{\rho}_l + \cdots + \beta_{\mathcal{L}}\hat{\rho}_{\mathcal{L}}\right) \\
\\
\bar{\alpha}_2 C_{11}\hat{H}_1(\Gamma_1) - \beta_2 C_{12}\hat{H}_2(\Gamma_1) = 0, \\
\quad \text{(pressure balance)} \\
\alpha_2\beta_2\hat{H}_2^{n_2}(\Gamma_1) = \hat{H}_1^{n_1}(\Gamma_1) \qquad (\rho-\text{jump}), \\
\omega_2\beta_2 C_{22} = C_{21} \quad \text{(scaling)}, \\
\ldots \\
C_{1l}\hat{H}_l + \hat{\Psi}_{l,\mathrm{tot}} + C_{2l}\hat{\Phi}_l = C_{3l}, \\
\hat{\rho}_l = \hat{H}_l^{n_l}, \quad \hat{H}_l(\Gamma_{l'}) \geq \hat{H}_l \geq \hat{H}_l(\Gamma_l), \\
\Delta\hat{\Psi}_{l,\mathrm{tot}} = 4\pi\frac{1}{\beta_l}\left(\hat{\rho}_1 + \beta_2\hat{\rho}_2 + \ldots \right. \qquad \text{(layer } l\text{)} \\
\qquad\qquad \left. + \beta_l\hat{\rho}_l + \cdots + \beta_{\mathcal{L}}\hat{\rho}_{\mathcal{L}}\right), \\
\\
\bar{\alpha}_l\beta_{l'} C_{1l'}\hat{H}_{l'}(\Gamma_{l'}) - \beta_l C_{1l}\hat{H}_l(\Gamma_{l'}) = 0, \\
\quad \text{(pressure balance)} \\
\alpha_l\beta_l\hat{H}_l^{n_l}(\Gamma_{l'}) = \beta_{l'}\hat{H}_{l'}^{n_{l'}}(\Gamma_{l'}) \qquad (\rho-\text{jump}), \\
\omega_l\beta_l C_{2l} = \beta_{l'} C_{2l'} \quad \text{(scaling)}, \\
\ldots \\
C_{1\mathcal{L}}\hat{H}_{\mathcal{L}} + \hat{\Psi}_{\mathcal{L},\mathrm{tot}} + C_{2\mathcal{L}}\hat{\Phi}_{\mathcal{L}} = C_{3\mathcal{L}}, \\
\hat{\rho}_{\mathcal{L}} = \hat{H}_{\mathcal{L}}^{n_{\mathcal{L}}}, \quad \hat{H}_{\mathcal{L}}(\Gamma_{\mathcal{L}-1}) \geq \hat{H}_{\mathcal{L}} \geq 0, \\
\Delta\hat{\Psi}_{\mathcal{L},\mathrm{tot}} = 4\pi\frac{1}{\beta_{\mathcal{L}}}\left(\hat{\rho}_l + \beta_2\hat{\rho}_2 + \ldots \right. \qquad \text{(layer } \mathcal{L}\text{)} \\
\qquad\qquad \left. + +\beta_l\hat{\rho}_l + \cdots + \beta_{\mathcal{L}}\hat{\rho}_{\mathcal{L}}\right).
\end{cases}
\tag{49}
$$

Note that all Poisson equations are formally equivalent. The total number of equations amounts to $5\mathcal{L}-2$. There are $\mathcal{L}$ enthalpies to determines and $4\mathcal{L}-1$ unknown constants (3 constants C_1, C_2l and C_3 for each layer and one constant β for each interface). There are $4\mathcal{L}-2$ input parameters (one polytropic index per layer, one mass density jump and one rotational discontinuity per interface) and $\mathcal{L}+1$ reference points to define A_1, A_2, …, $\mathrm{A}_{\mathcal{L}-1}$, $\mathrm{A}_{\mathcal{L}}$, and $\mathrm{B}_{\mathcal{L}}$.

5.3 The Virial test

At equilibrium, the Virial equation, which accounts for all layers, writes

$$W_{\mathrm{tot}} + 2T_{\mathrm{tot}} + U_{\mathrm{tot}} = 0. \tag{50}$$

The gravitational term can be written in the form

$$
\begin{aligned}
\frac{W_{\mathrm{tot}}}{G\rho_0^2 L^5} &= \frac{1}{2}\int \hat{\rho}_1 \underbrace{\left(\hat{\Psi}_1 + \cdots + \beta_l\hat{\Psi}_l + \cdots + \beta_{\mathcal{L}}\hat{\Psi}_{\mathcal{L}}\right)}_{\hat{W}_{1,\mathrm{tot}}} d\tilde{V}_1 \\
&\quad + \ldots \\
&\quad + \beta_l^2 \times \frac{1}{2}\int \hat{\rho}_l \underbrace{\left(\frac{\hat{\Psi}_1}{\beta_l} + \cdots + \hat{\Psi}_l + \cdots + \frac{\beta_{\mathcal{L}}}{\beta_l}\hat{\Psi}_{\mathcal{L}}\right)}_{\hat{W}_{2,\mathrm{tot}}} d\hat{V}_l \\
&\quad + \ldots \\
&\quad + \beta_{\mathcal{L}}^2 \times \frac{1}{2}\int \hat{\rho}_{\mathcal{L}} \underbrace{\left(\frac{\hat{\Psi}_1}{\beta_{\mathcal{L}}} + \cdots + \frac{\beta_l}{\beta_{\mathcal{L}}}\hat{\Psi}_l + \cdots + \hat{\Psi}_{\mathcal{L}}\right)}_{\hat{W}_{\mathcal{L},\mathrm{tot}}} d\hat{V}_{\mathcal{L}}, \\
&= \hat{W}_{1,\mathrm{tot}} + \cdots + \beta_l^2\hat{W}_{l,\mathrm{tot}} + \cdots + \beta_{\mathcal{L}}^2\hat{W}_{\mathcal{L},\mathrm{tot}},
\end{aligned}
\tag{51}
$$

where $d\hat{V}_l = 2\pi\hat{a}d\hat{a}d\hat{z}$ is the elementary volume. The kinetic and pressure terms are respectively

$$
\begin{aligned}
\frac{T_{\mathrm{tot}}}{G\rho_0^2 L^5} &= \frac{1}{2}\int \hat{\rho}_1 C_{21}\hat{\Omega}_1^2\hat{a}^2 d\tilde{V}_1 + \ldots \\
&\quad + \beta_l^2 \times \frac{1}{2}\int \hat{\rho}_l C_{2l}\hat{\Omega}_l^2\hat{a}^2 d\hat{V}_l + \ldots \\
&\quad + \beta_{\mathcal{L}}^2 \times \frac{1}{2}\int \hat{\rho}_{\mathcal{L}} C_{2\mathcal{L}}\hat{\Omega}_{\mathcal{L}}^2\hat{a}^2 d\hat{V}_{\mathcal{L}}, \\
&= C_{21}\hat{T}_1 + \cdots + \beta_l^2 C_{2l}\hat{T}_l + \cdots + \beta_{\mathcal{L}}^2 C_{2\mathcal{L}}\hat{T}_{\mathcal{L}}
\end{aligned}
\tag{52}
$$

and

$$
\begin{aligned}
\frac{U_{\mathrm{tot}}}{G\rho_0^2 L^5} &= \frac{3C_{11}}{1+n_1}\int \hat{\rho}_1\hat{H}_1 d\tilde{V}_1 + \ldots \\
&\quad + \beta_l^2 \times \frac{3C_{1l}}{1+n_l}\int \hat{\rho}_l\hat{H}_l d\hat{V}_l + \ldots \\
&\quad + \beta_{\mathcal{L}}^2 \times \frac{3C_{1\mathcal{L}}}{1+n_{\mathcal{L}}}\int \hat{\rho}_l\hat{H}_{\mathcal{L}} d\hat{V}_{\mathcal{L}} \\
&= \hat{U}_1 + \cdots + \beta_l^2\hat{U}_l + \cdots + \beta_{\mathcal{L}}^2\hat{U}_{\mathcal{L}}.
\end{aligned}
\tag{53}
$$

In dimensionless form, (50) becomes

$$
\begin{aligned}
\underbrace{\hat{W}_1 + 2\hat{T}_1 + \hat{U}_1}_{\mathrm{VP}_1} + \cdots + \beta_l^2 \underbrace{\left(\hat{W}_l + 2\hat{T}_l + \hat{U}_l\right)}_{\mathrm{VP}_l} + \ldots \\
+ \beta_{\mathcal{L}}^2 \underbrace{\left(\hat{W}_{\mathcal{L}} + 2\hat{T}_{\mathcal{L}} + \hat{U}_{\mathcal{L}}\right)}_{\mathrm{VP}_{\mathcal{L}}} = 0.
\end{aligned}
\tag{54}
$$

By dividing this equation by the gravitational term, we have

$$\mathrm{VT} = \frac{\sum_{l=1}^{\mathcal{L}}\mathrm{VP}_l}{|\sum_{l=1}^{\mathcal{L}}\beta_l^2\hat{W}_l|}, \tag{55}$$

which is the quantity retained to check the numerical solutions.

5.4 Major remarks

Again, some interesting properties follow from (49). As for the bipolytope case, each leayer is strongly influenced by the remaining, $\mathcal{L}-1$ ones. Even in the case $\mathcal{L}=3$, it seems complicated to analyze the role of the polytropic indices, mass density jumps and rotational discontinuities on each component, and subsequently on the global structure. In

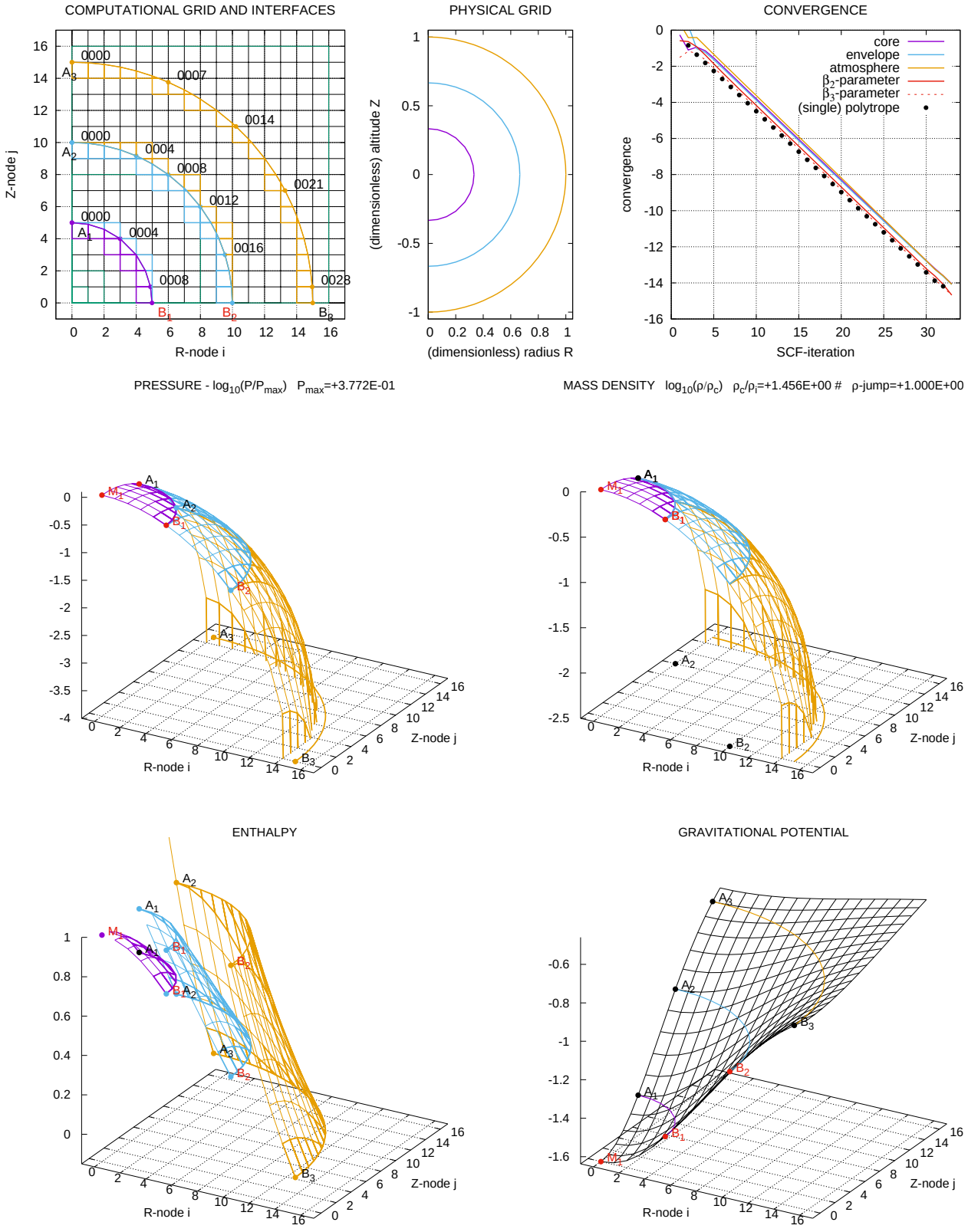

Figure 14. Same legend and same conditions as for Fig. 2, but for the non-rotating tripolytrope with $n_1 = n_2 = n_3 = 1.5$ and $q_1 = q_2 = \frac{1}{3}$. Output quantities obtained for $\ell = 7$ are listed in Tab. C1.

fact, we can easily derive the analog of (17), (16) and (18) by considering two adjacent layers. For any point at $\Gamma_{l'}$, we get (still for $l \in [2, \mathcal{L}-1]$, $l' = l-1$, $n_l > 0$ assumed for all layers)

$$\left\{\begin{array}{l} \frac{1+n_l}{1+n_{l'}} \frac{C_{1l'}}{C_{1l}} \beta_l^{\frac{1}{n_l}-1} \beta_{l'}^{1-\frac{1}{n_l}} \alpha_l(\Gamma_{l'})^{1+\frac{1}{n_l}} \\ \quad -\hat{H}_{l'}(\Gamma_{l'})^{\frac{n_{l'}}{n_l}-1} = 0, \\ \\ \frac{1+n_l}{1+n_{l'}} \beta_{l'}^2 C_{1l'} \hat{H}_{l'}(\Gamma_{l'})^{1+n_{l'}} \\ \quad -\beta_l^2 C_{1l} \hat{H}_l(\Gamma_{l'})^{1+n_l} = 0, \\ \\ \beta_{l'} C_{1l'} \hat{H}_{l'}(\Gamma_{l'}) \left[1 - \bar{\alpha}_l(\Gamma_{l'})\right] \\ \quad +\beta_{l'} C_{2l'} \left[\hat{\Phi}_{l'}(\Gamma_{l'}) - \frac{1}{\omega_l} \hat{\Phi}_l(\Gamma_{l'})\right] \\ \quad +\beta_l C_{3l} - \beta_{l'} C_{3l'} = 0. \end{array}\right. \tag{56}$$

Helped with the discussion in Sect. 2.5, we come to the conclusions that, for two adjacent layers :

- if the polytropic indices are equal, then the mass density jump is uniform along the common interface,
- if the mass density jump varies along the common interface, then the enthalpy is not uniform either
- there is no rotational discontinuity without mass density jump, unless $\omega_l \hat{\Phi}_{l'} - \hat{\Phi}_l = 0$ at the common interface,
- a non-uniform mass density jump along the common interface is compatible with a rotational discontinuity.

5.5 The procedure in details

The solutions can efficiently be captured through the SCF-method. The principle is the same as for the bipolytrope. We proceed from the outermost layer to the deepest one. At the two references points $\mathrm{A}_{\mathcal{L}}$ and $\mathrm{B}_{\mathcal{L}}$ located respetively at the pole and at the equator of $\Gamma_{\mathcal{L}}$ (see Fig. 13), the enthalpy is zero, and we use the normalisation condition at $\mathrm{M}_{\mathcal{L}}$=$\mathrm{A}_{\mathcal{L}-1}$ of $\Gamma_{\mathcal{L}-1}$, i.e. $\hat{H}_{\mathcal{L}}(\mathrm{A}_{\mathcal{L}-1}) = 1$. From these 3 values, the three quantities $\beta_{\mathcal{L}} C_{1\mathcal{L}}$, $\beta_{\mathcal{L}} C_{2\mathcal{L}}$ and $\beta_{\mathcal{L}} C_{3\mathcal{L}}$ for the layer $\mathcal{L}$ are fully determined (see Sec. 3.1). We then go the next layer. From the scaling relationship (45) and the equation for pressure balance (46), we first deduce $\beta_{\mathcal{L}-1} C_{2\mathcal{L}-1}$ and $\beta_{\mathcal{L}-1} C_{3\mathcal{L}-1}$. The normalisation of $\hat{H}_{\mathcal{L}-1}$ at $\mathrm{M}_{\mathcal{L}-1}$=$\mathrm{A}_{\mathcal{L}-2}$, i.e. $\hat{H}_{\mathcal{L}-1}(\mathrm{A}_{\mathcal{L}-2}) = 1$, yields the third quantity $\beta_{\mathcal{L}-1} C_{1\mathcal{L}-1}$. This is repeated down to layer 2. Once the core is reached, we proceed in the same way to get C_{21} and C_{31}. The normalisation of enthalpy of the core is obtained by searching the point M_1 where $\hat{H}_1$ is maximum, which yields C_{11} (M_1 does not necessarily stands on the polar axis). Given all these values, all the enthlapies $\hat{H}_1$, $\hat{H}_2$, …, $\hat{H}_{\mathcal{L}}$ can be determined in space, namely

$$\begin{aligned} \hat{H}_l(\vec{r}) &= \frac{1}{C_{1l}} \left\{ C_{3l} - \left[\hat{\Psi}_{l,\mathrm{tot}}(\vec{r}) + C_{2l} \hat{\Phi}_l(\vec{r}) \right] \right\}, \\ &= \frac{1}{\beta_l C_{1l}} \left\{ \beta_l C_{3l} - \left[\hat{\Psi}_{1,\mathrm{tot}}(\vec{r}) + \beta_l C_{2l} \hat{\Phi}_l(\vec{r}) \right] \right\}. \end{aligned} \tag{57}$$

Then comes the update of the β_l-parameters, which is performed from the mass-density jump conditions. The details of the procedure are summarized in Tab. A2. At the beginning, the enthalpies for the core, and layers above and the contrast parameters, respectively $\hat{H}_1(0)$, $\hat{H}_2(0)$, …, $\hat{H}_{\mathcal{L}}(0)$ and $\beta_{l\in[2,\mathcal{L}]}(0)$ are guessed (again, we use paraboloids that fulfill the normalisation and jump conditions). Theses quantities, together with the $3\mathcal{L}$ constants and the $\mathcal{L}$ interfaces evolve during the cycle. It is stopped when all quantities are stabilized. In practical, the convergence is decided from the variations of the constants in each layer from one step to the other; see (27).

5.6 First example : a false tripolytrope

The first example is a false tripolytrope which consists in 3 non-rotating layers having the same polytropic index, without any mass density jump and rotational discontinuity at the interfaces. We mostly use the same input parameters as in Tab. B1. The core, the envelope and the "atmosphere" (layer $l = 3$) have the same polar extension, i.e. $q_1 = q_2 = \frac{1}{3}$. The input parameters and output values are listed in Tab. C1. The structure at equilibrium is shown in Fig. 14. There is no great change with respect to the case $\mathcal{L} = 2$, in particular on the precision. We notice the excellent agreement between this 3-layer configuration and the single polytrope. The impact of q_1 and q_2 on the results is weak, again, as checked.

5.7 Yet another example of degenerate configurations

As mentioned in Sec. 4.7, two different configurations can share the same shape (equatorial size and the same axis ratio of the outermost layer), mass and surface velocity, making them indistinguishable from each other for an observer, at order zero at least. For a $\mathcal{L}$-layer star, the total mass and the square of the rotation velocity at the equator are respectively given by $M_{\mathrm{tot.}} = \hat{M}_{\mathrm{tot.}} \times \rho_{10} L^3$ and $C_{2\mathcal{L}} \times G \rho_{0\mathcal{L}} L^2$. We can then define the analog of (35), namely

$$\frac{C_{2\mathcal{L}} \beta_{\mathcal{L}}}{\hat{M}_{\mathrm{tot.}}(\mathcal{L})} \equiv \Xi_{\mathcal{L}}. \tag{58}$$

So, two systems having respectively $\mathcal{L}$ and $\mathcal{L}'$ layers are, on this basis, degenerate as soon as $\Xi_{\mathcal{L}} = \Xi_{\mathcal{L}'}$. The ratio of the central densities is then given by the inverse of the dimensionless mass ratio, i.e.

$$\frac{\rho_{0\mathcal{L}}}{\rho_{0\mathcal{L}'}} = \frac{\hat{M}_{\mathrm{tot.}}(\mathcal{L}')}{\hat{M}_{\mathrm{tot.}}(\mathcal{L})}. \tag{59}$$

We give in Tab. C2 the data (input and output) corresponding to a 3-layer system having the same degenaracy parameter as the 2-layer configuration discussed above (see Sec. 4.7). Figure 15 shows the interfaces.

6 SUMMARY

Diagnostics tools capable of modelling and understanding the internal structure of self-gravitating systems that are known to possess a significant stratification are of fundamental importance. In this article, we have presented a method to model layered spheroids assuming axial and equatorial symmetries, cylindral symmetry for the rotation profiles and a polytropic equation-of-state. In a more innovative way, we have considered the simultaneous occurence of a mass density jump and a rotational discontinuity at each interface (Maeder 1971; Kiuchi et al. 2010; Kadam et al. 2016).

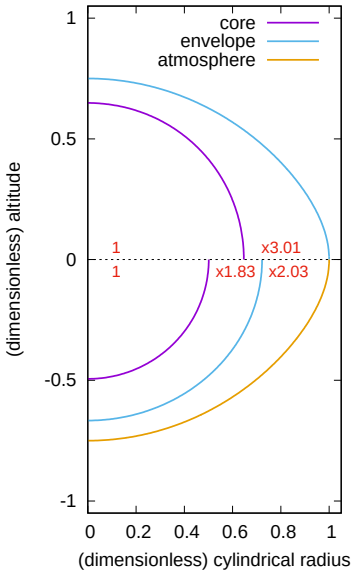

Figure 15. Interfaces for two different configurations sharing the same size, surface velocity and total mass (and same degeneracy parameter Ξ): a 2-layers (*top*) and 3-layers (*bottom*). Input parameters are from Tabs. B3 and B9, respectively. The shape of the envelope is almost unchanged, in constrat to the core. Labels (*red*) correspond to the rotation rate of each layer relative to the core, i.e. $\frac{1}{\sqrt{\omega_l}}$.

Clearly, this open onto new exciting horizons in terms of permitted configurations, in particular to investigate the interior of stars and planets (e.g. Helled 2018).

The full equation set consisting of the Bernoulli equation, the Poisson equation and the equation for the pressure balance for each layer has been derived in the case of a $\mathcal{L}$-layer system. A few critical points have been considered with caution, namely : i) the localization of the interfaces, and subsequently the identification of all the layers on the computational grid, from a boundary detection method, ii) the computation of the gravitational potential of each layer separately (the presence of mass density jumps is problematic in determining directy the total potential), and iii) the use of mass density scaling specific to each layer. A procedure based on the Self-Consistent Field method enabling to capture the numerical, self-normalized solutions for the mass density field, pressure, etc. has been discussed in details. Several tests and examples proving the reliability of the method have been proposed. The main results the analysis are the following:

- for a $\mathcal{L}$-layer spheroid, there are $4\mathcal{L}-2$ input parameters. A possible set is : the polytropic indices $n_{l\in[1,\mathcal{L}]}$, the polar extentions $q_{l\in[2,\mathcal{L}]}$, the axis ratio of the outemoster layer $e_{\mathcal{L}}$, the mass density jumps $\alpha_{l\in[2,\mathcal{L}]}$, the rotational discontinuities $\omega_{l\in[2,\mathcal{L}]}$.
- the method is robust in the sense that the solution is reliable whatever the relative size of the layers. Imprecisions, however, may arise as soon as a layer is not enough resolved, numerically (i.e. $q_l \to 0$).
- the global equilibrum is very sensitive i) to the magnitude of the mass density jump, and ii) to the rotational discontinuity. In the presence of rotation, all the layer are not affected with the same amplitude.
- an increase in the mass density jump decreases the mass of the system (for a given central mass density).
- when the core rotates faster than the envelope (or for to adjacent layers l' and $l = l' + 1$), the oblateness of the core increases, the total mass tends to be larger when the polytropic index of the envelope is larger than the polytropic index of the core (for a given central mass density), while the shape are weakly affected in comparison.
- there is a relative decoupling between the shape of the deepest layer and the shape of the outermost one. Actually, the impact of rotation is different for each layer. Within reasonable limits, the core remains very close to spherical if the surface layer rotates faster. Conversely, a core rotating faster than the surface layer flattens while the shape of surface layer remains wealy impacted.
- there is a tight connection between the rotational discontinuity and the mass density jump. The presence of a mass density jump does not imply a rotational discontinuity. The reverse proposition is weaker in the sense that a mass density jump is necessary to the presence of rotational discontinuity.
- if the polytropic indices of two adjacent layers are equal, then the mass density jump is uniform along the common interface.
- a non-uniform mass density jump along the common interface is compatible with a rotational discontinuity.
- two multilayer configurations having the same degeneracy parameter Ξ have the same global observables, i.e. size, oblateness, surface velocity field and total mass, in spite of different structure; see (59).

It would be interesting to perform a full exploration of the parameter space, in order to extract more precise trends. This is a complicated and tedious task, even for the 2-layer case since there are already 6 input parameters.

ACKNOWLEDGEMENTS

We would like to dedicate this paper to our colleague and friend Franck Hersant who sadly passed away on 2020, March. Until recently, he took an active part to the project on rotating polytropes started in 2010.

REFERENCES

Adams E. R., Seager S., Elkins-Tanton L., 2008, ApJ, 673, 1160
Amendt P., Lanza A., Abramowicz M. A., 1989, ApJ, 343, 437
Ball W. H., Tout C. A., Żytkow A. N., 2012, MNRAS, 421, 2713
Baraffe I., Chabrier G., Fortney J., Sotin C., 2014, in Beuther H., Klessen R. S., Dullemond C. P., Henning T., eds, Protostars and Planets VI Planetary Internal Structures. p. 763
Beech M., 1986, A&A, 156, 391
Brooks J., Schwab J., Bildsten L., Quataert E., Paxton B., 2017, ApJ, 834, L9
Broomhall A. M., Chatterjee P., Howe R., Norton A. A., Thompson M. J., 2014, Space Sci. Rev., 186, 191
Caimmi R., 2016, ArXiv e-prints
Chandrasekhar S., 1969, Ellipsoidal figures of equilibrium. Yale Univ. Press
Chiang E. I., Goldreich P., 1997, ApJ, 490, 368

Christensen-Dalsgaard J., 2020, arXiv e-prints, p. arXiv:2007.06488
Curry C. L., McKee C. F., 2000, ApJ, 528, 734
D'Alessio P., Cantö J., Calvet N., Lizano S., 1998, ApJ, 500, 411
Eggenberger P., 2013, in European Physical Journal Web of Conferences Vol. 43 of European Physical Journal Web of Conferences, Rotation and stellar evolution. p. 01005
Eggleton P. P., Faulkner J., Cannon R. C., 1998, MNRAS, 298, 831
Fujisawa K., 2015, MNRAS, 454, 3060
Fujisawa K., Eriguchi Y., 2014, MNRAS, 438, L61
Fujisawa K., Eriguchi Y., 2015, PASJ, 67, 53
Gholipour M., 2018, ApJ, 864, 108
Hachisu I., 1986, ApJS, 61, 479
Hekker S., Christensen-Dalsgaard J., 2017, A&ARv, 25, 1
Helled R., 2018, The Interiors of Jupiter and Saturn. p. 175
Helled R., Guillot T., 2018, Internal Structure of Giant and Icy Planets: Importance of Heavy Elements and Mixing. p. 44
Horedt G. P., ed. 2004, Polytropes - Applications in Astrophysics and Related Fields Vol. 306 of Astrophysics and Space Science Library
Horedt G. P., Hubbard W. B., 1983a, Moon and Planets, 29, 229
Horedt G. P., Hubbard W. B., 1983b, Moon and Planets, 29, 229
Huré J.-M., 2000, A&A, 358, 378
Huré J.-M., Hersant F., 2017, MNRAS, 464, 4761
Huré J.-M., Hersant F., Nasello G., 2018, MNRAS, 475, 63
Jackson S., MacGregor K. B., Skumanich A., 2005, ApJS, 156, 245
Kadam K., Motl P. M., Frank J., Clayton G. C., Marcello D. C., 2016, MNRAS, 462, 2237
Kiuchi K., Nagakura H., Yamada S., 2010, ApJ, 717, 666
Kong D., Liao X., Zhang K., Schubert G., 2014, MNRAS, 445, L26
Kong D., Zhang K., Schubert G., 2010, Journal of Geophysical Research (Planets), 115, E12003
Kong D., Zhang K., Schubert G., 2016, ApJ, 826, 127
Kramm U., Nettelmann N., Redmer R., Stevenson D. J., 2011, A&A, 528, A18
Kubo-Oka T., Nakazawa K., 1997, A&A, 324, 785
Léger A., Selsis F., Sotin C., Guillot T., Despois D., Mawet D., Ollivier M., Labèque A., Valette C., Brachet F., Chazelas B., Lammer H., 2004, Icarus, 169, 499
Lunine J. I., Stevenson D. J., Yung Y. L., 1983, Science, 222, 1229
MacGregor K. B., Jackson S., Skumanich A., Metcalfe T. S., 2007, ApJ, 663, 560
Maeder A., 1971, A&A, 14, 351
Maeder A., 2009, Physics, Formation and Evolution of Rotating Stars
Milne E. A., 1936a, MNRAS, 96, 207
Milne E. A., 1936b, MNRAS, 96, 184
Mousis O., Deleuil M., Aguichine A., Marcq E., Naar J., Aguirre L. A., Brugger B., Gonçalves T., 2020, ApJ, 896, L22
Odrzywołek A., 2003, MNRAS, 345, 497
Ostriker J. P., Mark J. W.-K., 1968, ApJ, 151, 1075
Remus F., Mathis S., Zahn J. P., Lainey V., 2012, A&A, 541, A165
Schönberg M., Chandrasekhar S., 1942, ApJ, 96, 161
Snellen I. A. G., Brandl B. R., de Kok R. J., Brogi M., Birkby J., Schwarz H., 2014, Nature, 509, 63
Spiegel E. A., Zahn J. P., 1992, A&A, 265, 106
Stancliffe R. J., Chieffi A., Lattanzio J. C., Church R. P., 2009, Publ. Astron. Soc. Australia, 26, 203
Toci C., Galli D., 2015, MNRAS, 446, 2110
Tricarico P., 2014, ApJ, 782, 99
Trimble V., Aschwanden M., 1999, PASP, 111, 385
Valencia D., O'Connell R. J., Sasselov D., 2006, Icarus, 181, 545
Viala Y., Bel N., Bonazzola S., 1978, A&A, 65, 393
Vinyoles N., Serenelli A. M., Villante F. L., Basu S., Bergström J., Gonzalez-Garcia M. C., Maltoni M., Peña-Garay C., Song N., 2017, ApJ, 835, 202
Weppner S. P., McKelvey J. P., Thielen K. D., Zielinski A. K., 2015, MNRAS, 452, 1375
Zahn J. P., 1992, A&A, 265, 115

	substep	operation
preliminaries	(interfaces, domains and Poisson equation)	
		β_2 and $\hat{H}_l(t)$ assumed to be known (starting guess, or from previous step $t-1$), for $l=1,2$
	1*	the interfaces Γ_l are determined, for $l=1,2$
	1	the mass density $\hat{\rho}_l$ is computed for each layer $l=1,2$ from $\hat{H}_l$
	2*	the potential $\hat{\Psi}_l$ is computed from the Poisson equation, i.e. (14c) and (14f), for $l=1,2$
	2	the potential $\hat{\Psi}_{l,\rm tot}$ is computed for the actual β_2 parameter, for $l=1,2$; see (10)
envelope	1	$\beta_2 C_{22}$ and $\beta_2 C_{32}$ are obtained from $\hat{\Psi}_{2,\rm tot}(\mathrm{A}_2)$ and $\hat{\Psi}_{2,\rm tot}(\mathrm{B}_2)$ by solving Eqs.(22a) and (22b),
	2	$\beta_2 C_{12}$ is obtained from (22c) and (22d), with $\mathrm{M}_2 = \mathrm{A}_1$
	3	$\beta_2 C_{12}\hat{H}_2(\vec{r})$ is computed from the Bernoulli equation, i.e. (23)
	4	the new enthalpy $\hat{H}_2(t+1) \leftarrow \hat{H}_2$ is deduced from substeps 2 et 3
		$\hat{H}_2(\mathrm{A}_1)$ must be unity (normalisation condition)
core	1	C_{21} is deduced from (24a)
	2	C_{31} is computed at A_1 from (24b)
	3	$C_{11}\hat{H}_1(\vec{r})$ is computed from the Bernoulli equation, i.e. (25)
	4	C_{11} is deduced from the normalisation condition, i.e. $\exists\ \mathrm{M}_1$ such that $C_{1l}\hat{H}_1(\ \mathrm{M}_1)$ is a maximum
	5	the new enthalpy $\hat{H}_1(t+1) \leftarrow \hat{H}_1$ is deduced from substeps 3 and 4,
		$\hat{H}_1(\mathrm{M}_1)$ should be unity (normalisation condition)
final stage	(release of new density contrast, mass-density jump and tests of convergence)	
	1	β_2 is found from (26) at point A_1
	2	if $\omega_1 \neq 1$, $\alpha_2(\Gamma_1)$ is computed from (17)
	3	if convergence is not achieved, then $t \leftarrow t+1$ and one goes for another iteration
		otherwise, output quantities can be determined (mass, volume, energies, Virial parameter, etc.)

Table A1. Main steps of one iteration of the SCF-cycle for a 2-layer system. The algorithm proceeds from the envelope to the core. The three reference points A_1, B_1 and A_2 are fixed (see Fig. 1); *optional.

APPENDIX A: DETAILS OF THE SCF PROCEDURES

	substep	operation
preliminaries	interfaces, layers and Poisson equation	
		β_l and $\hat{H}_l(t)$ assumed to be known (starting guess, or from previous step $t-1$), for $l=1,2,\ldots,\mathcal{L}$, $(\beta_1=1)$
	1^*	the interfaces Γ_l are determined for $l=1,\ldots,\mathcal{L}-1$
	1	the mass density $\hat{\rho}_l$ is computed for each layer $l=1,2,\ldots,\mathcal{L}$ from $\hat{H}_l$
	2^*	the potential $\hat{\Psi}_l$ is computed from the Poisson equation, see (49) for $l=1,2,\ldots,\mathcal{L}$
	2	the potential $\hat{\Psi}_{1,\rm tot}$ is computed for the actual set of β_l-parameters; $\beta_l\hat{\Psi}_{l,\rm tot}=\hat{\Psi}_{1,\rm tot}$
top layer	1	values for $\beta_{\mathcal{L}}C_{2\mathcal{L}}$ and $\beta_{\mathcal{L}}C_{3\mathcal{L}}$ are obtained from $\hat{\Psi}_{\mathcal{L}}(\mathrm{A}_{\mathcal{L}})$ and $\hat{\Psi}_{\mathcal{L}}(\mathrm{B}_{\mathcal{L}})$,
$l=\mathcal{L}$	2	$\beta_l C_{1\mathcal{L}}$ is obtained from the normalisation condition, i.e. $\hat{H}_l(\mathrm{A}_{\mathcal{L}-1})=1$
	3	$\beta_l C_{1\mathcal{L}}\hat{H}_{\mathcal{L}}$ is computed from the Bernoulli equation for the top layer, see (57)
	4	the new enthalpy $\hat{H}_{\mathcal{L}}(t+1)\leftarrow\hat{H}_{\mathcal{L}}$ is deduced from substeps 2 and 3,
		$\hat{H}_{\mathcal{L}}(\mathrm{A}_{\mathcal{L}-1})$ must be unity (normalisation condition)
	...	
intermediate layer	1	$\beta_l C_{2l}$ is deduced from (45)
$\mathcal{L}-l+1$	2	$\beta_l C_{3l}$ is computed from (38a) and (46)
$l=2,\ldots,\mathcal{L}-1$	3	$\beta_l C_{1l}\hat{H}_l$ is computed from the Bernoulli equation, see (57)
	4	$\beta_l C_{1l}$ is deduced from the normalisation condition at A_{l-1}
	5	the new enthalpy $\hat{H}_l(t+1)\leftarrow\hat{H}_l$ is deduced from substeps 3 and 4,
		$\hat{H}_l(\mathrm{A}_{l-1})$ must be unity (normalisation condition)
	...	
deepest layer	1	$\beta_1 C_{21}$ is deduced from (45)
(core) $l=1$	2	$\beta_1 C_{31}$ is computed from (38a) and (46)
	3	$\beta_l C_{11}\hat{H}_1$ is computed from the Bernoulli equation, see (57)
	4	$\beta_l C_{1l}$ is deduced from the normalisation condition, i.e. $\exists\ \mathrm{M}_1$ such that $\beta_l C_{1l}\hat{H}_1$ is a maximum
	5	the new enthalpy $\hat{H}_1(t+1)\leftarrow\hat{H}_1$ is deduced from substeps 3 and 4,
		$\hat{H}_1(\mathrm{M}_1)$ must be unity (normalisation condition)
	final stage, release of new β_l coefficients from the jump conditions	
final stage	(release of new density contrast, mass-density jump and tests of convergence)	
		if convergence is not achieved, then $t\leftarrow t+1$ and go for another iteration, step 0

Table A2. Main steps of one iteration of the SCF-cycle for a $\mathcal{L}$-layer system. The algorithm proceeds from the outermost layer to the deepest one. The three reference points A_l for $l=[1,\mathcal{L}]$, and $\mathrm{B}_{\mathcal{L}}$ are fixed.*optional

APPENDIX B: BIPOLYTROPES

		polytrope	Hachisu	false bipolytrope ($\mathcal{L}=2$)		
		($l=\mathcal{L}=1$)	(1986)	core ($l=1$)	env. ($l=2$)	total
number of node per direction	N	129	>128			129
polytropic index of the core	n_l	+1.5000E+00	+1.5000E+00	+1.5000E+00	+1.5000E+00	
altitude of point A_l	$\hat{z}(\mathrm{A}_l)$	+1.0000E+00	+1.0000E+00	+6.6667E-01	+1.0000E+00	
polar extension of the core	q_l	+1.0000E+00	+1.0000E+00	+6.6667E-01	+3.3333E-01	
mass density jump	$\alpha_l(\mathrm{A}_l)$				+1.0000E+00	
rotational discontinuity	ω_l				+1.0000E+00	
	SCF-iterations	29				29
core enthalpy at A_l	$\hat{H}_l(\mathrm{A}_l)$	+0.0000E+00		+3.3798E-01	+1.0000E+00	
contrast paremeter	β_l			+1.0000E+00	+1.9649E-01	
number of nodes for the interface	nodes Γ_l	251		167	251	
volume	$\hat{V}_l$	+4.1883E+00	+4.17E+00	+1.2407E+00	+2.9482E+00	+4.1890E+00
mass	$\hat{M}_l$	+6.9919E-01	+6.99E-01	+5.3071E-01	+8.5843E-01	+6.9938E-01
first constant	C_{1l}	+9.4134E-01		+9.4136E-01	+1.6192E+00	
second constant	C_{2l}	+3.3196E-06		-1.2064E-04	-6.1399E-04	
third constant	C_{3l}	-6.9920E-01		-6.9934E-01	-3.5592E+00	
angular momentum	J_l	+2.6064E-04	+0.00E+00	+8.3701E-04	+3.7415E-03	+1.5722E-03
kinetic energy	$\hat{T}_l$	+2.3744E-07	+0.00E+00	-4.5967E-06	-1.0457E-04	-8.6340E-06
gravitational energy	$\hat{W}_l$	-4.1904E-01	-4.19E-01	-3.4269E-01	-1.9815E+00	-4.1919E-01
internal energy	$\hat{U}_l$	+4.1906E-01	+4.19E-01	+3.7708E-01	+1.0891E+00	+4.1913E-01
Virial parameter	VP	+1.5278E-05				-7.8934E-05
normalized Virial par.	VT	+3.6460E-05	< +1.E-03			-1.8830E-04

Table B1. Input (*top*) and output (*bottom*) quantities for the false non-rotating bipolytrope in the conditions of Fig. 2, but for $\ell = 7$. The results obtained in the same conditions for the polytrope are given in the second column.

bipolytrope $\mathcal{L}=2$	core ($l=1$)	envelope ($l=2$)	total
N			129
n_l	+1.5000E+00	+1.5000E+00	
$z(A_l)$	+6.6667E-01	+1.0000E+00	
q_l	+6.6667E-01	+3.3333E-01	
$\alpha_l(\mathrm{A}_l)$		+4.0000E+00	
ω_l		+1.0000E+00	
SCF-iterations			29
$\hat{H}_l(\mathrm{A}_l)$	+6.7475E-02	+1.0000E+00	
$\beta_l^\dagger$	+1.0000E+00	+4.3818E-03	
nodes Γ_l	167	251	
$\hat{V}_l$	+1.2407E+00	+2.9485E+00	+4.1892E+00
$\hat{M}_l$	+2.6666E-01	+7.9958E-01	+2.7017E-01
C_{1l}	+4.9808E-01	+3.0679E+01	
C_{2l}	+5.3597E-06	+1.2232E-03	
C_{3l}	-3.7099E-01	-6.1657E+01	
J_l	+6.5682E-05	+7.2936E-04	+6.8878E-05
$\hat{T}_l$	+7.6030E-08	+1.9268E-04	+7.9730E-08
$\hat{W}_l$	-8.4990E-02	-3.2467E+01	-8.5614E-02
$\hat{U}_l$	+8.5263E-02	+1.8763E+01	+8.5623E-02
VP			+9.3160E-06
VT			+1.0881E-04

Table B2. Input (*top*) and output (*bottom*) quantities for the static bipolytrope with mass density jump $\alpha_2 = 4$ (see Fig. 5). See Tab. B1 for the meaning of the variables.

bipolytrope $\mathcal{L}=2$	core ($l=1$)	envelope ($l=2$)	total
N			129
n_l	+1.5000E+00	+1.5000E+00	
$z(A_l)$	+5.0000E-01	+7.5000E-01	
q_l	+6.6667E-01	+3.3333E-01	
$\alpha_l(\mathrm{A}_l)$		+4.0000E+00	
ω_l		+1.0000E+00	
SCF-iterations			41
$\hat{H}_l(\mathrm{A}_l)$	+7.0193E-02	+1.0000E+00	
$\beta_l^\dagger$	+1.0000E+00	+4.6493E-03	
nodes Γ_l	151	251	
$\hat{V}_l$	+6.0218E-01	+2.3359E+00	+2.9381E+00
$\hat{M}_l$	+1.2796E-01	+4.8909E-01	+1.3024E-01
C_{1l}	+2.9748E-01	+1.7965E+01	
C_{2l}	+8.3597E-02	+1.7981E+01	
C_{3l}	-2.3498E-01	-3.7067E+01	
J_l	+2.5264E-03	+4.2020E-02	+2.7218E-03
$\hat{T}_l$	+3.6523E-04	+1.3066E+00	+3.9348E-04
$\hat{W}_l$	-2.4972E-02	-1.1065E+01	-2.5212E-02
$\hat{U}_l$	+2.4289E-02	+6.3688E+00	+2.4427E-02
VP			+2.1788E-06
VT			+8.6419E-05

Table B3. Input (*top*) and output (*bottom*) quantities for the rigidly rotating bipolytrope with a mass density jump $\alpha_2 = 4$ and $e_2 = 0.75$ as the axis ratio (see Fig. 6). See Tab. B1 for the meaning of the variables.

bipolytrope $\mathcal{L}=2$	core ($l=1$)	envelope ($l=2$)	total
N			129
n_l	+1.5000E+00	+1.5000E+00	
$z(A_l)$	+4.3927E-01	+6.5890E-01	
q_l	+6.6667E-01	+3.3333E-01	
$\alpha_l(\mathrm{A}_l)$		+4.0000E+00	
ω_l		+1.0000E+00	
SCF-iterations			42
$\hat{H}_l(\mathrm{A}_l)$	+7.0399E-02	+1.0000E+00	
$\beta_l^\dagger$	+1.0000E+00	+4.6697E-03	
nodes Γ_l	143	251	
$\hat{V}_l$	+4.1276E-01	+1.8320E+00	+2.2448E+00
$\hat{M}_l$	+8.7627E-02	+3.4528E-01	+8.9239E-02
C_{1l}	+2.3065E-01	+1.3909E+01	
C_{2l}	+8.9802E-02	+1.9231E+01	
C_{3l}	-1.8303E-01	-2.8763E+01	
J_l	+1.3982E-03	+2.4624E-02	+1.5131E-03
$\hat{T}_l$	+2.0949E-04	+7.9009E-01	+2.2672E-04
$\hat{W}_l$	-1.3285E-02	-6.0071E+00	-1.3416E-02
$\hat{U}_l$	+1.2889E-02	+3.4478E+00	+1.2964E-02
VP			+1.9585E-06
VT			+1.4599E-04

Table B4. Input (*top*) and output (*bottom*) quantities for the rotating bipolytrope with mass density jump $\alpha_2 = 4$ at critical rotation (see Fig. 7). See Tab. B1 for the meaning of the variables.

bipolytrope $\mathcal{L}=2$	core ($l=1$)	envelope ($l=2$)	total
N			129
n_l	+1.5000E+00	+1.5000E+00	
$z(A_l)$	+5.0000E-01	+7.5000E-01	
q_l	+6.6667E-01	+3.3333E-01	
$\alpha_l(\mathrm{A}_l)$		+4.0000E+00	
ω_l		+2.0000E+00	
SCF-iterations			46
$\hat{H}_l(\mathrm{A}_l)$	+7.3827E-02	+1.0000E+00	
$\beta_l^\dagger$	+1.0000E+00	+5.0149E-03	
nodes Γ_l	161	251	
$\hat{V}_l$	+7.7608E-01	+2.1953E+00	+2.9714E+00
$\hat{M}_l$	+1.5341E-01	+3.9258E-01	+1.5538E-01
C_{1l}	+3.2191E-01	+1.8956E+01	
C_{2l}	+1.8853E-01	+1.8797E+01	
C_{3l}	-2.7469E-01	-4.0557E+01	
J_l	+5.5445E-03	+5.4590E-02	+5.8183E-03
$\hat{T}_l$	+1.2037E-03	+1.1816E+00	+1.2334E-03
$\hat{W}_l$	-3.3411E-02	-9.3243E+00	-3.3645E-02
$\hat{U}_l$	+3.1063E-02	+4.6898E+00	+3.1181E-02
VP			+2.3341E-06
VT			+6.9375E-05

Table B5. Input (*top*) and output (*bottom*) quantities for the rotating bipolytrope with axis ratio $e_2 = 0.75$, mass density jump $\alpha_2 = 4$ and rotational discontinuity $\omega_2 = 2$ (see Fig. 8). See Tab. B1 for the meaning of the variables.

bipolytrope $\mathcal{L}=2$	core ($l=1$)	envelope ($l=2$)	total
N			129
n_l	+1.0000E+00	+2.0000E+00	
$z(A_l)$	+5.0000E-01	+7.5000E-01	
q_l	+6.6667E-01	+3.3333E-01	
$\alpha_l(\mathrm{A}_l)$		+4.0000E+00	
ω_l		+2.0000E+00	
SCF-iterations			46
$\hat{H}_l(\mathrm{A}_l)$	+6.4945E-02	+1.0000E+00	
$\beta_l^\dagger$	+1.0000E+00	+1.6236E-02	
nodes Γ_l	164	251	
$\hat{V}_l$	+8.4114E-01	+2.1654E+00	+3.0065E+00
$\hat{M}_l$	+2.8134E-01	+2.8188E-01	+2.8591E-01
C_{1l}	+4.2501E-01	+1.0200E+01	
C_{2l}	+3.2386E-01	+9.9732E+00	
C_{3l}	-5.0766E-01	-2.2767E+01	
J_l	+1.7641E-02	+4.9628E-02	+1.8446E-02
$\hat{T}_l$	+5.0195E-03	+4.3486E-01	+5.1342E-03
$\hat{W}_l$	-9.8506E-02	-3.8160E+00	-9.9512E-02
$\hat{U}_l$	+8.8811E-02	+1.6494E+00	+8.9246E-02
VP			+2.3311E-06
VT			+2.3425E-05

Table B6. Input (*top*) and output (*bottom*) quantities for the rotating bipolytrope with axis ratio $e_2 = 0.75$, mass density jump $\alpha_2 = 4$ and rotational discontinuity $\omega_2 = 2$ when $n_1 < n_2$ (see Figs. 8 and 9). See Tab. B1 for the meaning of the variables.

bipolytrope $\mathcal{L}=2$	core ($l=1$)	envelope ($l=2$)	total
N			129
n_l	+2.0000E+00	+1.0000E+00	
$z(A_l)$	+5.0000E-01	+7.5000E-01	
q_l	+6.6667E-01	+3.3333E-01	
$\alpha_l(\mathrm{A}_l)$		+4.0000E+00	
ω_l		+2.0000E+00	
SCF-iterations			47
$\hat{H}_l(\mathrm{A}_l)$	+8.5709E-02	+1.0000E+00	
$\beta_l^\dagger$	+1.0000E+00	+1.8365E-03	
nodes Γ_l	159	251	
$\hat{V}_l$	+7.4083E-01	+2.2098E+00	+2.9506E+00
$\hat{M}_l$	+8.7209E-02	+5.9537E-01	+8.8302E-02
C_{1l}	+2.4351E-01	+3.0305E+01	
C_{2l}	+1.1095E-01	+3.0207E+01	
C_{3l}	-1.5115E-01	-6.3360E+01	
J_l	+1.8902E-03	+6.8595E-02	+2.0162E-03
$\hat{T}_l$	+3.1481E-04	+3.1103E+00	+3.2530E-04
$\hat{W}_l$	-1.2248E-02	-2.1469E+01	-1.2320E-02
$\hat{U}_l$	+1.1629E-02	+1.2490E+01	+1.1671E-02
VP			+1.4776E-06
VT			+1.1993E-04

Table B7. Input (*top*) and output (*bottom*) quantities for the rotating bipolytrope with axis ratio $e_2 = 0.75$, mass density jump $\alpha_2 = 4$ and rotational discontinuity $\omega_2 = 2$ when $n_1 > n_2$ (see Figs. 8 and 9). See Tab. B1 for the meaning of the variables.

bipolytrope $\mathcal{L}=2$	core ($l=1$)	envelope ($l=2$)	total
N			129
n_l	+3.0000E+00	+3.0000E+00	
$z(A_l)$	+5.0000E-01	+6.0000E-01	
q_l	+8.3333E-01	+1.6667E-01	
$\alpha_l(\mathrm{A}_l)$		+1.6660E+00	
ω_l		+5.7337E-01	
SCF-iterations			66
$\hat{H}_l(\mathrm{A}_l)$	+3.8157E-02	+1.0000E+00	
$\beta_l^\dagger$	+1.0000E+00	+3.3346E-05	
nodes Γ_l	153	267	
$\hat{V}_l$	+5.1975E-01	+2.7533E+00	+3.2730E+00
$\hat{M}_l$	+2.0306E-02	+3.4159E+00	+2.0419E-02
C_{1l}	+1.0401E-01	+1.9828E+02	
C_{2l}	-3.3110E-03	-1.7317E+02	
C_{3l}	-2.8792E-02	-6.1403E+02	
J_l	+3.7686E-05	+5.3134E-02	+3.9457E-05
$\hat{T}_l$	-1.0842E-06	-7.9955E+01	-1.1732E-06
$\hat{W}_l$	-9.6949E-04	-1.8486E+03	-9.7154E-04
$\hat{U}_l$	+9.2914E-04	+8.7832E+02	+9.3011E-04
VP			-4.3775E-05
VT			-4.5057E-02

Table B8. Input (*top*) and output (*bottom*) quantities for the white dwarf considered in Sec. 4.6 (see Fig. 11). See Tab. B1 for the meaning of the variables.

bipolytrope $\mathcal{L}=2$	core ($l=1$)	envelope ($l=2$)	total
N			129
n_l	+5.0000E-01	+3.0000E+00	
$z(A_l)$	+6.4881E-01	+7.5000E-01	
q_l	+8.6508E-01	+1.3492E-01	
$\alpha_l(\mathrm{A}_l)$		+7.0000E+00	
ω_l		+1.1032E-01	
SCF-iterations			35
$\hat{H}_l(\mathrm{A}_l)$	+1.0087E-02	+1.0000E+00	
$\beta_l^\dagger$	+1.0000E+00	+1.4348E-02	
nodes Γ_l	190	251	
$\hat{V}_l$	+1.1429E+00	+1.7940E+00	+2.9369E+00
$\hat{M}_l$	+6.5706E-01	+1.0494E+00	+6.7211E-01
C_{1l}	+7.2364E-01	+9.4965E+00	
C_{2l}	+4.7589E-02	+3.0066E+01	
C_{3l}	-1.0184E+00	-6.1991E+01	
J_l	+2.0445E-02	+9.3217E-02	+2.1782E-02
$\hat{T}_l$	+2.2300E-03	+6.4236E+00	+3.5524E-03
$\hat{W}_l$	-4.4404E-01	-3.5518E+01	-4.5136E-01
$\hat{U}_l$	+4.4238E-01	+9.3063E+00	+4.4430E-01
VP			+4.5970E-05
VT			+1.0185E-04

Table B9. Input (*top*) and output (*bottom*) quantities for the configuration sharing the same degeneracy parameter as for the one corresponding to Tab B3. See Tab. B1 for the meaning of the variables.

	polytrope ($l=\mathcal{L}=1$)	Hachisu (1986)	false tripolytrope ($\mathcal{L}=2$) core ($l=1$)	env. ($l=2$)	atm. ($l=3$)	total
N	129	>128				129
n_l	+1.5000E+00	+1.5000E+00	+1.5000E+00	+1.5000E+00	+1.5000E+00	
$\hat{z}(A_l)$	+1.0000E+00	+1.0000E+00	+3.3333E-01	+6.6667E-01	+1.0000E+00	
q_l	+1.0000E+00	+1.0000E+00	+3.3333E-01	+3.3333E-01	+3.3333E-01	
$\alpha_l(\mathrm{A}_l)$				+1.0000E+00	+1.0000E+00	
ω_l				+1.0000E+00	+1.0000E+00	
SCF-iterations	29					31
$\hat{H}_l(\mathrm{A}_l)$	+0.0000E+00		+7.7815E-01	+4.3432E-01	+0.0000E+00	
β_l		+1.0000E+00	+6.8643E-01	+1.9647E-01		
nodes Γ_l		251	84	168	251	
$\hat{V}_l$	+4.1883E+00	+4.17E+00	+1.5495E-01	+1.0861E+00	+2.9479E+00	+4.1889E+00
$\hat{M}_l$	+6.9919E-01	+6.99E-01	+1.2440E-01	+5.9220E-01	+8.5830E-01	+6.9953E-01
C_{1l}	+3.3196E-06		+9.4134E-01	+9.4133E-01	+1.0671E+00	+1.6192E+00
C_{2l}	-1.4787E-04		-2.1542E-04	-7.5264E-04		
C_{3l}	-6.9920E-01		-6.9948E-01	-1.0190E+00	-3.5602E+00	
J_l	+2.6064E-04	+0.00E+00	+6.4185E-05	+1.2569E-03	+4.1416E-03	+1.7406E-03
$\hat{T}_l$	+2.3744E-07	+0.00E+00	-3.9025E-07	-1.1133E-05	-1.2817E-04	-1.0583E-05
$\hat{W}_l$	-4.1904E-01	-4.19E-01	-9.4361E-02	-5.2741E-01	-1.9816E+00	-4.1936E-01
$\hat{U}_l$	+4.1906E-01	-4.19E-01	+1.2205E-01	+5.4161E-01	+1.0889E+00	+4.1928E-01
VP	+1.5278E-05					-1.0400E-04
VT	+3.6460E-05					-2.4800E-04

Table C1. Same legend as for Tab. B1 but for the tripolytrope in the conditions of Fig. 14, but for $\ell = 7$. See Tab. B1 for the meaning of the variables.

tripolytrope $\mathcal{L}=3$	core ($l=1$)	envelope ($l=2$)	atmosphere ($l=3$)	total
N				129
ℓ				7
n_l	+5.0000E-01	+1.5000E+00	+3.0000E+00	
$z(A_l)$	+4.9405E-01	+6.6667E-01	+7.5000E-01	
q_l	+6.5873E-01	+2.3016E-01	+1.1111E-01	
$\alpha_l(\mathrm{A}_l)$		+3.0000E+00	+2.0000E+00	
ω_l		+3.0000E-01	+8.1100E-01	
SCF-iterations				33
$\hat{H}_l(\mathrm{A}_l)$	+8.3511E-02	+9.3796E-02	+0.0000E+00	
$\beta_l^\dagger$	+1.0000E+00	+9.6328E-02	+1.3836E-03	
Q_l	+5.0113E-01	+2.2100E-01	+0.0000E+00	
nodes Γ_l	146	202	251	
$\hat{V}_l$	+5.1967E-01	+9.3630E-01	+1.4830E+00	+2.9389E+00
$\hat{M}_l$	+3.2418E-01	+3.7558E-01	+5.7257E-01	+3.6115E-01
C_{1l}	+4.6852E-01	+2.0309E+00	+4.2441E+01	
C_{2l}	+5.6399E-02	+1.9516E+00	+1.6755E+02	
C_{3l}	-6.7476E-01	-5.3801E+00	-3.4540E+02	
J_l	+6.7792E-03	+2.1185E-02	+7.0840E-02	+8.9179E-03
$\hat{T}_l$	+8.0497E-04	+8.7048E-02	+2.2504E+01	+1.6558E-03
$\hat{W}_l$	-1.4607E-01	-1.2358E+00	-1.0026E+02	-1.5773E-01
$\hat{U}_l$	+1.4841E-01	+6.4561E-01	+1.8938E+01	+1.5444E-01
VP				+2.0997E-05
VT				+1.3312E-04

Table C2. Input (*top*) and output (*bottom*) quantities for the tripolytropic configuration sharing the same size, surface velocity and total mass as for the bipolytropes considered in Tabs. B3 and B9. See Tab. B1 for the meaning of the variables.

APPENDIX C: TABLES (TRIPOLYTROPES)

Bibliography

Abramowicz, M. A., Karas, V., and Lanza, A. (1998). On the runaway instability of relativistic tori. A&A, 331:1143–1146. 4

Aikawa, Y., Herbst, E., Roberts, H., and Caselli, P. (2005). Molecular evolution in collapsing prestellar cores. iii. contraction of a bonnor-ebert sphere. *The Astrophysical Journal*, 620(1):330. 1.2.1

Alves, J. F., Lada, C. J., and Lada, E. A. (2001). Internal structure of a cold dark molecular cloud inferred from the extinction of background starlight. Nature, 409(6817):159–161. 1.2.1

Amendt, P., Lanza, A., and Abramowicz, M. A. (1989). Baroclinic toroidal figures of equilibrium. ApJ, 343:437–444. 3.1

André, P. (2017). Interstellar filaments and star formation. *Comptes Rendus Geoscience*, 349(5):187–197. 1.2.1

André, P., Di Francesco, J., Ward-Thompson, D., Inutsuka, S.-i., Pudritz, R. E., and Pineda, J. (2014). From filamentary networks to dense cores in molecular clouds: toward a new paradigm for star formation. *Protostars and Planets VI*, 27. 2.1.5

André, P., Di Francesco, J., Ward-Thompson, D., Inutsuka, S. I., Pudritz, R. E., and Pineda, J. E. (2014a). From Filamentary Networks to Dense Cores in Molecular Clouds: Toward a New Paradigm for Star Formation. In Beuther, H., Klessen, R. S., Dullemond, C. P., and Henning, T., editors, *Protostars and Planets VI*, page 27. 1.2.1

André, P., Könyves, V., Arzoumanian, D., and Palmeirim, P. (2014b). Unraveling the Labyrinth of Star Formation with Herschel. In *The Labyrinth of Star Formation*, volume 36, page 225. 1.2.1

Ansorg, M., Kleinwächter, A., and Meinel, R. (2003). Uniformly rotating axisymmetric fluid configurations bifurcating from highly flattened maclaurin spheroids. *Monthly Notices of the Royal Astronomical Society*, 339(2):515–523. (document), 4, 4.1, 4.2, 4.3.1, 4.3.1, **??**, 4.6, 4.4.1, 4.5

Arzoumanian, D., André, P., Didelon, P., Könyves, V., Schneider, N., Men'shchikov, A., Sousbie, T., Zavagno, A., Bontemps, S., di Francesco, J., Griffin, M., Hennemann, M., Hill, T., Kirk, J., Martin, P., Minier, V., Molinari, S., Motte, F., Peretto, N., Pezzuto, S., Spinoglio, L., Ward-Thompson, D., White, G., and Wilson, C. D. (2011). Characterizing interstellar filaments with Herschel in IC 5146. A&A, 529:L6. 1.2.1

Bacmann, A., André, P., Puget, J. L., Abergel, A., Bontemps, S., and Ward-Thompson, D. (2000). An ISOCAM absorption survey of the structure of pre-stellar cloud cores. A&A, 361:555–580. 1.2.1

Ball, W. H., Tout, C. A., and Żytkow, A. N. (2012). Quasi-stars, giants and the schönberg–chandrasekhar limit. *Monthly Notices of the Royal Astronomical Society*, 421(3):2713–2721. 5.1.2

Baraffe, I., Chabrier, G., Fortney, J., and Sotin, C. (2014). Planetary Internal Structures. In Beuther, H., Klessen, R. S., Dullemond, C. P., and Henning, T., editors, *Protostars and Planets VI*, page 763. 1.2.4

Basillais, B. and Huré, J. M. (2019). Rigidly rotating, incompressible spheroid-ring systems: new bifurcations, critical rotations, and degenerate states. MNRAS, 487(4):4504–4509. (document), 4, 4.6, 4.5

Baumgarte, T. W., Shapiro, S. L., and Shibata, M. (2000). On the maximum mass of differentially rotating neutron stars. *The Astrophysical Journal*, 528(1):L29–L32. 1.2.3

Beech, M. (1988). A double polytropic model for low-mass stars. *Astrophysics and space science*, 146(2):299–310. 5.1.2

Bender, C. M., Milton, K. A., Pinsky, S. S., and Simmons Jr, L. (1989). A new perturbative approach to nonlinear problems. *Journal of mathematical Physics*, 30(7):1447–1455. 2.2

Beust, H. and Dutrey, A. (2005). Dynamics of the young multiple system gg tauri-i. orbital fits and inner edge of the circumbinary disk of gg tau a. *Astronomy & Astrophysics*, 439(2):585–594. 6.3, 7.5

Beust, H. and Dutrey, A. (2006). Dynamics of the young multiple system gg tauri-ii. relation between the stellar system and the circumbinary disk. *Astronomy & Astrophysics*, 446(1):137–154. (document), 6.3, 6.5, 6.3.4, 6.6, 7.5

Bjorkman, K. S., Meade, M. R., Nordsieck, K. H., Anderson, C. M., Babler, B. L., Clayton, G. C., Code, A. D., Magalhaes, A. M., Schulte-Ladbeck, R. E., Taylor, M., and Whitney, B. A. (1993). Ultraviolet Spectropolarimetry of the Be Star PP Carinae with the Wisconsin Ultraviolet Photo-Polarimeter Experiment. ApJ, 412:810. 1.2.3

Bohr, A. and Mottelson, B. R. (1979). Physics of rapidly rotating nuclei. *Physics Today*, 32(6):25–31. 1.4

Bonnor, W. B. (1956). Boyle's Law and gravitational instability. MNRAS, 116:351. 1.1, 1.2.1

Boutin-Basillais, B. and Huré, J.-M. (2018). Multi-body figures of equilibrium in axial symmetry. *sf2a*, page Di. 4

Braess, D. (1981). The contraction number of a multigrid method for solving the poisson equation. *Numerische Mathematik*, 37(3):387–404. 3.2.3

Brauer, R., Pantin, E., Di Folco, E., Habart, E., Dutrey, A., and Guilloteau, S. (2019). Gg tauri a: dark shadows on the ringworld. *Astronomy & Astrophysics*, 628:A88. (document), 6.3

Briggs, W. L., Henson, V. E., and McCormick, S. F. (2000). *A multigrid tutorial*. SIAM. 3.2.3

Buccino, D. R., Helled, R., Parisi, M., Hubbard, W. B., and Folkner, W. M. (2020). Updated Equipotential Shapes of Jupiter and Saturn Using Juno and Cassini Grand Finale Gravity Science Measurements. *Journal of Geophysical Research (Planets)*, 125(8):e06354. 1.2.4, 5.4.5

Caimmi, R. (1986). A special case of two-component polytropes with rigid rotation. A&A, 159(1-2):147–156. 5

Caimmi, R. (2016). Multi-component, rigidly rotating polytropes: improved and extended theory. *ArXiv e-prints*. 4

Cardoso, V. (2008). The many shapes of spinning drops. *Physics Online Journal*, 1:38. 1.4

Carrasco-González, C., Henning, T., Chand ler, C. J., Linz, H., Pérez, L., Rodríguez, L. F., Galván-Madrid, R., Anglada, G., Birnstiel, T., van Boekel, R., Flock, M., Klahr, H., Macias, E., Menten, K., Osorio, M., Testi, L., Torrelles, J. M., and Zhu, Z. (2016). The VLA View of the HL Tau Disk: Disk Mass, Grain Evolution, and Early Planet Formation. ApJ, 821(1):L16. 4.5

Carrasco-González, C., Sierra, A., Flock, M., Zhu, Z., Henning, T., Chandler, C., Galván-Madrid, R., Macías, E., Anglada, G., Linz, H., Osorio, M., Rodríguez, L. F., Testi, L., Torrelles, J. M., Pérez, L., and Liu, Y. (2019). The Radial Distribution of Dust Particles in the HL Tau Disk from ALMA and VLA Observations. ApJ, 883(1):71. 4.5

Cassinelli, J. P., Brown, J. C., Maheswaran, M., Miller, N. A., and Telfer, D. C. (2002). A Magnetically Torqued Disk Model for Be Stars. ApJ, 578(2):951–966. 1.2.3

Chandrasekhar, S. (1931). The Maximum Mass of Ideal White Dwarfs. ApJ, 74:81. 1.2.3

Chandrasekhar, S. (1933a). The equilibrium of distorted polytropes. I. The rotational problem. MNRAS, 93:390–406. 2.2, 2.2, 6

Chandrasekhar, S. (1933b). The equilibrium of distorted polytropes. IV. the rotational and the tidal distortions as functions of the density distribution. MNRAS, 93:539–574. 2.2

Chandrasekhar, S. (1969). *Ellipsoidal figures of equilibrium*. Yale Univ. Press. (document), 1.1, 2.3.2, 6

Chandrasekhar, S. and Fermi, E. (1953). Problems of Gravitational Stability in the Presence of a Magnetic Field. ApJ, 118:116. 2.1.5

Chandrasekhar, S. and Lebovitz, N. R. (1962). On the oscillations and the stability of rotating gaseous masses. iii. the distorted polytropes. *The Astrophysical Journal*, 136:1082. 6

Chavanis, P.-H. and Sire, C. (2008). Critical mass of bacterial populations in a generalized Keller Segel model. Analogy with the Chandrasekhar limiting mass of white dwarf stars. *Physica A Statistical Mechanics and its Applications*, 387(8-9):1999–2009. 1.4

Cohen, S., Plasil, F., and Swiatecki, W. (1974). Equilibrium configurations of rotating charged or gravitating liquid masses with surface tension. ii. *Annals of Physics*, 82(2):557–596. 1.4, 1.4

Cohl, H. S. and Tohline, J. E. (1999). A Compact Cylindrical Green's Function Expansion for the Solution of Potential Problems. ApJ, 527(1):86–101. 6

Coughlin, E. R. and Nixon, C. J. (2020). The Gravitational Instability of Adiabatic Filaments. ApJS, 247(2):51. 1.1, 2.1.5

Crapsi, A., Caselli, P., Walmsley, M. C., and Tafalla, M. (2007). Observing the gas temperature drop in the high-density nucleus of L 1544. A&A, 470(1):221–230. 1.2.1

Curry, C. L. and McKee, C. F. (2000). Composite Polytrope Models of Molecular Clouds. I. Theory. ApJ, 528(2):734–755. 5

Dalla Vedova, G., Millour, F., Domiciano de Souza, A., Petrov, R. G., Moser Faes, D., Carciofi, A. C., Kervella, P., and Rivinius, T. (2017). VLTI/PIONIER images the Achernar disk swell. A&A, 601:A118. 4.5

Di Folco, E., Dutrey, A., Le Bouquin, J.-B., Lacour, S., Berger, J.-P., Köhler, R., Guilloteau, S., Piétu, V., Bary, J., Beck, T., et al. (2014). Gg tauri: the fifth element. *Astronomy & Astrophysics*, 565:L2. 6.3

Domiciano de Souza, A., Kervella, P., Jankov, S., Abe, L., Vakili, F., di Folco, E., and Paresce, F. (2003). The spinning-top Be star Achernar from VLTI-VINCI. A&A, 407:L47–L50. 1.2.3

Dullemond, C. P. and Natta, A. (2003). An analysis of two-layer models for circumstellar disks. A&A, 405:597–605. 5

Dunham, E. T., Desch, S. J., and Probst, L. (2019). Haumea's Shape, Composition, and Internal Structure. ApJ, 877(1):41. 1.2.5

Durand, E. (1953). Electrostatique et magnétostatique. 6.2.1

Durand, E. (1953). *Electrostatique. Vol. I. Les distributions.* Ed. Masson. 3.2.3, 5.7.1

Dutrey, A., Guilloteau, S., and Guelin, M. (1997). Chemistry of protosolar-like nebulae: The molecular content of the dm tau and gg tau disks. *Astronomy and Astrophysics*, 317:L55–L58. 6.3.7

Ebert, R. (1955). Über die Verdichtung von H I-Gebieten. Mit 5 Textabbildungen. ZAp, 37:217. 1.1, 1.2.1

Eggleton, P. P., Faulkner, J., and Cannon, R. C. (1998). A small contribution to the giant problem. *Monthly Notices of the Royal Astronomical Society*, 298(3):831–834. 5.1.2

Emden, R. (1907). *Gaskugeln*. 2.1, 2.1.1

Eriguchi, Y. and Hachisu, I. (1983). Gravitational equilibrium of a multi-body fluid system. *Progress of theoretical physics*, 70(6):1534–1541. 4

Eskridge, P. B. and Frogel, J. A. (1999). What is the True Fraction of Barred Spiral Galaxies? Ap&SS, 269:427–430. 1.2.5

Evans, Neal J., I., Rawlings, J. M. C., Shirley, Y. L., and Mundy, L. G. (2001). Tracing the Mass during Low-Mass Star Formation. II. Modeling the Submillimeter Emission from Preprotostellar Cores. ApJ, 557(1):193–208. 1.2.1

Fagotto, F., Bressan, A., Bertelli, G., and Chiosi, C. (1994). Evolutionary sequences of stellar models with new radiative opacities. IV. Z=0.004 and Z=0.008. A&AS, 105:29–38. 1.2.3

Fock, V. (1930). Näherungsmethode zur Lösung des quantenmechanischen Mehrkörperproblems. *Zeitschrift fur Physik*, 61(1-2):126–148. 3.2.1

Freeman, H. (1961). On the encoding of arbitrary geometric configurations. *IRE Transactions on Electronic Computers*, (2):260–268. 3.2.4

Galli, D., Walmsley, M., and Gonçalves, J. (2002). The structure and stability of molecular cloud cores in external radiation fields. A&A, 394:275–284. 1.2.1

Geroyannis, V. S. (1993). A Global Polytropic Model for the Solar System - Planetary Distances and Masses Resulting from the Complex Lane-Emden Differential Equation. *Earth Moon and Planets*, 61(2):131–139. 2.1.3

Geroyannis, V. S. and Dallas, T. G. (1994). Comments on a Global Polytropic Model for the Solar and Jovian Systems. *Earth Moon and Planets*, 65(1):15–19. 2.1.3

Geroyannis, V. S. and Valvi, F. N. (1994). Application of a Global Polytropic Model to the Jupiter's System of Satellites: A Numerical Treatment. *Earth Moon and Planets*, 64(3):217–225. 2.1.3

Gheller, C., Sartoretto, F., and Guidolin, M. (2004). Gamms: a multigrid-amr code for computing gravitational fields. In *Astronomical Data Analysis Software and Systems (ADASS) XIII*, volume 314, page 670. 3.2.3

Gong, M. and Ostriker, E. C. (2015). Prestellar Core Formation, Evolution, and Accretion from Gravitational Fragmentation in Turbulent Converging Flows. ApJ, 806(1):31. 1.2.1

Guillet, T. and Teyssier, R. (2011). A simple multigrid scheme for solving the poisson equation with arbitrary domain boundaries. *Journal of Computational Physics*, 230(12):4756–4771. 3.2.3

Guillot, T. (1999). A comparison of the interiors of Jupiter and Saturn. Planet. Space Sci., 47(10-11):1183–1200. 1.2.4, 5.4.5

Guillot, T., Stevenson, D. J., Hubbard, W. B., and Saumon, D. (2004). *The interior of Jupiter*, volume 1, pages 35–57. 1.2.4, 5.4.5

Guilloteau, S., Dutrey, A., and Simon, M. (1999). Gg tauri: the ring world. *Astronomy and Astrophysics*, 348:570–578. 6.3, 6.3.3, 7.5

Hachisu, I. (1986). A versatile method for obtaining structures of rapidly rotating stars. *The Astrophysical Journal Supplement Series*, 61:479–507. (document), 1.1, 2.3, 2.3.1, 3, 3.2, 3.2.1, 3.2.2, 3.5, 3.3, 3.4.1, 3.7, 3.4.2, 3.8, 4.2.2

Hachisu, I. and Eriguchi, Y. (1983). Bifurcations and phase transitions of self-gravitating and uniformly rotating fluid. *Monthly Notices of the Royal Astronomical Society*, 204(2):583–589. 4, 4.3.1, 4.5

Hachisu, I. and Eriguchi, Y. (1984a). Binary fluid star. PASJ, 36(2):259–276. 4.3.1

Hachisu, I. and Eriguchi, Y. (1984b). Fission Sequence and Equilibrium Models of Rigidity Rotating Polytropes. Ap&SS, 99(80):71. (document), 2.5, 2.4, 2.6

Hachisu, I., Eriguchi, Y., and Nomoto, K. (1986a). Fate of Merging Double White Dwarfs. ApJ, 308:161. 1.2.3

Hachisu, I., Eriguchi, Y., and Nomoto, K. (1986b). Fate of merging double white dwarfs. II - Numerical method. ApJ, 311:214–225. 1.2.3, 4

Haensel, P., Potekhin, A. Y., and Yakovlev, D. G. (2007). *Neutron stars 1: Equation of state and structure*, volume 326. Springer Science & Business Media. 1.2.3

Hansen, C. J., Kawaler, S. D., and Trimble, V. (2004). *Stellar interiors : physical principles, structure, and evolution*. 1.2.3

Hartree, D. R. (1928). The Wave Mechanics of an Atom with a Non-Coulomb Central Field. Part I. Theory and Methods. *Proceedings of the Cambridge Philosophical Society*, 24(1):89. 3.2.1

He, J.-H. (1999). Homotopy perturbation technique. *Computer methods in applied mechanics and engineering*, 178(3-4):257–262. 2.2

Helled, R. (2019). *The Interiors of Jupiter and Saturn*, page 175. **??**, 7.4

Helled, R. and Guillot, T. (2018). *Internal Structure of Giant and Icy Planets: Importance of Heavy Elements and Mixing*, page 44. 1.2.4

Hill, R. J. A. and Eaves, L. (2008). Nonaxisymmetric Shapes of a Magnetically Levitated and Spinning Water Droplet. Phys. Rev. Lett., 101(23):234501. 1.4

Hill, T., Motte, F., Didelon, P., Bontemps, S., Minier, V., Hennemann, M., Schneider, N., André, P., Men'shchikov, A., Anderson, L. D., Arzoumanian, D., Bernard, J. P., di Francesco, J., Elia, D., Giannini, T., Griffin, M. J., Könyves, V., Kirk, J., Marston, A. P., Martin, P. G., Molinari, S., Nguyen Luong, Q., Peretto, N., Pezzuto, S., Roussel, H., Sauvage, M., Sousbie, T., Testi, L., Ward-Thompson, D., White, G. J., Wilson, C. D., and Zavagno, A. (2011). Filaments and ridges in Vela C revealed by Herschel: from low-mass to high-mass star-forming sites. A&A, 533:A94. 1.2.1

Horedt, G. P. (2004). *Polytropes: applications in astrophysics and related fields*, volume 306. Springer Science & Business Media. (document), 1.5, 2.1.1, 2.3, 2.3.2

Horedt, G. P. (2013). Early Evolution of Prestellar Cores. ApJ, 773(2):131. 1.2.1

Hu, S.-t. (1959). *Homotopy theory*. Academic press. 2.2

Huat, A. L., Hubert, A. M., Baudin, F., Floquet, M., Neiner, C., Frémat, Y., Gutiérrez-Soto, J., Andrade, L., de Batz, B., Diago, P. D., Emilio, M., Espinosa Lara, F., Fabregat, J., Janot-Pacheco, E., Leroy, B., Martayan, C., Semaan, T., Suso, J., Auvergne, M., Catala, C., Michel, E., and Samadi, R. (2009). The B0.5IVe CoRoT target HD 49330. I. Photometric analysis from CoRoT data. A&A, 506(1):95–101. 1.2.3

Hubbard, W. B. (1974). Gravitational field of a rotating planet with a polytropic index of unity. AZh, 51:1052. 1.2.4

Huré, J. M., Basillais, B., Karas, V., Trova, A., and Semerák, O. (2020). The exterior gravitational potential of toroids. MNRAS, 494(4):5825–5838. 6, 6.2.1

Huré, J. M. and Hersant, F. (2017). Toroidal figures of equilibrium from a second-order accurate, accelerated SCF method with subgrid approach. MNRAS, 464(4):4761–4776. 1.1, 1.5, 3.2, 3.2.4

Huré, J. M., Hersant, F., and Nasello, G. (2018). The equilibrium of overpressurized polytropes. MNRAS, 475(1):63–78. 1.5, 3.2

Huré, J. M., Trova, A., Karas, V., and Lesca, C. (2019). Interior potential of a toroidal shell from pole values. MNRAS, 486(4):5656–5669. 6

Jacobi, C. G. J. (1834). Ueber die Figur des Gleichgewichts. *Annalen der Physik*, 109(8):229–233. 1.1, 2.3

James, R. (1964). The structure and stability of rotating gas masses. *The Astrophysical Journal*, 140:552–882. 3

Johnstone, D. and Bally, J. (1999). JCMT/SCUBA Submillimeter Wavelength Imaging of the Integral-shaped Filament in Orion. ApJ, 510(1):L49–L53. 1.2.1

Kadam, K., Motl, P. M., Frank, J., Clayton, G. C., and Marcello, D. C. (2016). A numerical method for generating rapidly rotating bipolytropic structures in equilibrium. *Monthly Notices of the Royal Astronomical Society*, 462(2):2237–2245. (document), 1.2.3, 5, 5.2.1, 5.2.3, 5.3, 5.3.2, 5.6, 5.6.1, 7.3

Kaminski, E., Frank, A., Carroll, J., and Myers, P. (2014). On the role of ambient environments in the collapse of bonnor-ebert spheres. *The Astrophysical Journal*, 790(1):70. 1.2.1

Kandori, R., Nakajima, Y., Tamura, M., Tatematsu, K., Aikawa, Y., Naoi, T., Sugitani, K., Nakaya, H., Nagayama, T., Nagata, T., Kurita, M., Kato, D., Nagashima, C., and Sato, S. (2005). Near-Infrared Imaging Survey of Bok Globules: Density Structure. AJ, 130(5):2166–2184. 1.2.1

Kellog, O. D. (1929). *Foundations of Potential-Theory.* na. 3.2.3, 6.2.1

Kepler, S. O., Kleinman, S. J., Nitta, A., Koester, D., Castanheira, B. G., Giovannini, O., Costa, A. F. M., and Althaus, L. (2007). White dwarf mass distribution in the SDSS. MNRAS, 375(4):1315–1324. 1.2.3

Kilic, M., Allende Prieto, C., Brown, W. R., and Koester, D. (2007). The Lowest Mass White Dwarf. ApJ, 660(2):1451–1461. 1.2.3

Kiuchi, K., Nagakura, H., and Yamada, S. (2010). Multi-layered Configurations in Differentially Rotational Equilibrium. ApJ, 717:666–673. 5, 5.2.1

Komacek, T. D. and Youdin, A. N. (2017). Structure and evolution of internally heated hot jupiters. *The Astrophysical Journal*, 844(2):94. 5.4

Kondratyev, B. (2018). Expansion of the potential of a homogeneous circular torus in terms of geometrical parameter. *Technical Physics*, 63(3):311–314. 6

Kong, D., Liao, X., Zhang, K., and Schubert, G. (2014). The shape, internal structure and gravity of the fast spinner β Pictoris b. MNRAS, 445:L26–L30. 1.2.4

Kong, D., Zhang, K., and Schubert, G. (2016). A Fully Self-consistent Multi-layered Model of Jupiter. ApJ, 826(2):127. 1.2.4, 5.4.5

Kovetz, A. (1968). Slowly rotating polytropes. *The Astrophysical Journal*, 154:999–1004. 6

Lane, H. J. (1870). On the theoretical temperature of the Sun, under the hypothesis of a gaseous mass maintaining its volume by its internal heat, and depending on the laws of gases as known to terrestrial experiment. *American Journal of Science*, 50(148):57–74. 1.1, 2.1

Laughlin, G., Bodenheimer, P., and Adams, F. C. (1997). The End of the Main Sequence. ApJ, 482(1):420–432. 1.2.3

Lee, U. and Saio, H. (1993). Angular momentum transfer by non-radial oscillations in massive main-sequence stars. MNRAS, 261(2):415–424. 1.2.3

Lock, S. J., Stewart, S. T., Petaev, M. I., Leinhardt, Z., Mace, M. T., Jacobsen, S. B., and Cuk, M. (2018). The origin of the moon within a terrestrial synestia. *Journal of Geophysical Research: Planets*, 123(4):910–951. 7.2

Lou, Y.-Q. and Hu, X.-Y. (2017). Gravitational collapse of conventional polytropic cylinder. MNRAS, 468(3):2771–2780. 2.1.5

Mach, P. (2012). All solutions of the n = 5 Lane-Emden equation. *Journal of Mathematical Physics*, 53(6):062503–062503. 2.1.1, 2.1.2, 2.1.2

Machida, M. N., Inutsuka, S.-i., and Matsumoto, T. (2014). Conditions for circumstellar disc formation: effects of initial cloud configuration and sink treatment. MNRAS, 438(3):2278–2306. 1.2.1

Maclaurin, C. (1742). *A treatise of fluxions*, volume 1. Ruddimans. 2.3

Maeder, A. (1971). The sch6nberg-chandrasekhar limit and rotation. *Astronomy and Astrophysics*, 14:351. 1.2.3, 5.6, 5.6.2, 7.3

Maeder, A. (2009). *Physics, Formation and Evolution of Rotating Stars*. (document), 1.2.2, 1.2.3, 1.2.3, 1.3, 1.3, 1.1

Majic, M. (2018). Exact gravitational potential of a homogeneous torus in toroidal coordinates and a surface integral approach to Poisson's equation. *arXiv e-prints*, page arXiv:1803.00003. 6

Mamajek, E. E. (2009). Initial Conditions of Planet Formation: Lifetimes of Primordial Disks. In Usuda, T., Tamura, M., and Ishii, M., editors, *Exoplanets and Disks: Their Formation and Diversity*, volume 1158 of *American Institute of Physics Conference Series*, pages 3–10. 1.3

Mamajek, E. E., Meyer, M. R., Hinz, P. M., Hoffmann, W. F., Cohen, M., and Hora, J. L. (2004). Constraining the Lifetime of Circumstellar Disks in the Terrestrial Planet Zone: A Mid-Infrared Survey of the 30 Myr old Tucana-Horologium Association. ApJ, 612(1):496–510. 1.3

Mankovich, C. R. and Fortney, J. J. (2020). Evidence for a Dichotomy in the Interior Structures of Jupiter and Saturn from Helium Phase Separation. ApJ, 889(1):51. 1.2.4, 5.4.5

Marsh, K. A., Griffin, M. J., Palmeirim, P., André, P., Kirk, J., Stamatellos, D., Ward-Thompson, D., Roy, A., Bontemps, S., di Francesco, J., Elia, D., Hill, T., Könyves, V., Motte, F., Nguyen-Luong, Q., Peretto, N., Pezzuto, S., Rivera-Ingraham, A., Schneider, N., Spinoglio, L., and White, G. (2014). Properties of starless and prestellar cores in Taurus revealed by Herschel: SPIRE/PACS imaging. MNRAS, 439(4):3683–3693. 1.2.1

Masuda, N., Nishida, S., and Eriguchi, Y. (1998). The runaway instability of self-gravitating tori with non-constant specific angular momentum around black holes. *Monthly Notices of the Royal Astronomical Society*, 297(4):1139–1144. 4

Mattern, M., Kainulainen, J., Zhang, M., and Beuther, H. (2018). Structure and fragmentation of a high line-mass filament: Nessie. A&A, 616:A78. 1.2.1

Maxwell, J. C. (1874). Statique expérimentale et théorique des Liquides soumis aux seules Forces moléculaires,. Nature, 10(242):119–121. 1.4

Medvedev, M. V. and Rybicki, G. (2001). The structure of self-gravitating polytropic systems with n around 5. *The Astrophysical Journal*, 555(2):863. 2.1.1, 2.1.2

Meilland, A., Stee, P., Vannier, M., Millour, F., Domiciano de Souza, A., Malbet, F., Martayan, C., Paresce, F., Petrov, R. G., Richichi, A., and Spang, A. (2007). First direct detection of a Keplerian rotating disk around the Be star α Arae using AMBER/VLTI. A&A, 464(1):59–71. 1.2.3

Meilland, A., Stee, P., Zorec, J., and Kanaan, S. (2006). Be stars: one ring to rule them all? *Astronomy & Astrophysics*, 455(3):953–961. 7.2

Men'shchikov, A., André, P., Didelon, P., Könyves, V., Schneider, N., Motte, F., Bontemps, S., Arzoumanian, D., Attard, M., Abergel, A., Baluteau, J. P., Bernard, J. P., Cambrésy, L., Cox, P., di Francesco, J., di Giorgio, A. M., Griffin, M., Hargrave, P., Huang, M., Kirk, J., Li, J. Z., Martin, P., Minier, V., Miville-Deschênes, M. A., Molinari, S., Olofsson, G., Pezzuto, S., Roussel, H., Russeil, D., Saraceno, P., Sauvage, M., Sibthorpe, B., Spinoglio, L., Testi, L., Ward-Thompson, D., White, G., Wilson, C. D., Woodcraft, A., and Zavagno, A. (2010). Filamentary structures and compact objects in the Aquila and Polaris clouds observed by Herschel. A&A, 518:L103. 1.2.1

Miguel, Y., Guillot, T., and Fayon, L. (2016). Jupiter internal structure: the effect of different equations of state. *Astronomy & Astrophysics*, 596:A114. 5.4

Milne, E. A. (1923). The equilibrium of a rotating star. MNRAS, 83:118–147. 2.2, 6

Milne, E. A. (1930). The analysis of stellar structure. *Monthly Notices of the Royal Astronomical Society*, 91:4–55. 5.1.1

Moeckel, N. and Burkert, A. (2015). The formation of filamentary bundles in turbulent molecular clouds. *The Astrophysical Journal*, 807(1):67. 2.1.5

Molinari, S., Swinyard, B., Bally, J., Barlow, M., Bernard, J. P., Martin, P., Moore, T., Noriega-Crespo, A., Plume, R., Testi, L., Zavagno, A., Abergel, A., Ali, B., Anderson, L., André, P., Baluteau, J. P., Battersby, C., Beltrán, M. T., Benedettini, M., Billot, N., Blommaert, J., Bontemps, S., Boulanger, F., Brand, J., Brunt, C., Burton, M., Calzoletti, L., Carey, S., Caselli, P., Cesaroni, R., Cernicharo, J., Chakrabarti, S., Chrysostomou, A., Cohen, M., Compiegne, M., de Bernardis, P., de Gasperis, G., di Giorgio, A. M., Elia, D., Faustini, F., Flagey, N., Fukui, Y., Fuller, G. A., Ganga, K., Garcia-Lario, P., Glenn, J., Goldsmith, P. F., Griffin, M., Hoare, M., Huang, M.,

Ikhenaode, D., Joblin, C., Joncas, G., Juvela, M., Kirk, J. M., Lagache, G., Li, J. Z., Lim, T. L., Lord, S. D., Marengo, M., Marshall, D. J., Masi, S., Massi, F., Matsuura, M., Minier, V., Miville-Deschênes, M. A., Montier, L. A., Morgan, L., Motte, F., Mottram, J. C., Müller, T. G., Natoli, P., Neves, J., Olmi, L., Paladini, R., Paradis, D., Parsons, H., Peretto, N., Pestalozzi, M., Pezzuto, S., Piacentini, F., Piazzo, L., Polychroni, D., Pomarès, M., Popescu, C. C., Reach, W. T., Ristorcelli, I., Robitaille, J. F., Robitaille, T., Rodón, J. A., Roy, A., Royer, P., Russeil, D., Saraceno, P., Sauvage, M., Schilke, P., Schisano, E., Schneider, N., Schuller, F., Schulz, B., Sibthorpe, B., Smith, H. A., Smith, M. D., Spinoglio, L., Stamatellos, D., Strafella, F., Stringfellow, G. S., Sturm, E., Taylor, R., Thompson, M. A., Traficante, A., Tuffs, R. J., Umana, G., Valenziano, L., Vavrek, R., Veneziani, M., Viti, S., Waelkens, C., Ward-Thompson, D., White, G., Wilcock, L. A., Wyrowski, F., Yorke, H. W., and Zhang, Q. (2010). Clouds, filaments, and protostars: The Herschel Hi-GAL Milky Way. A&A, 518:L100. 2.1.5

Montesinos, M. (2012). Review: Accretion Disk Theory. *arXiv e-prints*, page arXiv:1203.6851. 1.3, 1.3

Mroz, P., Poleski, R., Gould, A., Udalski, A., Sumi, T., Szymanski, M. K., Soszynski, I., Pietrukowicz, P., Kozlowski, S., Skowron, J., Ulaczyk, K., Albrow, M. D., Chung, S. J., Han, C., Hwang, K. H., Jung, Y. K., Kim, H. W., Ryu, Y. H., Shin, I. G., Shvartzvald, Y., Yee, J. C., Zang, W., Cha, S. M., Kim, D. J., Kim, S. L., Lee, C. U., Lee, D. J., Lee, Y., Park, B. G., and Pogge, R. W. (2020). A terrestrial-mass rogue planet candidate detected in the shortest-timescale microlensing event. *arXiv e-prints*, page arXiv:2009.12377. 1.2.4

Murphy, J. (1980). On the f and m type solutions of the lane-emden equation. *Publications of the Astronomical Society of Australia*, 4(1):41–43. 2.1.2

Murphy, J. (1983). Composite and analytical solutions of the lane-emden equation with polytropic indices n= 1 and n= 5. In *Proceedings of the Astronomical Society of Australia*, volume 5, pages 175–179. 2.1.2

Myers, P. C. (2009a). Filamentary Structure of Star-forming Complexes. ApJ, 700(2):1609–1625. 1.2.1

Myers, P. C. (2009b). On the Distribution of Protostar Masses. ApJ, 706(2):1341–1352. 1.2.1

New, K. C. B. and Tohline, J. E. (1997). The Relative Stability against Merger of Close, Compact Binaries. ApJ, 490(1):311–327. 1.2.3

O'Donoghue, J., Moore, L., Connerney, J., Melin, H., Stallard, T. S., Miller, S., and Baines, K. H. (2019). Observations of the chemical and thermal response of 'ring rain' on Saturn's ionosphere. Icarus, 322:251–260. 1.3

Ortiz, J. L., Santos-Sanz, P., Sicardy, B., Benedetti-Rossi, G., Bérard, D., Morales, N., Duffard, R., Braga-Ribas, F., Hopp, U., Ries, C., Nascimbeni, V., Marzari, F., Granata, V., Pál, A., Kiss, C., Pribulla, T., Komžík, R., Hornoch, K., Pravec, P., Bacci, P.,

Maestripieri, M., Nerli, L., Mazzei, L., Bachini, M., Martinelli, F., Succi, G., Ciabattari, F., Mikuz, H., Carbognani, A., Gaehrken, B., Mottola, S., Hellmich, S., Rommel, F. L., Fernández-Valenzuela, E., Campo Bagatin, A., Cikota, S., Cikota, A., Lecacheux, J., Vieira-Martins, R., Camargo, J. I. B., Assafin, M., Colas, F., Behrend, R., Desmars, J., Meza, E., Alvarez-Candal, A., Beisker, W., Gomes-Junior, A. R., Morgado, B. E., Roques, F., Vachier, F., Berthier, J., Mueller, T. G., Madiedo, J. M., Unsalan, O., Sonbas, E., Karaman, N., Erece, O., Koseoglu, D. T., Ozisik, T., Kalkan, S., Guney, Y., Niaei, M. S., Satir, O., Yesilyaprak, C., Puskullu, C., Kabas, A., Demircan, O., Alikakos, J., Charmandaris, V., Leto, G., Ohlert, J., Christille, J. M., Szakáts, R., Takácsné Farkas, A., Varga-Verebélyi, E., Marton, G., Marciniak, A., Bartczak, P., Santana-Ros, T., Butkiewicz-Bąk, M., Dudziński, G., Alí-Lagoa, V., Gazeas, K., Tzouganatos, L., Paschalis, N., Tsamis, V., Sánchez-Lavega, A., Pérez-Hoyos, S., Hueso, R., Guirado, J. C., Peris, V., and Iglesias-Marzoa, R. (2017). The size, shape, density and ring of the dwarf planet Haumea from a stellar occultation. Nature, 550(7675):219–223. 1.2.5

Ostriker, J. (1964). The Equilibrium of Polytropic and Isothermal Cylinders. ApJ, 140:1056. 2.1.5

Ostriker, J. P. and Mark, J. W.-K. (1968). Rapidly rotating stars. I. The self-consistent-field method. ApJ, 151:1075–1088. 1.1, 3, 3.2.1

Owocki, S. P., Cranmer, S. R., and Gayley, K. G. (1996). Inhibition FO Wind Compressed Disk Formation by Nonradial Line-Forces in Rotating Hot-Star Winds. ApJ, 472:L115. 1.2.3

Pattle, K. and Ward-Thompson, D. (2015). A full virial analysis of the prestellar cores in the Ophiuchus molecular cloud. In *IAU General Assembly*, volume 29, page 2245772. 1.2.1

Phuong, N., Dutrey, A., Di Folco, E., Guilloteau, S., Pierens, A., Bary, J., Beck, T. L., Chapillon, E., Denis-Alpizar, O., Diep, P., et al. (2020). Planet-induced spirals in the circumbinary disk of gg tauri a. *Astronomy & Astrophysics*, 635:L9. (document), 6.4, 6.3.7, 6.9

Phuong, N. T., Chapillon, E., Majumdar, L., Dutrey, A., Guilloteau, S., Piétu, V., Wakelam, V., Diep, P. N., Tang, Y. W., Beck, T., and Bary, J. (2018). First detection of H_2S in a protoplanetary disk. The dense GG Tauri A ring. A&A, 616:L5. 6.3.7

Phuong, N. T., Dutrey, A., Diep, P. N., Guilloteau, S., Chapillon, E., Di Folco, E., Tang, Y. W., Piétu, V., Bary, J., Beck, T., Hersant, F., Hoai, D. T., Huré, J. M., Nhung, P. T., Pierens, A., and Tuan-Anh, P. (2020). GG Tauri A: gas properties and dynamics from the cavity to the outer disk. A&A, 635:A12. 6.3.7

Pluriel, W., Marcq, E., and Turbet, M. (2019). Modeling the albedo of Earth-like magma ocean planets with H_2O-CO_2 atmospheres. Icarus, 317:583–590. 1.2.4

Poeckert, R. and Marlborough, J. (1978). Be star models: observable effects of model parameters. *The Astrophysical Journal Supplement Series*, 38:229–252. 1.2.3

Poisson, E. and Will, C. M. (2014). *Gravity: Newtonian, Post-Newtonian, Relativistic*. Cambridge University Press. 2.1.6, 2.3.2

Porter, J. M. and Rivinius, T. (2003). Classical Be Stars. PASP, 115(812):1153–1170. 1.2.3

Prouteau, M., Desfosses, A., Sieben, C., Bourgoint, C., Lydia Mozaffari, N., Demurtas, D., Mitra, A. K., Guichard, P., Manley, S., and Loewith, R. (2017). TORC1 organized in inhibited domains (TOROIDs) regulate TORC1 activity. Nature, 550(7675):265–269. 1.4

Pugliese, D. and Stuchlík, Z. (2015). Ringed Accretion Disks: Equilibrium Configurations. ApJS, 221(2):25. 4.5

Pugliese, D. and Stuchlík, Z. (2017). Ringed Accretion Disks: Evolution of Double Toroidal Configurations. ApJS, 229(2):40. 4.5

Pugliese, D. and Stuchlik, Z. (2019). On the accreting tori sequences in Ringed Accretion Disks models. Polytropic equations of state and toroidal magnetic fields. *arXiv e-prints*, page arXiv:1910.04413. 4.5

Quirrenbach, A., Bjorkman, K. S., Bjorkman, J. E., Hummel, C. A., Buscher, D. F., Armstrong, J. T., Mozurkewich, D., Elias, N. M., I., and Babler, B. L. (1997). Constraints on the Geometry of Circumstellar Envelopes: Optical Interferometric and Spectropolarimetric Observations of Seven Be Stars. ApJ, 479(1):477–496. 1.2.3

Ramos, J. (2008). Series approach to the lane–emden equation and comparison with the homotopy perturbation method. *Chaos, Solitons & Fractals*, 38(2):400–408. 2.2

Rasio, F. A. and Shapiro, S. L. (1992). Hydrodynamical Evolution of Coalescing Binary Neutron Stars. ApJ, 401:226. 1.2.3

Rasio, F. A. and Shapiro, S. L. (1994). Hydrodynamics of Binary Coalescence. I. Polytropes with Stiff Equations of State. ApJ, 432:242. 1.2.3

Rivinius, T., Baade, D., Stefl, S., Stahl, O., Wolf, B., and Kaufer, A. (1998). Stellar and circumstellar activity of the Be star MU Centauri. I. Line emission outbursts. A&A, 333:125–140. 1.2.3

Rivinius, T., Baade, D., and Štefl, S. (2003). Non-radially pulsating Be stars. A&A, 411:229–247. 1.2.3

Rivinius, T., Baade, D., Štefl, S., Townsend, R. H. D., Stahl, O., Wolf, B., and Kaufer, A. (2001). Stellar and circumstellar activity of the Be star mu Centauri. III. Multiline nonradial pulsation modeling. A&A, 369:1058–1077. 1.2.3

Rivinius, T., Townsend, R. H. D., Baade, D., Carciofi, A. C., Leister, N., and Štefl, S. (2016). The Variable Line Width of Achernar. In Sigut, T. A. A. and Jones, C. E., editors, *Bright Emissaries: Be Stars as Messengers of Star-Disk Physics*, volume 506 of *Astronomical Society of the Pacific Conference Series*, page 17. 4.5

Roberts, I. (1963a). On highly rotating polytropes. *The Astrophysical Journal*, 137:1129. 2.2

Roberts, P. (1963b). On highly rotating polytropes. ii. *The Astrophysical Journal*, 138:809. 2.2

Rucinski, S. M. (1988). Rotational properties of composite polytrope models. AJ, 95:1895–1907. 5

Sackmann, I. J., Boothroyd, A. I., and Kraemer, K. E. (1993). Our Sun. III. Present and Future. ApJ, 418:457. 1.2.3

Schneider, S. and Elmegreen, B. G. (1979). A catalog of dark globular filaments. ApJS, 41:87–95. 1.2.1

Schönberg, M. and Chandrasekhar, S. (1942). On the evolution of the main-sequence stars. *The Astrophysical Journal*, 96:161. 1.2.3, 5.1.2

Schuster, A. (1883). On the Internal Constitution of the Sun. *Report of the British Association for the Advancement of Science*, 53:427–429. 2.1

Shukhman, I. G. (1983). Equilibrium and stability of a self-gravitating torus in the field of a large central mass. AZh, 60:227–241. 1.1

Sipilä, O., Caselli, P., and Juvela, M. (2017). On the stability of nonisothermal Bonnor-Ebert spheres. III. The role of chemistry in core stabilization. A&A, 601:A113. 1.2.1

Sipilä, O., Harju, J., and Juvela, M. (2011). On the stability of non-isothermal Bonnor-Ebert spheres. A&A, 535:A49. 1.2.1

Sipilä, O., Harju, J., and Juvela, M. (2015). On the stability of nonisothermal Bonnor-Ebert spheres. II. The effect of gas temperature on the stability. A&A, 582:A48. 1.2.1

Smoluchowski, R. (1967). Internal structure and energy emission of jupiter. *Nature*, 215(5102):691–695. 5.4

Snellen, I. A. G., Brandl, B. R., de Kok, R. J., Brogi, M., Birkby, J., and Schwarz, H. (2014). Fast spin of the young extrasolar planet β Pictoris b. Nature, 509(7498):63–65. 1.2.4

Sofue, Y. (2013). Rotation curve and mass distribution in the galactic center—from black hole to entire galaxy—. *Publications of the Astronomical Society of Japan*, 65(6):118. 3.1.1

Srivastava, S. (1962). A New Solution of the Lane-Emden Equation of Index n=5. ApJ, 136:680–681. (document), 2.1.1, 2.1.2, 2.2

Stodólkiewicz, J. S. (1963). On the Gravitational Instability of Some Magneto-Hydrodynamical Systems of Astrophysical Interest. Part III. Acta Astron., 13:30–54. 2.1.5

Sumi, T., Kamiya, K., Bennett, D. P., Bond, I. A., Abe, F., Botzler, C. S., Fukui, A., Furusawa, K., Hearnshaw, J. B., Itow, Y., Kilmartin, P. M., Korpela, A., Lin, W., Ling, C. H., Masuda, K., Matsubara, Y., Miyake, N., Motomura, M., Muraki, Y., Nagaya, M., Nakamura, S., Ohnishi, K., Okumura, T., Perrott, Y. C., Rattenbury, N., Saito, T., Sako, T., Sullivan, D. J., Sweatman, W. L., Tristram, P. J., Udalski, A., Szymański, M. K., Kubiak, M., Pietrzyński, G., Poleski, R., Soszyński, I., Wyrzykowski, Ł., Ulaczyk, K., and Microlensing Observations in Astrophysics (MOA) Collaboration (2011). Unbound or distant planetary mass population detected by gravitational microlensing. Nature, 473(7347):349–352. 1.2.4

Tang, Y.-W., Dutrey, A., Guilloteau, S., Chapillon, E., Pietu, V., Di Folco, E., Bary, J., Beck, T., Beust, H., Boehler, Y., Gueth, F., Huré, J.-M., Pierens, A., and Simon, M. (2016). Mapping CO Gas in the GG Tauri A Triple System with 50 au Spatial Resolution. ApJ, 820(1):19. 6.3.7

Taniguchi, K. and Nakamura, T. (2000). Equilibrium sequences of irrotational binary polytropic stars: The case of double polytropic stars. Phys. Rev. D, 62(4):044040. 4

Toci, C. and Galli, D. (2015a). Polytropic models of filamentary interstellar clouds - I. Structure and stability. MNRAS, 446(2):2110–2117. 1.1, 2.1.5

Toci, C. and Galli, D. (2015b). Polytropic models of filamentary interstellar clouds - II. Helical magnetic fields. MNRAS, 446(2):2118–2124. 1.1, 2.1.5

Tohline, J. (1984). The collapse of rotating stellar cores-equilibria between white dwarf and neutron star densities. *The Astrophysical Journal*, 285:721–728. 1.2.3

Townsend, R. H., Owocki, S. P., and Howarth, I. D. (2004). Be-star rotation: how close to critical? *Monthly Notices of the Royal Astronomical Society*, 350(1):189–195. 1.2.3

Townsend, R. H. D. and Owocki, S. P. (2005). A rigidly rotating magnetosphere model for circumstellar emission from magnetic OB stars. MNRAS, 357(1):251–264. 1.2.3

Trova, A. (2013). *Gravité des systèmes verticalement homogènes: applications aux disques astrophysiques*. PhD thesis. 3.3

Vandervoort, P. O. (1980). The equilibrium of a galactic bar. ApJ, 240:478–487. 1.1, 1.2.5, 2.3.1

Vazan, A., Helled, R., Podolak, M., and Kovetz, A. (2016). The evolution and internal structure of jupiter and saturn with compositional gradients. *The Astrophysical Journal*, 829(2):118. 5.4

von Zeipel, H. (1924). The radiative equilibrium of a rotating system of gaseous masses. MNRAS, 84:665–683. 2.2

Wang, K., Testi, L., Ginsburg, A., Walmsley, C. M., Molinari, S., and Schisano, E. (2015). Large-scale filaments associated with Milky Way spiral arms. MNRAS, 450(4):4043–4049. 1.2.1

Ward-Thompson, D., André, P., and Kirk, J. M. (2002). The initial conditions of isolated star formation - V. ISOPHOT imaging and the temperature and energy balance of pre-stellar cores. MNRAS, 329(2):257–276. 1.2.1

White, R. J. and Hillenbrand, L. A. (2005). A Long-lived Accretion Disk around a Lithium-depleted Binary T Tauri Star. ApJ, 621(1):L65–L68. 1.3

Wisdom, J. and Tremaine, S. (1988). Local simulations of planetary rings. *The Astronomical Journal*, 95:925–940. 7.2

Wong, C. Y. (1973). Toroidal and spherical bubble nuclei. *Annals of Physics*, 77(1):279–353. (document), 1.1, 1.5, 6, 6.1, 6.1, 6.1, 6.1, 6.1, 6.2.3

Wong, C.-Y. (1974). Toroidal figures of equilibrium. ApJ, 190:675–694. 1.1, 6

Zeilik, M. and Gregory, S. (1998). *Introductory Astronomy and Astrophysics*. 1.2.3

Zucconi, A., Walmsley, C. M., and Galli, D. (2001). The dust temperature distribution in prestellar cores. A&A, 376:650–662. 1.2.1